# NEUTRONS TO PROBE NANOSCALE MAGNETISM IN PERPENDICULAR MAGNETIC RECORDING MEDIA

**Vikash Venkataramana**

**A Thesis Submitted for the Degree of PhD**
**at the**
**University of St. Andrews**

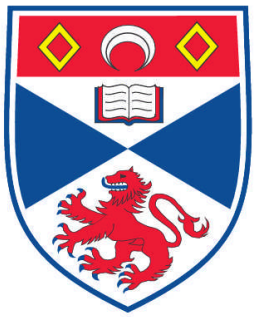

**2012**

# Neutrons to probe Nanoscale Magnetism in Perpendicular Magnetic Recording Media

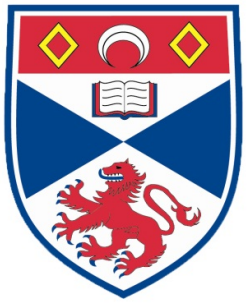

University
of
St Andrews

Dissertation

for

Doctor of Philosophy in Physics
(Ph. D.)

at the

University of St Andrews, UK

VikashVenkataramana

St Andrews, September 2011

## Abstract

Magnetic recording media refers to the disc shaped thin film magnetic medium present inside the hard disk drive of a computer. Magnetic recording is an important function of the hard disk drive by which information such as text, pictures, audios and videos are stored. Information is broken down to a simple binary format and is stored as magnetised bits along the tracks of the disk forming the hard drive. Over the years advancements in research on the type of magnetic materials used has allowed increased data storage capacities by reducing magnetic bit sizes.

It is with this advancement in magnetic data storage, that we have today's hard disk drive technology, which uses a perpendicular magnetic medium to store data. A perpendicular magnetic medium is a multilayered magnetic thin film structure with the topmost layer comprising nanoscale magnetic grains of high perpendicular anisotropy. The topmost recording layer (RL) is mapped into individual bits of 80-100 $nm^2$ area that consist of 5-10 nm diameter CoCrPt grains, embedded in an oxide matrix. A bit area is defined to ensure a significant number of stable grains allowing data to be stored in each bit as a '0' or a '1' depending on its switched magnetic state. The magnetic grains if sputtered below a threshold grain size tend to suffer from thermal fluctuation and instability due to super-paramagnetic effects, hence bringing limitations to grain size. As a result of this, research in recent years has been directed at introducing a softer magnetic exchange coupled composite (ECC) layer above the recording layer. This layer facilitates the delicate balance of switching smaller grains with strong magneto-crystalline anisotropy at lower magnetic fields, by exchange coupling with the CoCrPt grains in the recording layer. However this technique of increasing the efficiency in the perpendicular magnetic medium by introducing 'facilitating' layers is an area that is still being widely researched and understood.

Although numerous surface and bulk analysis techniques exist to study magnetic and surface properties of these materials, there is limited information on the structural and magnetic properties of these materials at the nanoscale level. The reported work investigates the structural and magnetic properties of the magnetic grains and multi-layersin the perpendicular magnetic medium using polarised neutron scattering and reflectivity techniques. The work investigates the structural and magnetic properties of the CoCrPt grains, apart from

understanding the CoCrPt magnetic grain switching. The work also investigates the magnetisation in the layers of the thin film perpendicular media structure using polarised neutron reflectivity (PNR).

Using polarised small angle neutron scattering (PolSANS), it has been shown that ferromagnetic ordered core region of the CoCrPt grain in the recording layer is smaller than the physical CoCrPt granular structure. The magnetic switching behaviour of the CoCrPt grain at different magnetic fields is also analysed and the experimental PolSANS data is fitted with non-interacting size-dependent analytical grain switching models. This result provides significant evidence that the magnetic anisotropy increases with grain size, with larger magnetic grains having larger magnetic anisotropy.

Polarised neutron scattering experiments are carried out with the magnetically softer exchange coupled composite (ECC) layer included in the thin film magnetic structure. The first experiments investigate if the ECC layer contributes to the nuclear and magnetic interference scattering term in the experimenting scattering data. The experiments clearly show that there is no contribution from the ECC layer in the nuclear and magnetic scattering interference term. The role of the ECC layer in the magnetic switching process is then investigated at different magnetic fields. The ECC layer was found to influence the size-dependentmagnetic grain switching of the CoCrPt grains in the recording layer and a detailed investigation is presented in the reported work.

Polarised neutron reflectivity (PNR) experiments have also been carried out with the ECC layer onthe perpendicular magnetic media samples. These experiments investigate the composition and thickness of the thin film structure, while also providing information on the magnetic state of the thin films under the influence of an in-plane magnetic field.The in-plane magnetisation in the recording and ECC layeris determined at different in-plane magnetic fields. The magnetisation values determined for the ECC layer and the recording layer (RL) at different in-plane magnetic fields help better understand the differences in their magnetic properties.

*to my dearest mummy and daddy.*

## Acknowledgements

I would like to firstly thank my supervisors Professor Stephen Lee and Dr. Stephen Lister for their inspiring discussions and their continued support. Dr Stephen Lister has on numerous occasions patiently explained to me complicated concepts, making sure I had a good understanding of the subject. I would also like to thank Professor Thomas Thomson from the University of Manchester who patiently shared his knowledge despite my many questions.

From the group, I would like to thank Dr. Matthew P. Wismayer, Dr. Mark de Vries and Dr. David Heron for their valuable guidance and timely advice that has been truly invaluable during the course of my PhD. I would also like to specially thank Soumya Jyoti Ray who through his motivating conversations ensured that I live up to whatever challenges I have had to face through the course of my PhD.

Iam also grateful to Dr. Joachim Kohlbrecher (PSI), Dr. Joachim Stahn (PSI), Dr. Charles Dewhurst (ILL) and Dr. Sean Langridge (ISIS) for the initial training and assistance provided while working in their facilities. I would also like to take the opportunity to thank Ken Takano, from Hitachi San Jose research center (USA) for providing me with a range of samples for my PhD project.

I am also deeply indebted to the wonderful people here at the School of Physics. I take the opportunity to thank all the people who have been involved in my life here at St Andrews, through the University student union, New hall and all my other commitments. I am indeed most indebted to St Andrews, for giving me such wonderful friends who I will cherish for life.

Finally, I wish to thank Scottish Universities Physics Alliance (SUPA) along with Hitachi Instruments (USA) in providing me financial support to pursue my PhD through the 'SUPA Prize Scholarship' as apart from supporting me in attending International Conferences, Workshops and Summer/Winter Schools through the Research Training and Support Grant.

Last but not the least, I would like to thank my wonderful mother, my doting father, my loving brother, my adorable dog and my best friends back home who have for a long time now been very supportive of my decisions even if it did require me having to live away from them for long periods of time. You guys mean the world to me and you know it.

*Thank you everybody for being in my life and making this happen.*

## Declaration

I, VikashVenkataramana, hereby certify that this thesis, which is approximately 40,000 words in length, has been written by me, that it is the record of work carried out by me and that it has not been submitted in any previous application for a higher degree.

I was admitted as a research student in September, 2007 and as a candidate for the degree of Doctor of Philosophy in September, 2011; the higher study for which this is a record was carried out in the University of St Andrews between September, 2007 and September, 2011.

(VikashVenkataramana) September 2011

I hereby certify that the candidate has fulfilled the conditions of the Resolution and Regulations appropriate for the degree of Doctor of Philosophyin the University of St Andrews and that the candidate is qualified to submit this thesis in application for that degree.

(Stephen Lee) September 2011

In submitting this thesis to the University of St Andrews I understand that I am giving permission for it to be made available for use in accordance with the regulations of the University Library for the time being in force, subject to any copyright vested in the work not being affected thereby. I also understand that the title and the abstract will be published, and that a copy of the work may be made and supplied to any bona fide library or research worker, that my thesis will be electronically accessible for personal or research use unless exempt by award of an embargo as requested below, and that the library has the right to migrate my thesis into new electronic forms as required to ensure continued access to the thesis. I have obtained any third-party copyright permissions that may be required in order to allow such access and migration, or have requested the appropriate embargo below,

*Access to printed copy and electronic publication of thesis through the University of St. Andrews.*

(VikashVenkataramana) (Stephen Lee) September 2011

## Contents

## Chapter 5 Investigating size dependant magnetic grain switching in the recording layer using PolSANS



## Chapter 6 Investigating the effect of the exchange layer on Perpendicular recording medium using PolSANS

## Chapter 7 Investigating magnetisation across the exchange and recording layer of the perpendicular magnetic medium using PNR



## Chapter 8 Summary and future work

# Chapter 1
# Perpendicular Magnetic Media

---

**Contents**



---

**Abstract**

A brief summary on the historical significance of today's hard disk drive technology is presented. The working of a hard disk drive, describing the working magnetics of the thin film magnetic structure in the perpendicular magnetic medium is introduced. The necessary theory covering magnetic anisotropies, the Stoner-Wohlfarth grain model, RKKY coupling, Néel's orange peel coupling, anisotropy fields, super-paramagnetic effects and the Néel- Arrhenius equation are described. A more detailed understanding of the structure and composition of the magnetic thin film medium is elucidated. Brief descriptions of existing characterisation techniques with their limitations are presented. Finally, the motivation and the objectives for the reported worked are highlighted.

## 1.1 Background and historical significance

Magnetic data storage has come a long way through the years, with the human race now being able to store and retrieve a wide range of information as ones and zeros on nanoscale magnetic materials [1,2,3]. The first major breakthrough in the advancement of this technology came in 1898 when Danish Engineer, Valdemar Poulsen developed the Telegraphone to successfully record the speech of the Austrian emperor Franz Joseph at the Exposition Universelle in Paris [1,4].

**Figure 1.1** A photograph of the Telegraphone developed by Poulsen in 1898 [4]

Figure 1.1 is a photograph of the Telegraphone in which the magnetic wire is used as the magnetic medium to store and retrieve data [4]. Since then magnetic tape, magnetic particles, magnetic cores, magnetic bubbles, magnetic drums have all been used over the years in the advancement of magnetic recording systems [5,6,7,8,9].The major breakthrough that led to the present day magnetic recording technology came in the 1956 when IBM first introduced its platter based recording technology called the IBM 350 Disk Storage [10].

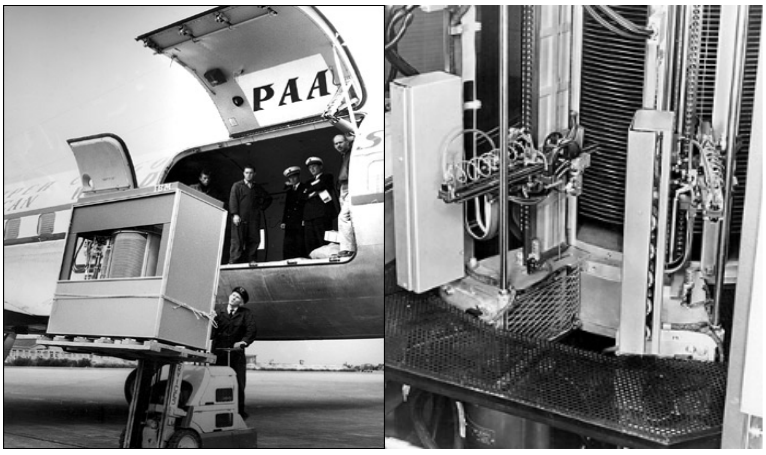


(a) (b)

**Figure 1.2** (a) IBM 350 Disk Storage being transported on a plane in 1956 [10] (b) First moving head hard disk drive IBM 350 Disk Storage designed in 1956 [10]

The IBM 350 Disk Storage is considered the closest ancestor to the modern day hard disk drive, as like a modern day perpendicular hard disk drive, the IBM 350 consisted of a number of aluminium/glass substrates coated with a magnetic film of numerous magnetic grains [10]. The platters were coated on both sides and stacked on top of each other with the whole setup occupying almost an entire room. Data was stored and retrieved by read/write heads located on both sides of each platter while a stack of platters rotate at approximately 3,600 to 10,000 revolutions per minute [10]. The IBM 350 Disk Storage shown in Figure 1.2 had a hard disk drive capacity of around 2,000 bits per square inch, and was capable of storing up to 50 million characters on its 24 inch diameter magnetic iron oxide coated platters [10,11]. The similarity in the working of the IBM 350 Disk Storage and present day hard disk drive is evident in Section 1.2 of this chapter where the working of a perpendicular magnetic medium hard disk drive is introduced.

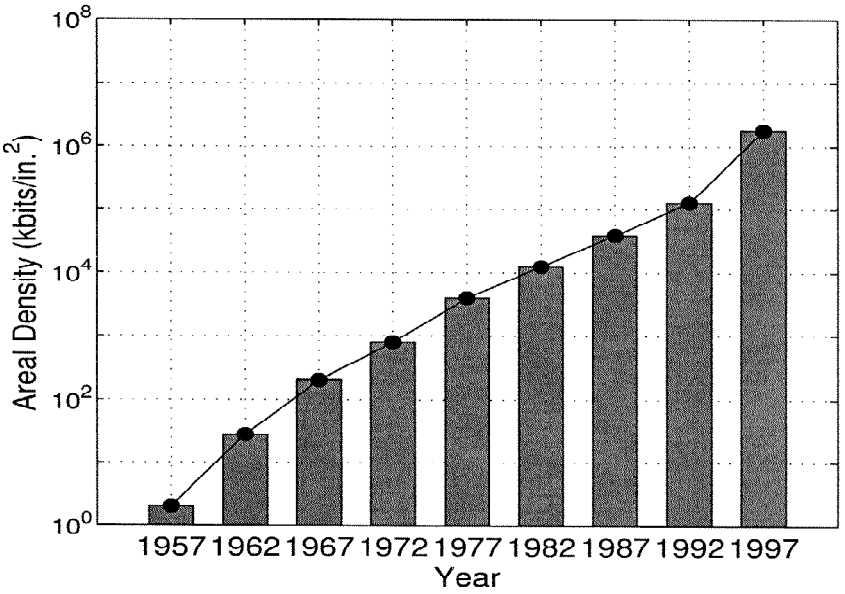


**Figure 1.3** Data storage road map plotting increasing areal density between the years 1957 and 1997 [12]

The major drawback for the IBM 350 Disk Storage was its large size making it impossible to be a part of a personal computer [10]. The advent of personal computers created the need for smaller data storage devices with larger data storage capacities [13]. This was only possible by scaling down the components of the data storage device while still being able to increase its areal data storage density [13]. This was achieved with the advent of advanced thin film growth and characterisation techniques in the 1980's [6,14]. Advances in thin film growth techniques allowed the growth of magnetic multilayers [6,14].

By controlling the properties of the thin film, it was possible to grow smaller magnetic grains in the thin film structure [6,14]. As a result of this technological advancement, the data storage medium shrunk considerably [14]. The platters in the IBM 350 Disk Storage unit were replaced by glass disks with magnetic grains present in the multi-layered thin film structure [14]. This technological advancement led to the manufacturing of the first 5.25-inch hard disk drive in 1980 by Seagate Technology (then Shugart Technology) [15]. Over time the areal data storage capacity increased as seen in Figure 1.3 and Figure 1.4, and by 2005 the storage capacity of magnetic hard disk drive reached 100 gigabits per square inch [12]. Please note that the vertical axis in Figure 1.4 is logarithmic, so the fit line corresponds to exponential growth. This period in magnetic data storage technology was called longitudinal magnetic media technology, as the magnetic easy axis of the grains in the storage medium was along the plane of the thin film [16].

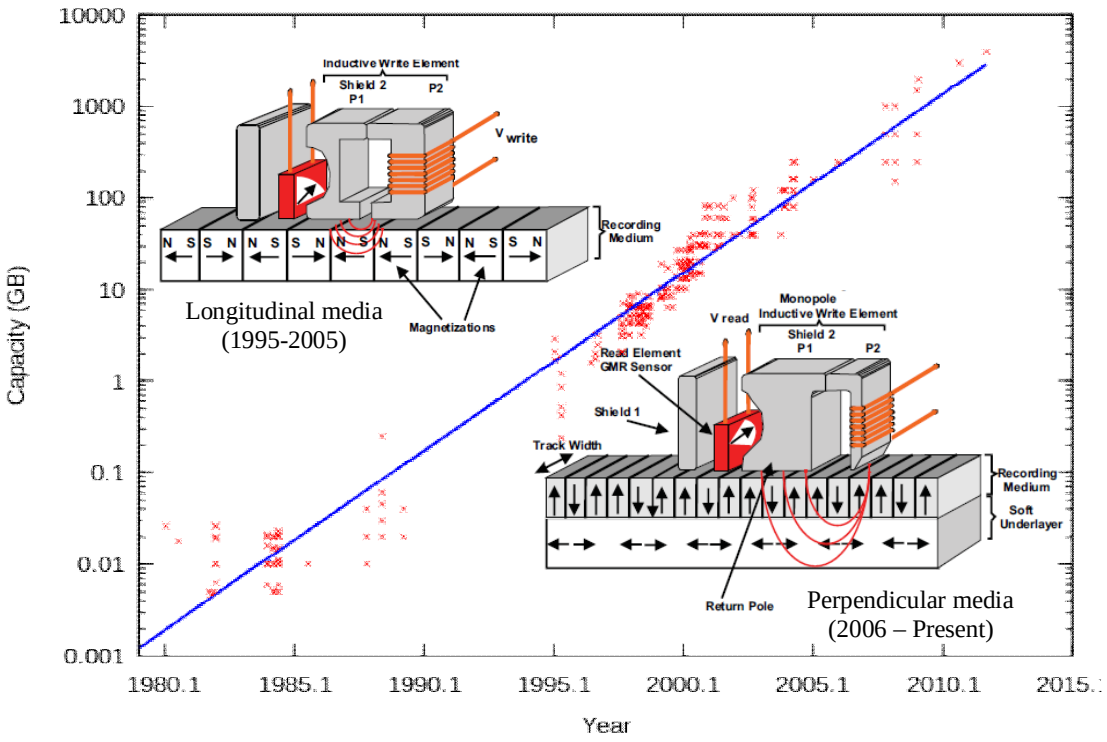


**Figure 1.4** The predicted data storage road map (red coloured data points) with a fitted line (blue) highlighting the increase in data storage capacity after the advent of thin film technology forecasted till the year 2015 [12]. Inset shows images of longitudinal and perpendicular magnetic media with their time frames.

The next technological advancement was made by significantly reducing the packing density of the grains [12]. This is achieved in the perpendicular magnetic medium where magnetic grains have an easy axis perpendicular to the plane of the thin film [17]. A magnetic easy axis perpendicular to the plane of the film facilitates increased packing densities allowing larger data storage capacity per square inch. This technology is called Perpendicular recording media technology and is introduced in Section 1.2 of this chapter [17]. Seagate very recently announced that their hard disks use perpendicular magnetic media that have storage capacities of 1 Terabyte memory on each platter of their hard disk drive [18]. This approximates to about a storage capacity of 625 gigabits of memory per square inch which at the time of writing is the largest areal data storage density [18].

## 1.2 Working of Perpendicular magnetic media

In order to understand the role of the perpendicular magnetic medium in a hard disk drive, an introduction to the working of a present day hard disk drive is necessary. This section gives a basic overview of the working magnetics of the perpendicular magnetic medium [17]. This is done by first introducing the various components in a hard disk drive and then briefly explains the working magnetics of the perpendicular magnetic medium. A more specialised understanding of the working of the perpendicular magnetic medium would require an introduction to the magnetic theory related to perpendicular magnetic media, while considering the composition of the multi-layered thin film magnetic structure [17]. This introduction to the magnetic theory and the composition of the perpendicular magnetic medium is given in Section 1.3 and Section 1.4 of the reported work.

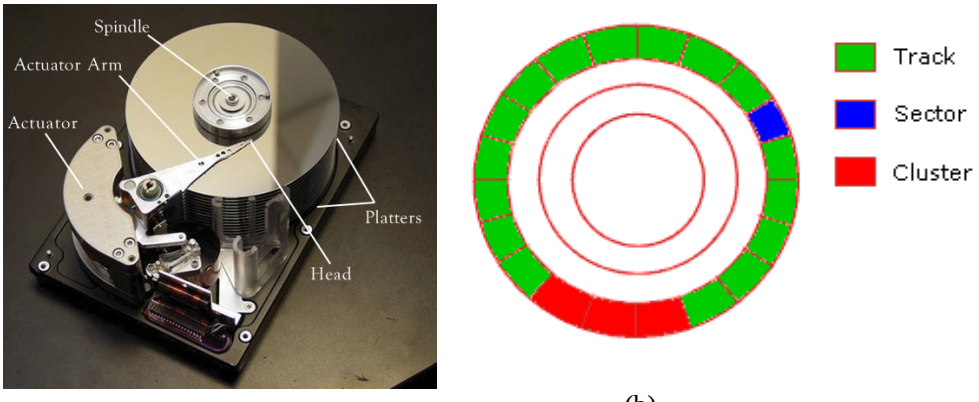


(a) (b)

**Figure 1.5** (a) A photograph of a magnetic hard disk with all its parts [19]
(b) A cartoon of a magnetic disk sectioned into tracks, sectors and clusters

It is evident in Figure 1.5a, that the 3.5-inch disk takes up the most amount of space on a hard disk drive [19]. The hard disk drive usually consists of two or more such disks held together by a spindle, rotated using a motor to speeds of around 3000 - 15,000 RPM. An actuator arm is used to read and write data on the disk [17,20]. The actuator arm is the access arm for the read/write heads that are strategically placed on the end of the arm [17,20]. The actuator arm is designed in a way to move over the disk using a voice coil motor (VCM) capable of accessing different sections of the disk [17,20,21]. The motors responsible for spinning the disks and moving the actuator are controlled by electronics mounted on a printed circuit board, providing instructions for data storage across the disk [20].

The 3.5-inch disk that constitutes the perpendicular magnetic media is divided further into tracks and sectors as shown in Figure 1.5(b) [17,21]. The data is stored in thin concentric bands called tracks with more than a thousand tracks present across a disk [21]. Each track is further broken into sectors, with the sector typically being the smallest physical storage unit on a disk capable of storing 512 bytes of data [21]. Data files of more than 512 bytes are stored in clusters, which are a group of easily accessible sectors, whose access instructions are given using the hard disk drive electronics [21].

*Magnetics of the perpendicular medium*

We know that the disk constitutes the magnetic multi-layered thin film structure called the perpendicular magnetic medium [17]. The read/write process that is used for data storage and retrieval in the perpendicular medium further explains the role of thin film structure and the need for the multi layered magnetic medium[17,22]

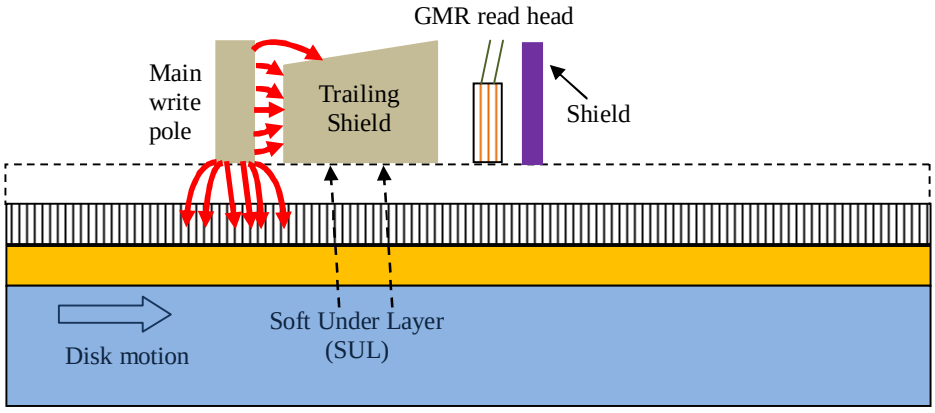


**Figure 1.6** Graphical interpretation of the read/write process on a perpendicular magnetic medium with all the components of perpendicular magnetic media technology.

Figure 1.6 is a cartoon of an advanced write head component that has been applied in recent perpendicular media technology. It is evident in Figure 1.6, that perpendicular magnetic recording technology uses the entire magnetic medium to generate a strong perpendicular write field [17]. This is achieved by introducing soft under layers beneath the recording layer and the seed layers in the magnetic medium [23]. The soft under layers generate a strong perpendicular component of magnetic field required to switch the perpendicular grains in the recording layer of the magnetic structure [23,24]. The single pole perpendicular magnetic field in combination with the soft under layers and a trailing shield (shown in Figure 1.6), facilitate the completion of a magnetic loop in the system [23]. The trailing shield head deployed in perpendicular magnetic recording technology is designed in such as way so as to ensure the completion of the magnetic loop in the hard disk drive [23,21]. This ensures that there is no residual magnetism providing better bit-error rate performance in the hard disk drive [25].

The read head of actuator arm uses Giant magneto resistance(GMR) technology, detecting the spin up and down states of the magnetic grains as '1''s and '0''s. A thin film spin valve sensor is used to detect the magnetisation state of the bit [26]. The magnetisation state is detected by measuring the change in the electrical resistance across the spin valve structure differentiating the magnetised states of the grains [26,27]. A detailed description of the components and the working magnetics of a perpendicular hard disk drive are beyond the scope of the reported work and can be looked up in these references [17,20,21,22,23,24].

## 1.3 Theory associated with Perpendicular magnetic media

This section gives a brief introduction to the necessary magnetic theory associated with perpendicular magnetic media. When considering a perpendicular magnetic medium, it is important to take into account both the magnetic properties of thin film structure and the nanoscale granular structure present in the topmost recording layer of the thin film multi-layered magnetic medium [27,28,29]. Hence, this section introduces both the magnetic theory associated with thin films and nanoscale magnetic grains present in the recording layer of the perpendicular magnetic medium.

### 1.3.1 Magnetism in thin films

In contrast to bulk magnetic materials, magnetic properties of the magnetic thin films are influenced by several additional factors [28,30]. The thin film growth technique used, the thickness of the thin film and the density of the thin film are some of the many factors that influence the properties of the magnetic thin film in a multi-layered thin film structure [30]. Apart from individual thin film magnetic properties, the presence of neighbouring magnetic thin films in a multi-layered structure and interface spacer layers between magnetic thin films induce RKKY (Ruderman-Kittel-Kasuya-Yosida) interactions [31]. This section discusses magnetic thin film properties directly relating to perpendicular magnetic recording media introducing thin film anisotropies, magnetic domain wall effects and the RKKY interactions.

*a. Anisotropy in Thin films*

A magnetic material is termed anisotropic when it exhibits a direction dependence of its magnetic properties, without the influence of an external field as a result of other physical parameters [27]. This is a result of an easy energetically favourable axis of orientation in the absence of a magnetic field. The effective anisotropy constant ($K_{eff}$) of a magnetic thin film can be expressed in terms of magnetic anisotropy energy (E) as [27,32],

$$E = K_{eff} \sin^2\theta \qquad (1.1)$$

The effective anisotropy term constant $K_{eff}$ has to take into consideration the anisotropy as a result of the magnetostatic contribution (shape anisotropy), magnetoelastic term, the surface anisotropy term and the magneto-crystalline anisotropy of the thin film [27,32]. The angle $\theta$ here is defined as the angle between normal to the surface and the direction of the magnetisation.

Let us first consider the surface anisotropy term of the effective anisotropy. The surface anisotropy in a thin film arises as a result of interface effects like that of broken symmetry between two thin films [27,32]. This anisotropy term is volume independent and its anisotropic energy can be defined as $\sigma = K_s \sin^2\theta$, where the anisotropy $K_s$ is perpendicular to the plane of the film when $\theta=90^o$.

The surface anisotropy energy term $E_s$ when considered over a film of thickness (d) and volume (V) can be written as [27,32].,

$$\frac{E_s}{V} = \frac{1}{d} K_s \sin^2 \theta \ (\text{nJ/cm}^3) \tag{1.2}$$

This term is usually described as $\frac{2K_s}{d}$, taking into the account the effect of two interfaces experienced by a thin film layer [27,28,32]. The effective anisotropy constant ($K_{eff}$) can now be broadly classified into a volume term ($K_v$) and a surface term ($K_s$),

$$K_{eff} = K_v + \frac{2K_s}{d} \tag{1.3}$$

The volume anisotropy term $K_v$ is further broken down into,

$$K_v = K_u + K_{me} - \frac{1}{2}\mu_0 M_s^2 \tag{1.4}$$

Here $K_u$ is the anisotropy constant as a result of the crystalline structure of the magnetic material, called the magneto-crystalline anisotropy [27,32]. The magneto-crystalline anisotropy is dependent on the crystalline structure of the material, playing an important role in materials that exhibit a crystal structure in the thin film [27,32]. $K_{me}$ called the magneto elastic anisotropy arises as a result of spin orbit interactions between neighbouring atoms in a lattice. Under the influence of stress (σ) induced strain (ε) the anisotropy constant term can be written in terms of the angle of the applied stress (θ) and magnetostriction constant (λ) for various crystal directions [27,32].

$$K_{me} = \frac{3}{2}\lambda\sigma\cos^2\theta \tag{1.5}$$

If λ is positive, the magnetic easy axis will be along the direction of the tensile stress, which is perpendicular to the plane of the thin film [27,32].

The shape anisotropy is the most influential anisotropy in an amorphous magnetic thin film [27,32]. This results in the dipole-dipole coupling encouraging an easy axis in plane magnetisation along the plane of the thin film. However the thickness of the magnetic thin film (d) plays a crucial in this dipole-dipole long range coupling, as the thickness of the thin film determines the extent of the strength of the long range dipole-dipole interaction [27,32]. Apart from thickness, the magnetic properties of the thin film and the strength of the applied

magnetic field also influence the long range dipole-dipole interaction in the thin film [27,29, 32]. From it is evident that for a uniform amorphous magnetic thin film, the extent of the long range dipole-dipole coupling influences the dominance of easy axis in plane magnetisation as result of shape anisotropy in the thin film [27,32]. This shape anisotropy energy per unit volume as a result of this dipolar coupling is given as $-\frac{1}{2}\mu_0 M_S^2$.

Hence if $K_{eff}>1$ in Equation 1.3, the anisotropy is perpendicular to the plane of the film from the other dominating anisotropy effects as a result of stress, interface effects and/or the crystalline nature of the thin film [27,32]. If $K_{eff}<1$ in Equation 1.3, the anisotropy is dominated by the easy magnetic axis of the thin film which is along the plane of the thin film [27,32].

*b. Exchange coupling between magnetic layers*

Exchange coupling occurs as a result of exchange forces between neighbouring atoms, giving rise to ferromagnetic behaviour in a material [27,33]. These exchange forces observed between neighbouring atoms in ferromagnetic materials, are observed in adjacent ferromagnetic thin films in a multi-layered thin film structure [33]. It was also found that by using a non-magnetic spacer layer between the two ferromagnetic layers, the exchange coupling between the magnetic layers would be ferromagnetic or anti-ferromagnetic depending on the properties and the thickness of the spacer layer used as shown in Figure 1.7. This type of interaction is called the Ruderman-Kittel-Kasuya-Yosida (RKKY) interaction [31,33].

Ruderman-Kittel-Kasuya-Yosida (RKKY) theory has been widely used to explain the nature of the exchange coupling between the two magnetic layers [31,33]. RKKY theory states that there exists a broad indirect exchange coupling between the nuclear magnetic moments of atoms through conduction electrons [31,33]. The conduction electrons interact with the nuclear spin of both atoms creating correlation energies between the two spins [31,33]. This interaction also depends on a number of other factors one of which is the distance between the nuclear magnetic moments [33].

Along with the RKKY type of interaction, a direct exchange coupling between the inner shell electrons and the conducting electrons is observed exhibiting localised disturbances resulting in energy oscillations [31,33]. These localised energy oscillations also influence the RKKY interactions present [31,33].

The RKKY type of interaction is also influenced by the crystalline structure of elements explained using crystal field theory [27,33]. Crystal field theory highlights the role of the shape of the atomic orbitals and their influence on the energy levels of the atoms with a crystalline structure [27,33]. Neighbouring atoms in a crystal have overlapping orbitals, whose shape and angular dependence varies depending on the type of orbital (s, p, d and f). The symmetry of atoms in a local environment would result in electrostatic interactions resulting in energy oscillations [27,33].

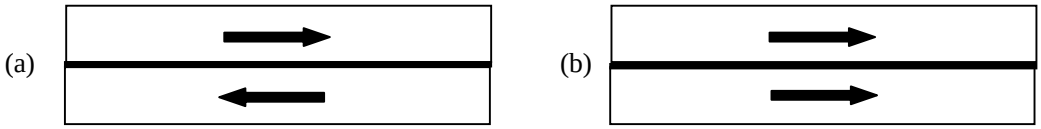


**Figure 1.7** (a) Anti-Ferromagnetic coupling and (b) Ferromagnetic coupling in thin films, determined by the nature of the RKKY interaction observed.

The RKKY interactions are also influenced by both the magnetic properties, and the thickness of the thin films in the multi-layered thin film structure [31,33]. Taking into account the thickness and the magnetic properties of the thin film and by using the right spacer layer, it is possible to control the energy oscillations by controlling the thickness of the spacer layer [33]. Depending on the thicknesses of the spacer layer used, the system oscillates between a ferromagnetic and an anti-ferromagnetic coupled state; while constantly aiming to achieve the most energetically favourable state [27,33].

Ferromagnetic coupling between two parallel ferromagnetic layers can be explained for very thin spacer layers using the pinhole theory [33]. Pinholes are caused as a result of a non-continuous spacer layer, resulting in direct contact between ferromagnetic layers [33]. This leads to direct coupling between ferromagnetic layers, favouring a parallel magnetic alignment along the dominant anisotropy in the magnetic material [33]. Figure 1.8a is a cartoon of two ferromagnetic layers separated by a non-magnetic spacer layer with a non-continuous spacing that facilitates a ferromagnetic coupling between the two magnetic layers.

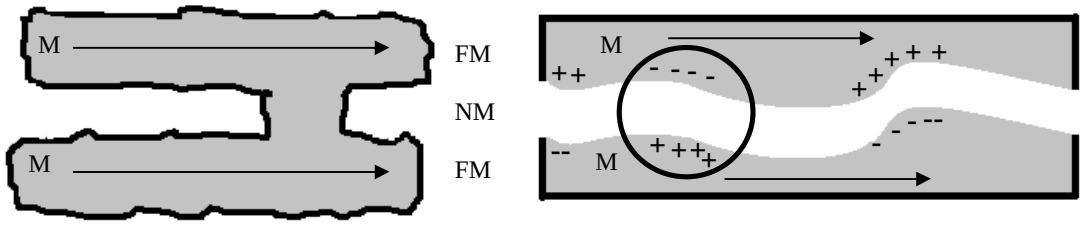


**Figure 1.8** (a) Pinhole coupling between the magnetic thin films (FM) using a non-magnetic spacer layer(NM) (b) Néel's orange peel coupling between ferromagnetic films (FM) as a result of correlated roughness separated by a non-magnetic spacer layer (NM). The interaction of opposite magneto-static charges across the non-magnetic spacer (NM) is shown in the figure.

Another type of ferromagnetic coupling observed in magnetic multilayers is the Néel's orange peel coupling [33]. Néel's orange peel type of coupling arises from correlated roughness between two magnetic layers separated by a non-magnetic spacer layer [33]. The opposite signs of the magneto-static charges present on the surface of the interfaces of the two magnetic layers align symmetrically. This encourages a positive dipolar interaction resulting in ferromagnetic coupling between the two magnetic layers on either side of the non-magnetic spacer layer [33]. Figure 1.8b is a cartoon showing Néel's orange peel theory of magnetic coupling between two magnetic thin films that are magnetised along the plane of the thin film, separated by a non-magnetic spacer layer.

### 1.3.2 Magnetism in single domain nanostructures

When the dimensions of a material are restricted in 3 dimensions to the nanoscale regime, the material begins to exhibit a single domain magnetic behaviour [29]. This single domain magnetic behaviour is governed by the sum of anisotropy energy term present in the single domain structure [34]. The magnetic grains in the recording layer of the perpendicular magnetic medium are single domain granular structures embedded in an oxide matrix[34].

This section discusses magnetic properties of single domain granular structures that are governed by a strong magneto-crystalline anisotropy. The anisotropy associated with a single domain granular structure is introduced and anisotropy energy for the hexagonal crystal phase (hcp) in Co is derived [35]. The Stoner-Wohlfarth ellipsoidal grain model is used to

explain the magnetic switching of the ellipsoidal grain with hysteresis loops [36,37]. The Super-paramagnetic effect is introduced and differences between the normal magnetisation process and the super-paramagnetic effects are illustrated using energy barrier diagrams [27,38]. Anisotropy fields with relevance to magneto-crystalline anisotropy are then introduced to diskuss the rate of magnetic switching using the Néel-Arrhenius equation [27, 39, 40].

### *a. Anisotropy in single domain granular nanostructures*

The magnetic grains in the perpendicular recording medium exhibit a single domain magnetic behaviour, having a large magnetic spin and a large magnetic coercivity [29]. The large magnetic coercivity associated with the grain requires a strong magnetic field to switch the magnetic state of the grain in order to store data as 1's and 0's depending on the switched magnetic state of the grain [29,34]. Considering the magnetic grains in the perpendicular medium to behave like a non-interacting system the anisotropy energy (E) associated with each individual grain in the system can be determined. This anisotropic energy (E) term for an individual grain is given as in Equation 1.1 as [34],

$$E = K_{eff} \sin^2\theta \text{ (nJ)} \qquad (1.1)$$

Here $K_{eff}$, the effective anisotropy can be described as the sum of a volume anisotropy term ($K_v$) and a surface anisotropy term ($K_s$) as described in Equation 1.4. Although the surface anisotropy term is present in the system, its presence is made insignificant by the anisotropy contribution of crystalline nature of the nanoscale grain [34].

The volume anisotropy term is dominated by the uniaxial anisotropy ($K_u$) term as a result of the strong magneto-crystalline anisotropy in the magnetic grain alloy [34]. The effect of strong uniaxial anisotropy results in a chosen easy magnetic axis of alignment, making it less energetically favourable for a magnetic grain to align in any other direction [34,35]. As a result of strong uniaxial anisotropy the granular structure exhibits a single domain magnetic behaviour, switching favourably along its easy magnetic axis with an applied magnetic field [27,34,35]. The magneto-crystalline anisotropy is as a result of the crystalline nature of the grain, arising mostly from spin orbit coupling in the crystal structure [34,35]. This magneto-crystalline energy is usually expressed as an expansion in direction cosines of magnetisations along a magnetisation vector $\vec{M} = M_s(\alpha, \beta, \gamma)$ and in its general form given as [35],

$$E_a(\theta,\phi) = \sum_{n=0}^{\infty}\sum_{m=0}^{n} K_n^m P_n^m(\cos\theta)\cos m\phi \quad \text{(nJ)} \tag{1.6}$$

Where $P_n^m$ represents the Legendre polynomials, $K_n^m$ represents the anisotropy constants, while θ and ϕ represent the polar and azimuthal angles of magnetisation direction. The magnetic grains in the perpendicular magnetic structure are found to have an easy out-of-plane magnetic axis as a result of closed packed hexagonal crystal phase (hcp) that governs the anisotropy term[35]. Figure 1.9 is a diagram of the hexagonal crystal phase (hcp) in Co, where the magnetisation vector M is mapped. The anisotropy energy for this phase is given as [35],

$$\frac{E}{V} = K_1\sin^2\theta + K_2\sin^4\theta + K_3\sin^4\theta\cos 6\phi \quad \text{(nJ/cm}^3\text{)} \tag{1.7}$$

where,

when $K_1=K_2=0$, the magnetic behaviour is isotropic.

when $K_1 > 0$ and $K_2 \geq 0$, the c axis is the easy axis.

when $K_1 < 0$ and $K_2 \leq 0$, the basal plane is the easy axis.

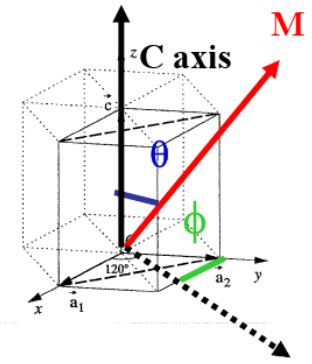


**Figure 1.9** Hexagonal crystal phase (hcp) observed in Co [35]

*b. Stoner-Wohlfarth model of magnetic switching*

To understand the switching of the single domain particle with uniaxial anisotropy the Stoner-Wohlfarth model is employed [36]. The Stoner-Wohlfarth model or the coherent rotation model is a simple but powerful micro-magnetic model used as a good approximation to understand the uniform magnetic switching of single domain nanoparticle under the influence of a static magnetic field [36,37].

The model assumes that in an individual nanoscale ferromagnet, there exists a strong exchange coupling between the atomic moments resulting in a constant magnetisation across the nanoscale ferromagnet [36,37]. The model limits itself to nanoscale dimensions and cannot be used for larger particles [36,37]. The model also assumes a temperature independent non-interacting system with no magnetostatic interactions between particles [36,37].

The model is a useful starting point to discuss the angular dependence of magnetisation curves from the principal magnetic axis of the nanoscale magnetic particle. An important prediction of the Stoner-Wolhfarth model is that the coercivity for an individual nanoscale magnetic particle is equal to the anisotropy field, in an individual nanoscale magnetic particle in a non-interacting system [36,37].

To better describe an individual magnetic grain in the recording layer, an ellipsoidal magnetic grain with a uniaxial anisotropy as seen in Figure 1.10a is considered. The magnetic grain has a uniaxial anisotropy along the major axis of the ellipsoid making it the easy axis (EA) of the ellipsoidal grain. An external magnetic field H is applied at an angle $\phi$ to the easy axis of the ellipsoidal magnetic grain [37]. A magnetic moment M evolves as a result of the applied field which is at an angle $\theta$ to the easy axis (uniaxial anisotropy axis) of the magnetic grain [37].

The magnetic moment M is subjected to two alignment forces, one due to K the anisotropy and the other due to H the applied static magnetic field. The total energy in the system is now written as the sum of the anisotropy energy ($E_A = K\sin^2\theta$) and the Zeeman energy ($E_Z = -M \bullet H$) as a result of the applied static field [37].

$$E = E_A + E_Z = K\sin^2\theta - HM_s\cos(\phi - \theta) \quad (nJ) \qquad (1.8)$$

The magnetic moment M will align in the direction where the total energy of the system is minimised. While considering a magnetic grain with strong uniaxial anisotropy the anisotropy energy is minimum when $\theta=0$ and $K > 1$ as stated in Equation 1.7.

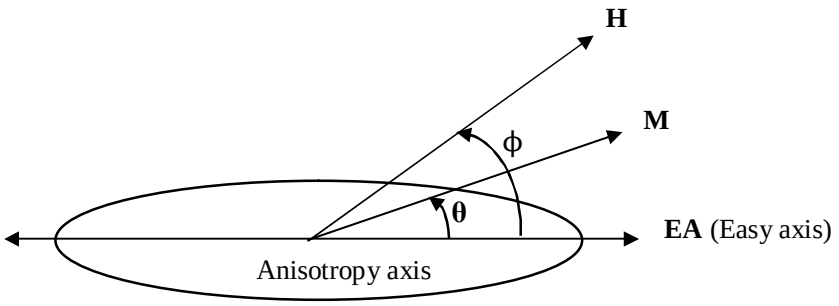


(a)

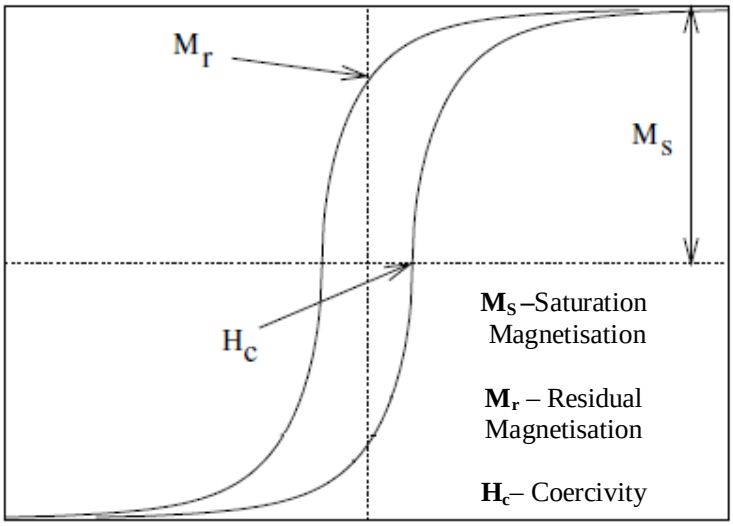


(b)

**Figure 1.10** (a) The magnetic moment (M) and the static magnetic field (H) are at angles θ and ϕ to the anisotropic easy axis of the ellipsoidal grain [37] (b) Hysteresis loop for the magnetisation of the ellipsoidal magnetic grain with respect to a static magnetic field (H) which is first increased and then decreased [37]

The model builds on the assumption that the magnetic switching of the ellipsoidal grain either occurs gradually or rapidly at a threshold magnetic field [37]. Rapid switching suggests that at a certain magnetic field the magnetisation is discontinuous, as at a threshold field the magnetic grain switches magnetic states. In Figure 1.10, when the angle ϕ between the easy axis (EA) of the ellipsoidal grain and the direction of the static magnetic field (H) is $0^o$, rapid magnetic switching between magnetic states occurs at the threshold magnetic field. No linear dependence of magnetisation with increasing/decreasing magnetic fields is evident. This type of switching is very similar to the magnetic switching observed in the CoCrPt magnetic grains present in the perpendicular magnetic medium [37].

In Figure 1.11, when $\phi = 0^o$, the hysteresis loop resembles a square and the ratio between saturation magnetisation ($M_s$) and the residual magnetisation ($M_r$) is close to one [37]. The squareness of the hysteresis loop is because for hard ferromagnetic materials, a strong coercive force is required to switch magnetic states thereby increasing the coercivity [37]. At this value of $\phi$, the angle between the magnetisation direction (M) and the easy anisotropic axis (EA) of the grain $\theta$ is 0, and the anisotropy K is taken to be greater than 1 under ideal conditions [37].

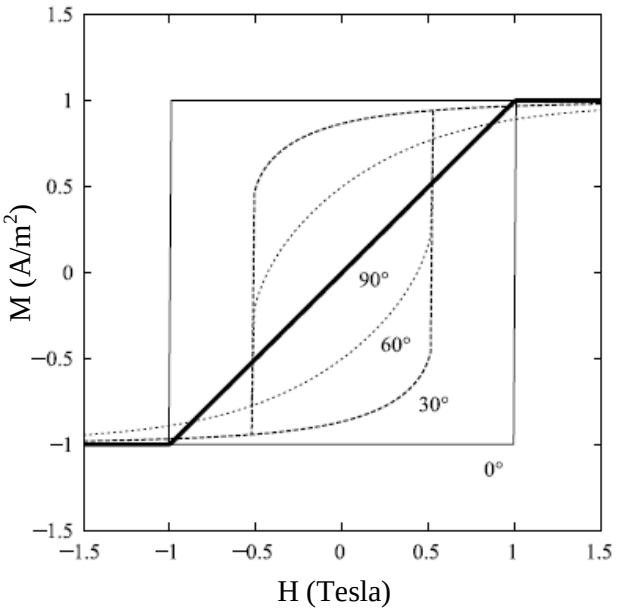


**Figure 1.11** Theoretically simulated hysteresis loops when the angle between the static magnetic field (H) and the easy/anisotropic axis is changed from $\phi = 0^o$ to $90^o$. This simulation considers a hard ferromagnetic material with a large coercivity [37]

In Figure 1.11, when $\phi$ changes from $0^o$ to $90^o$ the direction of the static magnetic field (H) moves from its initial ellipsoid grain easy axis (EA) direction at $\phi = 0^o$, to the ellipsoid grain hard axis direction at $\phi = 90^o$. It is evident that the hysteresis loop also changes as $\phi$ changes from $0^o$ to $90^o$. The square hysteresis loop previously observed at $\phi = 0^o$ gradually changes its shape with the initial square shape completely disappearing at $\phi = 90^o$. At $\phi = 90^o$ the magnetic field is along the hard axis of the ellipsoid [37]. At $\phi = 90^o$, the magnetisation (M) linearly increases/decreases with an increasing/decreasing static magnetic field (H). This gradual rise/fall in magnetisation observed with an increasing/decreasing magnetic field in the hysteresis loop when $\phi = 90^o$, is different from the rapid magnetic switching observed in the hysteresis loop when $\phi = 0^o$. The hysteresis loops in Figure 1.11 highlight the differences in magnetic switching when magnetic grains is magnetised along the easy and the hard axes of the ellipsoidal grain [37].

*c. Super-paramagneticsm in nanostructures*

In 1949, Néel first observed that when the volume of the single domain particle falls below a threshold value, the thermal energy in the system was capable of reversing the easy axis magnetisation orientation of a particle in the absence of an external magnetic field. This phenomenon is called the super-paramagnetic effect [27,38]. This phenomenon was observed when the total anisotropy energy ($\Delta E = KV$) approximates to the thermal energy of the particle ($k_BT$) [27,38]. Here $k_B$ is the Boltzmann constant, V is the volume of the particle, K its anisotropy constant and T the absolute temperature. The limitations in reducing granular volume are apparent, as reducing the volume of the grain would affect the energy balance in the system resulting in the reversing the spin state of the magnetisation in the magnetic grain[27,38]. Figure 1.12 illustrates the differences in the normal magnetic switching process and the effects of super-paramagnetism with an energy barrier diagram. Figure 1.12(a) illustrates a normal magnetisation reversal process where the ball depicting the ability to switch magnetic states confronts a significant larger energy barrier ($\Delta E_o$) to overcome as a result of larger grain volume ($V_o$), make the system more dependent on the static applied field to switch magnetic states. Figure 1.12(b) illustrates the super-paramagnetic effect where a fall in the energy barrier ($\Delta E_1 < \Delta E_o$) is observed as a result of smaller grain volume ($V_1$), making the system more vulnerable to thermal energies ($\Delta E_1 \sim k_BT$) that are now responsible for magnetic switching, even in the absence of a static magnetic field [38]. Please note that Figure 1.12 does not take into account the static applied field that would be responsible for magnetic switching of the grain when the volume of the grain is above the threshold volume, much above the super-paramagnetic effect limit.

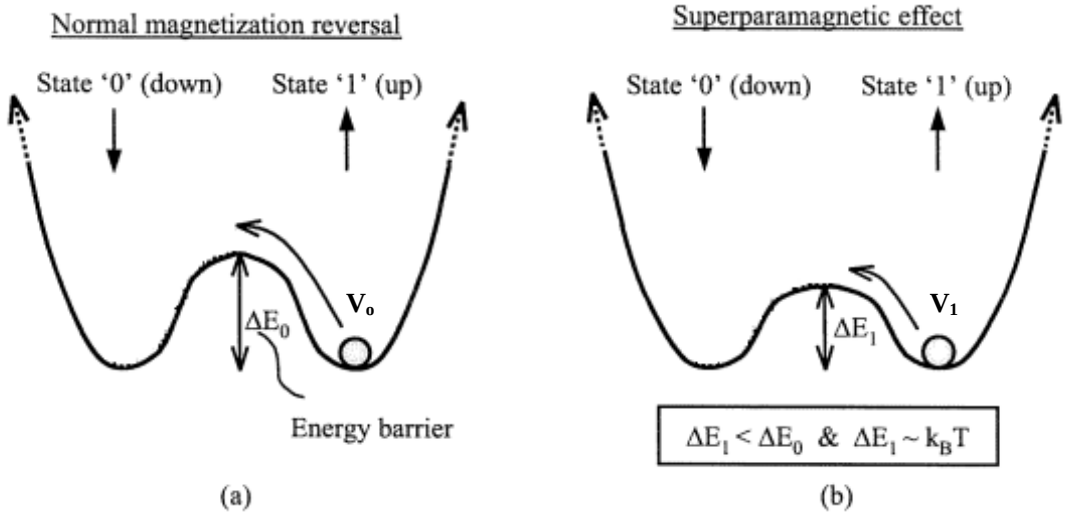


**Figure 1.12** Energy barrier diagram comparing normal magnetisation processes with the super-paramagnetic effect [38].

*d. Anisotropy fields, Néel-Arrhenius equation and the rate of switching*

For a nanoscale magnetic particle with a strong magneto-crystalline anisotropy, there exist crystal anisotropy forces that hold the spontaneous net magnetisation ($M_s$) of the grain along the direction of the easy axis of the grain [27,39]. These crystal anisotropy forces generate an anisotropy field ($H_k$) that ensures that the magnetisation aligns along the easy anisotropic axis of the magnetic grain [27,39]. The anisotropy field ($H_k$) aligns along the easy axis of the nanoscale magnetic particle and has a magnitude such that if the spontaneous magnetisation ($M_s$) has small deviations of θ from the easy axis, the anisotropy field ($H_k$) exerts a torque on spontaneous magnetisation ($M_s$), to align the spontaneous magnetisation ($M_s$) along the direction of the magnetic easy axis of the nanoscale particle [27,39]. The resultant torque as a result of the anisotropy field ($H_k$) is written as $H_kM_s\sin\theta$ and for small values of θ as $H_kM_s\theta$ [27,39].

This torque is found to be equal to the torque exerted on $M_s$ by the crystal with an anisotropy constant K, written as $2K\sin\theta$ or $2K\theta$ for small values of θ [39]. Now the anisotropy field $H_k$ can be written as,

$$H_k = 2K/\mu_o M_s \text{ (T)} \tag{1.9}$$

Now considering the nanoscale magnetic particle to be a cylinder with a volume, $V_i$. The volume of the magnetic cylinder of radius $r_i$ and height $t_i$ is given as $V_i = \pi r_i^2 t_i$. The anisotropy field for a cylinder of volume $V_i$ is rewritten as,

$$H_k = 2KV_i/\mu_o M_s \text{ (T)} \tag{1.10}$$

*Néel-Arrhenius equation*

In the super-paramagneticsm section, a relation between the anisotropy energy (ΔE) and the thermal energy ($k_BT$) of a nanoscale particle was introduced. From this relation, it is possible to determine the mean time between two switched magnetic states of a magnetic nanoparticle, using the Néel-Arrhenius equation [27,39]. The Néel-Arrhenius equation determines the Néel relaxation time, which is the switching time between two magnetic states as a result of thermal fluctuations caused by the super-paramagnetic effect. The Néel's relaxation time ($\tau_N$) is given as[39],

$$\tau_N = \tau_0 exp\left(\frac{KV}{k_BT}\right) \text{ (s)} \tag{1.11}$$

where,

$\tau_N$ is the Néel's relaxation time (s)

$\tau_0$ is called the attempt time which differs with individual materials (s)

K is the magneto-crystalline anisotropy of the material

V is the volume of the nanoscale particle ($m^3$)

$k_B$ is the Boltzmann constant ($k_B = 1.38 \times 10^{-23}$ $JK^{-1}$)

By measuring the net magnetisation of the nanoparticle it is possible to determine the magnetisation time ($\tau_M$) of the nanoscale particle [39]. If the magnetisation time is much larger than the Néel's relaxation time ($\tau_M >> \tau_N$), it infers that the magnetisation flips several times as a result of thermal fluctuations (super-paramagnetic effect) before the measured magnetisation averages to 0. However if $\tau_M << \tau_N$, it infers that magnetisation did not flip during measurement and the nanoparticle remains at a blocked state at this temperature [39]. Hence the magnetic state of the nanoparticle (super-paramagnetic or blocked state) is determined by the measurement time. The measurement time ($\tau_M$) can be written as [39],

$$\tau_M = \tau_0 exp\left(\frac{KV}{k_B T}\right) \text{ (s)} \quad (1.12)$$

and when $\tau_M = \tau_N$, $T_B$ is the known as the blocking temperature given as[39],

$$T_B = \frac{KV}{k_B ln(\frac{\tau_M}{\tau_o})} \text{ (K)} \quad (1.13)$$

The measurement time can also be written in terms of rate of switching ($\lambda$) for a static magnetic field (H) as [39,40],

$$\lambda(H) = f_0 exp\left(\frac{\Delta E}{k_B T}\right) \quad (1.14)$$

where $f_o$ is the characteristic frequency. From this the characteristic time (t) can be rewritten as [40],

$$t = \ln(2)/\lambda(H) \text{ (s)} \quad (1.15)$$

For a static magnetic field (H) that is applied along the easy axis direction, the resulting total anisotropy energy ($\Delta E$) for a cylindrical nanoscale grain of volume ($V_i$), the anisotropy field ($H_k$), and anisotropy constant K is given as[40],

$$\Delta E = KV_i [1-(H/H_k)]^2 \quad (1.16)$$

which when substituted in Equation 1.14 gives the rate of switching ($\lambda(H)$), from which the characteristic time (t) in Equation 1.15 is obtained.

In Section 5.4.3 of Chapter 5, the characteristic time (t) is determined for a size-independent magnetic grain model (simple Sharrock model) and a size-dependent magnetic grain model (modified Sharrock model) using experimental magnetic field (H) data and measurement time ($\tau_M$) data [40]. These results are compared with size dependent magnetic grain switching data, for different applied static magnetic fields (H) and the analysis is reported.

## 1.4 Structure and composition of Perpendicular magnetic media

Perpendicular magnetic media is a thin film multi-layered magnetic structure, in which the topmost active recording layer consists of nanoscale magnetic grains with a magnetic easy axis perpendicular to the plane of the thin film structure [17]. Perpendicular recording media is an advancement of its immediate predecessor longitudinal recording media, with its advantage of being able to achieve increased areal packing densities by controlling the magnetic properties of the grains [17,22,25]. However this has not been possible without the use of other layers, that have been used to engineer the out-of-plane anisotropy in the magnetic grains [17,22,25]. Apart from imparting magnetic structure in the grains, soft magnetic under layers are introduced to facilitate the magnetic writing process and a brief description of this is given in the working of perpendicular recording media in Section 1.2 [23].

The thin film structure in Figure 1.13 is an example of a conventional perpendicular magnetic recording medium. The structure has an exchange coupled composite (ECC) layer above the recording layer, which is magnetically softer than the recording layer [41]. The exchange coupled composite (ECC) layer is used to facilitate the delicate balance of switching smaller grains with strong magneto-crystalline anisotropies at lower magnetic fields, by exchange

coupling with the recording layer[41]. Present day perpendicular media technology does not use an ECC layer however the reported work investigates the advantages of an exchange coupled composite (ECC) layer in the perpendicular magnetic medium [41]. The other layers present in the thin film structure are the recording layer, the seed layers, the soft under layers, the silicon/glass substrate and a protective carbon overcoat [17].

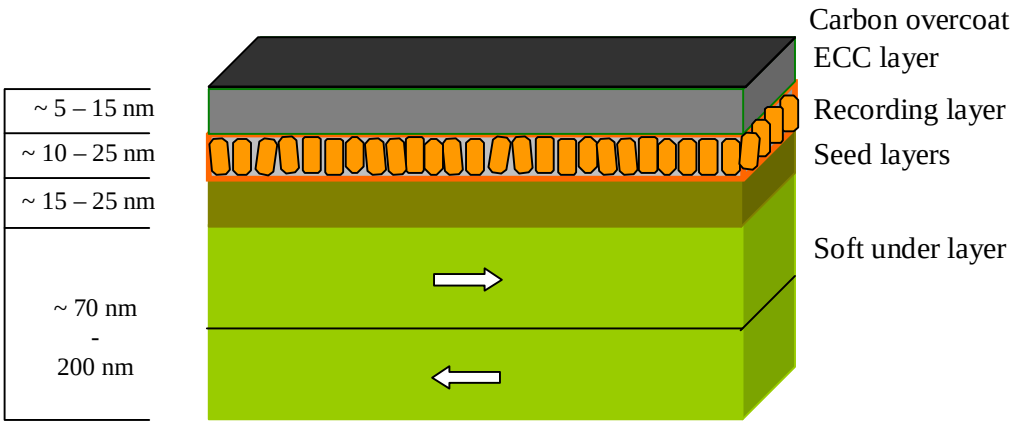


**Figure 1.13** Composition and structure of perpendicular magnetic media with approximate thicknesses

### 1.4.1 Soft under layers

The soft under layers are thicker and magnetically softer layers than the recording layer. The soft under layers are found beneath the recording layer and seed layers as shown in Figure 1.13. These soft under layers play a vital role during the data-write process allowing the magnetic flux to permeate through them, completing the magnetic flux loop in the system [23]. A soft ferromagnetic material with low coercivity that allows the easy passage of magnetic flux through the layers is usually chosen as the soft under layer [23]. The samples use FeCo to achieve these magnetic properties [23,42].

Two FeCo layers split using a ruthenium spacer layer to facilitate anti-ferromagnetic coupling between the two FeCo layers as shown in Figure 1.14 are used. The anti-ferromagnetic coupling assures an energetically stable state in the soft under layers, in the absence of a magnetic field [23,42]. The anti-ferromagnetic coupling also ensures that there is very little magnetic contribution from the soft under layers to influence the stability of the magnetic grains in the recording layer, in the absence of a magnetic field [23,42].

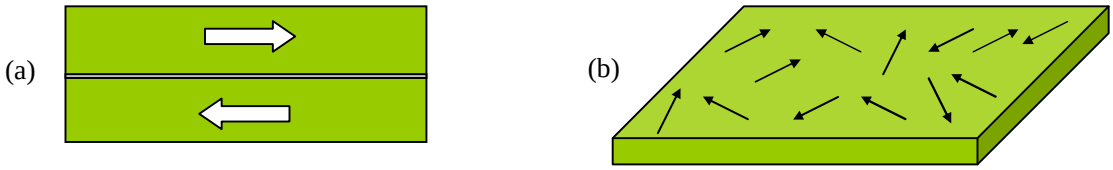


**Figure 1.14**(a) Soft underlayers split using a Ru spacer layer. (b)Individual magnetic moment orientation in a FeCo soft under layer (not anti-ferromagnetically coupled) governed by the shape anisotropy that dominates a thin film.

During a data write process, a magnetic write field is applied perpendicular to the thin film structure to magnetise the grains present in the recording layer [23,42]. However this magnetic write field needs to complete its magnetisation loop, making sure that there exist no stray magnetic fields in the perpendicular magnetic medium that could affect the stability of the medium. This is where the soft under layers play their role in the perpendicular magnetic medium [23,42]. The antiparallel soft under layers conduct the magnetic flux from the write head to the trailing component of the write head, allowing the magnetic flux to permeate through the layers facilitating the completion of the magnetic flux loop. This allows writing on high anisotropy grains with better thermal stability [23,42]. One of most important aspects of the recording process is not allowing the saturation of the soft under layers in any magnetised state from its initial anti-ferromagnetic coupled state, as this would deteriorate the completion of the magnetic loop in the data write process [23,42,43]. Careful considerations of the area of the write pole, magnetisation of the write pole tip, the area of the soft under layers and the magnetisation of the material used in the soft under layers are calculated, ensuring that change in magnetic properties of the soft under layers complement the thickness of the layers and the properties/dimensions of the write head [23,42,43]. Keeping all this in mind the materials usually used are FeCo, NiFe, FeAlN etc [23,42,44,45].

### 1.4.2 Seed Layers

The seed layers facilitate high anisotropy stable magnetic grains with grain sizes within the limits of thermal stability [46,47]. The seed layers influence texture, microstructure and morphology in the recording layer that largely comprises Co-alloy grains with good c-axis orientation [46,47]. A lot of research is being carried out on the use of seed layers, as a good understanding of the effect of controlling the thickness and the type of seed layers used, would shed more light on its role in enhancing anisotropy of the magnetic grains in the recording layer [46,47]. It was found that introducing several intermediate seed layers also enhances c-axis orientation ensuring stable nanoscale ferromagnetic grains [47]. The literature reports studies of changing c-axis orientation of the recording layer for varying thin film thicknesses of Ru, Ru-O, Ta, Ti, NiP, NiAl [46,47,48,49]. A general trend suggests that the thickness of the intermediate seed layers influence the Co-alloy grain formation, with thinner layers showing better the c-axis orientation in the grains [50]. Plane-view TEM images of Ru seed layers and a cartoon of the Co alloy grain formation on the ruthenium seed layers in Figure 1.15; show the physical structure and the significance of the seed layers, in the recording layer magnetic grain formation.

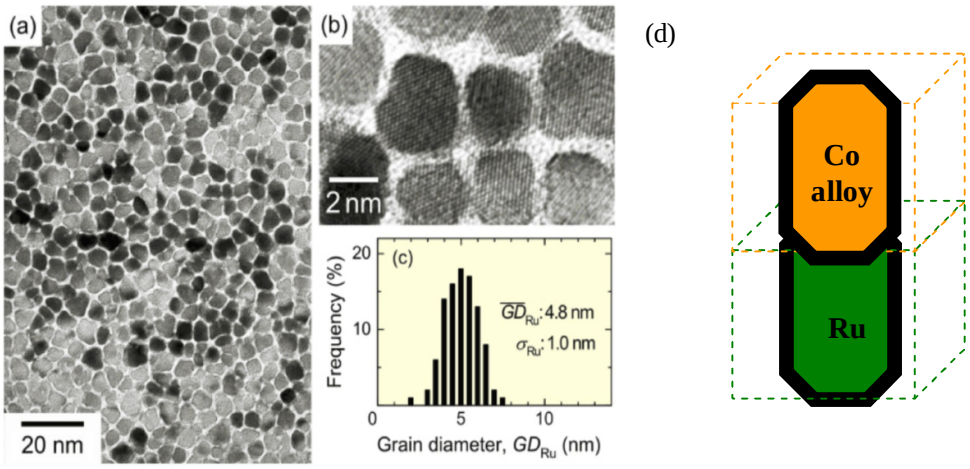


**Figure 1.15** (a), (b) Plane-view TEM images of the 4.8nm diameter Ru–$SiO_2$ layer grown on Ru seed layers [50] and (c) Histogram for the grain diameters of the Ru–$SiO_2$ layer [50](d) Cartoon of Cobalt alloy grain growth on Ruthenium seed layer.

### 1.4.3 Recording Layer

The recording layer constitutes nanoscale ferromagnetic CoCrPt grains present in an oxide matrix [17,24]. Cobalt in its hcp phase was the obvious choice for perpendicular magnetic media with its natural c-axis orientation [35]. However, the CoCrPt-Oxide composition was chosen to be used in commercial perpendicular recording media technology, only after a lot of research [51]. Some other Co alloys researched include CoCrTa, CoCrNb, CoCrPtNb and CoPtCrO [52,53,54,55]. CoCrPt grains dispersed in $SiO_x$ are also widely researched in order to achieve better magnetic grain formation [56]. The oxide present in the recording layer segregates the CoCrPt grains allowing high anisotropy magnetic grain formation [55,56]. The quantity of Cr sputtered is also tightly controlled, as Cr serves as the grain boundary in a CoCrPt alloy further segregating the active magnetic material in the alloy from oxide matrix that separates the CoCrPt grains from each other [17,51].

The literature shows that on addition of $SiO_2$ we obtain segregated CoCrPt grains with a well-defined structure, good thermal stability and smaller grain sizes with an increased signal to noise ratio [46,56]. The grains also have been reported to show higher coercivity, lower number of stacking faults, larger squareness enabling better recording performance than other Co-alloy perpendicular media [46,56].

Although characterisation techniques have shed light on the shape and to some extent the composition of the granular structure; conventional characterisation techniques have revealed very little information on the magnetism of the nanoscale granular structure [22,57]. The reported work looks to provide insight on the physical and magnetic properties of the CoCrPt grains, determining the average size, shape and distribution of the CoCrPt grains in the recording layer. Figures 1.16 are cartoons depicting the magnetisation of a bit and the shape of the magnetic grains in the recording layer of the perpendicular magnetic medium.

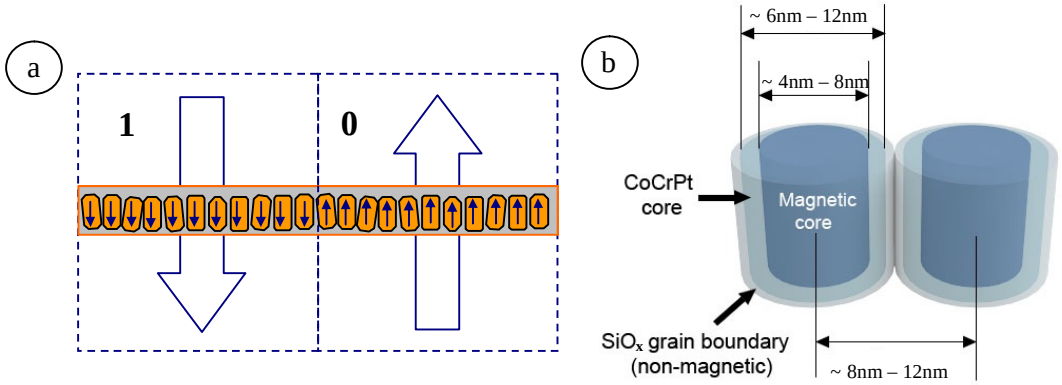


**Figure 1.16** (a) Cartoon depicting two bits with 'spin up' and 'spin down' states next to each other. (b) Cartoon depicting the CoCrPt grain with approximate dimensions and predicted core-shell structure.

### 1.4.4 Exchange coupled composite (ECC) Layer

While coming to terms with thermal magnetic instabilities in nanoscale magnetic grains, research has been directed at overcoming the size threshold by working with smaller grains within the thermal stability limit [41]. Thermally stable nanoscale magnetic grains of smaller volumes (smaller size) with higher anisotropy are used in the recording layer to store data, using an applied static magnetic field [41,58].

However increasing the anisotropy of the grain requires an increase in the applied static magnetic field to switch magnetic grains in a data write process [41,58]. To overcome this limitation, a softer magnetic layer is sputtered above the recording layer. The new layer has been designed to be magnetically softer than the recording layer and is called the exchange coupled composite layer [41,58]. An alloy of CoCrPt is used as the exchange coupled composite layer and the magnetically softer exchange coupled composite layer is not expected to have magnetic grain formation like that present in the recording layer, as seen in Figure 1.17 [41,58].

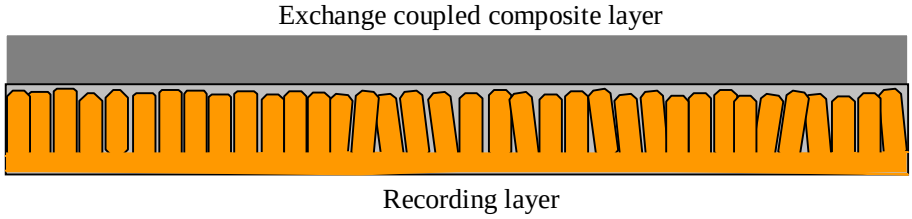


**Figure 1.17** A cartoon depicting the exchange coupled composite layer present above the recording layer

When subjected to a magnetic write field the exchange coupled composite layer magnetically exchange couples with the recording layer switching the CoCrPt grains of the recording layer at lower magnetic write fields [41,58]. This layer facilitates high anisotropy magnetic grain switching at smaller write fields [41,58]. The CoCrPt grains in the recording layer experience an increased magnetisation at lower fields from both magnetic exchange coupling effects and the applied static magnetic write field [41,58]. This enhanced magnetisation resulting from both the applied magnetic field and the magnetic exchange coupling facilitates magnetic switching at smaller magnetic write fields. Similar studies have also been carried out on CoCrPt-Oxide exchange coupled composite layer s on CoCrPtB media stacks [55]. Research has also been directed at introducing a spacer layer between the exchange and the recording layer to anti-ferromagnetically couple the two layers [59].

## 1.5 Characterisation of magnetic media with its limitations

Several magnetic characterisation techniques exist to investigate the magnetic properties of materials. These characterisation techniques can be broadly classified into bulk magnetic characterisation and localised magnetic characterisation techniques [27, 57].

Bulk characterisation techniques use magnetometers to give bulk magnetic information of the material. In a bulk characterisation measurement, magnets and experimental setups are designed to best suit the requirements of that particular experiment. Based on the type of experiment required to be carried out magnetometers can be classified into two basic types, namely scalar magnetometers and vector magnetometers [60,61]. Scalar magnetometers are used to measure magnetisation, while vector magnetometers have the capability to measure the component of the magnetisation in a particular direction, relative to the direction of the applied magnetic field [60]. For this capability, vector magnetometers have been widely used to carry out in-plane and out-of-plane measurements in thin films, enabling magnetic characterisation of thin films [27,61].

In the case of a perpendicular magnetic medium, the magnetic profile of the entire multi-structure is present making it difficult to probe the magnetisation of individual layers in the magnetic medium [22]. The results reported in this work use a DMS-10 vector VSM to investigate the out of plane magnetic properties of the recording layer [62]. In a VSM, the sample placed in the sample holder (as shown in Figure 1.18b) undergoes sinusoidal motion (mechanically vibrated) in the presence of a static magnetic field [27]. The magnetic flux changes from this mechanical vibration induce a voltage in the sensing coils as seen in Figure 1.18b. This voltage is found to be proportional to the magnetic moment of the sample. Therefore by using this technique, the magnetic moment of the sample can be measured as a function of magnetic field, temperature and time [27,62]. The VSM can be used to magnetically characterise a wide range of samples that include powders, liquids, solids, bulk, and thin films using specially designed sample holders [27,62].

Apart from hysteresis loops the VSM can also be used to measure remanence curves. The reported work presents recording layer remanence curve data obtained by pinning the soft under layers using an in-plane field, and only measuring the moment from the orthogonal recording layer [62]. This data is introduced in Chapter 5 and Chapter 6, when discussing the magnetic switching results. Figure 1.18a is a photograph of the DMS-10 vector VSM that was used for the experiments.

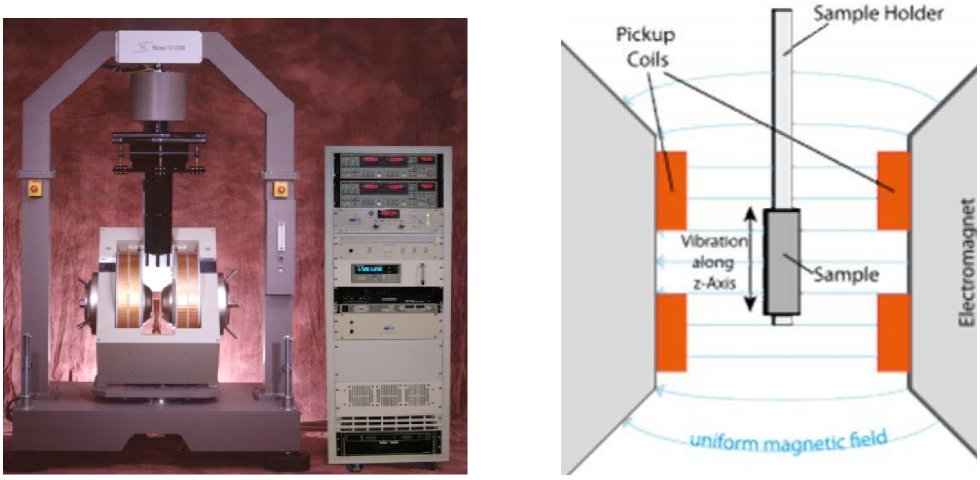


(a) (b)

**Figure 1.18** (a) A photograph of the DMS-10 vector VSM used for the experiments in the reported work (b) A cartoon of the working of the VSM, with the vibrating sample holder placed in the presence of static magnetic field. The pickup coils present sense the change in magnetic flux in the setup[27,62].

Apart from the VSM, several similar magnetometers have been designed to carry out bulk magnetisation measurements on powders, thin films, crystals and soft materials to observe magnetisation at different possible environmental conditions that can be created in a laboratory environment. Examples of such magnetometers are the vector magnetometers, superconducting quantum interference device (SQUID), alternating gradient force magnetometer etc [27,61,62].

However, bulk magnetic characterisation techniques come with their limitations. Bulk magnetic characterisation techniques are incapable of providing localised magnetic information on specific regions or parts of a larger magnetic medium [22,63]. Bulk magnetic characterisation techniques also cannot characterise surface magnetic properties or magnetic properties of nanoscale features embedded inside magnetic or non-magnetic material [63]. To compensate for these limitations several small localised magnetic probing techniques are used [63].

Magnetic force microscopy is a magnetic surface characterisation technique that is used to characterise nanoscale magnetic features on flat surfaces [64]. The magnetic force microscope (MFM) is a profilometer that uses a nanoscale magnetic tip to detect the magnetic state of the material as shown in Figure 1.19a. The MFM is a development of an atomic force

microscope (AFM), which uses a magnetic tip to scan across the surface of the material providing a magnetic surface map across the nanoscale region under investigation. A detailed description of the components and working of an MFM is beyond the scope of the reported work and can be looked at, in this reference [64].

Another technique that provides a surface magnetic profile is the MOKE (Magneto-optic Kerr effect) [65]. MOKE detects the magneto-optical effects induced on a polarised beam of light, after it has been reflected of a magnetic surface. This detected change in polarisation and reflected intensity provides insight into the magnetic state of the system. Figure 1.19b shows the various components of a MOKE setup and a better description of its working can be looked up in this reference [65].

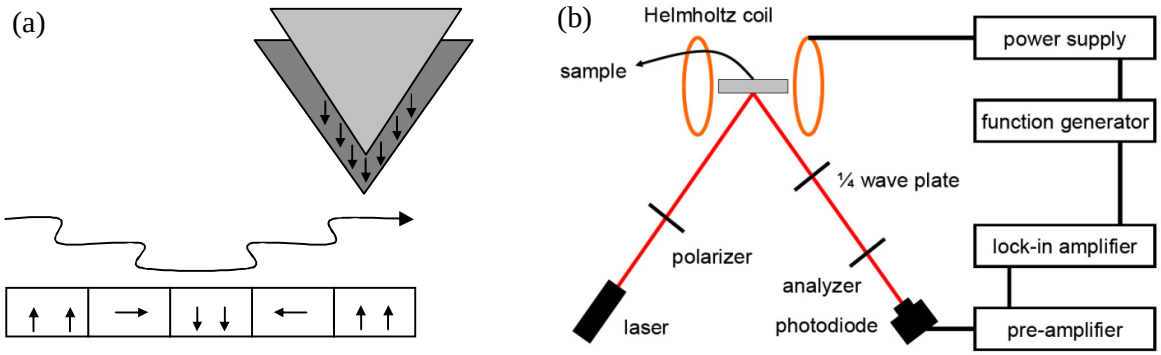


**Figure 1.19** (a) Cartoon of a magnetic tip of an MFM at work, detecting the magnetic state of the surface under investigation. (b) A complete MOKE setup with the labels for the various components used.

The MOKE is usually used to investigate larger surface areas, providing magnetic information in the micron scale range making it more of an averaging technique in comparison to an MFM [64,65]. Both systems have been known to work under different environmental conditions capable of observing magnetic effects under different temperature and vacuum conditions.

It is evident that although both bulk and surface characterisation techniques are capable of characterising magnetic properties and features they have their limitations [64,65]. Both techniques have limited spatial resolution when characterising nanoscale features across larger length scales [64,65]. These limitations in laboratory bulk and surface techniques have been part of the motivation for using large scale facility techniques to achieve the required spatial resolution.

## 1.6 Motivation for reported work

A perpendicular magnetic medium is a complex thin film system that consists of both granular and soft magnetic layers with intermediate non-magnetic seed layers [17]. Using bulk characterisation techniques the general magnetic behaviour of the system as a whole can be determined, however determining magnetic properties of nanoscale features embedded in a magnetic/non-magnetic medium at different magnetic fields requires a more localised detail oriented technique [63,66] .

Localised surface characterisation techniques have previously been used to provide a magnetic surface profile of the CoCrPt grains in the recording layer [64,65]. However, magnetic surface characterisation techniques are again limited by length scales [64,65]. By increasing the surface area investigated, it was found that the spatial resolution of the magnetic information obtained is greatly affected when using surface characterisation techniques like magnetic force microscopy [64]. Another important limitation is the inability of a surface characterisation technique to provide magnetic information across the '3 dimensional' CoCrPt granular structure [63,64,65]. This is because surface characterisation techniques provide only surface magnetic information of the CoCrPt grains embedded in the oxide matrix [64].

These limitations in surface and bulk magnetisation techniques have failed to provide specific information on the size, shape and the distribution of the magnetic grains in the recording layer of the perpendicular magnetic medium [63,64,65]. Apart from this, the nanoscale magnetic switching of individual CoCrPt grains at different magnetic fields has also not been understood using conventional characterisation techniques [65]. The reported work investigates the use of neutrons to overcome these limitations, providing nanoscale magnetic and structural information of the CoCrPt grains with high spatial resolution.

Small angle neutron scattering has previously been used to investigate nanoscale magnetic grains in longitudinal magnetic media [66,67]. Neutrons scattering has also been used to study the magnetic properties of the CoCrPt grains present in the recording layer of the perpendicular magnetic medium [68]. The presented work uses polarised small angle neutron scattering to characterise both the granular and magnetic properties of the CoCrPt grains in the recording layer of the perpendicular magnetic medium [68, 69].

The reported work first identifies the magnetic component of the physical CoCrPt grain, distinguishing the magnetic component of the grain from its physical structure [68,69]. The size, shape and distribution of the CoCrPt grains in the recording layer are then investigated.

The reported work also examines the magnetic grain switching at different fields and compares this data with analytical models that predict the switching behaviour of the magnetic grain in the perpendicular medium [68,69].

Perpendicular magnetic recording media samples used in the reported work were obtained from Hitachi Global Storage Technologies (GST) San Jose research centre at California. Different samples with varying recording layer thickness were obtained. C4-'Oxide only', C9 -'Oxide only' and C13-'Oxide only' are the three variants of the samples thickness used in the reported work. A perpendicular magnetic media sample with the exchange coupled composite (ECC) layer identified as C9-'FS' sample has also been used in the reported work. The structure and composition of samples are introduced in individual chapters when discussing the experimental results.

The reported work also uses Polarised neutron reflectivity (PNR) to investigate the in-plane magnetisation in the thin film structure [70]. Special samples that have non-magnetic soft under layers and seed layers are used for the experiments. The in-plane magnetisation experienced by the recording layer and exchange coupled composite layer in the perpendicular magnetic media structure at different in-plane magnetic fields are investigated using polarised neutron reflectivity [70].

## 1.7 References


[1] Eric D. Daniel, C. Denis Mee, Mark H. Clark, Eds. “Magnetic recording: the first 100 years” Wiley-IEEE Press, New York (1998) (ISBN 978-0-7803-4709-0)

[2] T. Thomson, L. Abelmann, J.P.J. Groenland "Magnetic data storage: Past present and future" in Magnetic Nanostructures in Modern technology (Spintronics, Magnetic MEMS and Recording) Eds. B. Azzerboni, G. Asti, L. Pareti, M. Ghidini Springer, Dordrecht (2008) (ISBN 978-1-4020-6336-7)

[3] Robert F. Service “Data Storage: Is the Terabit Within Reach?” Science, 314(5807), (2006) p. 1868-1870 (DOI: 10.1126/science.314.5807.1868)

[4] IEEE Global History Network. “Telegraphone” Last modified December 15, 2011. http://www.ieeeghn.org/wiki/index.php/Telegraphone

[5] S.B Luitjens, A.M.A Rijckaert “The history of consumer magnetic video tape recording, from a rarity to a mass product” Journal of Magnetism and Magnetic Materials, 193(1-3), (1999) p.17-23 (DOI: 10.1016/S0304-8853(98)00398-9)

[6] Mark H. Kryder “Magnetic thin films for data storage” Thin Solid Films, 216(1), (1992) p.174-180 (DOI: 10.1016/0040-6090(92)90890-N)

[7] L.A. Russell “High-Speed Magnetic-Core Memory Technology” Advances in Electronics and Electron Physics, 21, (1966) p.249-286 (DOI: 10.1016/S0065-2539(08)61011-2)

[8] Charles Reece “Bubble memory in data processing” Data Processing, 26(8), (1984) p.26-28 (DOI: 10.1016/0011-684X(84)90197-7)

[9] C.W. Chen “Recent developments in soft magnetic materials” Journal of Magnetism and Magnetic Materials, 7(1-4), (1978) p.308-311 (DOI: 10.1016/0304-8853(78)90209-3)

[10] IBM Archives. “IBM 350 disk storage unit” Last modified December 15, 2011.

http://www-03.ibm.com/ibm/history/exhibits/storage/storage_350.html

[11] Calvin C. Gotlieb “General-Purpose Programming for Business Applications” Advances in Computers, 1, (1960) p.1-42 (DOI: 10.1016/S0065-2458(08)60605-1)

[12] E. Grochowski, R. D. Halem “Technological impact of magnetic hard disk drives on storage systems” IBM Systems Journal, 42(2), (2003) p.338-346 (DOI: 10.1147/sj.422.0338)

[13] George Sollman “Trends in rotating storage technology” Data Processing, 24(5), (1982) p. 6-9 (DOI: 10.1016/0011-684X(82)90002-8)

[14] B. Cord, W. Maass, J. Schroeder, K.-H. Schuller, U. Patz “Application of magnetic thin films for high-density data storage” Thin Solid Films, 175, (1989) p. 287-293 (DOI: 10.1016/0040-6090(89)90841-9)

[15] D. Abramovitch, G. Franklin “A brief history of disk drive control” IEEE Control Systems, 22(3), (2002) p. 28-42 (DOI: 10.1109/MCS.2002.1003997)

[16] Pawel Glijer, Kyusik Sin, John M. Sivertsen, Jack H. Judy “Structural design of CoCrPt(Ta,B)/Cr magnetic thin film media for ultra high density longitudinal magnetic recording” Scripta Metallurgica et Materialia, 33(10-11), (1995) p. 1575-1584 (DOI: 10.1016/0956-716X(95)00402-H)

[17] S. N. Piramanayagam “Perpendicular recording media for hard disk drives” J. Appl. Phys. 102, 011301 (2007) (DOI: 10.1063/1.2750414)

[18] Seagate Technology. “Seagate Barracuda Hard Drive” Last modified December 15, 2011. http://www.seagate.com/www/en-au/products/desktops/barracuda_hard_drives/

[19] Stellar data recovery. “Parts of a hard disk drive” Last modified December 15, 2011. http://www.stellarinfo.co.in/

[20] Karl Paulsen "Hard Drive Anatomy" in Moving Media Storage Technologies Elseiver

Inc, Oxford (2011) p. 73-108 (ISBN-13: 978-0240814483)

[21] Andrei Khurshudov, Peter Ivett “Head–disk contact detection in the hard-disk drives” Wear, 255(7–12) (2003) p.1314-1322 (DOI: 10.1016/S0043-1648(03)00201-1)

[22] Roger Wood, Yoshiaki Sonobe, Zhen Jin, Bruce Wilson “Perpendicular recording: the promise and the problems” Journal of Magnetism and Magnetic Materials, 235(1–3), (2001) p.1-9 (DOI: 10.1016/S0304-8853(01)00290-61)

[23] Dmitri Litvinov, Mark H Kryder, Sakhrat Khizroev “Recording physics of perpendicular media: soft underlayers” Journal of Magnetism and Magnetic Materials, 232(1–2), (2001) p.84-90 (DOI: 10.1016/S0304-8853(01)00216-5)

[24] Dmitri Litvinov, Mark H Kryder, Sakhrat Khizroev “Recording physics of perpendicular media: hard layers” Journal of Magnetism and Magnetic Materials, 241(2–3), (2002) p.453-465 (DOI: 10.1016/S0304-8853(02)00023-9)

[25] Yoshihisa Nakamura “Perpendicular magnetic recording — progress and prospects” Journal of Magnetism and Magnetic Materials, 200 (1–3), (1999) p.634-648 (DOI: 10.1016/S0304-8853(99)00445-X)

[26] Jean Pierre Lazzari “Single pole, single turn, probe GMR head and micro-actuator for high-density perpendicular recording” Journal of Magnetism and Magnetic Materials, 235 (1–3), (2001) p. 362-367 (DOI: 10.1016/S0304-8853(01)00380-8)

[27] Stephen Blundell "Magnetism in Condensed Matter" Oxford University Press, Oxford (2001) (ISBN-13: 978-0198505921)

[28] L.M. Falicov “Surface, interface and thin film magnetism: an overview” Thin Solid Films, 216 (1), (1992) p.169-173 (DOI: 10.1016/0040-6090(92)90889-J)

[29] Olivier Fruchart, André Thiaville “Magnetism in reduced dimensions” Comptes Rendus Physique, 6 (9), (2005) p.921-933 (DOI: 10.1016/j.crhy.2005.10.011)

[30] R. Allenspach “Ultrathin films: magnetism on the microscopic scale” Journal of

Magnetism and Magnetic Materials, 129(2–3), (1994) p.160-185 (DOI: 10.1016/0304-8853(94)90108-2)

[31] Tadeusz Balcerzak “A comparison of the RKKY interaction for the 2D and 3D systems and thin films” Journal of Magnetism and Magnetic Materials, 310(2), (2007) p.1651-1653 (DOI: 10.1016/j.jmmm.2006.10.494)

[32] G. Bottoni “Investigation on the magnetic anisotropy of particulate and thin film recording media” Journal of Magnetism and Magnetic Materials, 322(9–12), (2010) p.1617-1619 (DOI: 10.1016/j.jmmm.2009.06.003)

[33] M. Hamedoun, K. Bouslykhane, H. Bakrim, A. Hourmatallah, N. Benzakour “Coupling and surface effects in magnetic thin films” Physica A: Statistical Mechanics and its Applications, 358(1), (2005) p. 102-113 (DOI: 10.1016/j.physa.2005.06.010)

[34] S.P Gubin, Yu.I Spichkin, Yu.A Koksharov, G.Yu Yurkov, A.V Kozinkin, T.I Nedoseikina, M.S Korobov, A.M Tishin “Magnetic and structural properties of Co nanoparticles in a polymeric matrix” Journal of Magnetism and Magnetic Materials, 265(2), (2003) p.234-242 (DOI: 10.1016/S0304-8853(03)00271-3)

[35] F. Ono, H. Maeta “Thermal expansion and magnetocrystalline anisotropy in hcp cobalt” Physica B: Condensed Matter, 161 (1–3), (1989) p.134-138 (DOI: 10.1016/0921-4526(89)90119-1)

[36] E.C. Stoner, E.P. Wohlfarth “A mechanism of magnetic hysteresis in heterogeneous alloys” Philosophical Transactions of the Royal Society A: Physical, Mathematical and Engineering Sciences, 240 (826), (1948) p.599–642 (DOI: 10.1109/TMAG.1991.1183750)

[37] C. Tannous, J. Gieraltowski “The Stoner–Wohlfarth model of ferromagnetism” Eur. J. Phys. 29 475, (2008) (DOI: 10.1088/0143-0807/29/3/008)

[38] Joyce Y. Wong “Perpendicular patterned media for high density magnetic storage” PhD Thesis, California Institute of Technology, (2000) US

[39] Y. Uesaka, Y. Nakatani, N. Hayashi, H. Fukushima “Longitudinal and Perpendicular Recording: Thermal Stability” in Encyclopaedia of Materials: Science and Technology (Second Edition), (2001) p.4627-4632 (DOI: 10.1016/B0-08-043152-6/00807-X)

[40] P. J. Flanders, M. P. Sharrock “An analysis of time-dependent magnetization and coercivity and of their relationship to print-through in recording tapes” J. Appl. Phys. 62, 2918 (1987) (DOI: 10.1063/1.339373)

[41] D. Goll, S. Macke, H. Kronmüller “Exchange coupled composite layers for magnetic recording” Physica B: Condensed Matter, 403(2–3), (2008) p.338-341 (DOI: 10.1016/j.physb.2007.08.044)

[42] E.P George, A.N Gubbi, I Baker, L Robertson “Mechanical properties of soft magnetic FeCo alloys” Materials Science and Engineering: A, 329–331, (2002) p.325-333 (DOI: 10.1016/S0921-5093(01)01594-5)

[43] S. Khizroev, Y. Liu, K. Mountfield, M.H. Kryder, D. Litvinov “Physics of perpendicular magnetic recording: writing process” Journal of Magnetism and Magnetic Materials, 246(1–2), (2002) p.335-344 (DOI: 10.1016/S0304-8853(01)00855-1)

[44] S. Das, S. Nakagawa “An approach to estimate the magnetic anisotropy constants in a CoCrPt recording layer with a NiFe soft underlayer” Journal of Magnetism and Magnetic Materials,287, (2005) p.308-313 (DOI: 10.1016/j.jmmm.2004.10.050)

[45] Yungui Ma, Xiaohong Li, Tian Xie, Fulin Wei, Zheng Yang “A study of sputtering process for nanocrystalline FeAlN soft magnetic thin films” Materials Science and Engineering: B, 103(3), (2003), p.233-240 (DOI: 10.1016/S0921-5107(03)00239-3)

[46] Chun-Tao Xiao, Yuki Inaba, Takehito Shimatsu, Hiroaki Muraoka “Microstructure, magnetic properties and their seed layer thickness dependences of granular CoPtCr–SiO2 perpendicular recording media” Solid State Communications, 144 (1–2), (2007), p.58-60 (DOI: 10.1016/j.ssc.2007.07.014)

[47] C.L. Platt, K.W. Wierman, E.B. Svedberg, T.J. Klemmer, J.K. Howard, David J. Smith "Structural and magnetic properties of CoCrPt perpendicular media grown on different buffer layers" Journal of Magnetism and Magnetic Materials, 247 (2), (2002) p.153-158 (DOI: 10.1016/S0304-8853(02)00041-0)

[48] E.W. Soo, J.P. Wang, C.J. Sun, Y.F. Xu, T.C. Chong, G.M. Chow "The effects of NiP seed layer in Co-alloy perpendicular thin film media" Journal of Magnetism and Magnetic Materials, 235(1–3), (2001), p.93-97 (DOI: 10.1016/S0304-8853(01)00306-7)

[49] Y. Ikeda, Y. Sonobe, G. Zeltzer, B.K. Yen, K. Takano, H. Do, P. Rice "Microstructure study of CoCrPt/Ti/NiAl perpendicular media" Journal of Magnetism and Magnetic Materials, 235(1–3), (2001), p.104-109 (DOI: 10.1016/S0304-8853(01)00308-0)

[50] Norikazu Itagaki, Shin Saito, Migaku Takahashi "4.8 nm diameter Ru grains grown on a large-grain seed layer for perpendicular magnetic recording media" Journal of Physics D: Applied Physics, 41(15), (2008) (DOI: 10.1088/0022-3727/41/15/152006)

[51] J.H. Judy "Advancements in PMR thin-film media" Journal of Magnetism and Magnetic Materials, 287, (2005), p.16-26 (DOI: 10.1016/j.jmmm.2004.10.004)

[52] T Asahi, M Ikeda, A Takizawa, T Onoue, T Osaka "Influence of substrates on magnetic property and crystalline orientation of CoCrTa/TiCr perpendicular magnetic recording medium" Journal of Magnetism and Magnetic Materials, 212 (1–2),(2000), p.293-299 (DOI: 10.1016/S0304-8853(99)00774-X)

[53] Jun Ariake, Naoki Honda, Toshiaki Keitoku, Kazuhiro Ouchi, Shun-ichi Iwasaki "Nb addition to Co□Cr media for perpendicular magnetic recording" Journal of Magnetism and Magnetic Materials, 155(1–3), (1996), p.228-230 (DOI: 10.1016/0304-8853(95)00743-1)

[54] M. Almasi Kashi, S.P.H. Marashi, R. Pouladi, P.J. Grundy "The effect of annealing on single-layer CoCrPtNb thin films" Thin Solid Films, 518 (8), (2010) p.2157-2162 (DOI: 10.1016/j.tsf.2009.09.066)

[55] G. Choe, M. Zheng, E.N. Abarra, B.G. Demczyk, J.N. Zhou, B.R. Acharya, K.E.

Johnson “High-performance CoPtCrO perpendicular media: optimizing exchange coupling and anisotropy orientation dispersion” Journal of Magnetism and Magnetic Materials, 287, (2005) p.159-166 (DOI: 10.1016/j.jmmm.2004.10.026)

[56] K. Srinivasan, S.N. Piramanayagam, R.W. Chantrell, Y.S. Kay “Microstructure and switching mechanism of stacked CoCrPt–$SiO_2$ perpendicular recording media” Journal of Magnetism and Magnetic Materials, 320(22), (2008), p.3036-3040 (DOI: 10.1016/j.jmmm.2008.08.065)

[57] J Schoenmaker, I.C Oppenheim, E.F Chinaglia “Magnetic and structural characterization of CoCrPt and CoCr thin films deposited by magnetron sputtering” Journal of Magnetism and Magnetic Materials, 226–230 (2), (2001), p.1653-1655 (DOI: 10.1016/S0304-8853(01)00097-X)

[58] D. Suess, J. Lee, J. Fidler, T. Schrefl “Exchange-coupled perpendicular media” Journal of Magnetism and Magnetic Materials, 321 (6), (2009) p.545-554 (DOI: 10.1016/j.jmmm.2008.06.041)

[59] Sebastiaan van Dijken, Matthew Crofton, J.M.D. Coey “Perpendicular exchange bias in nickel/antiferromagnetic bilayers” Journal of Magnetism and Magnetic Materials, 290–291(2), (2005) p.1290-1293 (DOI: 10.1016/j.jmmm.2004.11.452)

[60] T. Aoyama, S. Okawa, K. Hattori, H. Hatate, Y. Wada, K. Uchiyama, T. Kagotani, H. Nishio, I. Sato “Fabrication and magnetic properties of CoPt perpendicular patterned media” Journal of Magnetism and Magnetic Materials, 235(1–3), (2001) p.174-178 (DOI: 10.1016/S0304-8853(01)00332-8)

[61] X.W. Wu, H. Zhou, R.J.M. van de Veerdonk, T.J. Klemmer, D. Weller “Measurement of the magnetic easy axis dispersion in perpendicular media” Journal of Magnetism and Magnetic Materials, 278(1–2), (2004) p.285-288 (DOI: 10.1016/j.jmmm.2003.12.1388)

[62] T. Thomson, B. Lengsfield, H. Do, B. Terris “Magnetic anisotropy and reversal mechanisms in dual layer exchanged coupled perpendicular media” Journal of Applied Physics, 103(7), (2008) (DOI: 10.1063/1.2839310)

[63] D. Robbes “Highly sensitive magnetometers—a review” Sensors and Actuators A: Physical, 129 (1–2), (2006) p.86-93 (DOI: 10.1016/j.sna.2005.11.023)

[64] Wenli Pei, J. Yuan, T. Wang, Y. Fu, T. Washiya, T. Hasagawa, H. Saito, S. Ishio, N. Honda “Study on magnetization reversal of perpendicular recording media by in-field MFM observation” Acta Materialia, 55(9), (2007) p.2959-2964 (DOI: 10.1016/j.actamat.2006.12.034)

[65] G. Bottoni, D. Candolfo, A. Cecchetti, P. Vavassori “Analysis of the magnetization switching in recording media thin films by magneto-optic Kerr effect vector magnetometry” Thin Solid Films, 433(1–2), (2003) p.259-262 (DOI: 10.1016/S0040-6090(03)00294-3)

[66] Sean Langridge, Stephen W. Lovesey “Uses of neutron and X-ray beams to investigate magnetism” Radiation Physics and Chemistry, 61( 3–6), (2001) p.235-239 (DOI: 10.1016/S0969-806X(01)00246-8)

[67] Michael F. Toney, Kurt A. Rubin, Sung-Min Choi, and Charles J. Glinka “Small-angle neutron scattering measurements of magnetic cluster sizes in magnetic recording disks” Appl. Phys. Lett. 82, 3050 (2003) (DOI: 10.1063/1.1571652)

[68] M. Wismayer, S. Lee, T. Thomson, F. Ogrin, C. Dewhurst, S. Weekes, R. Cubitt “Using small-angle neutron scattering to probe the local magnetic structure of perpendicular magnetic recording media” Journal of Applied Physics, 99(8), (2006) (DOI: 08e707 10.1063/1.2165798)

[69] S. J. Lister, M. P. Wismayer, V. Venkataramana, M. A. de Vries, S. J. Ray, S. L. Lee, T. Thomson, J. Kohlbrecher, H. Do, Y. Ikeda, K. Takano, and C. Dewhurst “Small-angle polarized neutron studies of perpendicular magnetic recording media” Journal of Applied Physics, 106(6),(2009) p. 063908 - 063908-4 (DOI: 10.1063/1.3213381)

[70] Hartmut Zabel “Spin polarized neutron reflectivity of magnetic films and superlattices” Physica B: Condensed Matter, 198(1–3), (1994) p.156-162 (DOI: 10.1016/0921-4526(94)90151-1)

# Chapter 2

# Polarised Neutron Diffraction

---

**Contents**



---

**Abstract**

The properties of neutrons are introduced, followed by a general introduction of an elastic wave diffraction process by introducing the reciprocal lattice. The neutron scattering instrumentation is then explained and a brief introduction into neutron scattering theory highlighting the geometry of the experiment is presented. The mathematical modelling used is later explained with simple examples to introduce the reader to analytical modelling approaches used later in chapters 3, 4, 5 and 6. Similarly the polarised neutron reflectivity instrument is explained before dealing with the necessary theory. The theory related to polarised neutron reflectivity as a result of its geometry is also elucidated. A simple example of polarised neutron reflectivity is then explained using the mathematical model developed based on polarised neutron reflectivity theory.

## 2.1 Why Neutrons ?

Neutrons have been widely used to study and understand nanoscale structures, providing a penetrative non-destructive technique to characterise nanoscale features across a range of length scales [1,2]. Neutrons possess a neutral charge and are capable of getting close to the nuclei, which is not possible in light scattering techniques as a result of coulombic interactions between the electromagnetic waves and the electrons [1,2,3]. This allows neutrons to be scattered by nuclear forces providing information on the nuclear structure of the material under investigation [1,2,3]. As a result of this neutrons are also highly penetrative providing depth profile information, while most light based diffraction techniques are restricted to surface characterisation [1, 2]. Another interesting property of thermal neutrons is their wavelength [1,2,3]. Thermal neutrons have wavelengths around those of inter-atomic distances in solids (~$A^o$) and liquids allowing them to be ideal probes for detailed atomic information using an appropriate experimental technique [1,2,3].

Neutrons also possess an inherent magnetic moment. This magnetic moment in a neutron is capable of interacting with the unpaired electrons of a magnetic atom, providing information on the arrangement of the electronic moments (magnetic spin state) as well as their density distribution in an atomic or nanoscale structure [3,4]. This magnetic moment is therefore capable of interacting with the internal magnetic fields in a material, resulting in strong magnetic scattering along with nuclear scattering [3,4]. Spin polarised neutrons are also used to study magnetic interactions in materials, and by polarising the neutron spin information specific to certain magnetic states in a material are extracted [5].

With all these unique properties, neutrons are presently being widely used for both inelastic and elastic diffraction experiments. Inelastic neutron diffraction experiments work on the principle of using the difference in energy between the initial and the scattered neutron energy to determine the energy excitations between interatomic forces [1,2,6]. Elastic neutron experiments on the other hand are carried out by fixing the energy band of the incident neutron and diffracted neutrons, to measure structural properties [1,2,6].

The experiments in the reported work use two elastic neutron diffraction techniques, namely neutron scattering and neutron reflectivity using polarised neutrons. Polarised neutrons have been used to obtain information on specific magnetised states of materials using a combination of analysis and subtraction techniques that are introduced in Section 2.3.3 and Section 2.4.2 of this chapter. A general introduction to neutron diffraction is first described introducing Ewald's sphere, the reciprocal lattice and Braggs law; before heading into the specific theory associated with neutron scattering and reflectivity [2,7,8].

## 2.2 General wave diffraction theory and the reciprocal lattice

In order to understand neutron reflectivity or neutron scattering, we consider a simple case of diffraction of a wave from a periodic lattice of scatterers. A neutron beam with wavelength 'λ' approaches a periodic lattice of scatterers that are separated by a distance 'd' . The entire beam is not scattered by a single point in a lattice [7,8]. The scatterers are periodic across the lattice and several scattering processes take place simultaneously as shown in Figure 2.1. This is similar to scattering from a diffraction grating in an optics experiment for which we know that the condition for constructive interference is given in Equation 2.1.

$$m\lambda = d \sin \theta \tag{2.1}$$

where $\theta$ is the angle between the incident wave and the diffracted wave.

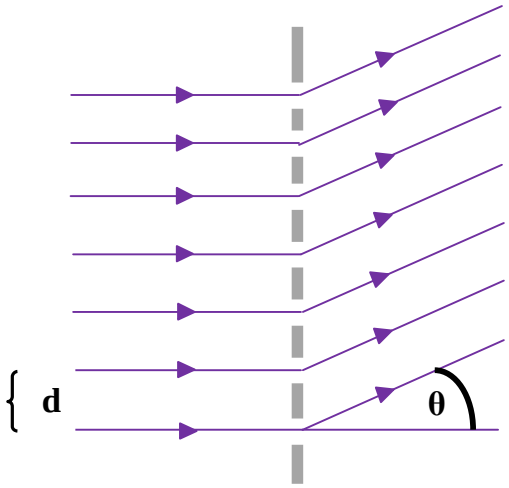


**Figure 2.1** Diffraction of a neutron beam of wavelength 'λ' by periodic slits separated by a distance 'd'

Let's consider the periodic lattice to be 3 dimensional as in reality most crystal structures show 3 dimensional periodicity. Let $\vec{a}_1$, $\vec{a}_2$ and $\vec{a}_3$ be the 3 translational vectors in a unit cell of the periodic lattice as shown in Figure 2.2.

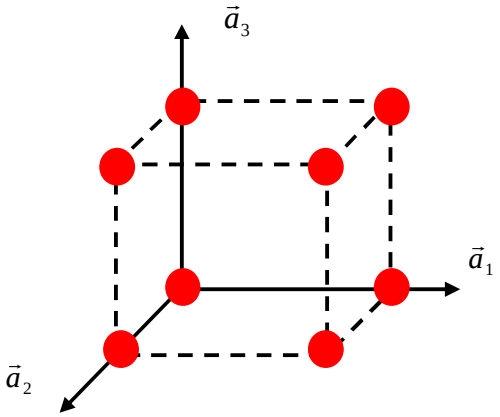


**Figure 2.2** Unit cell of a simple cubic lattice with $\vec{a}_1$, $\vec{a}_2$ and $\vec{a}_3$ as the 3 translational vectors

The periodic lattice can now be defined for a Bravais lattice by,

$$\vec{r} = m_1\vec{a}_1 + m_2\vec{a}_2 + m_3\vec{a}_3 \tag{2.2}$$

Where $m_1$, $m_2$ and $m_3$ can be any integer and $\vec{a}_1$, $\vec{a}_2$ and $\vec{a}_3$ are the primitive vectors. At any lattice position vector $\vec{r}$, the lattice looks exactly the same in all directions and the reciprocal lattice for $\vec{a}_1$, $\vec{a}_2$ and $\vec{a}_3$ can be defined as,

$$\vec{a}_1^{\,*} = \frac{2\pi}{V_o}\vec{a}_2 \times \vec{a}_3$$

$$\vec{a}_2^{\,*} = \frac{2\pi}{V_o}\vec{a}_3 \times \vec{a}_1$$

$$\vec{a}_3^{\,*} = \frac{2\pi}{V_o}\vec{a}_1 \times \vec{a}_2 \tag{2.3}$$

Where $V_o$ the volume of a unit cell is, $\vec{a}_1 \cdot (\vec{a}_2 \times \vec{a}_3) = \vec{a}_2 \cdot (\vec{a}_3 \times \vec{a}_1) = \vec{a}_3 \cdot (\vec{a}_1 \times \vec{a}_2)$

Considering that the neutrons are incident on a crystal lattice. At any lattice vector $\vec{r}$, the amplitude of the incident neutron wave vector $\vec{K}$ is given as [1,2,7,8],

$$A = A_o e^{i\vec{K}\cdot\vec{r}} \tag{2.4}$$

Here again the incident neutron wave vector $\vec{K}$ at any point of the lattice determined by the lattice vector $\vec{r}$. After an elastic neutron diffraction process, a fraction of neutrons say 'f' are scattered and the diffracted wave vector is given as $\vec{K}'$. The scattering amplitude observed at a point vector $\vec{R}$ following a diffraction process is rewritten as,

$$A = A_o e^{i\vec{K}'\cdot\vec{R}} f e^{i(\vec{K}'-\vec{K}).\vec{r}} \tag{2.5}$$

Where $\vec{K}'$ is the diffracted wave vector, $\vec{K}$ is the incident wave vector, $\vec{R}$ is the point vector at which the scattering amplitude is measured and 'f' is the fraction of neutrons scattered at any point on the lattice vector $\vec{r}$. This is pictorially depicted in Figure 2.3.

The difference between the diffracted wave vector $\vec{K}'$ and the incident wave vector $\vec{K}$ gives us the scattering vector $\vec{Q}$ of the system [1,2,7,8].

$$\vec{Q} = \vec{K}' - \vec{K} \tag{2.6}$$

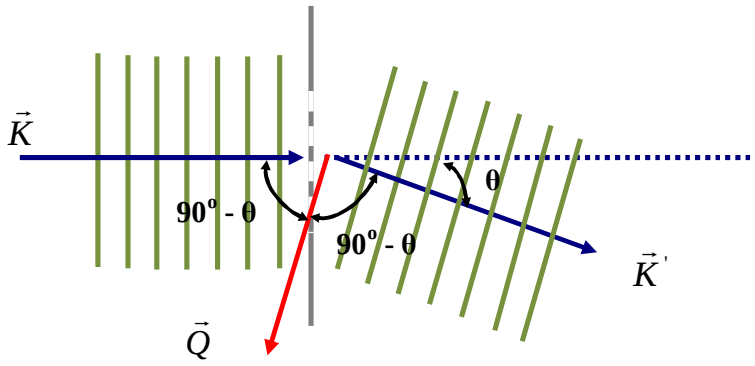


**Figure 2.3** Depiction of scattering vector ( $\vec{Q}$ ) with respect to incident $\vec{K}$ and diffracted vectors $\vec{K}'$

Taking into consideration the entire periodic lattice, the sum of neutron scattering from the entire lattice structure Equation 2.5 is rewritten as [1,2,8],

$$A = A_o e^{i\vec{K}'\cdot\vec{R}} f \sum_{m_1 m_2 m_3} e^{i(\vec{K} - \vec{K}')\cdot(m_1\vec{a}_1 + m_2\vec{a}_2 + m_3\vec{a}_3)} \tag{2.7}$$

It is evident that in order to see a non – zero diffraction all unit cells must add up in phase. In order to understand this in reciprocal space, Laue defined 3 conditions for incident waves to be diffracted by a crystal lattice in reciprocal space [7,8].

$$\begin{aligned} \vec{Q}\cdot\vec{a}_1 &= 2\pi h \\ \vec{Q}\cdot\vec{a}_2 &= 2\pi k \\ \vec{Q}\cdot\vec{a}_3 &= 2\pi l \end{aligned} \tag{2.8}$$

Where h, k and l are reciprocal lattice indices called the Miller indices. From Equation 2.3 and Equation 2.8, the reciprocal lattice vector with Miller indices h, k and l can be written as,

$$\vec{Q} = h\vec{a}_1^{\,*} + k\vec{a}_2^{\,*} + l\vec{a}_3^{\,*} \tag{2.9}$$

In real space, the three Miller indices denote planes orthogonal to the reciprocal lattice vector. [7,8] We know already that diffraction occurs only when the 3 Laue equations are satisfied. This condition occurs whenever a reciprocal lattice vector lies exactly on the Ewald

sphere. From the Ewald sphere shown in Figure 2.4 it is evident that the scattering vector lies along the reciprocal lattice vector within the Ewald sphere [7,8].

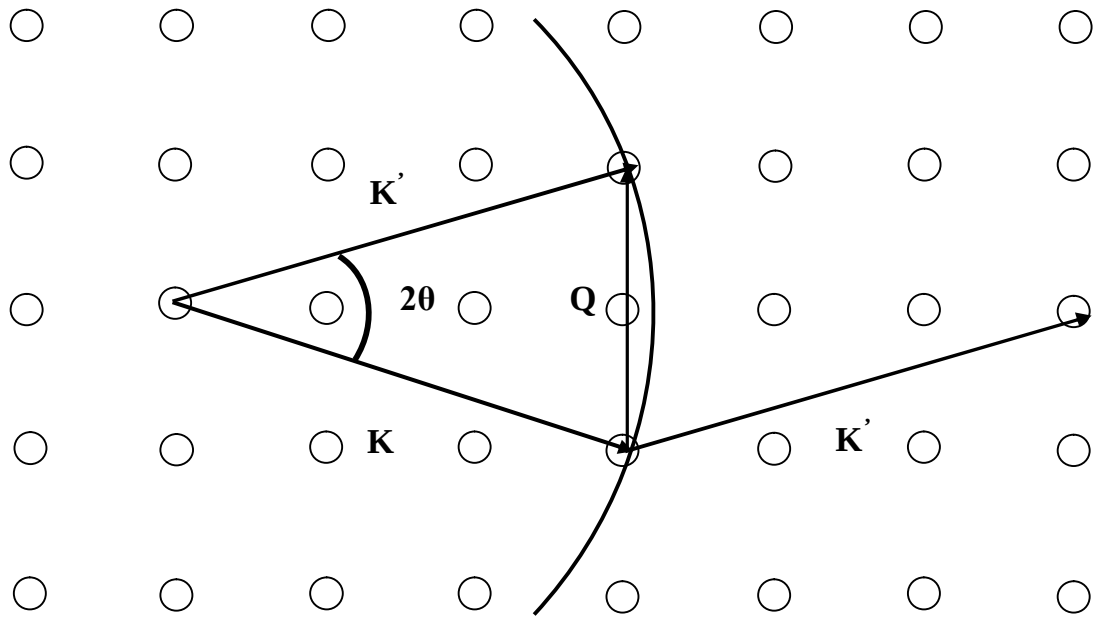


**Figure 2.4** The Ewald sphere construct is satisfied with the reciprocal lattice points passing through the Ewald sphere and the scattering vector coinciding with the reciprocal lattice vector

This shows that for an elastic neutron diffraction process (where $\vec{Q} = \vec{K} - \vec{K}'$**)** the Braggs condition is satisfied [1,2]. As from the Ewald sphere construct Q is given as,

$$Q = 2\,K \sin\theta \qquad (2.10)$$

which is equivalent to the condition for Bragg's law. This demonstrates that Bragg's law is all that is necessary for a simple neutron diffraction experiment; and by defining the geometry and the incident wavelength band a simple neutron reflectivity or scattering experiment can be carried out [1,2,7,8]. This also shows that ad hoc assumptions of Bragg's law are actually justified even for a neutron diffraction experiment.

## 2.3 Polarised Neutron Scattering (PolSANS)

### 2.3.1 Instrument

The experiments were carried out at SANS – I, SINQ; a spallation neutron source based at the Paul Scherrer Institute (PSI), Switzerland [9]. Neutrons for the experiment are generated by bombarding the target nuclei with accelerated (80% the speed of light) protons [10]. This causes highly excited inter-nuclear collisions, resulting in high energy neutrons and significantly fewer protons [10]. The high energy neutrons are then passed through moderators that moderate the incoming neutrons by a number of inelastic collisions with $D_2O$, creating a high flux of low energy neutrons of the order of meV [1,10]. This energy range corresponds to the most probable velocity at a temperature of 290 K, the mode of the Maxwell-Boltzmann distribution for this temperature [1,10].

In Figure 2.5, the neutrons are initially passed through a velocity selector, where the neutron wavelength range used is controlled [10]. The neutrons are then transferred using a Ni coated guide tube, designed in a curved fashion to absorb the remaining high-energy neutrons through a process of specular reflection [9,10]. The SINQ facility at PSI also has a cold neutron facility with extremely cold heavy hydrogen integrated to further decelerate the neutrons to match the nanoscale dimensions of the investigating material [10].

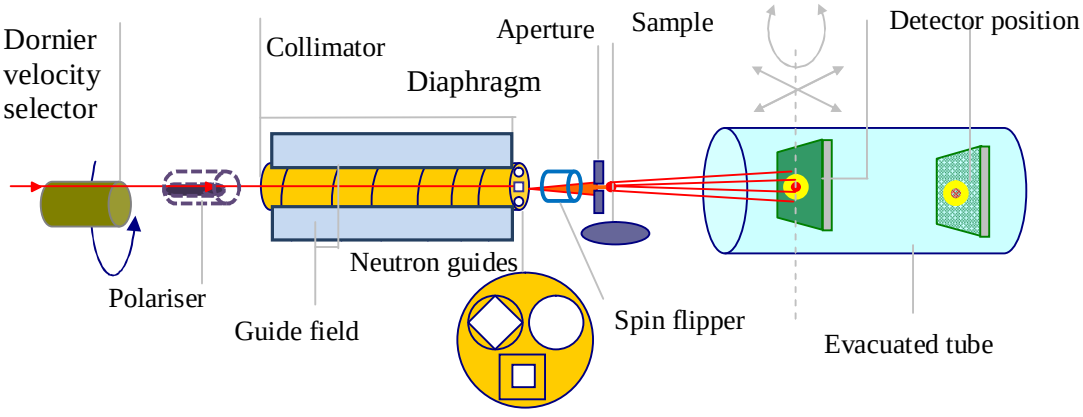


**Figure 2.5** A schematic of SANS-I instrumental setup with its various components [9]

This experimental wavelength range is achieved by passing the beam through a Dornier velocity selector, which chops other wavelengths of the beam giving a monochromatic beam with an adjustable 10% allowance on wavelength spread [1,10]. The next part of the experimental setup shown in Figure 2.5 is a beam attenuator, which regulates the intensity of the beam within experimental requirements [1,9,10]. The neutrons are passed through a series of guide tubes and slits in the collimator that focus the beam onto the sample. The end of the collimator comprises an aperture as seen in Figure 2.5 [1,9,10].

The aperture is used to regulate the divergent beam and uses a neutron absorbent like Boron carbide ($B_4C$) [9,10]. The next part of the instrument setup is the sample, which for the experiment is mounted onto the sample stick of the 11 T cryomagnet and is placed in line with the neutron beam. Note that 11 T cryomagnet was used for the experiment to achieve high magnetic fields, within temperature ranges of 1.8 K and 300 K [9,10]. The last bit of the instrument is the detector as seen in Figure 2.5[11].

The SANS-I instrument houses a two-dimensional $^3$He multiwire proportional counter, which consists of an array of cathode-anode reaction chambers each filled with helium. The helium atoms capture the scattered neutrons that are detected and converted to an array of digital pixels [9,11]. A beam stop is placed in front of the detector to protect the detector from high intensity neutrons that undergo little or no scattering, posing a potential damage to the detector [9,11]. Note that the detector and collimator can be repositioned to accommodate various ‘q’ ranges, through the experiment. The detector at SANS-I is placed on a rail-guided trolley, which allows the detector position to be adjusted [9,11].

The PolSANS option in SANS-I uses a spin filter that allows only a single neutron spin state. This is achieved by using a transmission polariser, polarising neutrons of 0.5 nm$<\lambda<$1 nm wavelength using a Mezei design polariser; before passing through a guide field and a spin flipper that controls the spin state of the incident neutrons [9,11]. Figure 2.6 is a photograph of the small angle neutron scattering setup at the Paul Scherrer Institute in Switzerland.

**Figure 2.6** A photograph of the SANS-I beamline at Paul Scherrer Institute, Switzerland

### 2.3.2. Theory

The theory associated with a neutron scattering experiment comes down to the scattering of a collimated neutron beam by the sample through an elastic process, considering the elastic process to be governed by the assumptions of Bragg's law. To break this down theoretically let us consider the incident neutron wave vector to be $\vec{K}$ and the scattered wave vector to be $\vec{K}'$, with E and E' being the initial and final energies of the neutrons [1, 2]. One can now draw the scattering triangle in Figure 2.7 for simple elastic scattering process for a scattered angle 2 θ as,

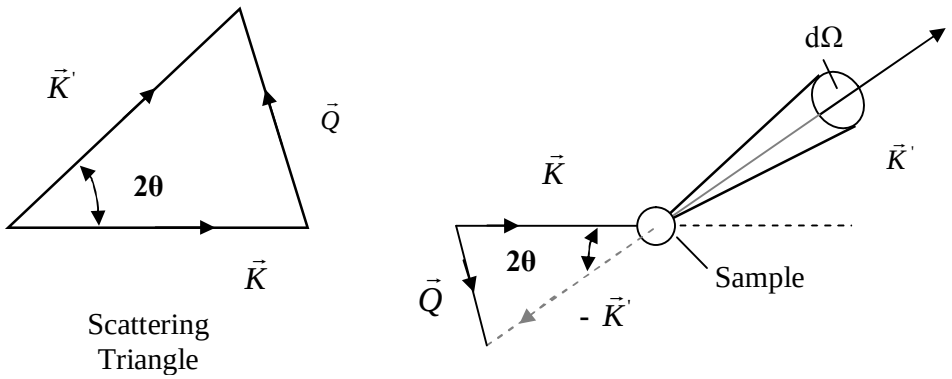


$$\vec{Q} = \vec{K} - \vec{K}'$$

**Figure 2.7** Scattering triangle and scattering geometry for a solid angle ΔΩ

Figure 2.7 considers that the sample constitutes a point scatterer, responsible for a solid angle of scattering (dΩ). This helps us to then define the neutron scattering cross section, from the point scatter through the solid angle (dΩ).

**Neutron scattering cross section**

The total neutron scattering cross section as a result of taking into account the neutrons scattered in any direction is given as [1, 2],

$$\sigma_{tot} = (\text{total number of neutrons scattered per second}) / \Phi_o \tag{2.11}$$

where $\Phi_o$ is the flux of the incident neutrons. The section of the neutrons scattered in a certain direction as a result of a point scatterer as a function of time can be now determined. The differential cross section is given as,

$$\frac{d\sigma}{d\Omega} = \frac{\left(\begin{array}{c}\text{number of neutrons scattered per second into the solid} \\ \text{angle } d\Omega \text{ in the direction } \theta, \Phi\end{array}\right)}{\phi d\Omega} \tag{2.12}$$

where $\Phi=\Phi_o$ and dΩ is the unit solid angle. Taking into consideration the expected final energy range ($E' + \Delta E'$) as a result of the unit solid angle dΩ, the partial or double differential equation that takes into account both the energy and the solid angle responsible for unidirectional scattering is given as,

$$\frac{d^2\sigma}{d\Omega dE'} = \frac{\left(\begin{array}{c}\text{number of neutrons scattered per second into the solid} \\ \text{angle } d\Omega \text{ in the direction } \theta, \Phi \text{ with final energy} \\ \text{between } E' \text{ and } E' + dE'\end{array}\right)}{\phi d\Omega dE'} \tag{2.13}$$

The partial differential cross section in a neutron scattering process can be expressed as the probability of transition from an initial state λ to the final state λ'. This transition probability is calculated using Fermi's Golden Rule [2].

This is because the interaction potential in a scattering process is found to be experimentally weak as a result of which the interaction between the neutron and the scatterer is treated as a perturbation. In general scattering theory, this equates to the Born approximation where the incoming and scattered beams are treated as plane waves λ and λ', for which the scattering cross section is given as [2]

$$\left(\frac{d^2\sigma}{d\Omega d\mathrm{E}'}\right)_{\lambda'}^{\lambda} = \frac{K'}{K}\left(\frac{m_n}{2\pi\hbar^2}\right)^2 \left|\left\langle \lambda' \left| V(\vec{Q}) \right| \lambda \right\rangle\right|^2 \delta(E_{\lambda'} - E_{\lambda} - \hbar\omega) \tag{2.14}$$

Where $V(\vec{Q})$ is given as the fourier transform of the neutron-scatterer interaction potential $V(\vec{r})$.

$$V(\vec{Q}) = \int V(\vec{r}) e^{(i\vec{Q}\cdot\vec{r})} d^3r \tag{2.15}$$

In order to determine the scattering cross-section for the whole process, it is important to take into account the scattering considering the initial ( $\vec{\sigma}$ ) and final ( $\vec{\sigma}'$ ) spin state of a neutron.

$$\frac{d^2\sigma}{d\Omega d\mathrm{E}'} = \frac{K'}{K}\left(\frac{m_n}{2\pi\hbar^2}\right)^2 \sum_{\sigma,\sigma'} p_\sigma \sum_{\lambda,\lambda'} p_\lambda \left|\left\langle \vec{\sigma}'\lambda' \left| V(\vec{Q}) \right| \vec{\sigma}\lambda \right\rangle\right|^2 \delta(\mathrm{E}_{\lambda'} - \mathrm{E}_{\lambda} - \hbar\omega) \tag{2.16}$$

Where $p_\lambda$ is the probability distribution for initial neutron wavelength state λ and $p_\sigma$ can be defined at the probability density distribution for neutrons with initial spin state $\vec{\sigma}$ .

The neutron scattering determined directly depends on $V(\vec{r})$ that defines the interaction of the neutron and the scatterrer [2]. This interaction is explained as nuclear and magnetic depending on the type of interaction taking place, which could be controlled further when using polarised neutrons.

**Nuclear Scattering**

Nuclear scattering is a short range elastic interaction acting over a distance of around $10^{-14}$ m, as a result of the neutron interacting with the nucleus of the sample through the strong nuclear force [1,4]. Hence, the nuclear cross section is given as the sum of two entities, one arising from the atomic positions in one unit cell and other the arrangement of all unit cells in a crystal structure [1,4]. Another assumption considered is taking into account only elastic scattering, as only interference from periodic structure in the sample would give rise to Bragg peaks in the intensity of the elastically scattered neutrons (E = E')[8].

The nuclear elastic differential scattering cross section when the position of the atoms is $(n_1\vec{a} + n_1\vec{a} + n_1\vec{a}) + \vec{r}_m$, where $\vec{r}_m$ is the atomic position within the unit cell is given as [1,2],

$$\frac{d^2\sigma}{d\Omega dE_f} = \left| \sum_{n_{1,2,3}} e^{2\pi i(n_1 h + n_2 k + n_3 l)} \sum_m b_m e^{i\vec{q}\cdot\vec{r}_m} \right|^2 \tag{2.17}$$

Where $b_m$ is the nuclear scattering length [1, 2]. The first term in Equation 2.17 represents the sum of delta functions positioned at the reciprocal lattice vectors given by $\vec{Q} = h\vec{a}^* + k\vec{b}^* + l\vec{c}^*$.

$$\left| \sum_{n_{1,2,3}} e^{2\pi i(n_1 h + n_2 k + n_3 l)} \right|^2 = \frac{(2\pi)^3}{V_0} N \sum_{\vec{Q}} \delta(\vec{q} - \vec{Q}) \tag{2.18}$$

Where N is the total number of unit cells and $V_0$ is the volume of the unit cell.

The nuclear structure factor that is summed over m extending to all nuclei at position $\vec{r}_m$ in one unit cell is given as

$$F(\vec{q}) = \sum_m b_m e^{i\vec{q}\cdot\vec{r}_m} \tag{2.19}$$

Hence the nuclear differential scattering in the system as a result of both the atomic positions in one unit cell and the arrangement of all unit cells in a crystal structure is given as [1,2],

$$V_N(\vec{Q}) = \frac{d^2\sigma}{d\Omega dE_f} = \frac{(2\pi)^3}{V_0}\sum_{\vec{Q}}\delta(\vec{q}-\vec{Q})\left|F(\vec{q})\right|^2 \tag{2.20}$$

**Magnetic Scattering**

Magnetic scattering is a result of the interaction of the neutron magnetic dipole moment and the intrinsic spin of the unpaired electrons in the magnetic ions present in the sample. The neutron magnetic moment is given as [1, 2],

$$\vec{\mu}_n = -\gamma\mu_N\vec{\sigma} \tag{2.21}$$

where $\gamma$ is the gyromagnetic ratio, $\vec{\sigma}$ is the Pauli spin operator and $\mu_N$ is the nuclear magneton. The scattering potential as a result of the neutron magnetic moment is given as,

$$V_M(\vec{r}) = -\vec{\mu}_n \cdot \vec{B}(\vec{r}) \tag{2.22}$$

$\vec{B}(\vec{r})$ here denotes the local magnetic flux density as a result of the intrinsic spin and the orbital motion of the unpaired electrons in the atom. To understand the cross section, the Fourier transform of the interaction potential is considered in the reciprocal lattice [1, 2]. The relation between magnetisation $\vec{M}(\vec{r})$ and local flux density $\vec{B}(\vec{r})$ obtained from Maxwell's equation, is substituted in Equation 2.22 potential giving,

$$V_M(\vec{Q}) = -\vec{\mu}_n \cdot \vec{B}(\vec{Q}) = \mu_o\vec{\mu}_n \cdot \vec{M}(\vec{Q}) \tag{2.23}$$

### 2.3.3. Polarised neutrons and experimental geometry

The reported work use polarised neutrons, capable of obtaining detailed information on the magnetic state of the system. This is achieved by controlling the spin state of the neutron (polarising), depending on the type of experiment being carried out. Before understanding the effect of controlling the neutron spin for our experiment, an understanding of how controlling the spin would affect the scattering cross section, the nuclear scattering and the magnetic scattering is introduced.

When considering polarised neutrons with initial and final spin states σ and σ' the neutron scattering cross section equation obtained at Equation 2.16 can be written as [2],

$$\left(\frac{d^2\sigma}{d\Omega dE'}\right)_{\lambda\to\lambda'} \propto \left|\left\langle \vec{\sigma}'\lambda'\middle|V(\vec{Q})\middle|\vec{\sigma}\lambda\right\rangle\right|^2 \tag{2.24}$$

Let us consider the initial magnetised spin state (σ) of the neutron to be along the z –axis ($\sigma_z$), hence the z-axis is the polarisation and the quantization direction of the neutron. The spin of the neutrons are denoted by $|\uparrow\rangle$ and $|\downarrow\rangle$ denoting the 'spin up' and 'spin down' state of the neutron with respect to the z-axis neutron polarisation.

The parallel and anti-parallel polarised neutrons are found to scatter in four possible ways depending on the nature of their spin after a scattering process. The processes $|\uparrow\rangle \to |\uparrow\rangle$ and $|\downarrow\rangle \to |\downarrow\rangle$ involve no change of spin and are called a Non Spin Flip (NSF) process [1]. The processes $|\uparrow\rangle \to |\downarrow\rangle$ and $|\downarrow\rangle \to |\uparrow\rangle$, involve a change of spin and are called Spin Flip (SF) processes [1]. The scattering potential can now be rewritten as,

$$V(\vec{Q}) = V_N(\vec{Q}) \bullet \vec{\sigma} + V_M(\vec{Q}) \bullet \vec{\sigma} \tag{2.25}$$

Where $V_N(\vec{Q})$ and $V_M(\vec{Q})$ are the nuclear and magnetic scattering while accounting for the polarised spin state of the system.

$V_N(\vec{Q})$ can be rewritten in terms of the scattering length $b_m$ and a spin dependent operator that denotes the interaction of the neutron with the nuclear spin $\vec{I}(\vec{Q})$.

$$V_N(\vec{Q}) = b_m + \vec{I}(\vec{Q}) \cdot \vec{\sigma} \tag{2.26}$$

Similarly the magnetic scattering $V_M(\vec{Q})$ can be written in terms of the interaction with the spin dependent magnetic moments ( $\vec{M}(\vec{Q})$ ) of the electrons as,

$$V_M(\vec{Q}) = \vec{\sigma} \cdot \vec{M}(\vec{Q}) \tag{2.27}$$

The nuclear scattering for the 'spin up' $\left|\uparrow\right\rangle$ and 'spin down' $\left|\downarrow\right\rangle$ state can be written in terms of the nuclear and magnetic components as,

$$\begin{aligned} V(\vec{Q})\left|\uparrow\right\rangle &= (b_m + I_z(\vec{Q}) + M_z(\vec{Q}))\left|\uparrow\right\rangle + \left[(I_x(\vec{Q}) + iI_y(\vec{Q})) + (M_x(\vec{Q}) + iM_y(\vec{Q}))\right]\left|\downarrow\right\rangle \\ V(\vec{Q})\left|\downarrow\right\rangle &= (b_m - I_z(\vec{Q}) - M_z(\vec{Q}))\left|\downarrow\right\rangle + \left[(I_x(\vec{Q}) - iI_y(\vec{Q})) + (M_x(\vec{Q}) - iM_y(\vec{Q}))\right]\left|\uparrow\right\rangle \end{aligned} \tag{2.28}$$

The four different Spin Flip (SF) and Non Spin Flip (NSF) scattering processes are written as,

$$\begin{aligned} \left\langle\uparrow\left|V(\vec{Q})\right|\uparrow\right\rangle &= (b_m + I_z(\vec{Q}) + M_z(\vec{Q})) \\ \left\langle\downarrow\left|V(\vec{Q})\right|\downarrow\right\rangle &= (b_m - I_z(\vec{Q}) - M_z(\vec{Q})) \\ \left\langle\downarrow\left|V(\vec{Q})\right|\uparrow\right\rangle &= (I_x(\vec{Q}) + iI_y(\vec{Q})) + (M_x(\vec{Q}) + iM_y(\vec{Q})) \\ \left\langle\uparrow\left|V(\vec{Q})\right|\downarrow\right\rangle &= (I_x(\vec{Q}) - iI_y(\vec{Q})) + (M_x(\vec{Q}) - iM_y(\vec{Q})) \end{aligned} \tag{2.29}$$

From this we observe that a Spin Flip (SF) is observed only when the sample is magnetised perpendicular to the direction of polarisation of the neutrons [2]. In all other cases no such spin flip is seen.

*PolSANS Experimental Geometry*

The samples used in the PolSANS experiment are magnetised perpendicular to the plane of the film parallel (and anti-parallel) to the polarisation state of the incoming neutrons. In the geometry shown in Figure 2.8, let $\vec{K}$ be the incoming wave vector, $\vec{K}'$ be the outgoing wave vector and $\vec{M}$ be the magnetisation perpendicular to the plane of the sample. In this geometry the scattering vector $\vec{Q}$ thus lies within the plane of the film and the $\vec{Q}$ -dependent scattering is measured along all directions in the plane using a two dimensional multi-detector.

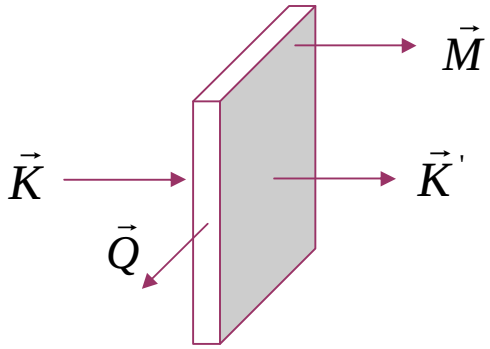


**Figure 2.8** Experimental scattering geometry

From the nuclear scattering theory for polarised neutrons, it is understood that when the sample is magnetised parallel (and anti-parallel) to the polarisation state of the incoming neutrons no spin flip occurs [1,2]. The equations are rewritten for the Non Spin Flip (NSF) cases with the nuclear and magnetic component of scattering as,

$$\begin{aligned} \left\langle \uparrow \left| V(\vec{Q}) \right| \uparrow \right\rangle &= (b_m + I_z(\vec{Q}) + M_z(\vec{Q})) \\ \left\langle \downarrow \left| V(\vec{Q}) \right| \downarrow \right\rangle &= (b_m - I_z(\vec{Q}) - M_z(\vec{Q})) \end{aligned} \tag{2.30}$$

In Equation 2.31, the nuclear spin contribution $\vec{I}_z(\vec{Q})$ to the scattering terms can be ignored as its contribution is not within the experimental 'q'-range. Equation 2.31 now reduces to,

$$\begin{aligned} \left\langle \uparrow \left| V(\vec{Q}) \right| \uparrow \right\rangle &= (b_m + M_z(\vec{Q})) \\ \left\langle \downarrow \left| V(\vec{Q}) \right| \downarrow \right\rangle &= (b_m - M_z(\vec{Q})) \end{aligned} \tag{2.31}$$

For the case of coherent scattering one has to evaluate the squares of the matrix elements. Equation 2.31 is hence expressed as,

$$\begin{aligned} \left\langle \uparrow \left| V(\vec{Q}) \right| \uparrow \right\rangle^2 &= (b_m + M_z(\vec{Q}))^2 \\ \left\langle \downarrow \left| V(\vec{Q}) \right| \downarrow \right\rangle^2 &= (b_m - M_z(\vec{Q}))^2 \end{aligned} \tag{2.32}$$

The difference between the two cases of Non Spin Flip (NSF) scattering gives,

$$\left\langle \uparrow \left| V(\vec{Q}) \right| \uparrow \right\rangle^2 - \left\langle \downarrow \left| V(\vec{Q}) \right| \downarrow \right\rangle^2 = 4\,\mathrm{Re}(b_m * M_z(\vec{Q})) \tag{2.33}$$

This experimental geometry is used to investigate the nuclear and magnetic properties of the CoCrPt grains in the perpendicular magnetic medium [12]. The CoCrPt magnetic grains have an easy magnetic axis perpendicular to the plane of the thin film medium [13]. Hence by applying an out-of-plane magnetic field the magnetic grains in the thin film can be saturated in the out-of-plane direction. A PolSANS experiment is then carried out in this geometry for the two spin states, and the difference in their scattering intensities gives the real product of the nuclear and magnetic scattering obtained from the CoCrPt grains. This difference in scattering intensity is understood using analytical models that also account for the size and distribution of the CoCrPt grains in the thin film structure [12,13,14].

### 2.3.4. Data analysis and mathematical modelling

GRASP is a MATLAB script application designed for the graphical inspection, analysis and reduction of multi-detector data produced by the Small-Angle Neutron Scattering instruments [15]. GRASP was developed at Institut Laue-Langevin, and is widely used to analyse neutron scattering data [15]. GRASP provides a graphical interpretation of the data on the detector, across the q range allowing further data processing and analysis. The GRASP software is used in the experiments to determine the difference in the non spin flip scattering intensities, and its outcome is observed in Figure 2.9 [15]. In principle the scattering data, or the difference in scattering intensities can be analysed across an experimental q range using the GRASP software [15].

Looking at the experimental geomtery in Figure 2.8, when the magnetisation is perpendicular to the plane of the film along the direction of the polarisation of the neutrons, a combination of nuclear and magnetic scattering specific to each spin state is observed. The data is gathered for the required q range over a significant period of time, resulting in high statistics data with higher signal to noise ratio's (SNR). GRASP obtains the difference in the intensities for the up and down spin scattering data, providing a visual tool to inspect its outcome [15].

$$\left\langle \uparrow \left| V(\vec{Q}) \right| \uparrow \right\rangle^2 - \left\langle \downarrow \left| V(\vec{Q}) \right| \downarrow \right\rangle^2 = 4\,\mathrm{Re}(b_m * M_z(\vec{Q})) \tag{2.33}$$

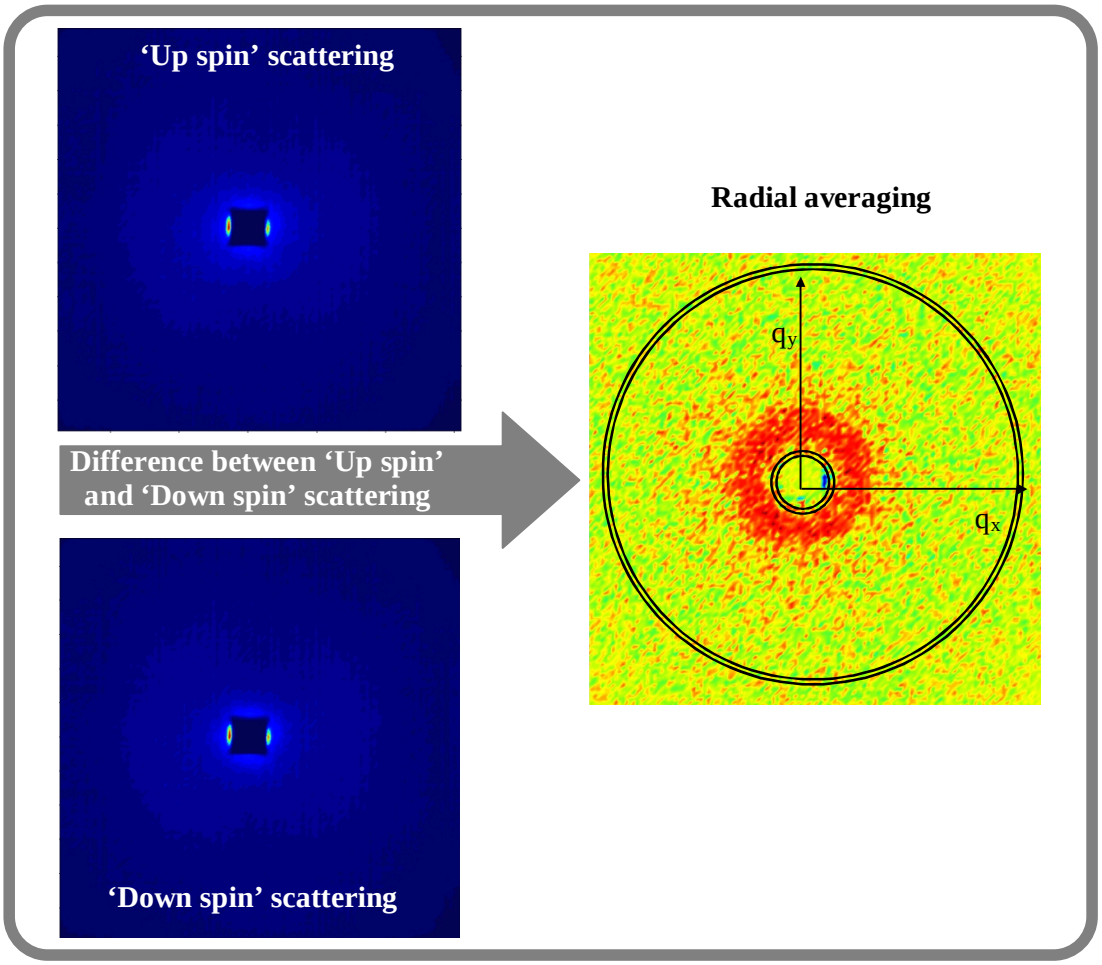


**Figure 2.9** GRASP images showing the graphical interpretation of the subtraction of intensities between two spin states across a 'q' range [15]

Figure 2.9 shows the graphical interpretation of the 'spin up' and 'spin down' scattering data visulaised using GRASP. Taking the difference in the intensities, gives a red annular ring that clearly stands out from the light green background observed. The two contrasting colours represent difference in intensities with the red ring like structure indicating an increase in intensity in comparison to the green background. A radial averaging program that comes with the GRASP package is used to determine the difference in scattering across the $q_{x-y}$ plane [15]. Radial averaging is carried out with incremented radius $q_i$ by a width $\Delta q_i$ across the q range. This is summed over values of a radial angle '$\theta$' that varies from 0 to $2\pi$ [15].

While carrying out a radial average, an increase in intensity as a result of the ring shaped structure is observed radially as a function of q. As $q_i$ radially varies from its initial value to its final value, with a width $\Delta q_i$ the intensity mapped across q gives us the neutron scattering observed in our experiment. Also note that the initial radius is set keeping in mind the attentuated direct beam at the center.

The work reported uses GRASP as a tool to carry out this subtraction, giving experimental scattering data with information on the nuclear and the magnetic structure of the grain at different magnetic fields [15]. The reported work uses different analytical and numerical methods/models to simulate the experimental scattering observed, in order to explain the experimental results. The reported work has used three different approaches to model and understand the experimental data. The first two approaches model the shape, size and distribution of the CoCrPt grains as form and structures factors; while the third approach uses transmission electron microscopy (TEM) images of the CoCrPt grains in the recording layer, to simulate the experimental results [16,17,18,19].

### *Mathematical Modelling*

In order to mathematically model the magnetic grains, an initial understanding of the shape and the size of the grains is necessary. Cross sectional and surface TEM images published in available literature show us that the shape of the CoCrPt grain, can to a reasonable approximation, taken to be that of a cylinder [19,20]. Figure 2.9a is a cross sectional TEM image of a CoCrPt that shows the uniform grain structure observed in the CoCrPt grain, providing more evidence for lateral uniformity when considering a cylinderical model CoCrPt grain [19,20].

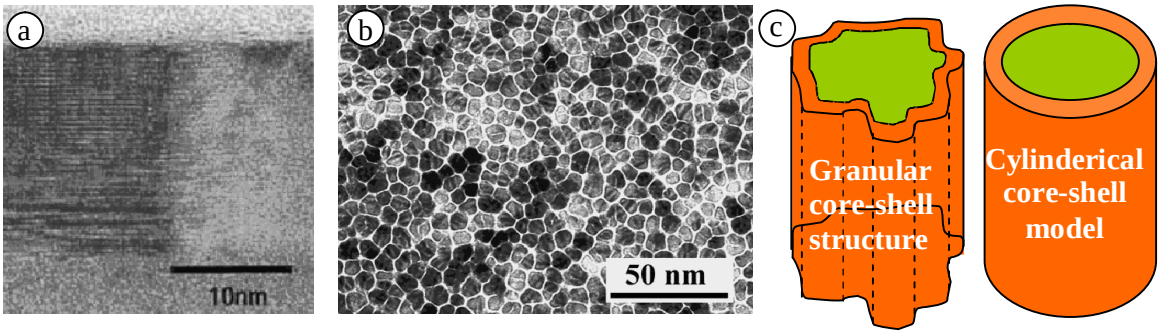


**Figure 2.10** a. Cross-sectional TEM of the recording layer[19] b. Surface TEM of the recording layer[7] c. Graphic illustration that shows the approximation taken between the speculated granular core-shell structure and a cylindrical core-shell model

Plane view TEM images of the CoCrPt grains in Figure 2.10b show that the grains have rounded edges that correspond closely to circular structures. Hence a cylindrical model is the closest approximation for the granular structure in the perpendicular magnetic medium. The grains were also found to be of different sizes and this polydispersity in grain sizes is accounted for in the mathematical models [19,20]. The CoCrPt grains by themselves have been reported to have smaller magnetic cores with an outer nonmagnetic shell [21,22]. This has been largely associated with grains having a larger concentration of the Co towards the core of the grain, which explains the more magnetic core in the CoCrPt grain [21,22]. These results have inspired a core shell model in our mathematical simulations to simulate the neutron scattering experimental data. The physical CoCrPt grain has an inner magnetic core whose size is determined by nuclear scattering, to be at a certain ratio to the physical size of the grain.

### (a) Form and structure factor models

An analytical model is built from the theoretical understanding of the contribution of nuclear and magnetic scattering while also considering the distribution of the CoCrPt grains in the recording layer. Equation 2.33 provides a general understanding on the effect of nuclear and magnetic scattering while calculating difference in intensities of ‘up’ and ‘down’ spin states. However, in practice this nuclear and magnetic scattering is a result of form (shape) and structure (distribution) factors that the analytical model looks to investigate [16,17,18].

Considering the form factor of the physical CoCrPt grain to be $f_n(k\sigma)$ and form factor of the magnetic grain to be $f_m(k\sigma)$ in a cylindrical core-shell model, the structure factor of the core-shell distribution is given as $S(k\sigma)$[23]. The scattering process also results in a significant amount of background scattering $I_{bkg}$, that we also look to take into account, when rewriting the net 'spin up' and 'spin down' scattering,

$$I^{\uparrow}(k\sigma) = \alpha S(k\sigma) f_n^2(k\sigma) + \beta S(k\sigma) f_m^2(k\sigma) + 2\gamma S(k\sigma) f_n(k\sigma) f_m(k\sigma) + I_{bkg} \tag{2.34}$$

$$I^{\downarrow}(k\sigma) = \alpha S(k\sigma) f_n^2(k\sigma) + \beta S(k\sigma) f_m^2(k\sigma) - 2\gamma S(k\sigma) f_n(k\sigma) f_m(k\sigma) + I_{bkg} \tag{2.35}$$

Where α, β and γ are numerical constants [2,23].

The difference in scattering cross term is given as [23],

$$I^{\uparrow}(k\sigma) - I^{\downarrow}(k\sigma) = 4\gamma S(k\sigma) f_n(k\sigma) f_m(k\sigma) \tag{2.36}$$

This relation gives us the general understanding of difference in scattering between up and down spin states [23]. However this approach considers a monodispersed CoCrPt grain system which in reality is not the case. Hence, a more detailed approach that looks at the influence of form factors over polydispersed diameters with a core-shell model is investigated. These models also investigate the use of different structure factor models to mathematically model the experimental data [16,17,18].

**(1)** ***Mono approximation analytical model***

The mono approximation model uses an analytical function that describes the structure-factor associated with a structure of a 3 dimensional liquid metal as described by Ashcroft and Lekner [16,17]. Although the paper discusses scattering intensity for a simple hard-sphere based structure factor model based on Percus and Yevick's work, our analytical function incorporates the core-shell cylindrical form factor over a Gamma-Schulz function that accounts for the polydispersity of the CoCrPt grains [16,17].

The structure factor $S(k\sigma)$ when $\sigma$ is the diameter of the hard sphere is given as,

$$S(k\sigma) = \{1 - nc(k\sigma)\}^{-1} \tag{2.37}$$

where n is the number density that can be calculated from the packing density factor and q is the modulus of the wave vector ($k = 2\pi\sin(\theta)/\lambda$ with scattering angle $2\theta$ and wavelength $\lambda$) [10]. The $c(k\sigma)$ term is then expressed as,

$$c(k\sigma) = -4\pi\sigma^3 \int_0^1 s^2 \frac{\sin sk\sigma}{sk\sigma}(\alpha + \beta s + \gamma s^3)ds \tag{2.38}$$

where the packing density parameter $\eta$ is defined by parameters $\alpha$, $\beta$, and $\gamma$ [16,17].

$$\begin{aligned} \eta &= (\pi/6)n\sigma^3 \\ \alpha &= (1+2\eta)^2/(1-\eta)^4 \\ \beta &= -6\eta(1+\eta/2)^2/(1-\eta)^4 \\ \gamma &= (1/2)\eta(1+2\eta)^2/(1-\eta)^4 \end{aligned} \tag{2.39}$$

The form factors for the granular $f(k\sigma_n)$ and the magnetic components $f(k\sigma_m)$ of the core-shell cylinder model with diameters $\sigma_n$ and $\sigma_m$ is given as [16,17],

$$\begin{aligned} f(k\sigma_n) &= 2\pi\left(\frac{\sigma_n}{2}\right)^2 J_1\left(k*\left(\frac{\sigma_n}{2}\right)^2\right)/\left(k*\left(\frac{\sigma_n}{2}\right)^2\right) \\ f(k\sigma_m) &= 2\pi\left(\frac{\sigma_m}{2}\right)^2 J_1\left(k*\left(\frac{\sigma_m}{2}\right)^2\right)/\left(k*\left(\frac{\sigma_m}{2}\right)^2\right) \end{aligned} \tag{2.40}$$

Where $J_1$ is a Bessel function of the first order and the diameter of the magnetic grain $\sigma_m$ is a certain fraction of the physical grain diameter $\sigma_n$, considering the core-shell model. This model relates a smaller magnetic core cylinder diameter '$\sigma_m$' with the entire physical grain cylinder diameter '$\sigma_n$' using a ratio '$\kappa$'.

$$\sigma = \sigma_m = \kappa * \sigma_n, \tag{2.41}$$

Where $\kappa$ here is a proper fraction. Now Equation 2.40 when taking into account a Gamma-Schulz function to account for the polydispersity in the system is given as,

$$I_S(k) = \left|I_\uparrow(k)\right|^2 - \left|I_\downarrow(k)\right|^2 = \left\langle S(k\sigma) * f(k\sigma_n) * f(k\sigma_m)\right\rangle = \int_0^\infty f(k\sigma_n) f(k\sigma_m) S(k\sigma) P(k\sigma) d\sigma \tag{2.42}$$

Here $P(k\sigma)$ is the probability of a particle having a diameter $\sigma$ and $I_s(k)$ is the net intensity averaged across a Gamma-Schulz function to account for the polydispersity in the form factors and structure factor using a basic Percus-Yevick model [16,17].

**(2)** ***Pair structure factor analytical model***

The pair structure factor is based on the work reported by Griffith et al [18], on deriving an analytical scattering function for a polydispersed Percus-Yevick fluid [16,18]. The scattering function now takes into account scattering from a range of different sized particles, which is formulated as an integral over the Gamma-Schulz distribution comprising of a set of partial structure factors $S_{ij}(k)$ for pairs of particles of diameters $\sigma_i$ and $\sigma_j$ [16,18].

$$I_P(k) = \left|I_\uparrow(k)\right|^2 - \left|I_\downarrow(k)\right|^2 \tag{2.43}$$

$$I_P(k) = \rho \int_0^\infty f_n^{(i)}(k\sigma) f_m^{(i)}(k\sigma) P(k\sigma_i) + \rho \int_0^\infty \int_0^\infty f_n^{(i)}(k\sigma) f_m^{(j)}(k\sigma)(S_{i,j}(k\sigma) - 1) P(k\sigma_i) P(k\sigma_j) d\sigma_i d\sigma_j \tag{2.44}$$

where $P(\sigma_i)$ is the probability of a particle having diameter $\sigma_i$ given by the Gamma-Schulz functions and $f_n^{(i)}(k\sigma)$ and $f_m^{(i)}(k\sigma)$ represents the form factor for a physical and magnetic grain of diameter $\sigma_i$ in our core-shell model [16,18]. While this is for diameter $\sigma_i$, the same probability and Gamma-Schulz function also extends to diameter $\sigma_j$.

The core-shell cylindrical form factor previously used in Equation 2.40 is used to describe the system for the pair of diameters $\sigma_i$ and $\sigma_j$ [16,18],

$$\begin{aligned} P(k\sigma_i) &= 2\pi\left(\frac{\sigma_i}{2}\right)^2 J_1\left(k * \left(\frac{\sigma_i}{2}\right)^2\right) / \left(k * \left(\frac{\sigma_i}{2}\right)^2\right) \\ P(k\sigma_j) &= 2\pi\left(\frac{\sigma_j}{2}\right)^2 J_1\left(k * \left(\frac{\sigma_j}{2}\right)^2\right) / \left(k * \left(\frac{\sigma_j}{2}\right)^2\right) \end{aligned} \tag{2.45}$$

where $J_1$ again here is a Bessel function of the first order, and here again the core-shell model actually represents a physical CoCrPt grain with a magnetic core [16,18].

In applying this to our core-shell cylindrical model approach, diameters $\sigma_i$ and $\sigma_j$ are used to denote the diameters of the physical and magnetic grain. The work also reports a partial correlation function $H_{i,j}(k\sigma)$ for a Gamma-Schulz averaged polydisperse diameter distribution. The partial pair correlation factor $H_{i,j}(k\sigma)$ can be rewritten in terms of the structure factor $S_{i,j}(k\sigma)$ as [16,18],

$$H_{i,j}(k\sigma) = (S_{i,j}(k\sigma) - 1) \tag{2.46}$$

Where,

$$H_{i,j}(k\sigma) = -2(\rho_i \rho_j)^{1/2} \frac{Z_2 Z_3 + Z_1 Z_4}{k^3 (X^2 + Y^2)} \tag{2.47}$$

where $\rho_i$, $\rho_i$ are the total particle number densities for diameters $\sigma_i$, $\sigma_j$; and a more detailed treatments of the terms $Z_1$, $Z_2$, $Z_3$, $Z_4$, X and Y is can be found in this reference [16,18].

**(b) Transmission Electron Microscopy (TEM) numerical model**

The TEM numerical approach uses real plane view TEM images of the recording layer. These TEM images show a clear distinction between the CoCrPt grain and the oxide spacer that separates the CoCrPt grains as seen in Figure 2.11a. The pixilated TEM images are interpreted as an array of numbers in MATLAB. This is done automatically by MATLAB that assigns a number to the each colour in the TEM image. This array of numbers now represent the 2-dimensional plane view of the TEM image, relating to the real size, shape and the spatial distribution of the CoCrPt grains in the oxide matrix. The granular structure in the image is then differentiated from the oxide by assigning a number say '1' denoting a colour in contrast to the oxide spacer layer that is associated with another colour denoted by another number say '0' as shown in Figure 2.11b.

A fast fourier transform (FFT) of the image is obtained giving a direct relation between the shape and the position of the granular structure. The intensity ($I_{TEM}$) is determined by radial

averaging across the data array from its center, using an averaging technique similar to that used by the GRASP software package [15]. The radial averaged intensity obtained as a function of cells in the matrix is thereby determined. This intensity was found to resemble the scattering intensity peak in the experimental data. By multiplying the TEM analysis by scaling factors relating to the dimensions of the TEM image it was found that $I_{TEM}$ directly matched the experimental neutron scattering data. This technique provides a means to numerically simulate the neutron scattering intensity by using TEM images.

$$I_{TEM} = \alpha \left\{ \left\langle \uparrow \left| V(\vec{Q}) \right| \uparrow \right\rangle^2 - \left\langle \downarrow \left| V(\vec{Q}) \right| \downarrow \right\rangle^2 \right\} \tag{2.48}$$

Where $\alpha$ is a scaling factor.

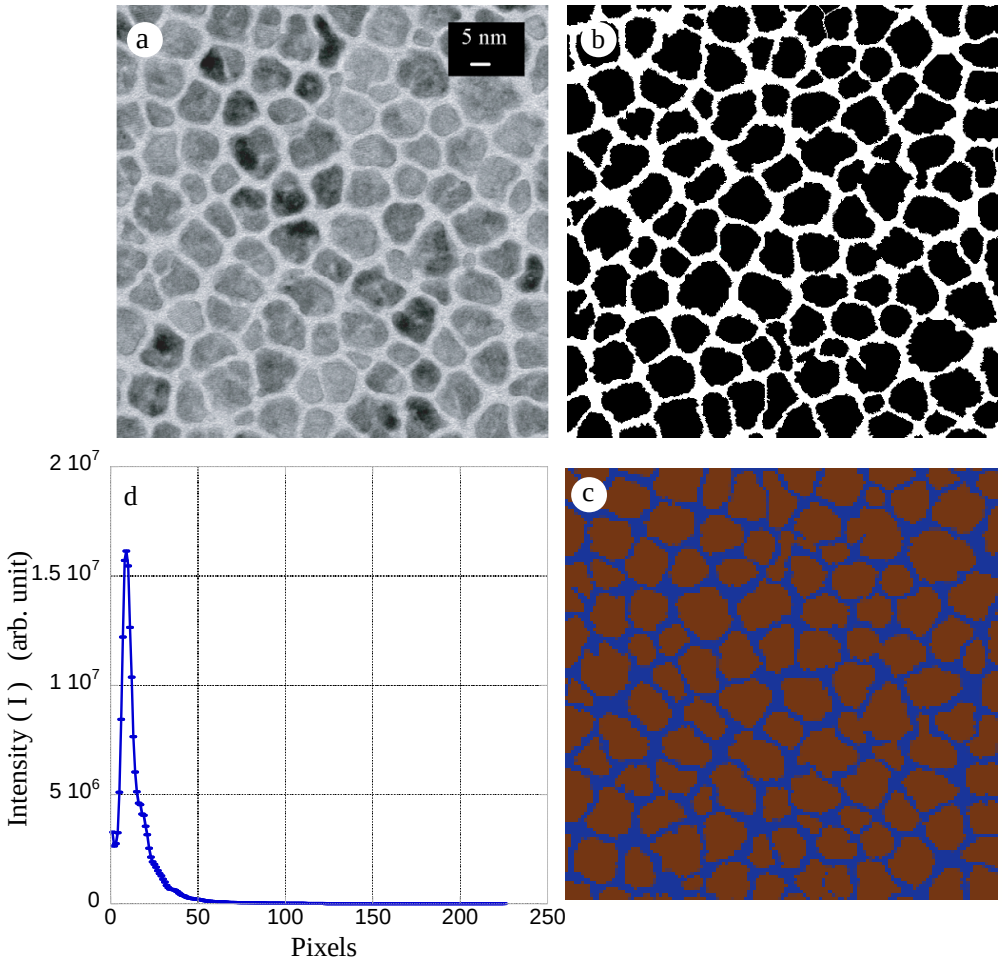


**Figure 2.11** a. Original TEM image [23] b. Digitised TEM image. c. Digitised TEM image on MATLAB and d. Scattering intensity from the radial averaged FFT of the image

In order to further distinguish the magnetic and the physical granular component of scattering, a more sophisticated numerical technique is used. This technique is introduced in Chapter 3 to distinguish the scattering from the structural and the magnetic grain separately [23]. The TEM model also numerically simulates the magnetic switching of the CoCrPt magnetic grains at different magnetic fields, introduced in Chapter 5 and Chapter 6 of the reported work [24].

## 2.4 Polarised Neutron Reflectivity (PNR)

The reported work uses polarised neutron reflectivity to shed light on the depth magnetic density profile of our multilayered structures [25,26]. In principle a general reflectivity process relies on observing the difference in the amplitude of the reflected and incident neutron beam from a planar surface or a multi-layered structure to reveal information on their structure [25,26]. Neutrons however have magnetic moments that interact with the magnetic moments of the material giving information on not just a nuclear density profile but also a magnetic density profile of the structure [25,26]. This reflectivity process can be both specular and off-specular and in a magnetic multilayer results in a more complex multiple reflection process [26,27].

Polarised neutron reflectivity uses polarised neutrons that are polarised using FeCoV/Ti multi-layered super mirrors [28]. The neutrons are then subjected to a guide field following which a spin flipper is used to control the spin state of the incoming neutrons [28]. The polarised neutrons now interact with the magnetic material to provide both specific magnetic information for a 'fixed neutron spin state-magnetic moment' interaction and nuclear structure information of the material under investigation [25,26]. This has applications in investigating the magnetic properties of thin film multi-layered structures [25]. As the perpendicular magnetic recording medium is a thin film magnetic multi-layered structure, this technique is capable of providing the depth magnetic profile of the in-plane magnetisation in the magnetic layers of the thin film structure [25]. The depth magnetic profile along with the nuclear structure allows a better understanding of the structure and the magnetic properties of the perpendicular magnetic medium.

### 2.4.1. Instrument

The polarised neutron reflectivity experiments were performed using AMOR (Apparatus for Multi Option Reflectometry) Instrument SINQ, at Paul Scherer Institut, Switzerland over the course of the research [28].

The PSI neutron source is again used for the production of neutrons. An introduction to the neutron production and moderation techniques is given in Section 2.3.1. The neutrons are passed through various moderation processes as like in the PolSANS setup in the SANS-I instrument [9]. The AMOR instrument can be adjusted to work in both the time-of-flight mode and also the 'θ-2θ' mode, but our experiments use the time-of-flight mode. In the time-of-flight mode, the frequency of the chopper, width of the gating window and the chopper-detector distance can be selected independently to provide a wide range of 'q' [28]. This 'q' range is usually achieved by tilting the deflection/frame overlap mirror thereby adjusting the angle of incidence so that the reflected neutrons are detected by the detector placed on a motorised vertical elevator. The incident wavelengths of neutrons in the experiment can be fixed between the 0.15 nm < λ< 1.3 nm while operating in the time-of-flight mode [28].

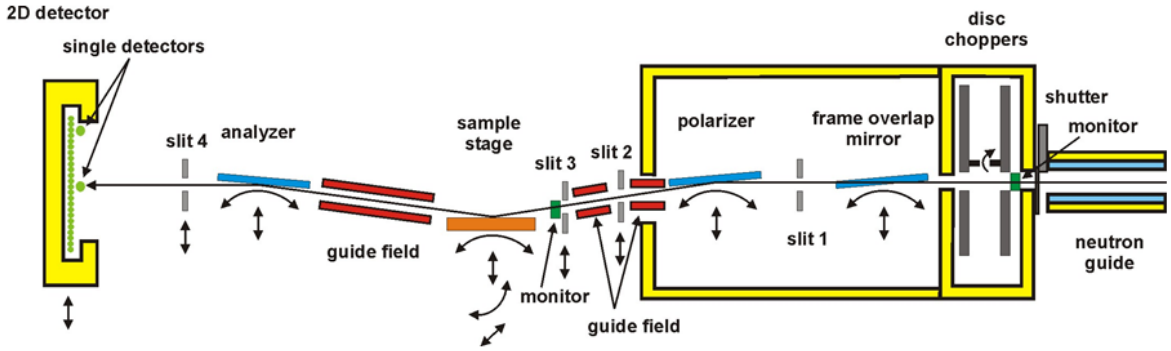


**Figure 2.12** Polarised neutron reflectivity experimental setup operating in the time-of-flight mode[28]

The experimental setup in Figure 2.12 shows that before the beam enters the instrument it passes through a collimator/shutter and disc chopper [28]. This collimator/shutter restricts beam dimensions and the chopper regulates beam wavelengths giving experimental wavelengths [28]. The system uses a double chopper that consists of two phase coupled chopper discs with slits at 180° and variable speeds depending on requirements. The 'q'-

range for a given inclination angle is controlled either by adjusting the angle on the frame overlap mirror (which is made of highly oriented pyrrolytic graphite (HOPG) double monochromator to give a monochromatic beam) or by tuning the angle of the sample stage. The collimated beam passes through a polariser that fixes a spin state to the incident neutrons by using polarised supermirrors in the setup [28]. The supermirrors shown in Figure 2.13 are made of FeCoV/Ti:N which can operate for a broad polarised neutron wavelength band [29]. The neutrons then pass through the guide field that align the neutrons parallel to the in-plane magnetic field, before they reach the sample after leaving slit S2 and S3 [28]. The neutrons are then reflected by the sample in the presence of a magnetic field.

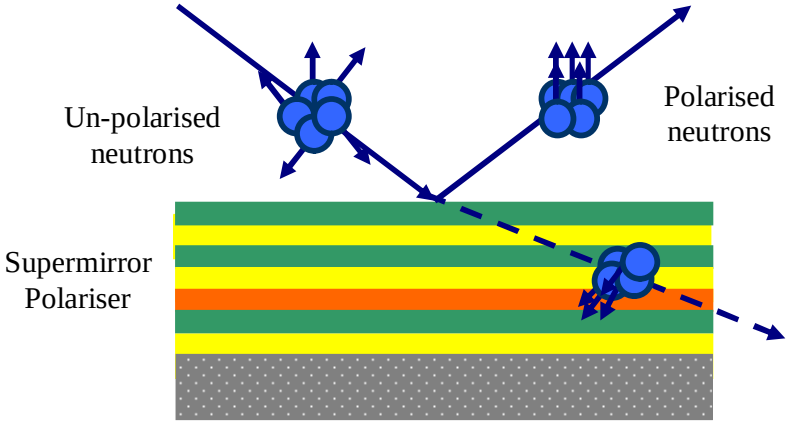


**Figure 2.13** Neutron super-mirror polariser

The detector are shown in Figure 2.12 can be adjusted along the vertical axis. The detector is made of two single $^{3}$He tubes placed on a motorised elevator, moving along the vertical axis and depending on the experimental 'q' range [28].

### 2.4.2. Theory and experimental geometry

Understanding neutron reflectivity is quite analogous to understanding reflectivity of light on a basic level when ignoring magnetic moment interactions between the incident beam and the interacting medium [30]. This phenomenon of reflectivity is best explained by Snell's law when considering specular reflection from a material. This would make sense when also considering a magnetic multi-structure as there exists the possibility of diffraction and multiple reflections in a multi-structure [30]. According to Snell's law the critical angle determines the probability of reflection and refraction between two media, which determines the 'refractive index' in a material [30].

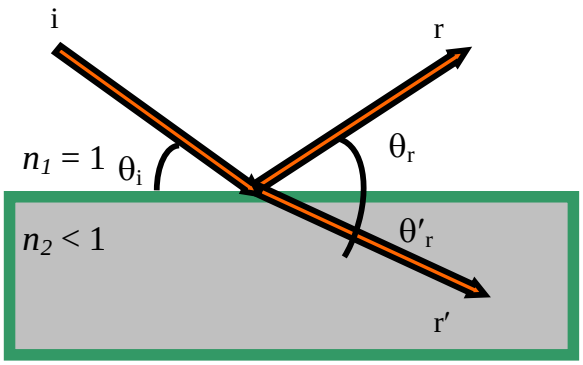


*Snell's law*

i and r are the incident ray and reflected ray
$n_1$ and $n_2$ are the refractive indexes
r′ is the refracted ray
$\theta_i$ is the angle of incidence
$\theta_r$ is the angle of reflection
$\theta'_r$ is the angle of refraction
$\theta_c$ is the critical angle that determines a reflection or a refraction process, and it can be defined as $\theta_c = \arcsin\left(\frac{n_2}{n_1}\sin\theta_2\right)$

**Figure 2.14** Snell's law in condensed matter [30]

The critical angle occurs at the interface of two different media, governed by the angle of incidence and the wavelength of the incident beam. In Figure 2.14 when incident wave 'i' has a wavelength 'λ', the critical angle determines whether a refraction or refraction process takes place. The wavelengths that are allowed to propagate through the medium are hence controlled by the refractive index and the critical angle of the medium [30].

However when this theory is put into practice in a multi-layered system with neutrons, the results are in the form of a multiple probability of refraction and reflection depending on the refractive index of the layers in contact with the neutron beam [31]. That is, if the neutron beam is refracted through a medium say at interface A and reflected at interface B in Figure 2.15, it has probability of being transmitted at C, or undergo a reflection which could lead to several such reflections and refraction at D, E etc [31]. A simpler model, that doesn't account for the numerous multiple reflections and refractions taking place in the multilayer, is shown in Figure 2.15b. This simplified model considers only one reflection from an interface is used in our theoretical approach to model the experimental data in Chapter 7 [31]. These assumptions made in the simplified model are found to simulate the experimental results, thereby adequately capturing the essence of a polarised neutron reflectivity experiment, which is to understand the physical and magnetic properties of individual layers in a multilayered thin film structure.

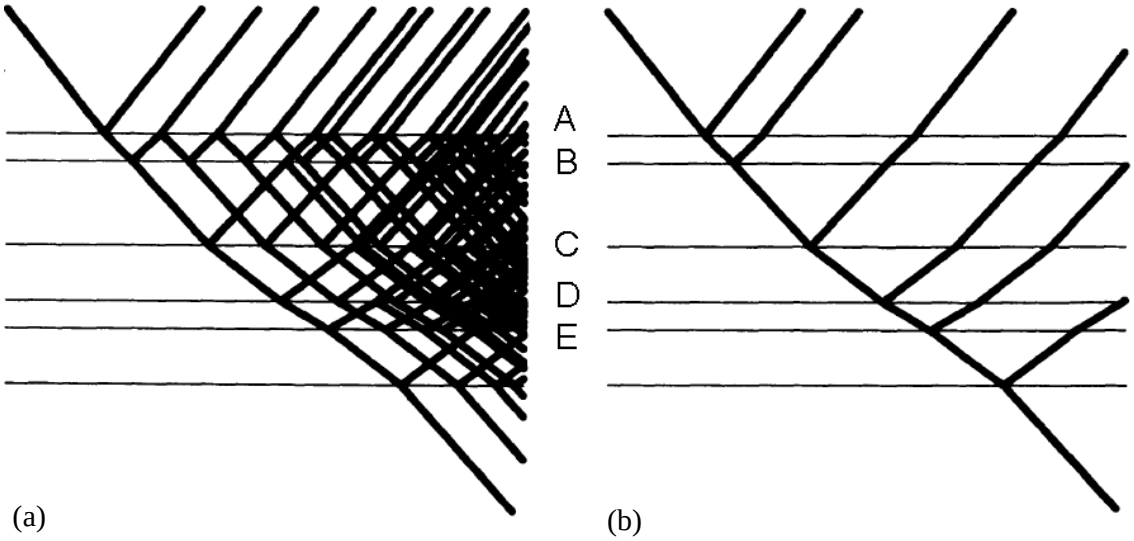


**Figure 2.15** (a) Multiple reflection/refraction from interfaces (b) Simplified model with single interface reflection [31]

*Nuclear and Magnetic Interaction*

Before understanding polarised neutron reflectivity from a multi-layered or single layered magnetic structure a basic overview of the types of interaction a neutron goes through when interacting with a magnetic thin film is shown. We have considered neutron interaction with a material to be quite analogous to light interaction however these assumptions slightly change on further analysis as neutrons have microscopic magnetic moments and possess a neutral charge in comparison to light [2].

To consider a very simple case of this interaction, let us consider a single layer of a magnetic material interacting with neutrons as shown in Figure 2.16. In principal the incoming neutrons sense both magnetic moment ($\vec{\mu}_n \cdot \vec{B}$) of the electrons along with nuclear contribution from the nucleus of the interacting atom. This potential energy (V) can be written as a sum of both nuclear and magnetic terms as [2],

$$V(\vec{r}) = h^2/(2\pi m_n)\ \rho b - \vec{\mu}_n \cdot \vec{B} \qquad (2.49)$$

Where $\vec{\mu}_n$ is the neutron moment, b the coherent scattering length, ρ is the atomic density and $\vec{B}$ is the internal magnetic field. When considering this with a parallel and anti-parallel spin arrangement, it is clear that the potential is split into two functions above and below the nuclear potential [2,25].

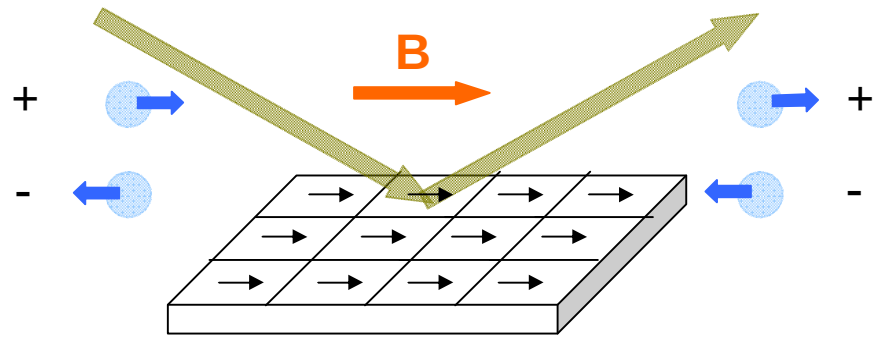


**Figure 2.16** Magnetic moments in the thin film interacting with neutron spin

### (a) Single layer magnetic thin film model

A more detailed understanding of a polarised neutron interaction with a magnetised single layer sample is demonstrated by first understanding the Schrodinger equation for a neutron with a wave function $\Psi(\vec{r})$ [2,25],

$$\left(-\frac{\hbar^2}{2m_n}\nabla^2 + V(\vec{r})\right)\Psi(\vec{r}) = E\Psi(\vec{r}) \qquad (2.50)$$

where $m_n$ is the neutron mass, $V(\vec{r})$ is the nuclear potential which when not considering the magnetic contribution is defined as $V = h^2/(2\pi m_n)\rho_n b_c$ where $\rho_n$ denotes the number density of the neutrons and the $b_c$ the coherent scattering length.

We also know their also exists a magnetic contribution that is determined by the neutron magnetic moment $\mu_n$ and the magnetisation ($\vec{M}(\vec{r})$) as a result of a magnetic field ($\vec{B}$).

$$V_m(\vec{r}) = -\vec{\mu}_n \cdot \vec{M}(\vec{r}) \tag{2.51}$$

where $\vec{\mu}_n$ is the neutron magnetic moment and $(\vec{M}(\vec{r}))$ is the magnetisation across the material under investigation[2,25].

The neutron magnetic moment ( $\vec{\mu}_n$ ) can be further written as,

$$\vec{\mu}_n = \gamma\mu\vec{\sigma} \tag{2.52}$$

where $\gamma$ is the magnetic dipole moment of a neutron, -1.913,
$\mu$ is nuclear magneton, $e\hbar/2m_p = 5.049 \times 10^{-27}$ $JT^{-1}$
and $\vec{\sigma}$ is a Pauli matrix.

Now looking at a typical polarised neutron reflectivity geometry, considering the thin film sample to be within the *x* and *y* plane with the *z*-axis perpendicular to the thin film; the neutrons are considered to be polarised along the *x*-axis [31]. From this arrangement the magnetisation contributing to neutron reflectivity is given as,

$$\vec{M}(\vec{r}) = M_x \hat{x} + M_y \hat{y} \tag{2.53}$$

and the Pauli matrix of the neutron is given as [31],

$$\vec{\sigma} = \begin{pmatrix} 1 & 0 \\ 0 & -1 \end{pmatrix}\hat{x} + \begin{pmatrix} 0 & 1 \\ 1 & 0 \end{pmatrix}\hat{y} + \begin{pmatrix} 0 & -i \\ i & 0 \end{pmatrix}\hat{z} \tag{2.54}$$

This breaks down Equation 2.51 to four separate magnetic potentials [31],

$$\left.\begin{aligned} V_m^{++}(\vec{r}) &= -\gamma\mu M_x(\vec{r}) \\ V_m^{--}(\vec{r}) &= \gamma\mu M_x(\vec{r}) \\ V_m^{+-}(\vec{r}) &= -\gamma\mu M_y(\vec{r}) \\ V_m^{-+}(\vec{r}) &= \gamma\mu M_y(\vec{r}) \end{aligned}\right\} \tag{2.55}$$

where

$^{++}$ represents the *'up'* spin of the incident neutron *'up'* spin of exiting neutron;

$^{--}$ represents the *'down'* spin of the incident neutron and *'down'* spin of exiting neutron;

$^{+-}$ represents the *'up'* spin of the incident neutron and *'down'* spin of exiting neutron;

$^{-+}$ represents the *'down'* spin of the incident neutron and *'up'* spin of exiting neutron;

From the above equations, it is evident that when the magnetisation $M_x \hat{x}$ is along the x-axis is in line with the polarisation of the neutrons, the polarised neutrons see a positive or negative potential step as a result of the magnetic contribution of the neutron moment interaction given as $V_m^{++}(\vec{r})$ and $V_m^{--}(\vec{r})$. A similar step potential can also introduced in the y-axis by using a perpendicular magnetic field, however our experimental geometry limits allows magnetisation only along the x-axis [31]. The Schrodinger equation can now be rewritten in terms of the step potentials $V_m^{++}(\vec{r})$ and $V_m^{--}(\vec{r})$ as,

$$\left.\begin{aligned}\left(-\frac{\hbar^2}{2m_n}\nabla^2 + V_n(\vec{r}) + V_m^{++}(\vec{r})\right)\Psi_+(\vec{r}) + V_m^{-+}\Psi_-(\vec{r}) = E\Psi_+(\vec{r})\\ \left(-\frac{\hbar^2}{2m_n}\nabla^2 + V_n(\vec{r}) + V_m^{--}(\vec{r})\right)\Psi_-(\vec{r}) + V_m^{+-}\Psi_+(\vec{r}) = E\Psi_-(\vec{r})\end{aligned}\right\} \qquad (2.56)$$

The equation is when considering both the contribution from the magnetic spin flip reflectivity $V_m^{+-}(\vec{r})$ and $V_m^{-+}(\vec{r})$ and the non-spin flip reflectivity $V_m^{++}(\vec{r})$ and $V_m^{--}(\vec{r})$. Although we measure both the non-spin flip and spin flip reflectivities, our present setup fails to distinguish them separately. However a more detailed analysis for various spin flip and non-spin flip cases is possible using an analyser to identify individual spin states [31].

**(b) Multi-layered magnetic thin film layer model**

This approach is extended for a simplified multilayer model that accounts for single interface reflection. The Schrodinger equation for a neutron wave function $\Psi(\vec{r})$ in Equation 2.50, is written in terms of the neutron wave vector parallel to the surface [31],

$$\Psi(\vec{r}) = \psi(y)e^{ik_{||}\vec{r}_{||}} \tag{2.57}$$

This can be written as,

$$\left[\frac{d^2}{dy^2} + \left[\frac{2m_n}{\hbar^2}(E-V) - k_{||}^{\ 2}\right]\right]\psi(y) = 0 \tag{2.58}$$

Figure 2.17 is the most simple geometry of PNR with an incident neutron wave $k_i$ and a reflected wave $k_r$. Here the perpendicular wave vector q is the only scattering wave vector considering a specular case where the magnetic thin films are uniformly flat. The x-axis in Figure 2.17 is taken to be along the plane of the thin film and the y-axis is perpendicular to the plane of the thin film.

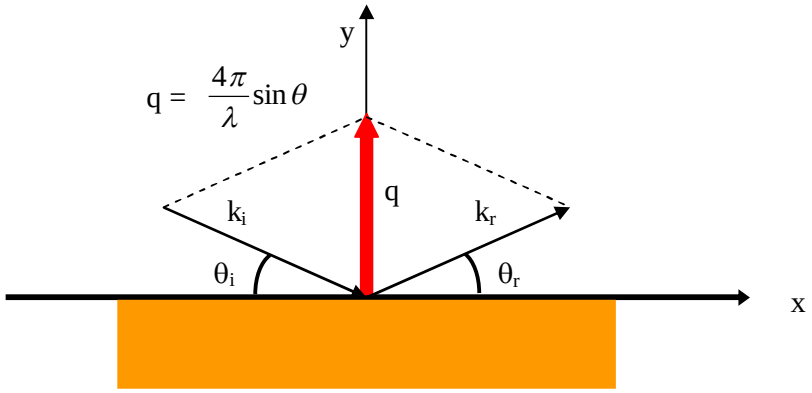


**Figure 2.17** Polarised neutron reflectivity geometry

This reduces Equation 2.58 to,

$$\frac{\hbar}{2m_n}(q + k_{||}^{\ 2}) = (E-V) \tag{2.59}$$

Now considering a multi-layered sample containing n regions numbered starting from vacuum above as '1' to the substrate 'n'. The thin film layers then fall between $2 \leq \alpha < n$, and for any layer α one has to solve the equation,

$$\left[\frac{d^2}{dy^2} + q_\alpha^2\right]\psi(y) = 0 \tag{2.60}$$

Where $q_\alpha$ can be written as,

$$q_\alpha = \left[ \frac{2m_n}{\hbar^2}\left(E_\perp - V_\alpha\right) \right]^{\frac{1}{2}} \tag{2.61}$$

and $E_\perp = E - \hbar^2 k_{||}^2 / 2m_n$. The solution for this is achieved by taking the sum of the right and the left travelling waves [31],

$$\psi_\alpha(y) = a_\alpha e^{iq_\alpha(y=y_\alpha)} + b_\alpha e^{-iq_\alpha(y=y_\alpha)} \tag{2.62}$$

At the interface $y = y_\alpha$, $\psi_\alpha(y)$ is represented by a vector,

$$\psi_\alpha(y) = \begin{pmatrix} a_\alpha \\ b_\alpha \end{pmatrix} \tag{2.63}$$

Then

$$\begin{pmatrix} 1 \\ r \end{pmatrix} = \begin{pmatrix} M_{11} & M_{12} \\ rM_{21} & M_{22} \end{pmatrix} \begin{pmatrix} t \\ 0 \end{pmatrix} \tag{2.64}$$

It is known that at the first interface y =$y_1$=0 so $\psi = \begin{pmatrix} 1 \\ r \end{pmatrix}$ and at the last interface y = $y_{n-1}$ so $\psi = \begin{pmatrix} t \\ 0 \end{pmatrix}$. The transmission and specular reflection coefficients are defined here as t = $1/M_{11}$ and r = $M_{21}/M_{11}$. The transfer matrix $\vec{M}$ is now defined as,

$$\vec{M} = \vec{D}^{-1}(q_1)\left[ \prod_{j=2}^{N-1} \left[ \vec{D}(1_j)\vec{P}(q_j, d_j)\vec{D}^{-1}(q_j) \right] \right] \vec{D}(q_N) \tag{2.65}$$

Where $\vec{D}(q_\alpha)$ is the transmission matrix $\vec{P}(q_\alpha, d_\alpha)$ is the propagation matrix and $d_\alpha = y_\alpha - y_{\alpha-1}$ is the width of the $\alpha^{th}$ region, which is the thickness of the layer.

By applying the boundary conditions that $\psi$ and $\frac{d\psi}{dy}$ are constant, it is shown that

$$\vec{D}(q_\alpha)=\begin{pmatrix}1 & 1\\ q_\alpha & -q_\alpha\end{pmatrix} \quad \text{and} \quad \vec{P}(q_\alpha,d_\alpha)=\begin{pmatrix}e^{-iq_\alpha d_\alpha} & 0\\ 0 & e^{-iq_\alpha d_\alpha}\end{pmatrix} \tag{2.66}$$

The neutron nuclear and magnetic interactions should also be accounted for in the various layers. Equation (2.49) is now rewritten as [31],

$$\vec{V}_\alpha=\frac{\hbar^2}{2\pi m_n}\rho_\alpha b_\alpha-\vec{\mu}_n\cdot\vec{B}_\alpha \tag{2.67}$$

Where $\vec{\mu}_n$ is the neutron moment, $b_\alpha$ the coherent scattering length, $\rho_\alpha$ is the atomic density and $\vec{B}_\alpha$ is the internal magnetic field in the region α. The spin dependent transfer matrix which is dictated by the neutron spin and magnetic field in each layer is given as [31],

$$\vec{M}=\vec{D}^{-1}(q_1,q_1)\vec{R}(\theta_{1.2})\left[\prod_{\alpha=2}^{N-1}\{\vec{D}(q_\alpha^{\uparrow},q_\alpha^{\downarrow})\vec{P}(q_\alpha^{\uparrow},q_\alpha^{\downarrow},d_\alpha)\vec{D}^{-1}(q_\alpha^{\uparrow},q_\alpha^{\downarrow})\vec{R}(\theta_{\alpha,\alpha+1})\}\right]\vec{D}(\alpha_N,\alpha_N) \tag{2.68}$$

Where a generalised 4x4 form of a transmission matrix and propagation matrix is given as [31],

$$\vec{D}(q_\alpha^{\uparrow},q_\alpha^{\downarrow})=\begin{pmatrix}\vec{D}(q_\alpha^{\uparrow}) & 0\\ 0 & \vec{D}(q_\alpha^{\uparrow})\end{pmatrix} \tag{2.69}$$

$$\vec{P}(q_\alpha^{\uparrow},q_\alpha^{\downarrow},d_\alpha)=\begin{pmatrix}\vec{D}(q_\alpha^{\uparrow},d_\alpha) & 0\\ 0 & \vec{D}(q_\alpha^{\downarrow},d_\alpha)\end{pmatrix} \tag{2.70}$$

The matrix responsible for rotating the magnetic field at the interface is given as [31],

$$\vec{R}(\theta_{\alpha,\alpha-1})=\begin{pmatrix}\cos(\theta_{\alpha,\alpha+1}/2)\vec{I} & \sin(\theta_{\alpha,\alpha+1}/2)\vec{I}\\ -\sin(\theta_{\alpha,\alpha+1}/2)\vec{I} & \cos(\theta_{\alpha,\alpha+1}/2)\vec{I}\end{pmatrix} \tag{2.71}$$

Where $\vec{I}$ is the identity matrix and from this the spin dependent transfer matrix is given as,

$$
\begin{aligned}
t_u^{\uparrow} &= M_{33}/(M_{11}M_{33} - M_{13}M_{31}) \\
t_u^{\downarrow} &= -M_{31}/(M_{11}M_{33} - M_{13}M_{31}) \\
r_u^{\uparrow} &= (M_{21}M_{33} - M_{23}M_{31})/(M_{11}M_{33} - M_{13}M_{31}) \\
r_u^{\downarrow} &= (M_{41}M_{33} - M_{43}M_{31})/(M_{11}M_{33} - M_{13}M_{31}) \\
t_d^{\uparrow} &= -M_{13}/(M_{11}M_{33} - M_{13}M_{31}) \\
t_d^{\downarrow} &= M_{11}/(M_{11}M_{33} - M_{13}M_{31}) \\
r_d^{\uparrow} &= (M_{23}M_{11} - M_{21}M_{13})/(M_{11}M_{33} - M_{13}M_{31}) \\
r_d^{\downarrow} &= (M_{43}M_{11} - M_{41}M_{13})/(M_{11}M_{33} - M_{13}M_{31})
\end{aligned}
\tag{2.72}
$$

Here the subscripts on M are the indices to the matrix elements. Also in the above equations the up and down spin of a neutron are denoted by u and d. The spin asymmetry is hence defined as [31],

$$
S = \frac{R_{\uparrow} - R_{\downarrow}}{R_{\uparrow} + R_{\downarrow}} \tag{2.73}
$$

Which can now be rewritten in terms of the four reflection processes in Equation 2.72 as [31],

$$
S = \frac{\left|r_u^{\uparrow}\right|^2 + \left|r_u^{\downarrow}\right|^2 - \left|r_d^{\uparrow}\right|^2 - \left|r_d^{\downarrow}\right|^2}{\left|r_u^{\uparrow}\right|^2 + \left|r_u^{\downarrow}\right|^2 + \left|r_d^{\uparrow}\right|^2 + \left|r_d^{\downarrow}\right|^2} \tag{2.74}
$$

### 2.4.3. Data analysis and mathematical modelling

A MATLAB script initially developed by Dr. Stephen Lister and enhanced over the course of the PhD work was used. This script is based on the theoretical work reported by Blundell *et al* [31]. The MATLAB script allows flexibility that facilitates building multi-layered thin film structures with controlled layer thickness, where each layer has a different number density and scattering length that represents either the element or the alloy used in that particular layer. To explain this better an example has been presented in Figure 2.18. The reflectivity plot in Figure 2.18 is for a 25 nm thick cobalt layer on a $SiO_2$ substrate. The number densities, scattering lengths and magnetisation of the layers are given beside the reflectivity plot.

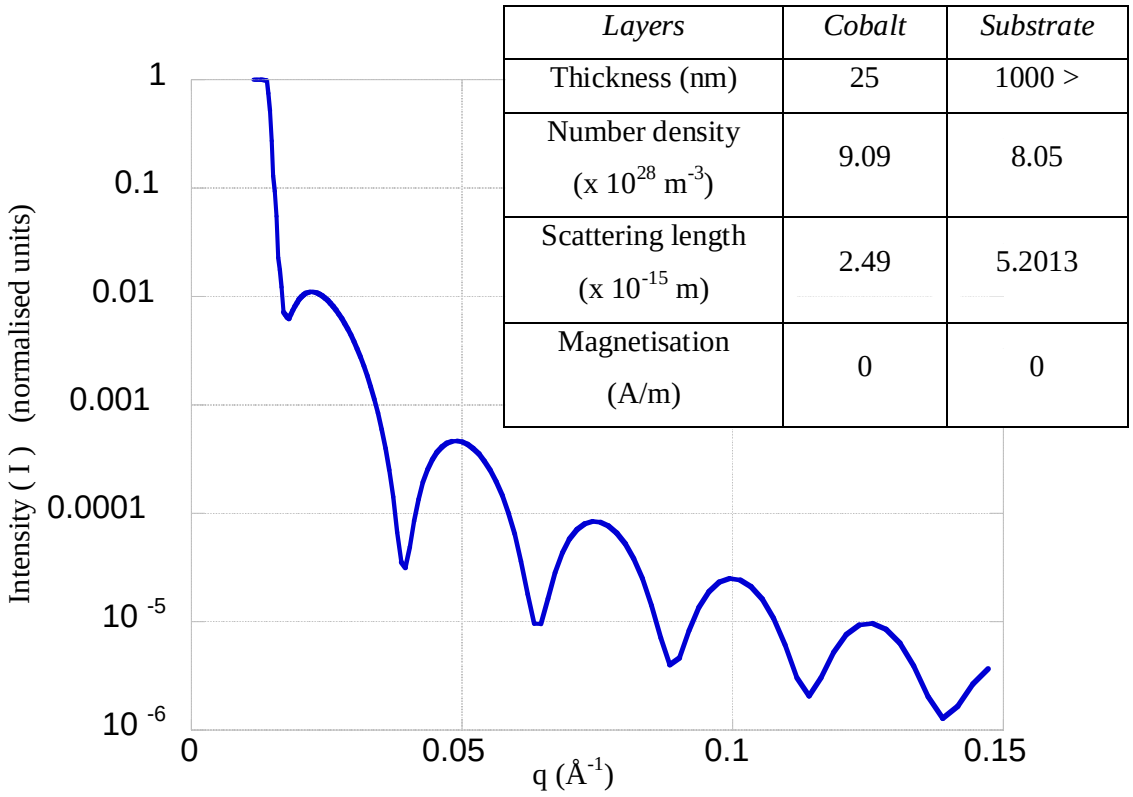


| *Layers* | *Cobalt* | *Substrate* |
|---|---|---|
| Thickness (nm) | 25 | 1000 > |
| Number density ($\times 10^{28}$ $m^{-3}$) | 9.09 | 8.05 |
| Scattering length ($\times 10^{-15}$ m) | 2.49 | 5.2013 |
| Magnetisation (A/m) | 0 | 0 |

**Figure 2.18** Simulated reflectivity plot for a 25 nm thick cobalt layer along with tabulated properties

The ripples seen in the falling intensity of the reflectivity plot are a result of the nuclear structure in the 25 nm thick layer, and the length scales of the ripples in 'q' space directly relate to the thickness of the thin film in real space. Factors like the scattering length and the number density that relate to the properties of the thin film layer/alloy also influence the reflectivity plot, and when considering a multi-layered system where we have different layers with different properties we get more complex reflectivity plots that relates to the various layers and their nuclear properties.

Now let us assume that the 25 nm cobalt layer is magnetised. Under the influence of a magnetic field let us assume that the magnetisation in the Co layer is 0.3 A/m. Now the 'spin up' and 'spin down' neutrons give two reflectivity plots, one as a result of the parallel spin neutrons interacting with the magnetised moments in the cobalt (Co) layer and the other from the anti-parallel spin neutrons interacting with the magnetised moments in the Cobalt (Co) layer. The two plots are shown in Figure 2.19 a, and they arise as a result of the composition and the magnetic state of the 25 nm thick cobalt layer.

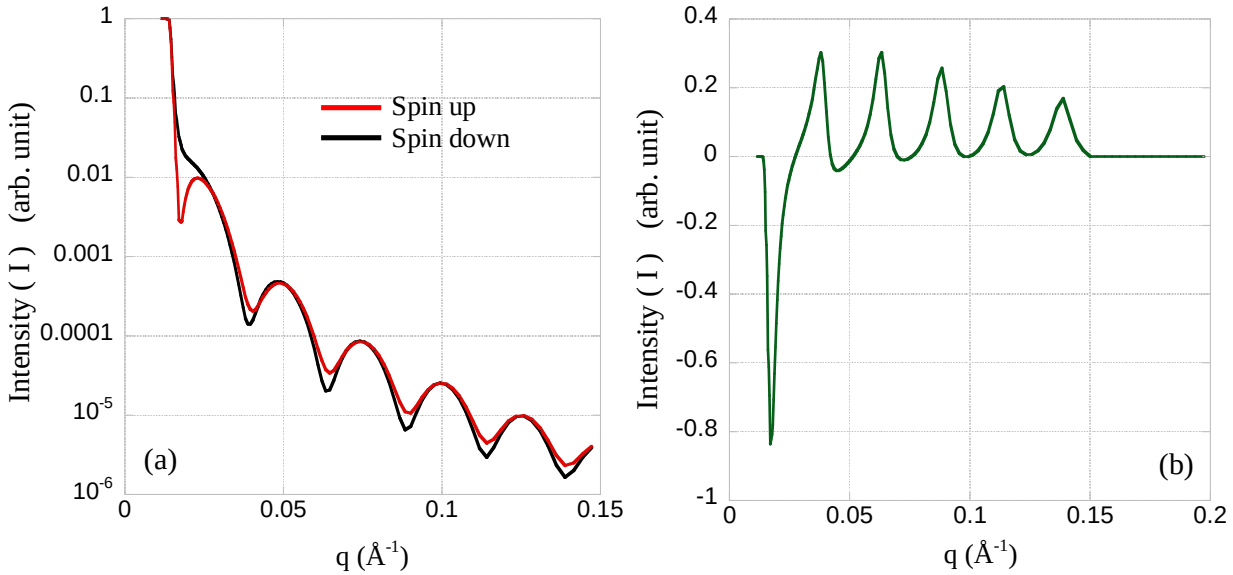


**Figure 2.19** (a) Simulated 'spin up' and 'spin down' reflectivity plots for the 25 nm thick Co sample with a magnetisation of 0.3 A/m (b) Simulated spin asymmetry plots for the 25 nm thick Co sample with a magnetisation of 0.3 A/m

Figure 2.19.a shows the simulated 'spin up' and 'spin down' reflectivity as a result of the magnetic state in the cobalt thin film and Figure 2.19.b shows the spin asymmetry that arises as a result of the ratio between the difference in the reflectivity and the sum of the reflectivity for the two different spin states. These models show that the theoretical work presented by Blundell and Bland [31], can be analytically modelled using MATLAB to build and analyse thin film multi-layered magnetic structures. This analytical model is later used to analyse the experimental data presented in Chapter 7 of the reported work.

## 2.5 References


[1] Albert Furrer, Joel Mesot, Thierry Strässle "Neutron Scattering in Condensed matter Physics" World Scientific Publishing Co. Ltd, Singapore (2009) (ISBN-13: 978-9810248314)

[2] Gordon Leslie Squires "Introduction to the Theory of Thermal neutron Scattering" Dover Publications, New York (1997) (ISBN-13: 978-0486694474)

[3] Sean Langridge, Stephen W. Lovesey "Uses of neutron and X-ray beams to investigate magnetism" Radiation Physics and Chemistry, 61( 3–6), (2001) p.235-239 (DOI: 10.1016/S0969-806X(01)00246-8)

[4] Christian Vettier "Neutrons and X-rays: two probes for magnetism" Radiation Physics and Chemistry, 61( 3–6), (2001) p.235-239 (DOI: 10.1016/0921-4526(93)90103-D)

[5] E. Ressouche "Investigating molecular magnetism with polarized neutrons" Physica B: Condensed Matter, 267–268, (1999) p.27-36 (DOI: 10.1016/S0921-4526(99)00063-0)

[6] Kineo Tsukada, Shigeya Tanaka, Yoshiaki Tomita, Michio Maruyama "Elastic and inelastic scattering of fast neutrons from iron, nickel and tungsten" Nuclear Physics A, 125(3), (1969) p.641-653 (DOI: 10.1016/0375-9474(69)90754-4)

[7] S. O. Pillai "Solid State Physics" New Age International Pvt Ltd Publishers, Delhi (c2009) (ISBN-13: 978-1906574109)

[8] Neil W. Ashcroft, N. David Mermin "Solid state physics" Holt, Rinehart and Winston : Harcourt Brace Jovanich, San Diego (c1976) (ISBN-13: 978-0030839931)

[9] J. Kohlbrecher, W. Wagner "The new SANS instrument at the Swiss spallation source SINQ", J. Appl. Cryst. 33, (2000) p.804-806 (DOI: 10.1107/S0021889800099775)

[10] A. Anghel *et al.* " The PSI ultra-cold neutron sourceNuclear Instruments and Methods in Physics Research Section A: Accelerators, Spectrometers, Detectors and Associated

Equipment, 611(2–3), (2009) p.272-275 (DOI: 10.1016/j.nima.2009.07.077)

[11] V.K. Aswal *et al.* "Characterisation of the polarised neutron beam at the small angle scattering instrument SANS-I with a polarised proton target" Nucl. Instr. and Meth. A 586(1), (2008), p.86-89 (DOI: 10.1016/j.nima.2007.11.062)

[12] Xiaofei Yang, Long You, Min Song, Gengqi Lin, Zuoyi Li "The magnetic properties of sputter-deposited and annealed CoCr/CoCrPt recording media" Materials & Design, 27(3), (2006) p.223-225 (DOI: 10.1016/j.matdes.2004.10.018)

[13] S. N. Piramanayagam "Perpendicular recording media for hard disk drives" J. Appl. Phys. 102, 011301 (2007) (DOI: 10.1063/1.2750414)

[14] J. Schweizer "Polarized Neutrons and Polarization Analysis" Neutron Scattering from Magnetic Materials, (2006) p.153-213(DOI:10.1016/B978-044451050-1/50005-7)

[15] Charles Dewhurst "GRAS$_{ans}$P: Graphical Reduction and Analysis SANS Manual" Institute Laue Langevin, France. Last modified December 15, 2011. http://www.ill.eu/?id=6300

[16] A. Guinier, G. Fournet "Small-Angle Scattering of X-Rays" John Wiley and Sons, New York (1955) (DOI: 10.1002/pol.1956.120199326)

[17] N.W. Ashcroft, J. Lekner "Structure and Resistivity of Liquid Metals" Phys. Rev. (145), (1966) p. 83–90 (DOI: 10.1103/PhysRev.145.83)

[18] W.L. Griffith, R. Triolo, A.L. Compere "Analytical scattering function of a polydisperse Percus-Yevick fluid with Schulz- ( Gamma -) distributed diameter" Phys Rev A, 35(5), (1987) p. 2200–2206 (DOI: 10.1103/PhysRevA.33.2197)

[19] R. Araki, Y. Takahashi, I. Takekuma, S. Narishige "High-Resolution TEM Analysis of Perpendicular CoCrPt-$SiO_2$ Media" IEEE Transactions on magnetics, 44 (11), (2008) p. 3496 – 3498 (DOI: 10.1109/TMAG.2008.2002415)

[20] Wenli Pei, J. Yuan, T. Wang, Y. Fu, T. Washiya, T. Hasagawa, H. Saito, S. Ishio, N. Honda "Study on magnetization reversal of perpendicular recording media by in-field

MFM observation" Acta Materialia, 55(9), (2007) p.2959-2964 (DOI: 10.1016/j.actamat.2006.12.034)

[21] M. Futamoto, N. Inaba, Y. Hirayama, K. Ito, Y. Honda "Microstructure and micromagnetics of future thin-film media" Journal of Magnetism and Magnetic Materials, 193(1–3), (1999) p. 36-43 (DOI: 10.1016/S0304-8853(98)00492-2)

[22] M. Wismayer, S. Lee, T. Thomson, F. Ogrin, C. Dewhurst, S. Weekes, R. Cubitt "Using small-angle neutron scattering to probe the local magnetic structure of perpendicular magnetic recording media" Journal of Applied Physics, 99(8), (2006) (DOI: 08e707 10.1063/1.2165798)

[23] S. J. Lister, M. P. Wismayer, V. Venkataramana, M. A. de Vries, S. J. Ray, S. L. Lee, T. Thomson, J. Kohlbrecher, H. Do, Y. Ikeda, K. Takano, and C. Dewhurst "Small-angle polarized neutron studies of perpendicular magnetic recording media" Journal of Applied Physics, 106(6),(2009) p. 063908 - 063908-4 (DOI: 10.1063/1.3213381)

[24] S. J. Lister, T. Thomson, J. Kohlbrecher, K. Takano, V. Venkataramana, S. J. Ray, M. P. Wismayer, M. A. de Vries, H. Do, Y. Ikeda, and S. L. Lee "Size-dependent reversal of grains in perpendicular magnetic recording media measured by small-angle polarized neutron scattering" Applied Physics Letters, 97 (11), (2010) (DOI: 10.1063/1.3486680)

[25] Hartmut Zabel "Spin polarized neutron reflectivity of magnetic films and superlattices" Physica B: Condensed Matter, 198(1–3), (1994) p.156-162 (DOI: 10.1016/0921-4526(94)90151-1)

[26] G.P. Felcher, S.G.E. te Velthuis, A. Rühm, W. Donner "Polarized neutron reflectometry: recent developments and perspectives" Physica B: Condensed Matter, 297(1–4), (2001), p.87-93 (DOI: 10.1016/S0921-4526(00)00821-8)

[27] G.P. Felcher, S.G.E. te Velthuis "Perspectives of polarized-neutron reflectometry: magnetic domains and off-specular scattering" Applied Surface Science, 182(3–4), (2001) p.209-215 (DOI: 10.1016/S0169-4332(01)00413-5)

[28] D. Clemens, P. Gross, P. Keller, N. Schlumpf, M. Könnecke “AMOR - the versatile reflectometer at SINQ” Physica B: Physics of Condensed Matter, 27, (2000) p. 140-141 (DOI: 10.1016/S0921-4526(99)01386-1)

[29] M. Senthil Kumar, P. Böni, M. Horisberger “Neutron reflectivity and interface roughness in Ni/Ti and FeCoV/TiNx supermirrors ” Nuclear Instruments and Methods in Physics Research Section A: Accelerators, Spectrometers, Detectors and Associated Equipment, 529(1-3), (2004), Pages 90-93 (DOI: 10.1016/j.nima.2004.04.184)

[30] Pochi Yeh “Optical waves in Layered Media” John Wiley & Sons, New York (1998) (ISBN: 978-0-471-73192-4)

[31] S. J. Blundell and J. A. C. Bland “Polarised neutron reflection as a probe of magnetic films and multilayers” Phys. Rev. B, 46(6), (1992) p.3391-3400 (DOI: 10.1103/PhysRevB.46.3391 )

# Chapter 3

# Understanding the granular structure of the recording layer using PolSANS

---

**Contents**



---

**Abstract**

This chapter describes how PolSANS can be used as an effective tool to study and understand the granular structure and distribution of CoCrPt grains in the recording layer of the thin film media structure. The experiments are carried out on the SANS-1 instrument at PSI, and the physical and magnetic structure of the CoCrPt grains are understood in terms of form and structure factors. The experimental data is supported by two analytical models and a numerically interpreted Transmission electron microscopy (TEM) image model to represent the size and the distribution of the CoCrPt grains in the recording layer. The analysis identifies the magnetic component of the physical CoCrPt grain, along with their average size, shape and inter-granular distance. The analytical model also investigates the effect of the changing grain sizes and grain packing densities on the simulated net scattering intensity.

## 3.1 Background and Introduction

The recording layer of the perpendicular magnetic medium constitutes nanoscale magnetic CoCrPt grains that are used as the magnetic data storage medium [1,2,3]. The size and shape of the magnetic core of the CoCrPt grains in the recording layer have been previously identified using conventional unpolarised SANS experiments. Although conventional unpolarised SANS is used to identify the magnetic component of the physical CoCrPt grain, very little information on the relationship between the physical grain and its magnetic core is determined using conventional SANS [4]. Conventional SANS experiments also come with limitations of large dominant background scattering, making it difficult to interpret the experimental data [5].

The work presented in this chapter uses polarised SANS to overcome these limitations [6]. Polarised SANS experiments provide an insight on the relation between the granular and magnetic scattering of the CoCrPt grains [7]. The large dominant background scattering present in a conventional SANS technique is removed using subtraction techniques in a PolSANS experiment [4,7]. This gives us only experimental scattering data that relates to an interference term between the granular and magnetic scattering from the CoCrPt grains in the perpendicular magnetic mediu as seen in Equation 2.33 [7]. The PolSANS experimental data is then analytically modelled; and the scattering from the physical grain and its magnetic component are distinctly separated. This was not possible in a conventional SANS experiment where information on only the magnetic properties of the CoCrPt grains is obtained [4,6,7].

A core-shell cylindrical analytical model introduced in Section 2.4.4 is used to model the CoCrPt grain with its magnetic core [8,9]. Two different analytical models that use different structure factors are used to simulate the experimental data [10,11]. The analytical models determine the average physical and magnetic grain sizes along with the distance between the CoCrPt grains in the recording layer of perpendicular magnetic medium [9,10,11]. TEM image analysis techniques introduced in Section 2.4.4 are also used to simulate neutron scattering data. TEM images of the CoCrPt grains in the recording layer give a direct physical understanding of the shape, size and spatial distribution of the grains in the recording layer [12,13]. This information is numerically processed and the scattering intensity simulated is compared with the experimental data [14].

## 3.2 Samples and Preparation

Perpendicular media samples were sputtered at Hitachi Global Storage Technologies(GST) San Jose research centre in California, USA. To increase the volume of the sample, the thin film structure is sputtered on both sides of the substrate. The samples have the full structure, comprising the silicon substrate, soft under layers (SUL), seed layers and the recording layer (RL) as seen in Figure 3.1 [15,16,17]. The SUL is expected to have thickness of less than 100 nm comprising of two layers (each ~50 nm) of FeCo, anti-ferromagnetically coupled using a thin (~ 1 nm) ruthenium layer. Seed layers of around 20 nm are grown followed by, CoCrPt+Oxide recording Layer (RL) of about 11nm. The samples are coated with a carbon overcoat that protects the samples. The samples are identified by Hitachi GST as the C9 – 'Oxide only' sample.

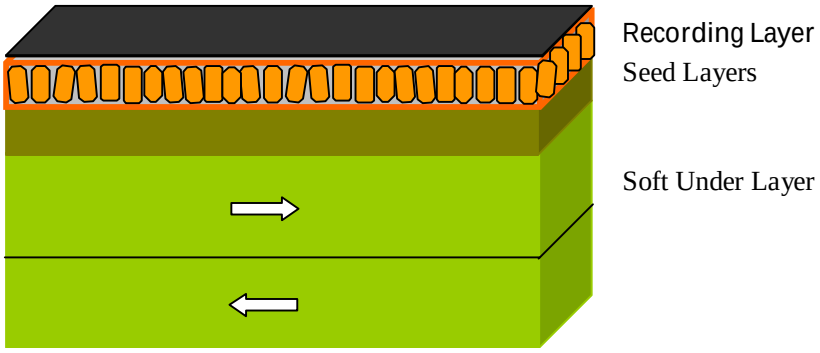


**Figure 3.1** C9 – 'Oxide only' sample structure

A stack of 10 samples of 15 mm length, 12 mm width and 0.8 mm thickness are placed in an aluminium sample holder as seen in Figure 3.2. Boron plates that absorb neutrons are used to shield the sample holder exposing only the sample stack to the neutron beam. Non-magnetic nylon screws are used to fasten the boron plates to further reduce background scattering in the setup [18].

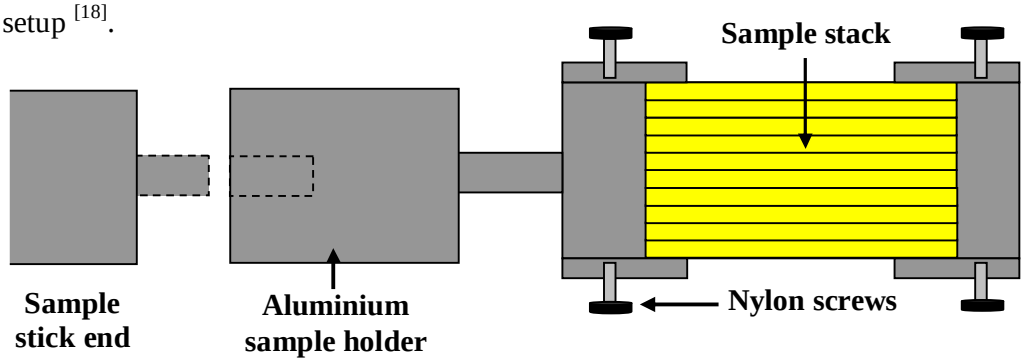


**Figure 3.2** Sample holder design

## 3.3 Experiment

The sample holder in Figure 3.2 is mounted onto a sample stick, which is placed in a cryostat that reaches temperatures as low as 1.5 K [19,20.21]. The PolSANS experiments are, however, carried out at 250 K and this temperature is chosen as it achieves close to room temperature conditions while still maintaining a relatively low rate of helium boil-off [20,21]. Once the temperature is set, the sample stick is placed in the cryostat. The cryostat used in the experiment has been specially designed for SANS experiments [20]. The cryostat is fitted with cryomagnet that reaches magnetic fields of up to 11 T [20]. This magnet is capable of delivering large horizontal magnetic fields required for our experiment [20]. Figure 3.3 shows how the sample stick positions itself in the magnet. Figure 3.3 also illustrates the neutron beam direction and magnetic field direction. The sample table beneath the magnet has the capability to adjust the position of the sample holder and the cryostat along the x-y-z axis while angular rotation is also possible using a goniometer. [20,21] The sample stick position is adjusted remotely using the SANS instrument software. The temperature of the cryostat is fixed at 250 K and the magnetic field is set to 0 T [20,21].

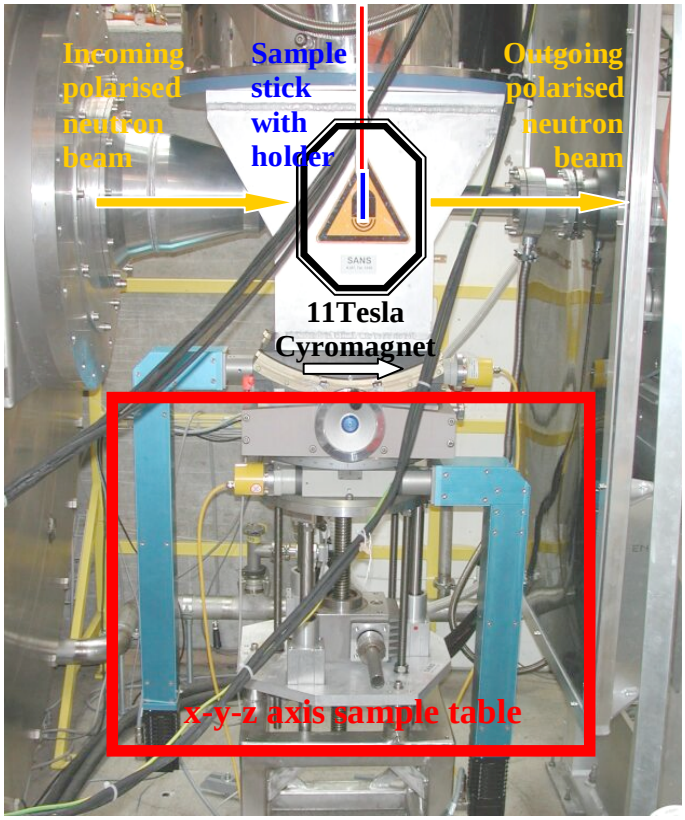


**Figure 3.3** Sample position in the cryostat with an overview of experimental conditions [20]

The CoCrPt grain sizes are expected to be around 5-15 nm for which the required 'q'- range is determined [1,3]. The determined 'q'- range directly relates to the size of the nanoscale structures under investigation. A 'q'- range of 0.04-0.3 ($Å^{-1}$) is set by approximating 'q' in real space to $2\pi/d$, where d is the diameter of the nanoscale grain. The 'q'- range is fixed by changing the collimation and detector distances [20,21]. A magnetic field is applied parallel to the beam and perpendicular to the plane of the sample. A high magnetic field of around 3 T is chosen to ensure that the magnetic moments in the recording layer saturate in the out-of-plane direction [7]. Following this, a 'spin up' and 'spin down' PolSANS experiment is performed and scattering data obtained is reduced using the GRASP software package [22].

## 3.4 Results and Analysis

The difference between the neutron spin scattering states is obtained using the GRASP software package [22]. The increased neutron intensity/count in the detector at the scattering q range is observed using the GRASP software package in Figure 3.4. An annular ring of a contrasting colour to the background is observed using the GRASP software package in Figure 3.4. The annular ring of increased neutron count intensity/count is the scattering q range observed on the detector [22].

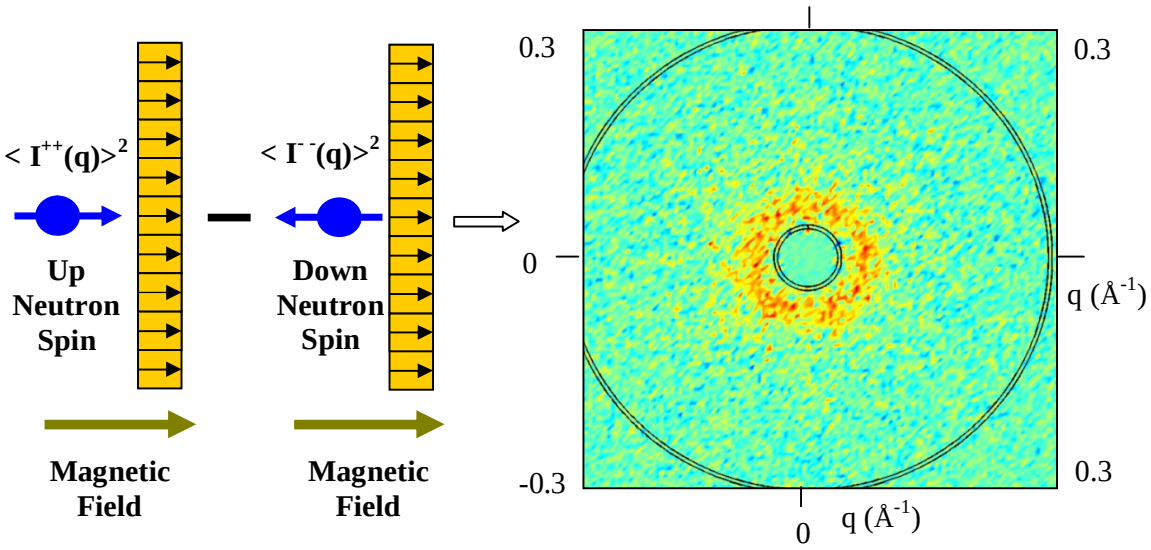


**Figure 3.4** An annular reddish ring that indicates increased scattering $\langle\uparrow|V(\vec{Q})|\uparrow\rangle^2 - \langle\downarrow|V(\vec{Q})|\downarrow\rangle^2$ in contrast to the green background is obtained using the GRASP software package [22]

The scattering q range can be interpreted as the interference of the physical granular ($b_m$) and magnetic ($M_z(\vec{Q})$) scattering from the CoCrPt grains in the recording layer from Equation 2.33 in Chapter 2 [7].

$$\left\langle \uparrow \left| V(\vec{Q}) \right| \uparrow \right\rangle^2 - \left\langle \downarrow \left| V(\vec{Q}) \right| \downarrow \right\rangle^2 = 4\,\mathrm{Re}(b_m * M_z(\vec{Q})) \tag{2.33}$$

This difference in scattering is then radially averaged as a function of q from the centre. This averaging is carried out while omitting contributions from the direct beam using a mask at the beam centre [22]. The radially averaged data is plotted as the difference in intensity varying radially as a function of q in Figure 3.5. The experimental data, extracted from the PolSANS experiments, is compared with analytical models that simulate the experimental data [9,10.11].

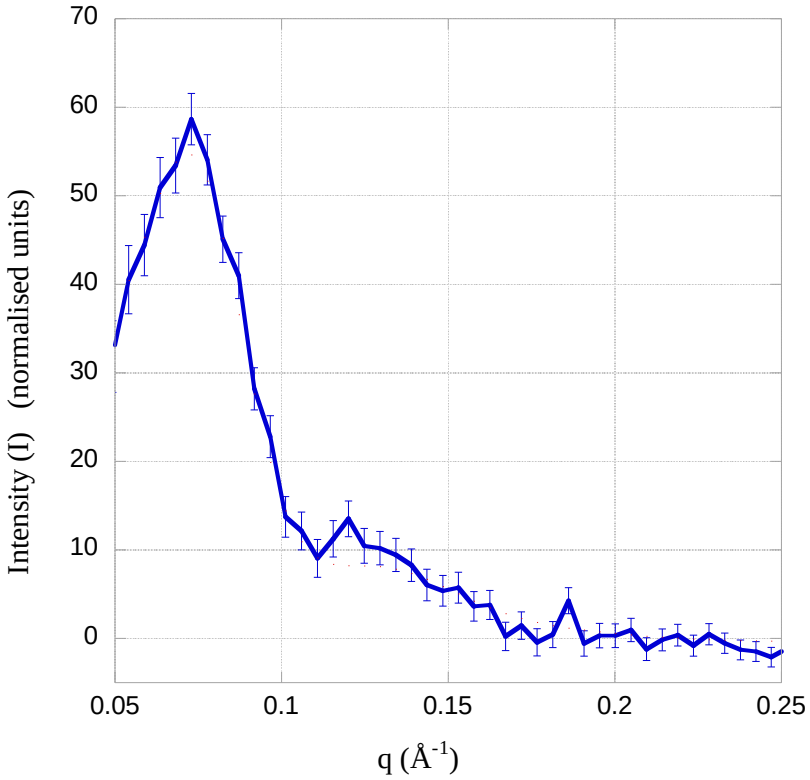


**Figure 3.5** Scattering intensity peak $\left\langle \uparrow \left| V(\vec{Q}) \right| \uparrow \right\rangle^2 - \left\langle \downarrow \left| V(\vec{Q}) \right| \downarrow \right\rangle^2$ extracted from the GRASP software package for the C9-Oxide only sample [22]

In Figure 3.5, a distinct scattering peak is observed in the experimental data between 0.05-0.1 $A^{-1}$, along with a gradual falling shoulder between 0.1-0.125 $A^{-1}$. The scattering peak shown in Figure 3.5, relates to the size, shape and the spatial distribution of the CoCrPt grains in the recording layer [9,10,11]. From the TEM images, we also find that the average grain sizes range

between 6-10 nm in diameter and the average inter-granular distance is of the same order[7,12,13]. When interpreting the reciprocal space peaks in real space with a simple approximation, it is evident that we are looking for features of around 5-12 nm. TEM images of the recording layer show us that these dimensions relate to average grain size and the average distance between the grains [7,12,13]. This initial approximation confirms that the scattering peaks are as a result of the CoCrPt grains in the recording layer. The experimental data is further analysed using analytical models, giving precise numbers on the size and the average distance between grains in the recording layer of the perpendicular magnetic medium [9,10,11].

### 3.4.1. Size, shape and distribution of the magnetic and physical grain supported by analytical modelling

Two different types of analytical models have been used to mathematically simulate the experimental data. Both approaches are used to explain the experimental results obtained in Figure 3.5. The effect of changing fit parameters is also examined and their impact on the net simulated scattering intensity is reported.

**a. Mono approximation model**

This model approximates the CoCrPt grain to a simple core-shell cylinder. A larger physical cylindrical grain with a smaller cylindrical magnetic core is considered in the model. The magnetic cylindrical grain is taken to be at a certain ratio (κ) to the physical grain. κ is defined as the ratio of the magnetic grain diameter to the physical grain diameter and is also sometimes referred to by a percentage value.

The structure factor used in the mono approximation analytical model is based on the packing of simple hard spheres by Ashcroft *et al.* [9,10] The analytical model proposed by Ashcroft *et al.* considers the structure factor distribution to be modelled like that of a liquid metal [10]. The simulated scattering intensity $I_s(k)$ determined for the mono approximation model $S(k\sigma)$ when the form factor for the physical grain and the magnetic grain are $f(k\sigma_n)$ and $f(k\sigma_m)$ is given as,

$$I_S(k) = \left\langle S(k\sigma) * f(k\sigma_n) * f(k\sigma_m) \right\rangle \tag{3.1}$$

The mono approximation model considers a monodispersed system of grains at any point in space, averaged over a Gamma-Schulz function that accounts for the polydispersity in the

system. From this assumption the physical and magnetic grains diameters at any point in space are taken to be similar in the mono approximation uncorrelated model [10]. TEM images of perpendicular magnetic media in Figure 2.11a show that this assumption is incorrect [7,12]. This is major drawback of the mono approximation model as it is not a direct representation of the CoCrPt grain sizes and distribution at any point in space. However the model is still a good approximation of the system and is used in the reported work to fit the experimental data.

By applying Equation 3.2, the intensity $I_s(k)$ averaged across a Gamma-Schulz function is calculated. Figure 3.6 shows the best fit to the experimental data obtained when the mean diameter of physical grain ($\sigma_n$) is 8.0±0.1 nm, the packing density factor (η) is 0.52±0.01 and magnetic grain diameter is 80% of that of the physical grain diameter. The magnetic grain diameter is calculated as 6.4±0.1 nm in diameter. The average distance between the centres of the grains is determined to be 8.8 ± 0.5 nm.

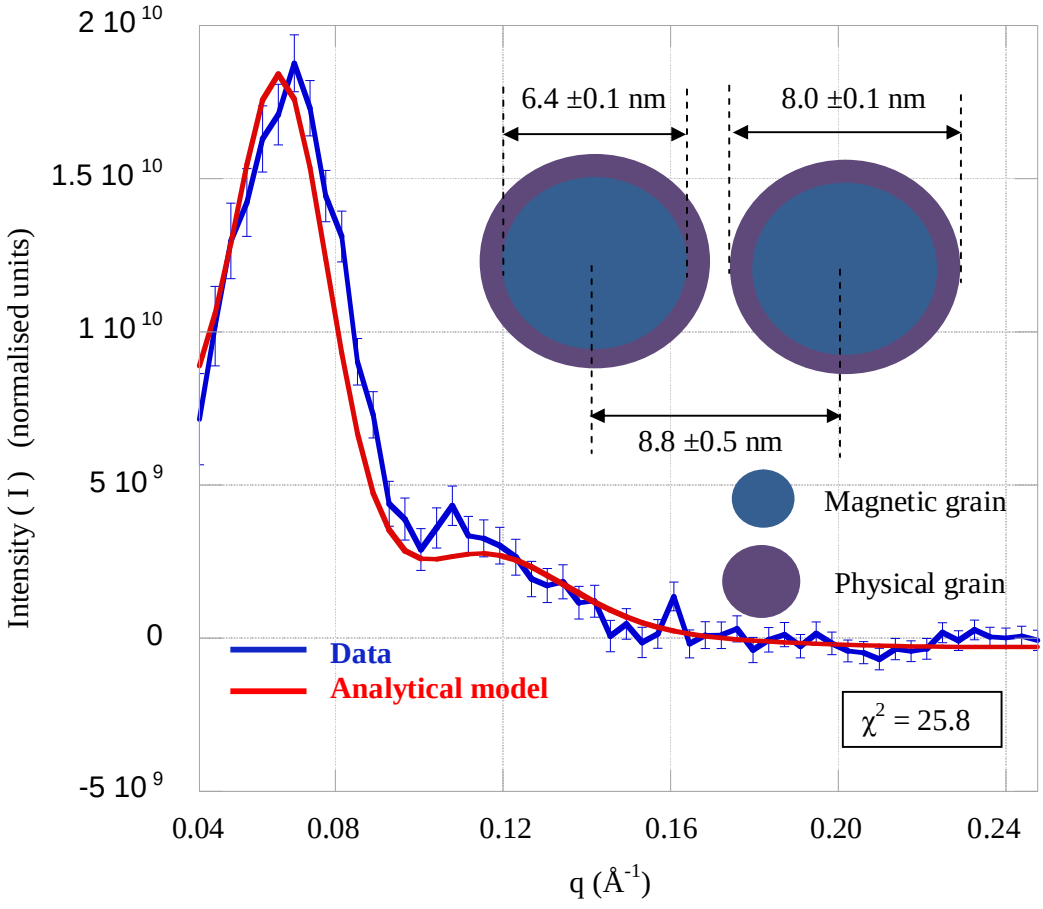


**Figure 3.6** Experimental scattering intensity data $\langle\uparrow|V(\vec{Q})|\uparrow\rangle^2 - \langle\downarrow|V(\vec{Q})|\downarrow\rangle^2$ from the C9-Oxide only sample fitted with the mono approximation analytical model [10]

This average distance between the grains is determined by a simple approximation that relates the structure factor dominated scattering intensity peak in real space to $2\pi/d$, where d is the average distance between the CoCrPt grains in the recording layer.

### b. Pair structure factor model

The pair structure factor model used in our analytical simulation is based on the work by Griffith *et al.* that derives an analytical expression for a scattering function from a polydispersed fluid [9,11]. This basically is an analytical scattering function for a Percus-Yevick type of fluid that is very similar to the Ashcroft *et al.* model used in the mono approximation model [10]. However there exist clear differences in the pair structure factor model and the mono approximation model in its analytical approach, which makes the latter a better representation of the polydispersed CoCrPt grains [10,11].

The pair structure factor model considers the product of terms involving different grain sizes at any point in space. However, the mono approximation model considers a monodispersed system of grains that are then averaged over a Gamma-Schulz function that account for the polydispersity in the system. This is what makes the pair structure factor model a better representation of the polydispersity of grain sizes in the recording layer, when compared to the mono approximation model [10, 11].

The pair structure factor model accounts for this polydispersity at any point in space using a pair structure factor function. This pair structure factor function correlates the distance between a pair of grains at point in space, thereby creating some methodology when accounting for the polydispersity of the CoCrPt grains in the model. The pair structure factor term that accounts for this polydispersity is $H_{i,j}(k\sigma)$ and a detailed theoretical derivation for this term is given in this reference [11].

The form factor of the grain that represents the size and shape of the CoCrPt grain is modelled based on a core-shell cylindrical model. The model considers a magnetic grain that constitutes the core of a larger physical grain whose diameter is determined by a ratio $\kappa$.

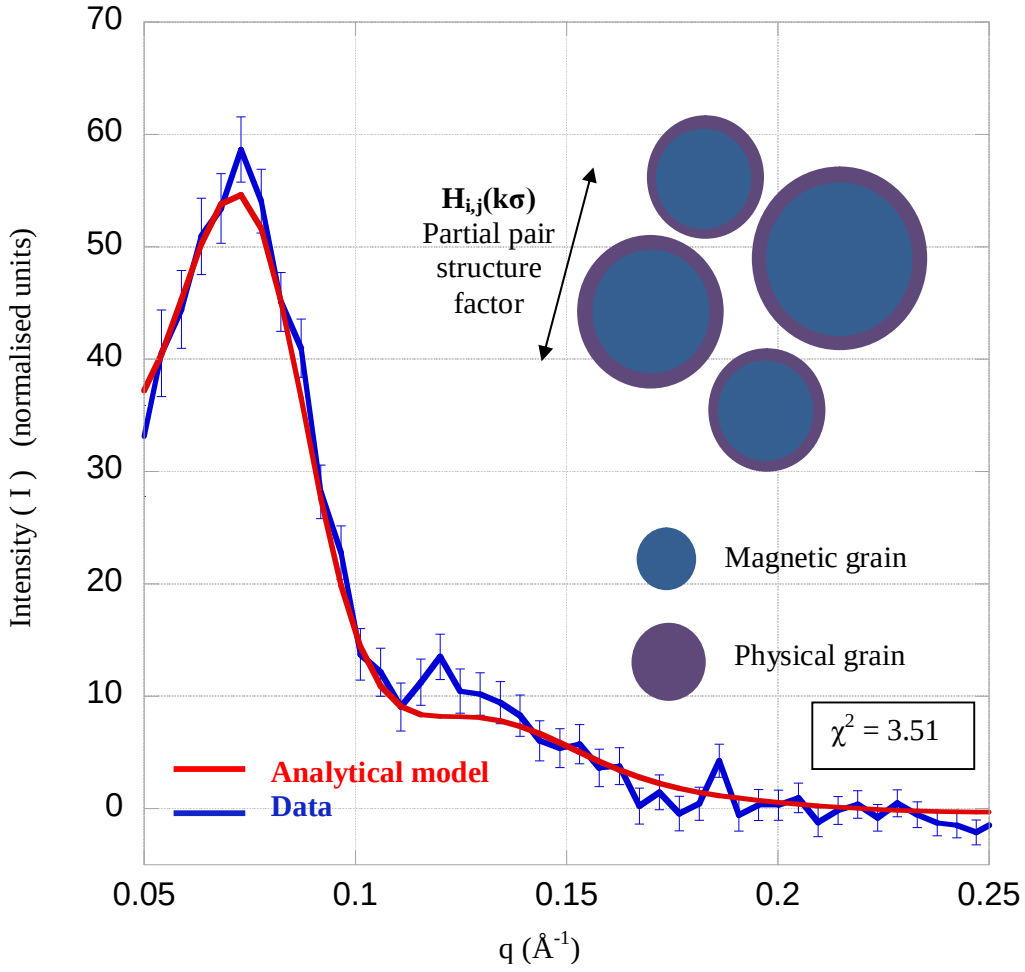


**Figure 3.7** Experimental scattering intensity data $\langle\uparrow|V(\vec{Q})|\uparrow\rangle^2 - \langle\downarrow|V(\vec{Q})|\downarrow\rangle^2$ from the C9-Oxide only fitted with a pair structure factor analytical model [11]

The average grain diameter of the physical grain ($\sigma_n$) is found to be 8.2±0.1 nm from this model. For a form factor ratio of 0.82, the analytical model is found to simulate the experimental data as shown in Figure 3.7. This determines the average diameter of the magnetic grain ($\sigma_m$) to be 6.7±0.1 nm. The packing fraction that provides information on the average inter-granular distance is also determined to be 0.50±0.01, giving us average inter-granular distances of 8.8±0.5 nm as shown in Figure 3.8.

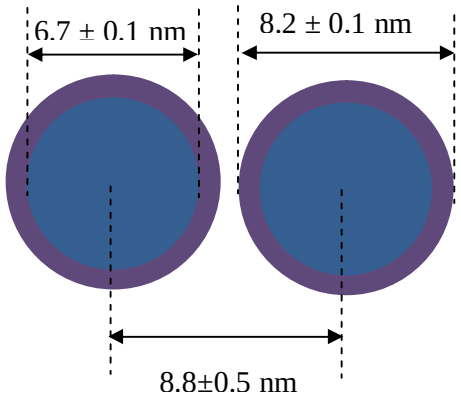


**Figure 3.8** Average distance between grains determined using the pair structure factor model

Using these parameters the analytical models were found to fit the experimental data well, giving $\chi^2$ of 25.8 and 3.51 for the mono approximation and the pair structure factor analytical model. However the influence of these parameters and how they affect the analytical calculations has not been described yet. The next sections illustrate the effect of changing vital parameters in the mono approximation analytical model [9,10]. The grain size, packing density factor ($\eta$) and the ratio between the magnetic and physical grain diameter ($\kappa$) are changed independently and the effect and significance this has on the simulated fit is investigated.

**(1) Influence of size of the grain**

The mean diameter of the physical grain ($\sigma_n$) across the Gamma-Schulz distribution is varied for two different mean diameters (7.8±0.1 nm and 8.2±0.1 nm) and the analytical model plotted is compared to the analytical model plotted for a mean physical grain diameter of 8.0±0.1 nm. Please note that all other parameters that include the ratio between the magnetic and physical grain diameter ($\kappa$) and the packing density factor ($\eta$) remain unchanged. Although this clearly defies the interdependence of the fit parameters, this assumption is made to introduce some methodology in understanding the influence of individual parameters on the simulated fit. The mean diameter of the magnetic grain ($\sigma_m$) for the 3 different models when $\kappa$ is maintained at 0.8 is calculated to be 6.3±0.1 nm, 6.4±0.1 nm and 6.6±0.1 nm. The scattering intensity modelled is given in Figure 3.9.

The yellow line in Figure 3.9 denotes the scattering intensity for a reduced physical grain (diameter $\sigma_n$ = 7.8±0.1 nm) and a magnetic grain (diameter $\sigma_m$ = 6.2±0.1 nm). It is evident from Figure 3.9 that the yellow intensity peak shifts slightly towards higher 'q' when compared to the red and green intensity peaks, and this shift is also observed in the peak shoulder. This is as a result of the decrease in grain diameter that, in reciprocal space, is seen as a shift towards the high 'q' region. One also sees a decrease in intensity as a result of smaller size, which directly relates to the drop in the volume of the scatterer. One also observes that when there is an increase in grain diameter, the analytical model plot (green line) shifts towards the low q region in the reciprocal space as expected.

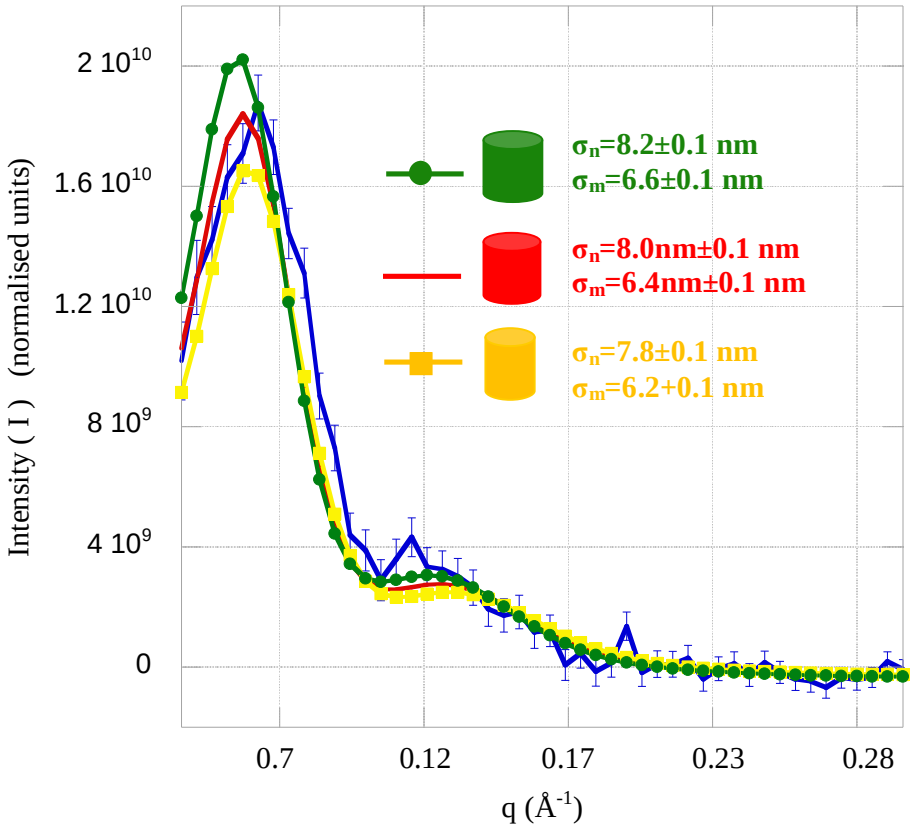


**Figure 3.9** Experimental scattering intensity data $\langle\uparrow|V(\vec{Q})|\uparrow\rangle^2 - \langle\downarrow|V(\vec{Q})|\downarrow\rangle^2$ with simulated analytical models highlighting the influence grain size on the scattering intensity

### (2) Influence of ratio between the magnetic and physical grain diameter (κ)

Another important factor that influences scattering intensity is the ratio between the magnetic grain diameter and the physical grain diameter that is denoted by κ. Here again all other parameters in the model remain unchanged and the effect of only changing the value of κ is investigated. In our simulated fit the value of κ used is 0.8. This denotes that the magnetic grain diameter is 80% of that of the physical grain diameter. The value of κ is changed to 1.0 and 0.6, to understand the significance of this ratio. The blue line in Figure 3.10 denotes the analytically determined scattering intensity for the simulated fit when κ is initially at 0.8 and the green and yellow represent the simulated scattering when the magnetic grain is taken to be 60% and 100% of the physical grain that is denoted by κ values of 0.6 and 1.0. The mono approximation model is used to analytically model the scattering intensity.

It is quite evident from the figure that there is marked difference in the scattering intensities when κ is changed. By increasing κ to 1.0 in the model, the magnetic grain diameter is the same as that of the physical grain diameter. The red line that denotes the scattering intensity simulated for κ to 1.0 in the Figure 3.10 is seen to be generally broader with a shoulder closer to its initial scattering peak. The scattering intensity simulated is also clearly positive. This is because at this value of κ, two similar form factor analytical functions for the physical and magnetic grain are multiplied. This is then equivalent to taking the square of the form factor that relates to all positive terms in the simulated net scattering intensity.

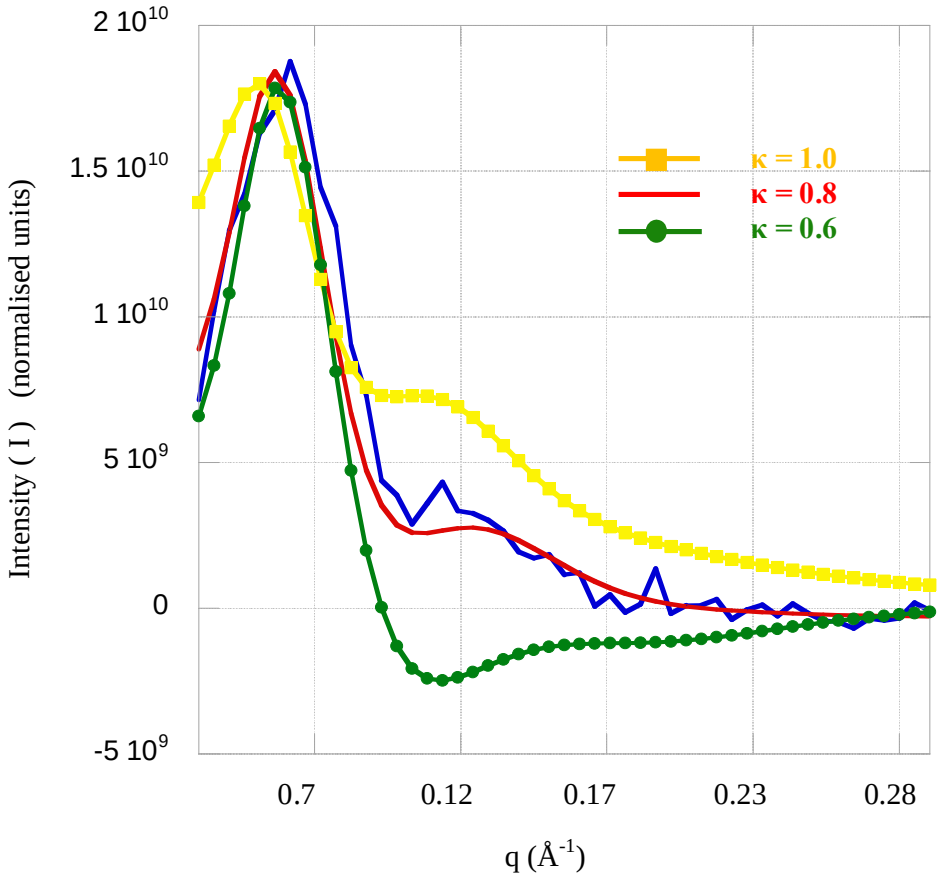


**Figure 3.10** Experimental scattering intensity data $\langle\uparrow|V(\vec{Q})|\uparrow\rangle^2 - \langle\downarrow|V(\vec{Q})|\downarrow\rangle^2$ with simulated analytical models highlighting the influence of ratio between the magnetic and physical diameter (κ) on the scattering intensity

However when κ changes to 0.8 and 0.6, the form factor plots for the physical and magnetic grains are not similar and a shift in the individual form factor oscillations results in the decrease of net simulated scattering intensity. This decrease in net scattering is observed in the red and green plots when the magnetic grain diameters are taken to be 80% and 60% of

that of the physical grain diameter. This effect is more prominent when $\kappa = 0.6$ (green line), with a dominant negative scattering arising from a clear phase shift between increasingly different form factors for the physical and magnetic grains.

From the simulated scattering intensity plots shown in Figure 3.10, it is evident that changing the value of $\kappa$ has a significant effect on the simulated net scattering intensity that makes this a very important parameter in the analytical model, that significantly influences the net scattering determined using the mono approximation model.

### (3) Influence of packing density factor ($\eta$)

Finally, the influence of changing the packing density factor ($\eta$) is investigated. Before investigating the effect of changing the packing density factor ($\eta$), it is important to note that the mono approximation model is based on Percus-Yevick type liquid metal model that represents the packing of simple hard spheres. This in reality is very different from cylindrical CoCrPt grains distributed in the recording layer of the perpendicular magnetic medium [1,2,3,7]. Although this analytical model approximately simulates the experimental scattering data, investigating the effects of packing density factor ($\eta$) is clearly pushing the limits of this simple approximated model [9,10].

However in any system, changing the packing density factor ($\eta$) affects both the number of scatterers in the system and the average distance between the scatterers in the system. Increasing the packing density factor increases the number of scatterers in the system creating a densely packed system where the average distance between the scatterers reduces [10]. This increase and decrease in the number of scatters in the system results in an increase or decrease in the scattering intensity simulated [10]. Figure 3.11 below shows the intensity for three packing density factors ($0.50\pm0.01$, $0.52\pm0.01$ and $0.54\pm0.01$) denoted by colours yellow, red and green. One clearly sees an increase in simulated scattering intensity when the packing density factor ($\eta$) is increased from $0.50\pm0.01$ to $0.54\pm0.01$.

Although it is difficult to relate the packing of cylinders to a hard sphere packing model, on a more basic level it can be said that increasing packing density factor ($\eta$) increases the scatters in the system thereby increasing the net scattering intensity. No attempt has been made to determine the change in average distance between the grains by changing packing density factors as this is clearly within the limitation of this approximated model [10].

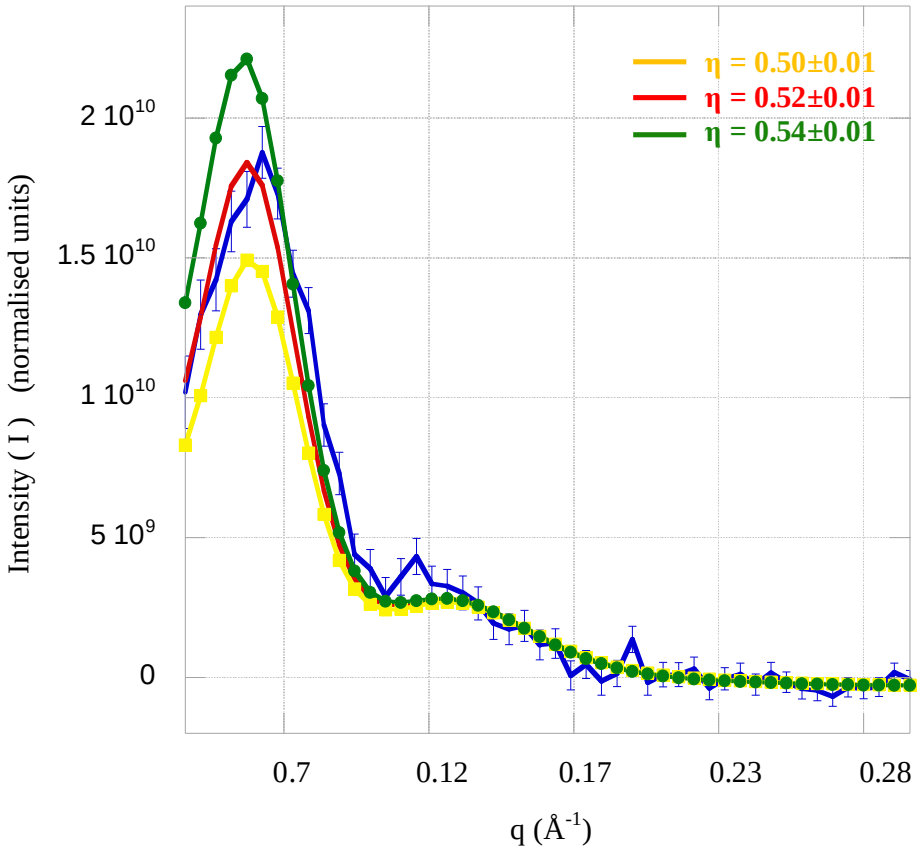


**Figure 3.11** Experimental scattering intensity data $\langle\uparrow|V(\vec{Q})|\uparrow\rangle^2 - \langle\downarrow|V(\vec{Q})|\downarrow\rangle^2$ with analytical models highlighting the influence of packing density factor (η) on simulated scattering

### 3.4.2. Size, shape and distribution of the magnetic and physical grain supported by a numerical TEM model

The numerical TEM models use real TEM images of the recording layer as seen in Figure 3.12. [7,12,13] The images provide a physical portrayal of the distribution of the CoCrPt grains in the recording layer that gives information on the size, shape and importantly the spatial distribution/correlation of the CoCrPt grains in the recording layer.

This is real physical data that supports the analytical form and structure factor models. Obtaining a fast fourier transform (FFT) of the image gives the spatial information in the frequency domain, which directly relates to the neutron scattering from a similar structure [14]. The process, by which the spatial information in the frequency domain is extracted, is described.

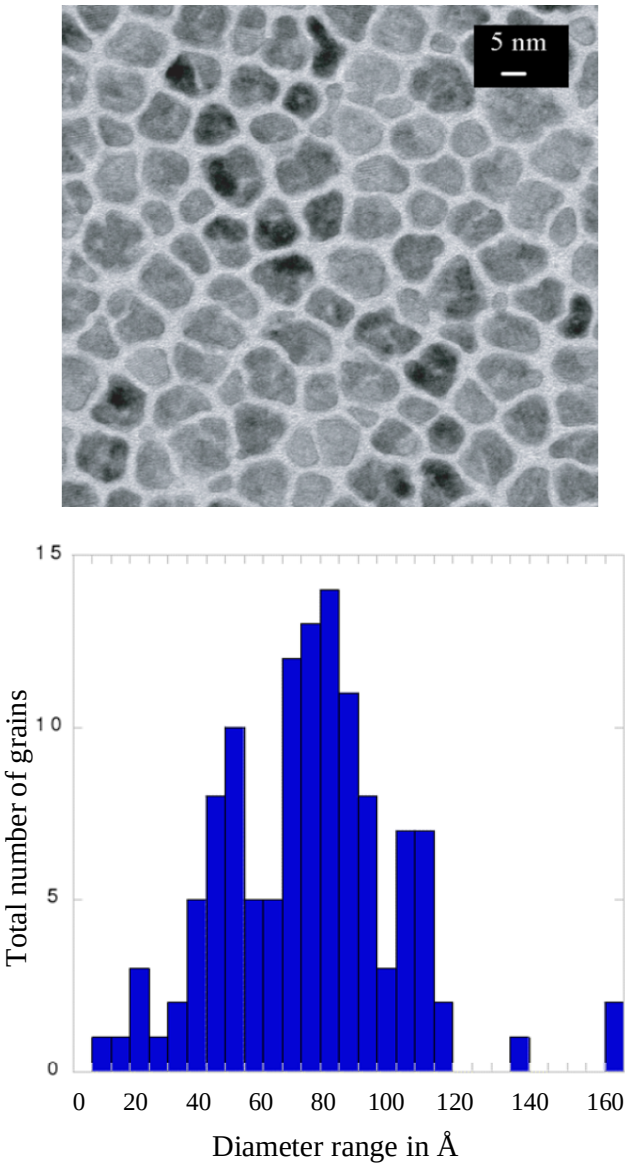


**Figure 3.12** TEM image and the diameter distribution of the grains in the sample in Å[7,14]

The TEM images are processed to clearly distinguish the granular structure from the oxide boundary in the system [14]. This is done by using image analysis software like CANVAS. The granular structure in the TEM image is highlighted, by assigning a colour different to the background oxide colour. This image is then imported by MATLAB to give a digitised image of 1's and 0's representing the granular structure with its boundaries. The chosen granular structure colour (black) is denoted by a number ('1') when imported in MATLAB, in contrast to its background (white) which is denoted by zero. The size of individual grains in the TEM image are reduced to 80% and 60% of their original size, giving TEM images that have smaller grain sizes when compared to its original size. This is done to distinguish the magnetic scattering and the granular scattering in the numerical model [14].

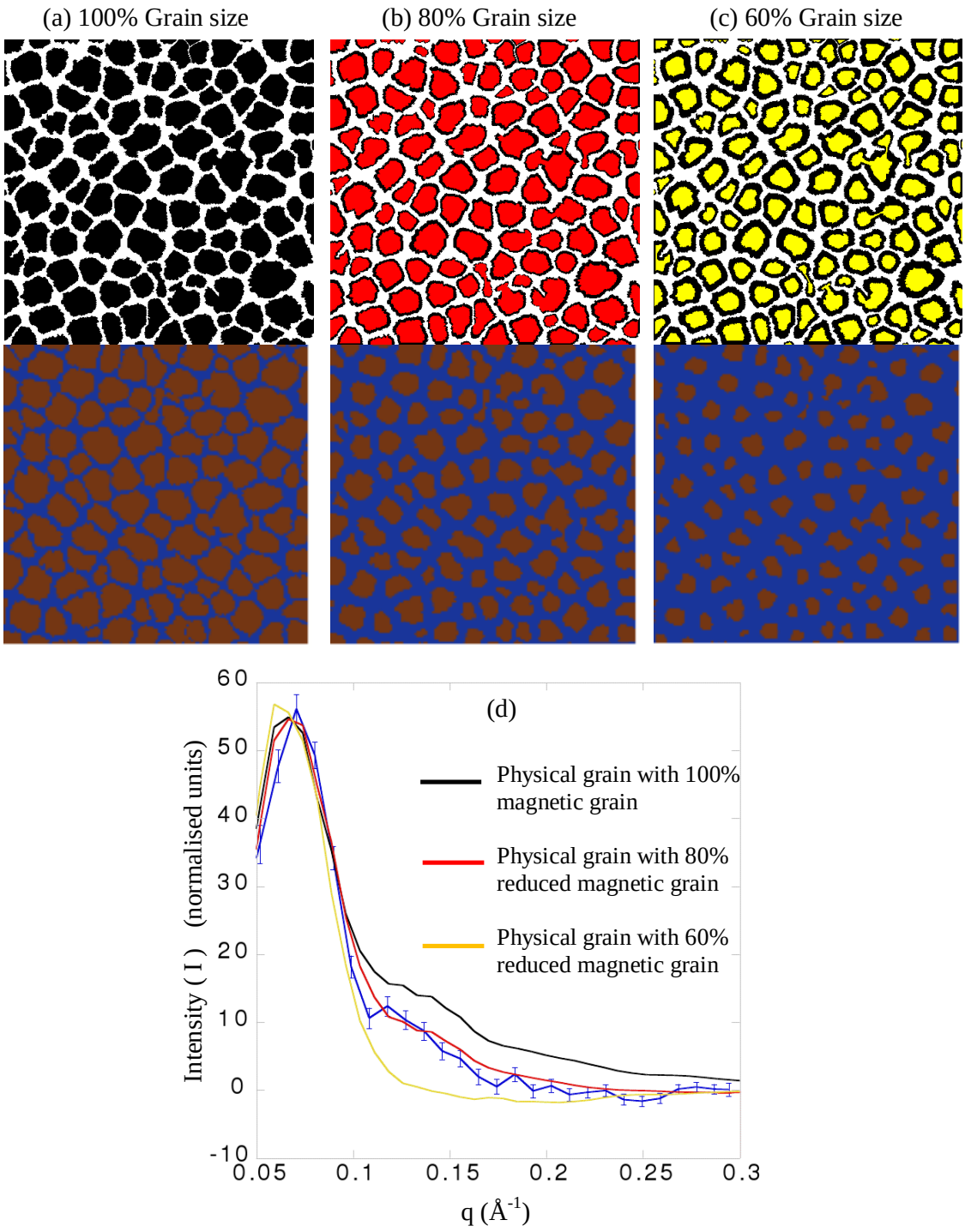


**Figure 3.13** (a). (b). (c). Processed TEM images with their graphical MATLAB interpretation for physical grains with 100%, 80% and 60% reduced magnetic grains. (d). Experimental scattering intensity data $\langle\uparrow|V(\vec{Q})|\uparrow\rangle^2 - \langle\downarrow|V(\vec{Q})|\downarrow\rangle^2$ along with simulated analytical models for magnetic grain sizes that are 100%, 80% and 60% of that of the physical grain [7,14].

A product of the fast fourier transform (FFT) of the original TEM image with 100% of its initial grain size relating to the physical grain is multiplied with the different variants of the reduced grain sizes. Three different models where the magnetic grain is 100% of the original physical grain, 80% of the physical grain and 60% of the physical grain are determined and a radial average of the FFT is interpreted in terms of the scattering intensity as a function q, while accounting for scaling factors [14].

It is evident from Figure 3.13 that when the radius of the CoCrPt grains are reduced to 80% of their initial size, the simulated TEM model scattering intensity is found to reasonably fit the experimental data. From this the ratio between the physical grain and magnetic grain in the CoCrPt granular structure is 0.8. This claim is supported by previous conclusions that analytically determine the ratio between the magnetic and physical grain using form and structure factor models.

## 3.5 Conclusion

To conclude, two different analytical models along with the TEM numerical model have been used to successfully simulate the experimental results. Both models were found to simulate the experimental results well. However by comparing the $\chi^2$ determined using the analytically models, it was found that the pair structure factor model provided a better fit to the data than the mono approximation model. A summary of the results are given in Table 2.1.

**Table 3.1** Table summarising the results from the pair structure factor model, the mono approximation model and the numerical TEM model

| *MODELS* | *Grain shape* | *Magnetic grain diameter (nm)* | *Physical grain diameter (nm)* | *Average intergranular distance (nm)* | $\kappa$ |
|---|---|---|---|---|---|
| PAIR STRUCTURE FACTOR MODEL | Cylinder | 6.7±0.1 | 8.2±0.1 | 8.8±0.5 | 0.82 |
| MONO APPROXIMATION MODEL | Cylinder | 6.4±0.1 | 8.0±0.1 | 8.8 ±0.5 | 0.80 |
| NUMERICAL TEM MODEL | - | 6.7±2.0 | 8.2±2.0 | 8.8 ±0.5 | 0.80 |

From Table 2.1, one can conclusively say that all three models give similar results. From the analytical models, it is evident that the shape of the CoCrPt grain is closest to that of the cylinder [7,23]. All three models predict that the magnetic component of the physical CoCrPt grain is smaller than of the physical CoCrPt grain [7,24]. It is also found that the magnetic component of the physical grain is at a certain ratio to the physical CoCrPt grain structure, and this ratio is determined using all three models. The average distance between the grains has also been determined, with similar results for all three models [7,25].

Hence using PolSANS, it has been possible to determine the average shape, size and inter-granular distance between the CoCrPt grains [6,7]. This is only technique that structurally and magnetically characterises the CoCrPt grains in the recording layer, giving detailed information on the properties of the CoCrPt grains [6,7]. This is also the first time the size and ratio of the magnetic component of the CoCrPt grain is determined [7]. This makes PolSANS a unique tool to characterise nanoscale magnetic structures, when comparing other bulk and surface characterisation techniques [6].

## 3.6 References


[1] S. N. Piramanayagam “Perpendicular recording media for hard disk drives” J. Appl. Phys. 102, 011301 (2007) (DOI: 10.1063/1.2750414)

[2] S.N. Piramanayagam, K. Srinivasan “Recording media research for future hard disk drives” Journal of Magnetism and Magnetic Materials, 321(6), (2009), p.485-494 (DOI: 10.1016/j.jmmm.2008.05.007)

[3] H.J. Richter “Density limits imposed by the microstructure of magnetic recording media” Journal of Magnetism and Magnetic Materials, 321(6), (2009), p.467-476 (DOI: 978-0-7803-4709-0)

[4] M. Wismayer, S. Lee, T. Thomson, F. Ogrin, C. Dewhurst, S. Weekes, R. Cubitt “Using small-angle neutron scattering to probe the local magnetic structure of perpendicular magnetic recording media” Journal of Applied Physics, 99(8), (2006) (DOI: 08e707 10.1063/1.2165798)

[5] Kenneth C. Littrell “A comparison of different methods for improving flux and resolution on SANS instruments” Nuclear Instruments and Methods in Physics Research Section A: Accelerators, Spectrometers, Detectors and Associated Equipment, 529(1–3), (2004) p.22-27 (DOI: 978-0-7803-4709-0)

[6] Albrecht Wiedenmann. “Polarized SANS for probing magnetic nanostructures” Physica B: Condensed Matter, 356(1–4), (2005) p. 246-253 (DOI : 10.1016/j.physb.2004.10.085)

[7] S. J. Lister, M. P. Wismayer, V. Venkataramana, M. A. de Vries, S. J. Ray, S. L. Lee, T. Thomson, J. Kohlbrecher, H. Do, Y. Ikeda, K. Takano, and C. Dewhurst “Small-angle polarized neutron studies of perpendicular magnetic recording media” Journal of Applied Physics, 106(6),(2009) p. 063908 - 063908-4 (DOI: 10.1063/1.3213381)

[8] M.R. Fitzsimmons, S.D. Bader, J.A. Borchers, G.P. Felcher, J.K. Furdyna, A. Hoffmann, J.B. Kortright, Ivan K. Schuller, T.C. Schulthess, S.K. Sinha, M.F. Toney, D. Weller, S. Wolf “Neutron scattering studies of nanomagnetism and artificially structured materials” Journal of Magnetism and Magnetic Materials, 271(1), (2004) p.103-146 (DOI:

10.1016/j.jmmm.2003.09.046)

[9] A. Guinier, G. Fournet “Small-Angle Scattering of X-Rays” John Wiley and Sons, New York (1955) (DOI: 10.1002/pol.1956.120199326)

[10] N.W. Ashcroft, J. Lekner “Structure and Resistivity of Liquid Metals” Phys. Rev. (145), (1966) p. 83–90 (DOI: 10.1103/PhysRev.145.83)

[11] W.L. Griffith, R. Triolo, A.L. Compere “Analytical scattering function of a polydisperse Percus-Yevick fluid with Schulz- ( Gamma -) distributed diameter” Phys Rev A, 35(5), (1987) p. 2200–2206 (DOI: 10.1103/PhysRevA.33.2197)

[12] R. Araki, Y. Takahashi, I. Takekuma, S. Narishige “High-Resolution TEM Analysis of Perpendicular CoCrPt-SiO2 Media” IEEE Transactions on magnetics, 44 (11), (2008) p. 3496 – 3498 (DOI: 10.1109/TMAG.2008.2002415)

[13] Wenli Pei, J. Yuan, T. Wang, Y. Fu, T. Washiya, T. Hasagawa, H. Saito, S. Ishio, N. Honda “Study on magnetization reversal of perpendicular recording media by in-field MFM observation” Acta Materialia, 55(9), (2007) p.2959-2964 (DOI: 10.1016/j.actamat.2006.12.034)

[14] S.J. Lister, J. Kohlbrecher, V. Venkataramana, T. Thomson, K. Takano, and S.L. Lee, "Analysing SANS data to determine magnetisation reversal processes in composite perpendicular magnetic recording media using TEM images" International Journal of Materials Research 102(9) (2011) p.1142-1146. (DOI: 10.3139/146.110562)

[15] Dmitri Litvinov, Mark H Kryder, Sakhrat Khizroev “Recording physics of perpendicular media: soft underlayers” Journal of Magnetism and Magnetic Materials, 232(1–2), (2001) p.84-90 (DOI: 10.1016/S0304-8853(01)00216-5)

[16] Dmitri Litvinov, Mark H Kryder, Sakhrat Khizroev “Recording physics of perpendicular media: hard layers” Journal of Magnetism and Magnetic Materials, 241(2–3), (2002) p.453-465 (DOI: 10.1016/S0304-8853(02)00023-9)

[17] Chun-Tao Xiao, Yuki Inaba, Takehito Shimatsu, Hiroaki Muraoka “Microstructure,

magnetic properties and their seed layer thickness dependences of granular CoPtCr–SiO2 perpendicular recording media" Solid State Communications, 144 (1–2), (2007), p.58-60 (DOI: 10.1016/j.ssc.2007.07.014)

[18] A.W. Dalton "Effects of elastic scattering on the low energy neutron detection efficiency of a lithium glass and boron-loaded liquid scintillator" Nuclear Instruments and Methods, 92(2), (1971) p.221-227 (DOI: 10.1016/0029-554X(71)90196-0)

[19] A. Anghel *et al.* " The PSI ultra-cold neutron sourceNuclear Instruments and Methods in Physics Research Section A: Accelerators, Spectrometers, Detectors and Associated Equipment, 611(2–3), (2009) p.272-275 (DOI: 10.1016/j.nima.2009.07.077)

[20] J. Kohlbrecher, W. Wagner "The new SANS instrument at the Swiss spallation source SINQ"**,** J. Appl. Cryst. 33, (2000) p.804-806 (DOI: 10.1107/S0021889800099775)

[21] V.K. Aswal *et al.* "Characterisation of the polarised neutron beam at the small angle scattering instrument SANS-I with a polarised proton target" Nucl. Instr. and Meth. A 586(1), (2008), p.86-89 (DOI: 10.1016/j.nima.2007.11.062)

[22] Charles Dewhurst "GRAS$_{ans}$P: Graphical Reduction and Analysis SANS Manual" Institute Laue Langevin, France. Last modified December 15, 2011. http://www.ill.eu/?id=6300

[23] G. Choe, S.J. Chung, R.M. Walser "Correlation between grain morphologies and magnetic properties of CoCrPtCr thin films" Thin Solid Films, 259(2), (1995) p.231-236 (DOI: 10.1016/0040-6090(94)06438-5)

[24] Yingfan Xu, Jian Ping Wang, Z.S Shan, Hua Jiang, Ying Su, Chong Tow Chong, Li Lu "Structural and magnetic properties of HCP-CoCrPt–SiO2 granular media" Journal of Magnetism and Magnetic Materials, 225(3), (2001) p.359-372 (DOI: 10.1016/S0304-8853(01)00063-4)

[25] M.E. McHenry, D.E. Laughlin " Nano-scale materials development for future magnetic applications" Acta Materialia, 48(1) , (2000) p. 223-238 (DOI : 10.1016/S1359-6454(99)00296-7)

# Chapter 4

# Understanding the effect of varying recording layer thickness on granular structure using PolSANS

---

**Contents**



---

**Abstract** This chapter investigates the effect of size, shape and the distribution of the CoCrPt grains when changing the thickness of the recording layer. PolSANS is used here as an effective tool to characterise the CoCrPt grains in the magnetic recording layer of samples with different recording layer thicknesses. The experiments were carried out on the SANS-1 instrument at PSI where four different samples with varying recording layer thicknesses were characterised. An analytical model is used to explain the difference in characteristics of the CoCrPt grain when the recording layer thickness is changed. A good understanding of the influence of varying recording layer thickness between samples and its effect on the CoCrPt grain structure is reported. The change in physical and magnetic grain diameter, average distance between the grains and the packing density used is then tabulated for the different recording layer thicknesses.

## 4.1 Background and Introduction

The recording layer of the perpendicular magnetic medium constitutes nanoscale CoCrPt grains, whose properties depend on the seed layers beneath the recording layer in the perpendicular magnetic medium [1,2,3]. Seed layers influence the size, shape and distribution of the CoCrPt grains in the recording layer and a lot of research has been carried out on the use of different seed layers, to control the properties of the CoCrPt grains [2,3,4].

In this chapter, the influence of varying the thickness of the recording layer and its effect on the properties of the CoCrPt grains is investigated using PolSANS [5,6]. The goals of the PolSANS experiments are to investigate the size, shape and the spatial distribution of the CoCrPt grains when thickness of the recording layer varies [5,6]. The experiments compare the scattering intensities for samples of different recording layer thicknesses determining the volume of the scatterer in each of the samples. The influence of layer thickness on the size of the magnetic component with respect to the physical grain size is also investigated using the mono approximation model introduced in Section 3.4.1 of Chapter 3 [7,8].

PolSANS experiments as described in Section 3.3 of Chapter 3 are carried out on 4 different samples with different recording layer thicknesses [9,10]. The net scattering intensities determined (from the difference in spin up and spin down scattering) are compared to investigate any differences between the 4 different samples. The simulated mono approximation model scattering intensities are compared with the experimental results [7,8]. The change in average magnetic and physical grain size and the packing density factor for different recording layer thicknesses are reported in this chapter.

## 4.2 Samples and Preparation

Perpendicular media samples were sputtered at Hitachi Global Storage Technologies (GST) San Jose research centre at California, USA. Three different samples with varying recording layer thicknesses were sputtered on both sides of the substrate to increase the volume of sample content on a substrate. The samples have the full structure, comprising the silicon substrate, soft under layers (SUL), seed layers and the recording layer (RL) [11,12,13].

**(a) C4 – 'Oxide only-Thin' Sample**

The SUL has a thickness of less than 100 nm comprising two layers (each ~50 nm) of FeCo, anti-ferromagnetically coupled using a thin (~1 nm) ruthenium layer. A seed layer of 20 nm is grown followed by a CoCrPt+Oxide RL of 6 nm. The samples are also coated with a carbon overcoat that protect the samples. This sample is identified by the Hitachi GST as the C4 – 'Oxide only-Thin' sample.

**(b) C9 – 'Oxide only' Sample**

The sample has SUL and seed layers of similar dimension and composition, followed by a CoCrPt+Oxide RL of about 11 nm. This sample is similar to one described in Chapter 3. The sample is also coated with a carbon overcoat which protect the sample. This sample is identified by Hitachi GST as the C9 – 'Oxide only' sample.

**(c) C13 – 'Oxide only-Thick' Sample**

The sample has SUL and seed layers of similar dimension and composition, followed by a CoCrPt+Oxide RL of about 16 nm thick being thicker than C9, which is around 11 nm. The samples are also coated with a carbon overcoat that protect the samples. This sample is identified by Hitachi GST as the C13 – 'Oxide only' sample.

**(d) C15 - 'No mag' sample**

These samples have just the SUL along with the seed layer on them. The sample SUL and seed layer dimensions are expected to match the samples C13, C9 and C4. The only difference between the C15 - 'No mag' sample and the other samples is the absence of the RL.

**Table 4.1** Different recording layer (RL) thicknesses tabulated for different samples

| *Sample* | *C4 – 'Oxide only-Thin'* | *C9 – 'Oxide only'* | *C13 – 'Oxide only-Thick'* | *C15 - 'No Mag'* |
|---|---|---|---|---|
| Thickness (nm) | 6 | 11 | 16 | 0 |

A stack of ten samples, were placed in an aluminium sample holder whose design is shown in Figure 3.2 of Chapter 3. The samples are then clamped together using nonmagnetic nylon screws and boron plates as described in Section 3.2 of Chapter 3.

## 4.3 Experiment

The cryostat temperature is brought to 250 K and magnetic field is set at 0 T. The sample holder is then mounted onto a sample stick, and placed in the cryostat. The detector and collimator are adjusted to fix the 'q' range [10]. The in-plane magnetic field is then raised to 3 T and a PolSANS experiment is performed as described in Section 3.3 of Chapter 3. The experimental geometry is seen in Figure 4.1 [10].

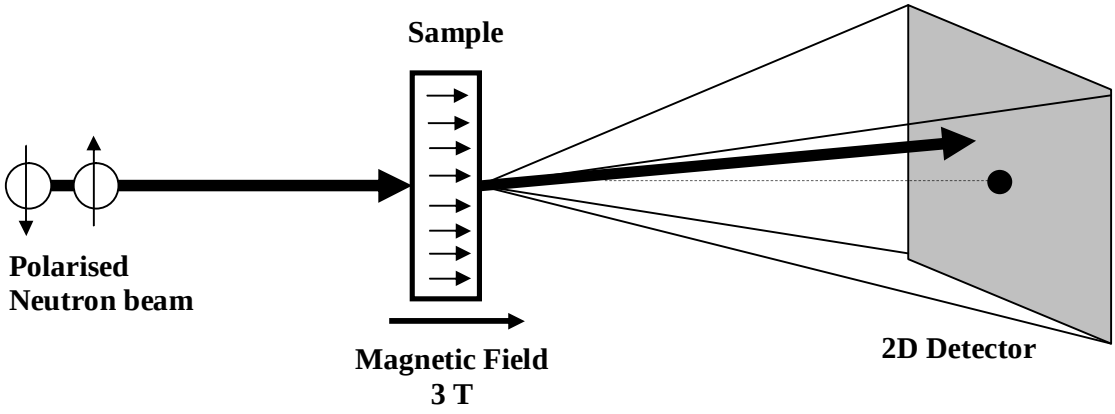


**Figure 4.1** Scattering diagram illustrating the geometry in a PolSANS experiment

The experiment described in Section 3.3 of Chapter 3, is repeated for samples C4 – 'Oxide only-Thin', C9 – 'Oxide only', C13 – 'Oxide only-Thick' and C15 – 'No Mag'. The 'spin up' and 'spin down' scattering is detected on the detector and the difference in scattering intensity between the spin up and down states is determined as explained in Section 3.4 of Chapter 3 [14]. This difference in intensity is interpreted as an interference term of the magnetic and structural scattering from the CoCrPt grains in the different samples. The interference term is obtained from Equation 2.33 in Chapter 2 [14].

$$\left\langle \uparrow \left| V(\vec{Q}) \right| \uparrow \right\rangle^2 - \left\langle \downarrow \left| V(\vec{Q}) \right| \downarrow \right\rangle^2 = 4\,\mathrm{Re}(b_m * M_z(\vec{Q})) \qquad (2.33)$$

Where '$b_m$' is the nuclear scattering and '$M_z(\vec{Q})$' is the magnetic scattering as a result of CoCrPt grains aligned perpendicular to the plane of the thin film structure. The difference in intensity between the up $\langle\uparrow|V(\vec{Q})|\uparrow\rangle^2$ and down spin states $\langle\downarrow|V(\vec{Q})|\downarrow\rangle^2$ is plotted as a function of q and the scattering intensities for all four samples are compared in Figure 4.2.

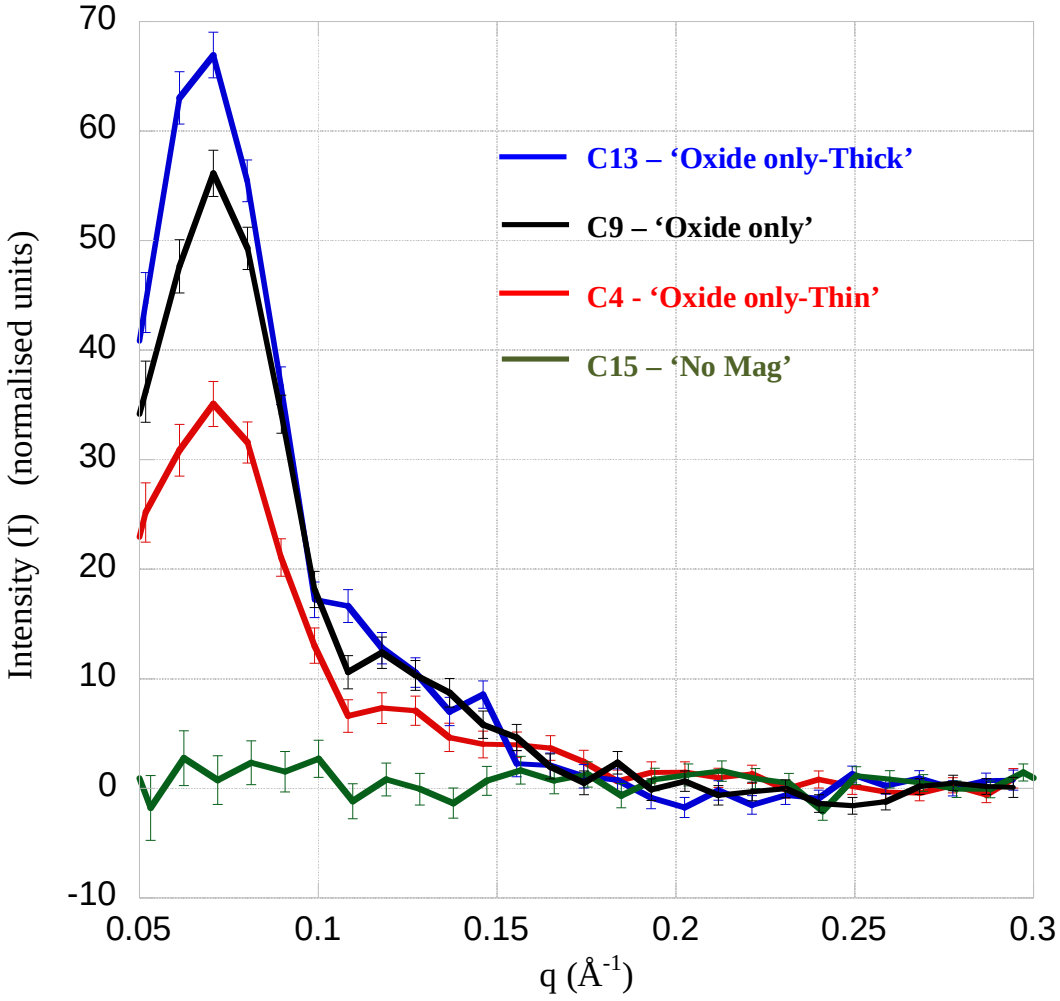


**Figure 4.2** Experimental scattering intensity data $\langle\uparrow|V(\vec{Q})|\uparrow\rangle^2 - \langle\downarrow|V(\vec{Q})|\downarrow\rangle^2$ for samples C15, C4, C9 and C13

## 4.4 Results and Analysis

The scattering intensity is measured across the plane of the detector from its centre, and the measured scattering intensity is plotted as a function of 'q'. It is evident from Figure 4.2 that sample C15 without its recording layer does not show a scattering intensity peak between 0.05-0.1 $A^{-1}$ in the reciprocal space. This is a remarkable result as it highlights the sensitivity of experimental technique in extracting only the interference of the magnetic and scattering from the CoCrPt grains in the recording layer while subtracting all other background scattering present in the system [15].

On comparing the intensities of samples C13, C9 and C4, it is evident that the samples with thicker recording layers show larger scattering intenstities. Figure 4.2 clearly shows that scattering intensity from C13 with its 16 nm thick recording layers is a lot larger than the scattering from sample C4 with its thin recording layers.

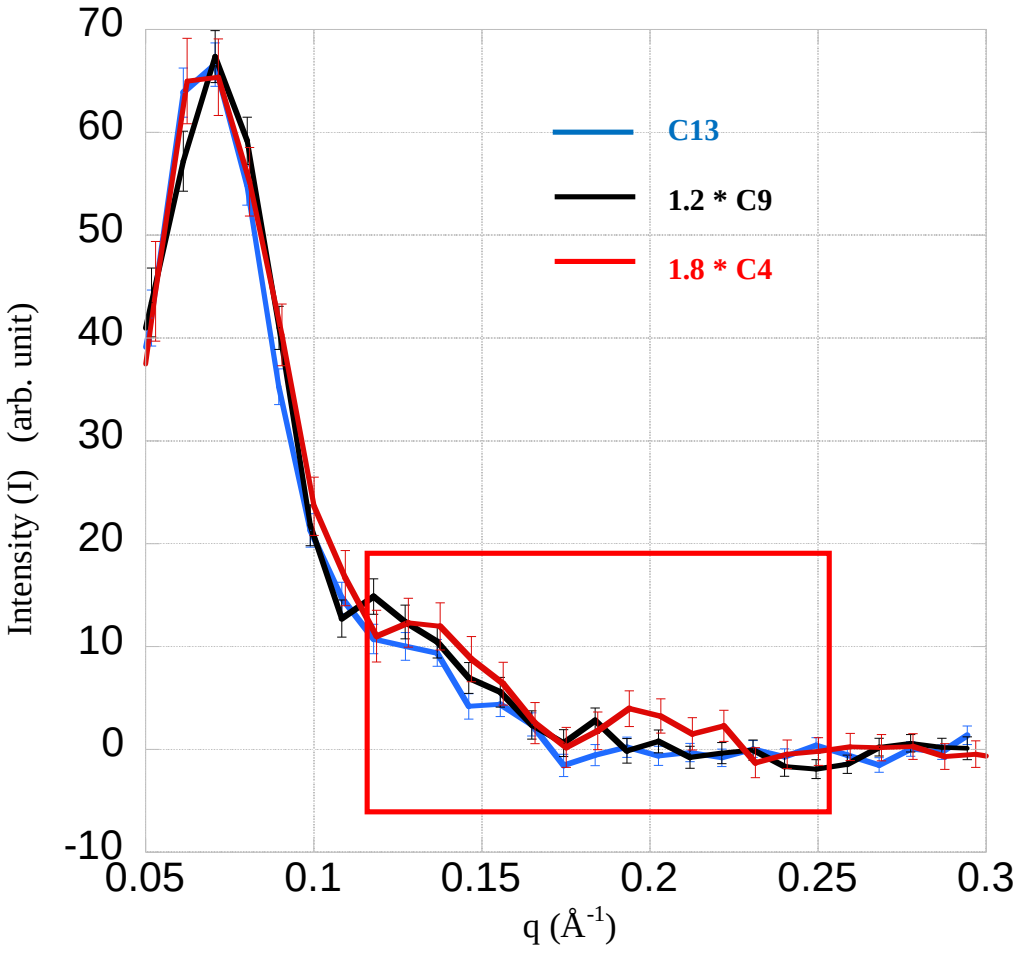


**Figure 4.3** Experimental scattering intensity data $\langle\uparrow|V(\vec{Q})|\uparrow\rangle^2 - \langle\downarrow|V(\vec{Q})|\downarrow\rangle^2$ for samples C4, C9 and C13 are scaled up and compared

The next question that needed to be addressed was what was responsible for increased scattering when the layer thickness increases. In order to understand this, the scattering intensities in samples C4 and C9 were scaled up to match the scattering intensity in sample C13. It was found that the scattering intensity of sample C9 was 83.3% of sample C13 and sample C4 was 55.6% of sample C13. Therefore by multiplying the scattering intensity of sample C9 by 1.2 and sample C4 by 1.8, the scattering intensities of C9 and C4 were scaled up to match the scattering intensity of sample C13.

Figure 4.3 with scaled up intensities shows that the scattering intensities nearly match each other, apart from the high 'q' region (red box) between 0.1-0.25 $A^{-1}$ where subtle oscillations are observed in sample C4. However these scattering intensity oscillations observed in the high 'q' region for the C4 sample are within the limits of the error bars, making it very difficult to interpret. To further understand the relation between the thickness and the scattering intensity, the ratio between scattering intensity and its thickness is compared for the three different samples. Figure 4.4 shows a comparison of the ratio between the maxmimum scattering intensity peak (I) and the thickness of the film (d) for the three different samples.

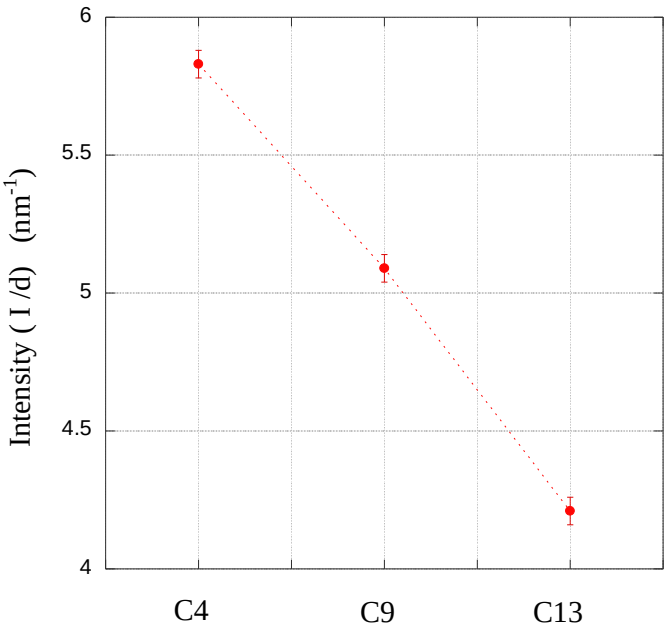


**Figure 4.4** Ratio of the maximum scattering intensity (I) $\langle\uparrow|V(\vec{Q})|\uparrow\rangle^2 - \langle\downarrow|V(\vec{Q})|\downarrow\rangle^2$ to the thickness of the recording layers (d) compared for three different samples C4, C9 and C13

When comparing the data in Figure 4.4 it is evident that the scattering intensities do not scale evenly with recording layer thicknesses. The trend in Figure 4.4 clearly suggests that as the recording layer thickness increases, scattering per nominal unit volume of the material decreases. This suggests that as the layer thickness increases, there exists an increase in non active material that reduces the scattering [16]. However, the scattering intensity is an interference term of the nuclear and magnetic scattering. This makes it very difficult to state that the reduced scattering intensity observed is as a result of nuclear or magnetic scattering.

*Mono approximation analytical models comparing samples C9, C13 and C4*

The mono approximation model explained in Section 3.4.1 of Chapter 3 is used analytically simulate the experimental results [7,8]. Although, differences are observed when comparing the experimental data of samples C9, C4 and C13 in Figure 4.3, the analytical model is used to fit the data as closely as possible. Figure 4.5 is a reproduction of the simulated fit using the mono approximation analytical model for the C9 – 'Oxide only' sample in Figure 3.6 of Chapter 3. The mono approximation model is also used to fit experimental data for the C4 and C13 sample and their differences are reported.

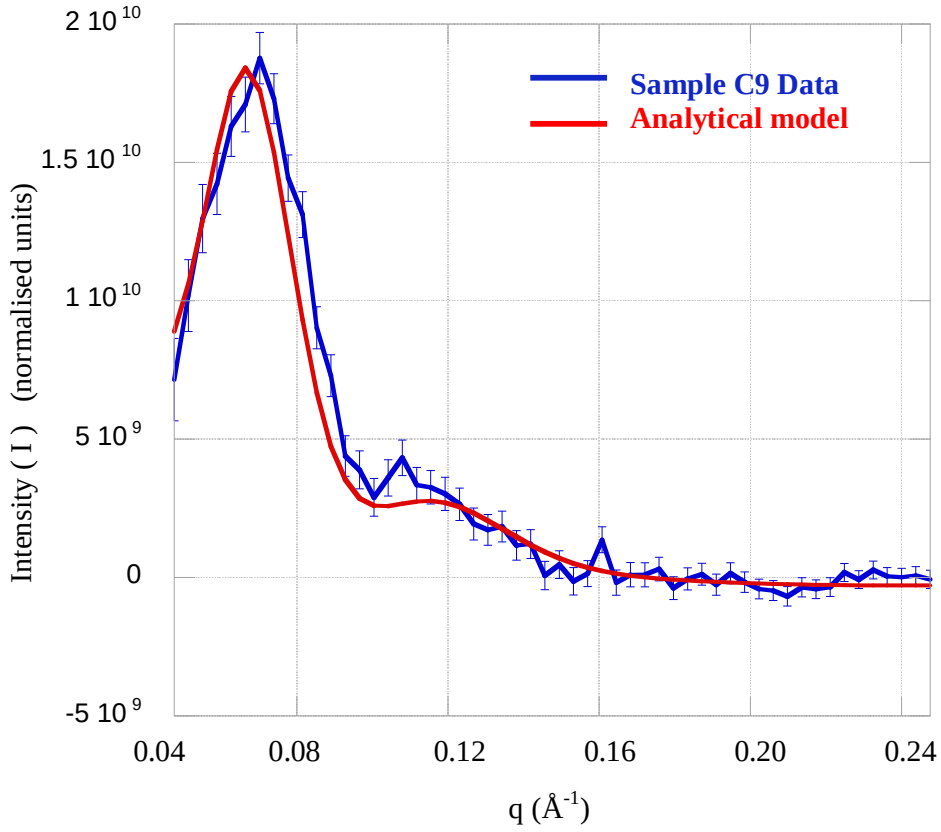


**Figure 4.5** Scattering intensity $\langle\uparrow|V(\vec{Q})|\uparrow\rangle^2 - \langle\downarrow|V(\vec{Q})|\downarrow\rangle^2$ for C9-Oxide only sample fitted with the mono approximation model

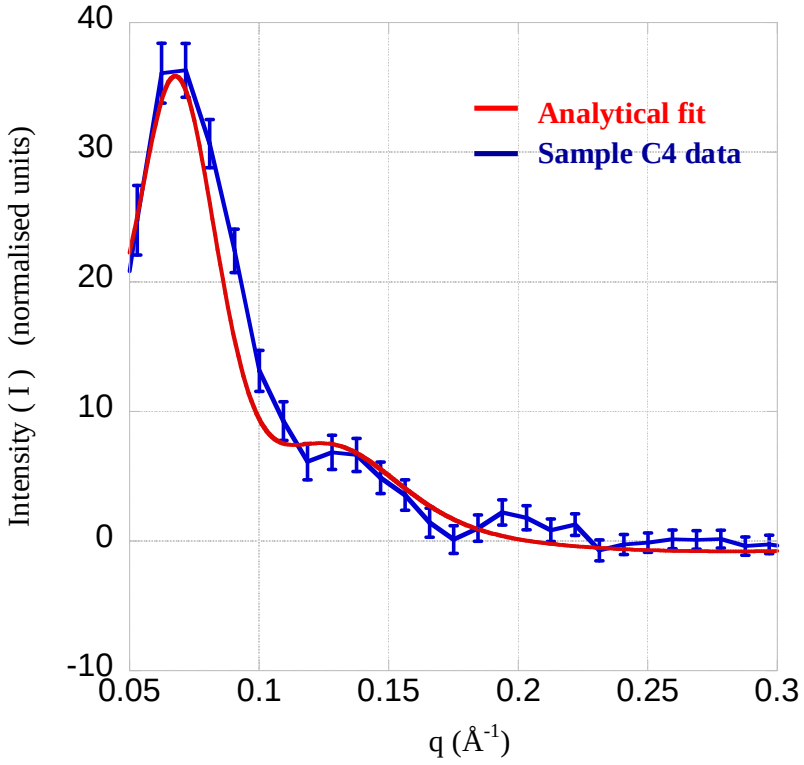


**Figure 4.6** Scattering intensity $\langle\uparrow|V(\vec{Q})|\uparrow\rangle^2 - \langle\downarrow|V(\vec{Q})|\downarrow\rangle^2$ for C4-Oxide only sample fitted with the mono approximation model

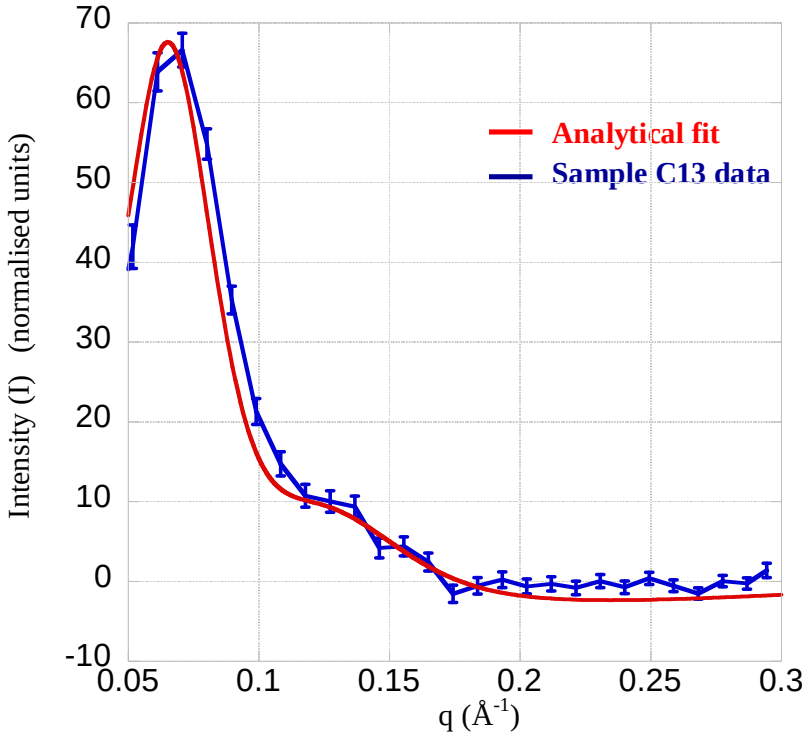


**Figure 4.7** Scattering intensity $\langle\uparrow|V(\vec{Q})|\uparrow\rangle^2 - \langle\downarrow|V(\vec{Q})|\downarrow\rangle^2$ for C13-Oxide only sample fitted with the mono approximation model

The average nuclear grain diameter, magnetic grain diameter, packing density factor and the ratio between the magnetic and physical grain determined by the mono analytical model are tabulated in Table 4.2[8]. No significant differences are seen in the tabulated values expect for a reduction in the ratio between the magnetic and nuclear grain for the sample C13.

**Table 4.2** Table summarising the results for the mono approximation analytical model when comparing sample C4, C9 and C13

| *Samples* | *Grain shape* | *Magnetic grain diameter* ($\sigma_m$ nm) | *Physical grain diameter* ($\sigma_n$ nm) | *Average intergranular distance* (nm) | $\kappa$ | *Packing density factor* ($\eta$) | *Width parameter* (z) |
|---|---|---|---|---|---|---|---|
| C4 | Cylinder | 6.4±0.1 | 8.0±0.1 | 8.8±0.5 | 0.80 | 0.52 | 25 |
| C9 | Cylinder | 6.4±0.1 | 8.0±0.1 | 8.8±0.5 | 0.80 | 0.52 | 30 |
| C13 | Cylinder | 6.1±0.1 | 8.0±0.1 | 8.8±0.5 | 0.76 | 0.52 | 25 |

The other change that was made to fit the C13 and the C4 data was a reduction in the width parameter (z) of the Gamma-Shultz function. This width parameter (z) is used to account for the polydispersity of the grains in the mono approximation analytical model. This reduction in the width parameter suggests the possibility of a large presence of CoCrPt grains that have diameters closer to the average grain diameter used in the model. However, looking at this level of detail is clearly within the limits of the model. This is because the structure factor used in this model represents a Percus-Yevick type liquid metal model that is used for the packing of simple hard spheres. We use this model on a basic level to understand the scattering intensity peak, and looking at finer details would require a structure factor model, that represents the packing of cylinders in a thin film better depicting the CoCrPt grains in the recording layer.

To summarise the results within the limits of this model, fine differences are seen between samples C9, C4 and C13. A more sophisticated structure factor model that represents the packing of cylinders in a thin film would be required to generate a better analytical simulation of the scattering data that could be used to fit the finer differences observed when comparing the scattering intensities of sample C13, C9 and C4.

## 4.5 Conclusion

The experimental results for samples C4, C9 and C13 with varying thicknesses of recording layers are compared. When normalised, differences between the scattering intensities for sample C4, C9 and C13 were observed. An attempt was made to fit these subtle differences in scattering intensities observed for C9, C13 and C4 samples using the mono approximation model [8]. The mono approximation model, failed to identify the significant differences as a result of the limitations in this model.

The comparison of the scattering intensities of the three recording layer samples (C9, C4 and C13) with the sample that has no recording layer (C15) highlights the remarkable sensitivity of this experimental technique [15]. The difference of the 'spin up' and 'spin down' scattering for the C15 sample showed no scattering intensity. This clearly states that by using this experimental geometry we only observe an interference term as a result of the magnetic and nuclear scattering from CoCrPt grains and all other background scattering present in the system is subtracted [14].

When comparing the maximum experimental scattering intensities determined with changing recording layer thickness for the three different samples (C4, C9 and C13) it was found that although scattering intensity by itself increased with increasing thickness, the amount of scattering per unit nominal volume decreased with increasing thickness. This decreasing trend observed when the ratio between the scattering intensity and layer thickness was determined suggests that the active scattering material reduces as we increase the thickness of the recording layer in samples C4, C9 and C13 [16,17]. The decrease in active scattering material over increasing recording layer thickness cannot be directly interpreted as a nuclear or magnetic contribution, as by using the present experimental geometry in PolSANS, we obtain an interference term that has contributions from both the nuclear and magnetic scattering components [14,15]. This result however opens up interesting questions that can be addressed by performing a conventional SANS type of experiment where we extract only the magnetic scattering from the CoCrPt grains [18]. This information could be used in combination with the PolSANS experimental data that gives us the interference term. With both of these results, it would be possible to determine if the decrease in active scattering material with increasing thickness is a magnetic or nuclear scattering contribution.

## 4.6 References


[1] S.N. Piramanayagam, H.B. Zhao "Effect of seed layers on the textured growth of Pd/Ru intermediate layers for perpendicular recording media" Journal of Magnetism and Magnetic Materials, 312 (2) , (2007) p.476-479 (DOI: 10.1016/j.jmmm.2006.10.466)

[2] Sangho Lee, Sanghoon Kim, Jaeyong Kang, Jongill Hong "Effect of various single metallic seed-layers on the magnetic properties of Co/Pd multilayers" Thin Solid Films, 519 (23), (2011), p.8363-8366 (DOI: 10.1016/j.tsf.2011.03.083)

[3] R.A. Morris, Y. Inaba, J.W. Harrell, G.B. Thompson " Influence of underlayers on the c-axis distribution in Co80Pt20 thin films" Thin Solid Films, 518(17), (2010) p.4970-4976 (DOI: 10.1016/j.tsf.2010.03.072)

[4] Migaku Takahashi, Shin Saito " Advanced granular-type perpendicular recording media" Journal of Magnetism and Magnetic Materials, 320(22), (2008) p.2868-2873 (DOI: 10.1016/j.jmmm.2008.07.039)

[5] Taek Dong Lee, Min Sig Hwang, Kyung Jin Lee "Effects of magnetic layer thickness on negative nucleation field and Cr segregation behavior in CoCrPt/Ti perpendicular media" Journal of Magnetism and Magnetic Materials, 235(1–3), (2001) p.297-304 (DOI: 10.1016/S0304-8853(01)00361-4)

[6] P. Glijer, J.M. Sivertsen, J.H. Judy "Effects of CoCrPt layer thickness on the magnetic and structural properties of CoCrPt/Cr thin films" IEEE Magnetics, 30(6), (1994) p.5070-5072 (DOI: 10.1109/20.334297)

[7] A. Guinier, G. Fournet "Small-Angle Scattering of X-Rays" John Wiley and Sons, New York (1955) (DOI: 10.1002/pol.1956.120199326)

[8] N.W. Ashcroft, J. Lekner "Structure and Resistivity of Liquid Metals" Phys. Rev. (145), (1966) p. 83–90 (DOI: 10.1103/PhysRev.145.83)

[9] A. Anghel *et al.* " The PSI ultra-cold neutron sourceNuclear Instruments and Methods in Physics Research Section A: Accelerators, Spectrometers, Detectors and Associated Equipment, 611(2–3), (2009) p.272-275 (DOI: 10.1016/j.nima.2009.07.077)

[10] J. Kohlbrecher, W. Wagner "The new SANS instrument at the Swiss spallation source SINQ"**,** J. Appl. Cryst. 33, (2000) p.804-806 (DOI: 10.1107/S0021889800099775)

[11] Dmitri Litvinov, Mark H Kryder, Sakhrat Khizroev "Recording physics of perpendicular media: soft underlayers" Journal of Magnetism and Magnetic Materials, 232(1–2), (2001) p.84-90 (DOI: 10.1016/S0304-8853(01)00216-5)

[12] Dmitri Litvinov, Mark H Kryder, Sakhrat Khizroev "Recording physics of perpendicular media: hard layers" Journal of Magnetism and Magnetic Materials, 241(2–3), (2002) p.453-465 (DOI: 10.1016/S0304-8853(02)00023-9)

[13] Chun-Tao Xiao, Yuki Inaba, Takehito Shimatsu, Hiroaki Muraoka "Microstructure, magnetic properties and their seed layer thickness dependences of granular CoPtCr–SiO2 perpendicular recording media" Solid State Communications, 144 (1–2), (2007), p.58-60 (DOI: 10.1016/j.ssc.2007.07.014)

[14] S. J. Lister, M. P. Wismayer, V. Venkataramana, M. A. de Vries, S. J. Ray, S. L. Lee, T. Thomson, J. Kohlbrecher, H. Do, Y. Ikeda, K. Takano, and C. Dewhurst "Small-angle polarized neutron studies of perpendicular magnetic recording media" Journal of Applied Physics, 106(6),(2009) p. 063908 - 063908-4 (DOI: 10.1063/1.3213381)

[15] Albrecht Wiedenmann "Polarized SANS for probing magnetic nanostructures" Physica B: Condensed Matter, 356(1–4), (2005) p. 246-253 (DOI : 10.1016/j.physb.2004.10.085)

[16] Kazumasa Shimoda, Toshio Sugimoto, Ryosaku Inamura, Takenori Ohshima, Daiju Kaneko, Sanae Takefusa, Takuya Uzumaki, Atsushi Tanaka "Recording characteristics of CoPtCr–SiO2 perpendicular media" Journal of Magnetism and Magnetic Materials, 287, (2005) p.176-180 (DOI : 10.1016/j.jmmm.2004.10.029)

[17] S. N. Piramanayagam "Perpendicular recording media for hard disk drives" J. Appl. Phys. 102, 011301 (2007) (DOI: 10.1063/1.2750414)

[18] M. Wismayer, S. Lee, T. Thomson, F. Ogrin, C. Dewhurst, S. Weekes, R. Cubitt “Using small-angle neutron scattering to probe the local magnetic structure of perpendicular magnetic recording media” Journal of Applied Physics, 99(8), (2006) (DOI: 08e707 10.1063/1.2165798)

# Chapter 5

# Investigating size-dependent magnetic grain switching in the recording layer using PolSANS

---

**Contents**



---

**Abstract** This chapter builds on the results of chapter 3 where the size, shape and the distribution of CoCrPt grains in the recording layer were investigated. The work presented in this chapter looks to understand the magnetic switching of the CoCrPt grains in the recording layer when the magnetic field is gradually reversed from its initial saturation magnetisation state. PolSANS experiments have been carried out at different reversed fields from the initial saturated state, and analytical and numerical models have been used to analyse the experimental data as magnetic grains are driven towards saturation in the opposite direction. Size-dependent magnetic grain switching models have been developed using analytical models and Transmission electron microscopy (TEM) images in order to understand the experimental data. Results obtained from the analytical and TEM models are then analysed using theoretical magnetic grain switching models proposed by Sharrock *et al*. [1]

## 5.1 Background and Introduction

The CoCrPt magnetic grains in the recording layer are well segregated with oxide present between the CoCrPt grains in the recording layer [1,2]. The oxide present in the recording layer discourages exchange coupling between the CoCrPt grains in the recording layer [3]. This encourages a non-interacting magnetic system where the CoCrPt magnetic grains behave like individual nanoscale magnets in the recording layer [4,5]. The CoCrPt magnetic grains also possess a strong out of plane magneto-crystalline anisotropy [1,6]. As a result of this strong magneto-crystalline anisotropy, an equally strong magnetic field is required to switch the magnetic grains in the recording layer.

This chapter investigates the switching of the CoCrPt magnetic grains in the recording layer, under the influence of an increasing static magnetic field [7,8,9]. This is done by saturating the CoCrPt magnetic grains along their easy axis, and gradually increasing the magnetic field in the direction opposite to initial magnetic saturation [7]. A PolSANS experiment is performed at each magnetic field and the scattering intensity data is obtained and compared [10]. A size dependent non-interacting magnetic grain switching model is used to determine the average magnetic grain size switched at increasing magnetic fields [5,11,12].

The average magnetic grain size switched at increasing magnetic fields is determined by the mono approximation and pair structure factor model introduced in Chapter 2[13,14,15]. The numerical TEM model is also used to determine the size dependent magnetic switching at increasing magnetic fields and the results are presented and compared [16,17]. This chapter also determines the characteristic time 't', at different magnetic fields for a size dependent and independent anisotropy field $H_k$. This analysis is based on the theoretical work carried out by Sharrock and Flanders to determine the rate of thermal activation for a non-interacting magnetic system, based on the Stoner-Wolhfarth switching model introduced in Chapter 1 [18,19,20].

## 5.2 Samples and Preparation

The C9 – 'Oxide only' sample described in Chapter 3 is used for this experiment. The sample has a recording layer (RL) thickness of around 11 nm and is double sided samples in order to maximise the volume of the sample in the experiment. The samples were sputtered at Hitachi

GST San Jose research centre at California (USA), who have collaborated on this work in analysing the magnetics of the CoCrPt grains in the RL.

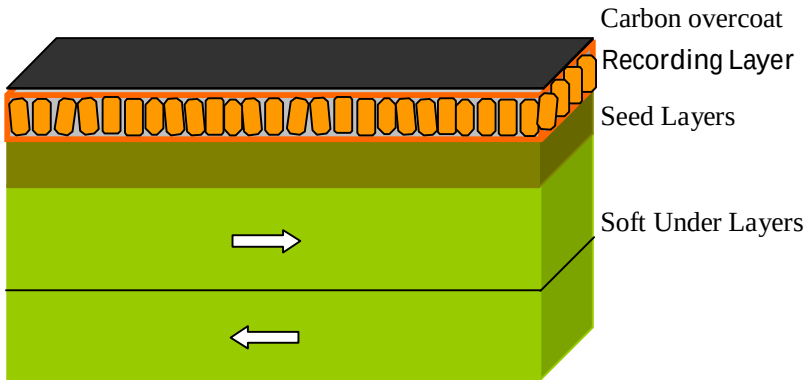


**Figure 5.1** C9 – 'Oxide only' sample structue

The full structure of the sample is seen in Figure 5.1. The soft under layer have thicknesses of around 100 nm and comprise two FeCo layers anti-ferromagnetically coupled using a Ru spacer layer. The seed layer used here is Ru with a thickness about 20 nm. The final layer on the top where the data is actually stored is the 11nm thick recording layer that comprises the CoCrPt grains embedded in an oxide matrix [21,22,23].

A stack of 10 double sided samples are placed in the sample holder on the sample stick, and the sample holder is then placed in the cryostat of the SINQ-SANS I instrument at PSI. The sample stick is placed so that the plane of the thin film is perpendicular to the direction of the beam and along the direction of the applied magnetic field, as described in Chapter 3[10,24].

## 5.3 Experiment

The experimental conditions are similar to those stated in Section 3.3 in Chapter 3 and Section 4.3 in Chapter 4 respectively. The cryostat temperature is set at 250 K and magnetic field is set to 0 T. The experimental q range is also set by adjusting the positions of the collimator and the detector [10]. Figure 5.2 is a cartoon of the experimental geometry used. Finally the magnetic field is ramped up to 3 T and a PolSANS experiment is performed [24]. The experimental data is extracted by obtaining the difference between the 'spin up' and 'spin down' scattering which is then radially averaged as a function of q. This experimental data is interpreted as an interference term of the nuclear ($b_m$) and magnetic ($M_z(\vec{Q})$)

scattering from the granular and the magnetic structure of the CoCrPt grains given in Equation 2.33 in Chapter 2 [24].

$$\left\langle \uparrow \left| V(\vec{Q}) \right| \uparrow \right\rangle^2 - \left\langle \downarrow \left| V(\vec{Q}) \right| \downarrow \right\rangle^2 = 4\,\mathrm{Re}(b_m * M_z(\vec{Q})) \tag{2.33}$$

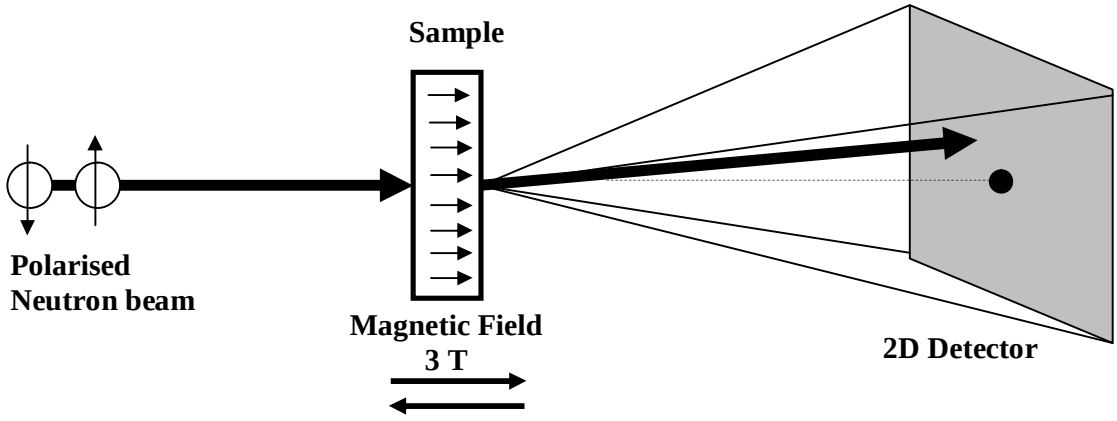


**Figure 5.2** PolSANS experimental geometry at an applied magnetic field of 3 T

At a magnetic field of 3 T the magnetic grains saturate along the direction of the applied magnetic field. The experimental data extracted for a PolSANS experiment at 3 T is interpreted in terms of the nuclear and the magnetic scattering from saturated magnetic CoCrPt grains. The magnetic field applied is then gradually reversed to understand how the experimental data extracted is influenced by changes in the magnetic state of the CoCrPt grains in the recording layer [25]. The magnetic field is first dropped to 0.025 T from its initial saturated state of 3 T and by carrying out a PolSANS experiment, the experimental data is extracted from the difference in 'spin up' and 'spin down' scattering. The magnetic field is then gradually reversed in the direction opposite to initial saturation, and at different fields the difference between the 'spin up' and 'spin down' scattering is determined. It is important to note that the physical CoCrPt grain remains unaffected by the changing magnetic fields and only the magnetic component of the CoCrPt grain is influenced by the effect of the reversed magnetic field. PolSANS experiments were performed at magnetic fields of 3 T, 0.025 T, -0.3 T, -0.45 T, -0.5 T, -0.6 T, -0.7 T, -0.75 T, -0.8 T, -0.85 T, -0.9 T, -1.0 T, -1.1 T, -1.15 T, -1.3 T, -1.5 T and -2 T. The experimental data obtained is analysed using analytical and numerical models, with the models now being extended to account for the influence of expected magnetic grain switching [13,14,15,25].

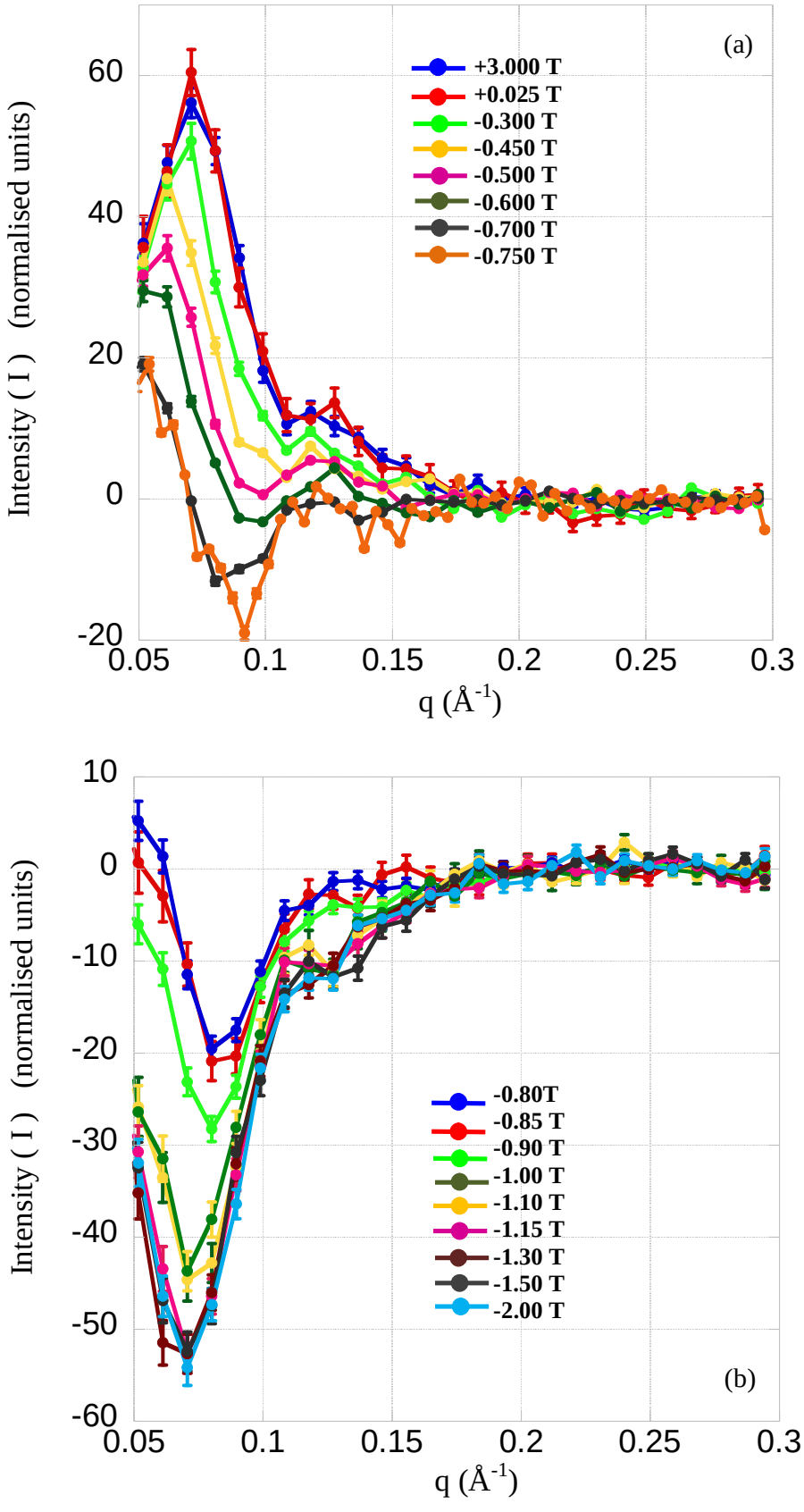


**Figure 5.3 (a)** and **(b)** Experimental scattering intensity data $\langle\uparrow|V(\vec{Q})|\uparrow\rangle^2 - \langle\downarrow|V(\vec{Q})|\downarrow\rangle^2$ at different magnetic fields[25]

The experimental data in Figure 5.3 shows that the net scattering that represents both the magnetic and nuclear scattering stays positive for a magnetic field of about -0.75 T. Beyond this field it is observed that the difference in scattering intensity extracted begins to move into the negative direction. It is hypothesised that this is as a result of the switching of the magnetic grains in the recording layer [25]. The experimental data is further analysed using analytical models that account for the expected magnetic grain switching. The analytical and numerical TEM models used in the reported work, account for the expected magnetic grain switching using a size dependent grain switching model [13,14,15].

The PolSANS experiments, to determine the magnetic switching of the CoCrPt grains in the recording layer, are supported by remanence curve experiments carried out on the C9-'Oxide only' samples using a DMS-10 vector vibrating sample magnetometer (VSM) [26]. The samples are magnetised out of plane and the remanence curve technique is used to separate the soft under layers from the CoCrPt recording layer. This is done by pinning the soft under layers using a small in plane magnetic field and only measuring the magnetic moment from the recording layer at different magnetic fields. This gives the remanence curve data for recording layer in the perpendicular magnetic medium as shown in Figure 5.4 [26]. This data was provided by Dr. Chris Morrison from the University of Manchester, UK.

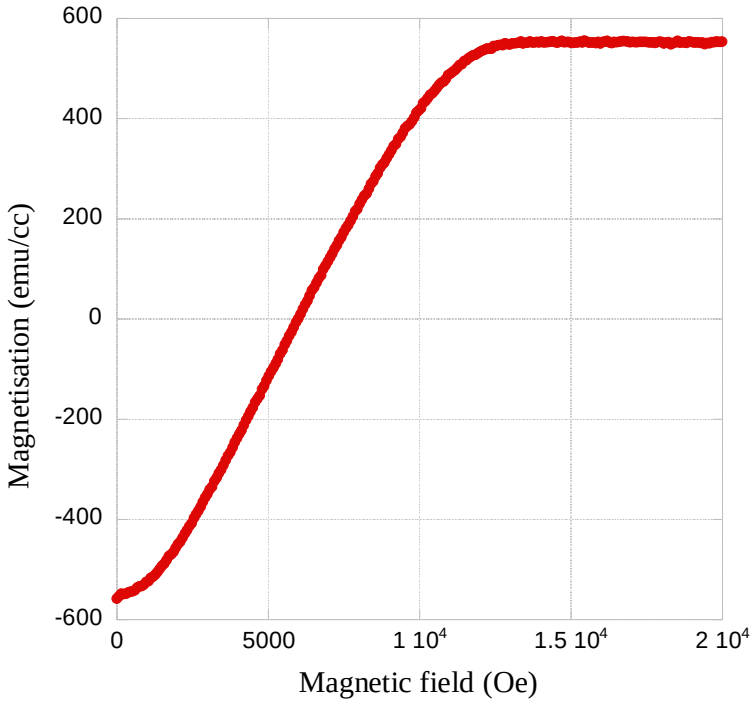


**Figure 5.4** The remanence curve for the recording layer of a C9-'Oxide only' sample obtained using the remanence curve technique on a vector VSM

In terms of reversal, the remanence curve is very identical to a hysteresis loop as there is very little reversal behaviour in these thin films [26]. From the remanence curve data in Figure 5.4 the magnetic behaviour of the CoCrPt grains at different magnetic fields along the hysteresis loop is predicted. The magnetic field, at which the all CoCrPt magnetic grains in the recording layer saturate, is also determined from the remanence curve data [26]. However, it is important to note that the measurement times of a conventional PolSANS experiment and the VSM technique are very different, having different characteristic times that affect their switching fields.

## 5.4 Results and Analysis

The analysis of the experimental data has again been carried out using three approaches. The conventional analytical models that use the form and structure factor have again been used to determine the magnetic grain size and shape of the CoCrPt grains at the saturated field. [13,14,15] The mono approximation model and the pair structure factor model have both been used. TEM data has also again been used to develop a numerical model to understand the magnetic switching data. [13,14,15,16,17]

All three models however use independent size-dependent switching model approaches, that that there is no inter granular magnetic interaction between the CoCrPt grains in the recording layer [5,11]. The CoCrPt grains are expected to follow a size-dependent switching model where smaller grains switch at lower reversed field and magnetic field is gradually increased the larger grains switch from their initial saturated magnetic state. [5,11,25] The analytical and numerical models are used to determine the threshold magnetic grain switching diameter ($d_c$), which is defined as the maximum magnetic grain diameter below which the magnetic grains have a switched magnetic state. This threshold magnetic diameter is determined for different magnetic fields and the threshold diameters are then plotted as a function of field for the different analytical and numerical models [25].

### 5.4.1. Grain switching analysed using analytical models

The analytical models used here again employ a common cylinder form factor while using two different types of structure factor, namely the mono approximation and the pair structure factor with their differences explained in Section 3.4 of Chapter 3 [13,14,15]. Both analytical models are used to investigate if there exist, any differences in the threshold magnetic grain switching diameters for the two models at different magnetic switching fields. The threshold magnetic diameter obtained for different magnetic fields are compared.

**(a) Mono approximation model**

The mono approximation model is explained in Section 3.4 of Chapter 3 [13,14]. The model has been slightly modified by introducing a threshold grain diameter ($d_c$) term that determines the threshold (minimal) grain diameter ($d_c$) below which the magnetic grains switch magnetic state. The form factor used here again is that of a cylinder, as this was found to best represent the shape of the grain [13,14].

Figure 5.5 a plots the scattering intensity peak with a mono approximation model simulated fit that clearly demonstrates that at the 3 T field all the magnetic grains are aligned along the direction of the magnetic field. Figure 5.5 b illustrates the magnetic switched states of the grains across the Gamma-Schulz size distribution of the polydispersed CoCrPt grains. By gradually reversing the field in Figure 5.6, Figure 5.7, Figure 5.8, Figure 5.9, Figure 5.10, Figure 5.11 and Figure 5.12; $d_c$ gradually increases across the Gamma-Schulz function and as field increases larger grains begin to switch magnetic states along the direction of the reversed field. The simulated models using the mono approximation model at increasing values of $d_c$ confirm that as the reversed field increases larger magnetic grains switch magnetic states along the direction of the reversed field. However, increased oscillations in the simulations are observed when the mono approximation model is used. These increased oscillations are clearly a limitation of the mono approximation model which is an inadequate representation of the system with many different grains shapes and sizes, as observed in TEM images [13,14,24,25].

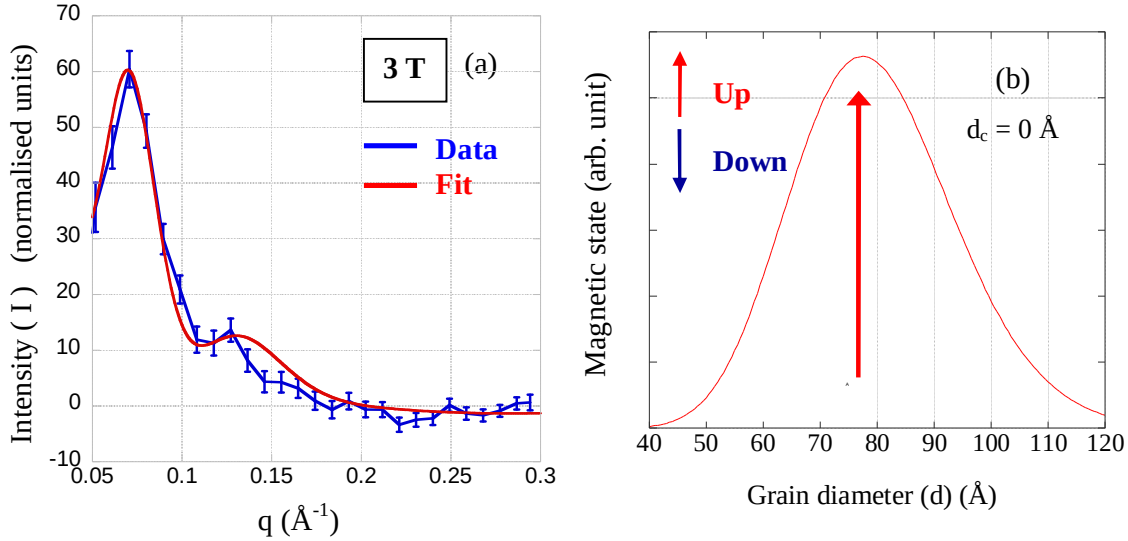


**Figure 5.5** (a) Experimental scattering intensity data $\langle\uparrow|V(\vec{Q})|\uparrow\rangle^2 - \langle\downarrow|V(\vec{Q})|\downarrow\rangle^2$ fitted with the mono approximation analytical model at 3 T
(b) Size-dependent magnetic state illustrated by the arrows across the Gamma-Schulz size distribution at an applied field of 3 T

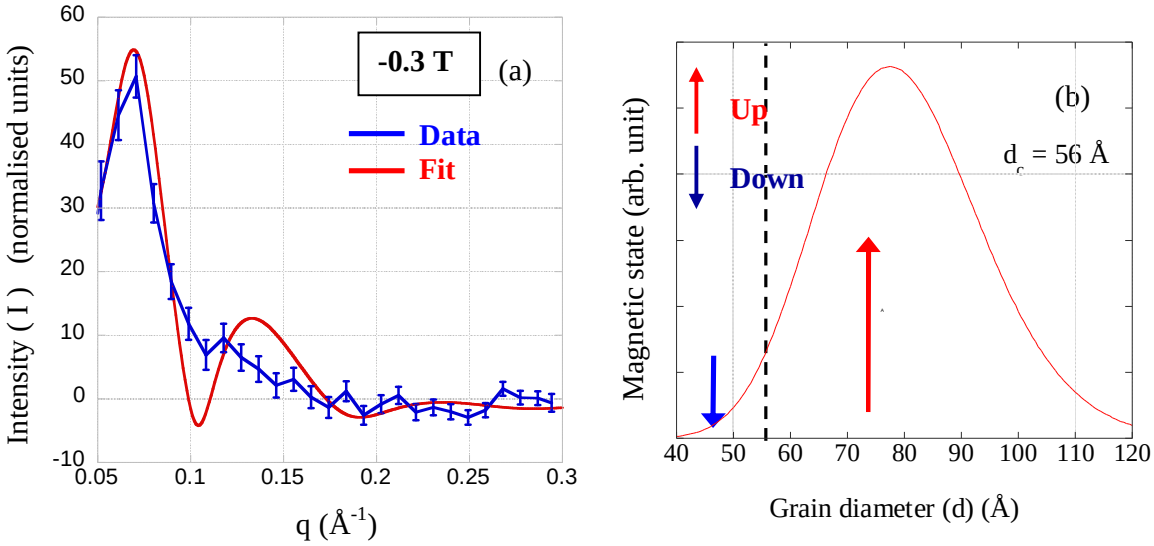


**Figure 5.6** (a) Experimental scattering intensity data $\langle\uparrow|V(\vec{Q})|\uparrow\rangle^2 - \langle\downarrow|V(\vec{Q})|\downarrow\rangle^2$ fitted with the mono approximation analytical model at -0.3 T
(b) Size-dependent magnetic state illustrated by the arrows across the Gamma-Schulz size distribution at an applied field of -0.3 T

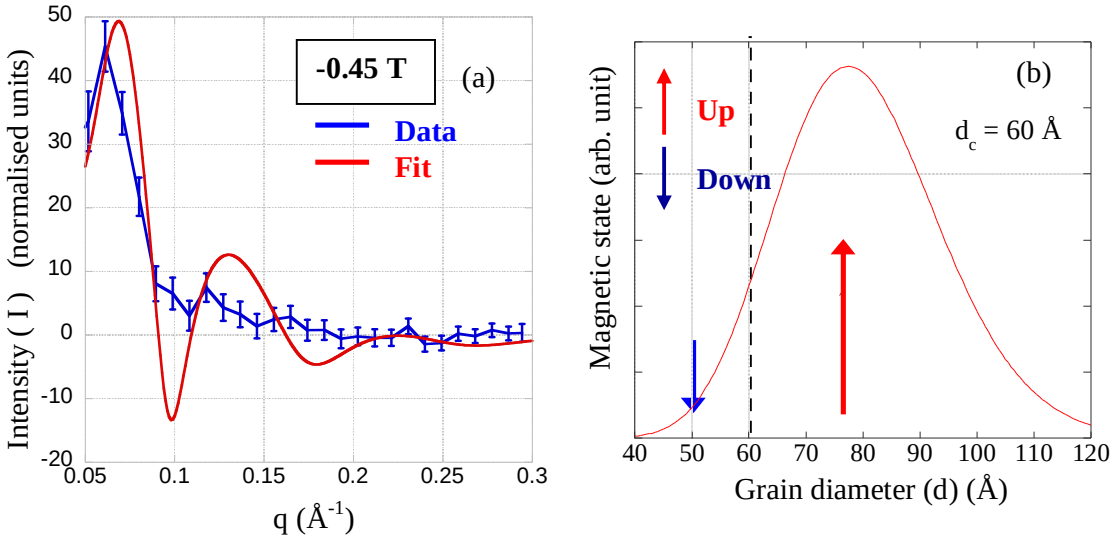


**Figure 5.7** (a) Experimental scattering intensity data $\langle\uparrow|V(\vec{Q})|\uparrow\rangle^2 - \langle\downarrow|V(\vec{Q})|\downarrow\rangle^2$ fitted with the mono approximation analytical model at -0.45 T
(b) Size-dependent magnetic state illustrated by the arrows across the Gamma-Schulz size distribution at an applied field of -0.45 T

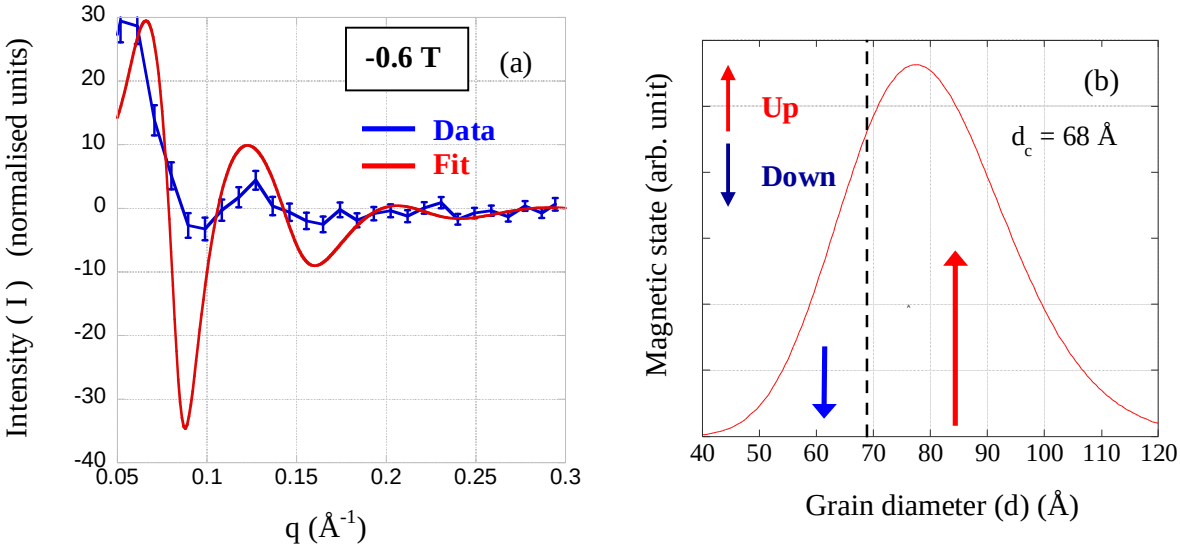


**Figure 5.8** (a) Experimental scattering intensity data $\langle\uparrow|V(\vec{Q})|\uparrow\rangle^2 - \langle\downarrow|V(\vec{Q})|\downarrow\rangle^2$ fitted with the mono approximation analytical model at -0.6 T
(b) Size-dependent magnetic state illustrated by the arrows across the Gamma-Schulz size distribution at an applied field of -0.6 T

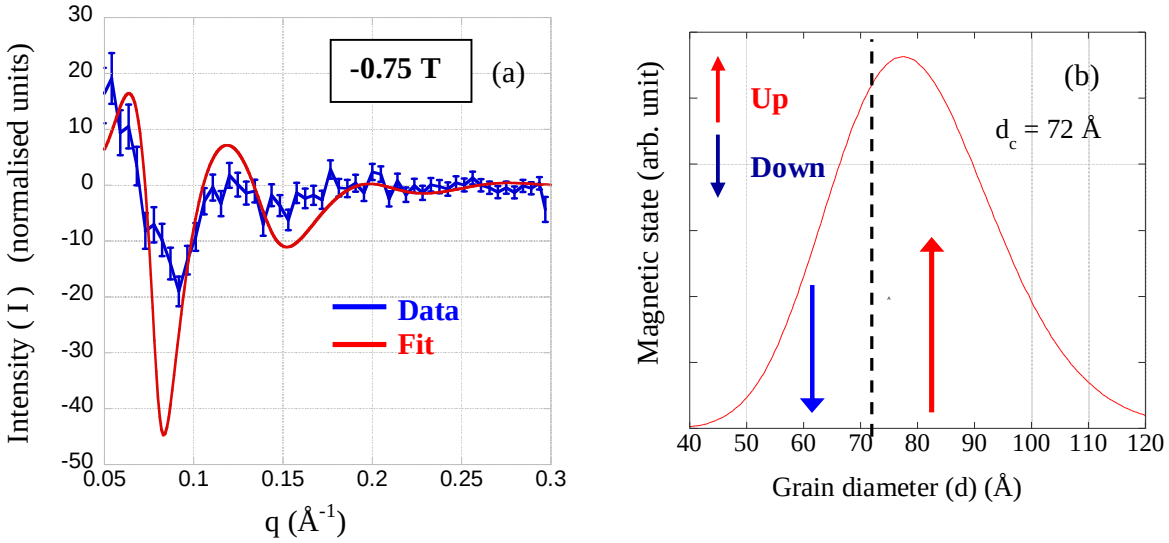


**Figure 5.9** (a) Experimental scattering intensity data $\langle\uparrow|V(\vec{Q})|\uparrow\rangle^2 - \langle\downarrow|V(\vec{Q})|\downarrow\rangle^2$ fitted with the mono approximation analytical model at -0.75 T
(b) Size-dependent magnetic state illustrated by the arrows across the Gamma-Schulz size distribution at an applied field of -0.75 T

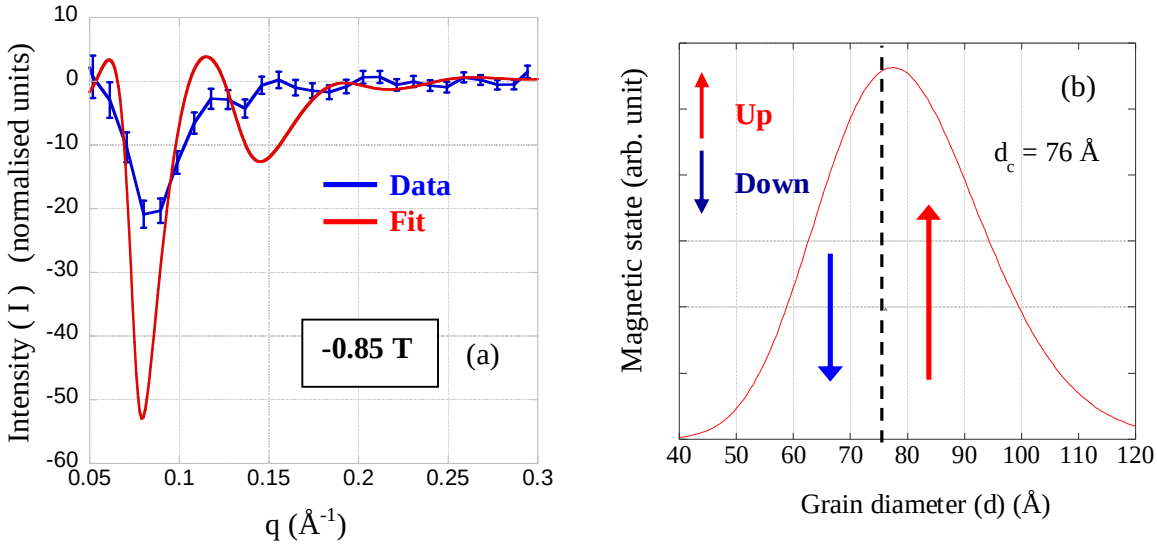


**Figure 5.10** (a) Experimental scattering intensity data $\langle\uparrow|V(\vec{Q})|\uparrow\rangle^2 - \langle\downarrow|V(\vec{Q})|\downarrow\rangle^2$ fitted with the mono approximation analytical model at -0.85 T
(b) Size-dependent magnetic state illustrated by the arrows across the Gamma-Schulz size distribution at an applied field of -0.85 T

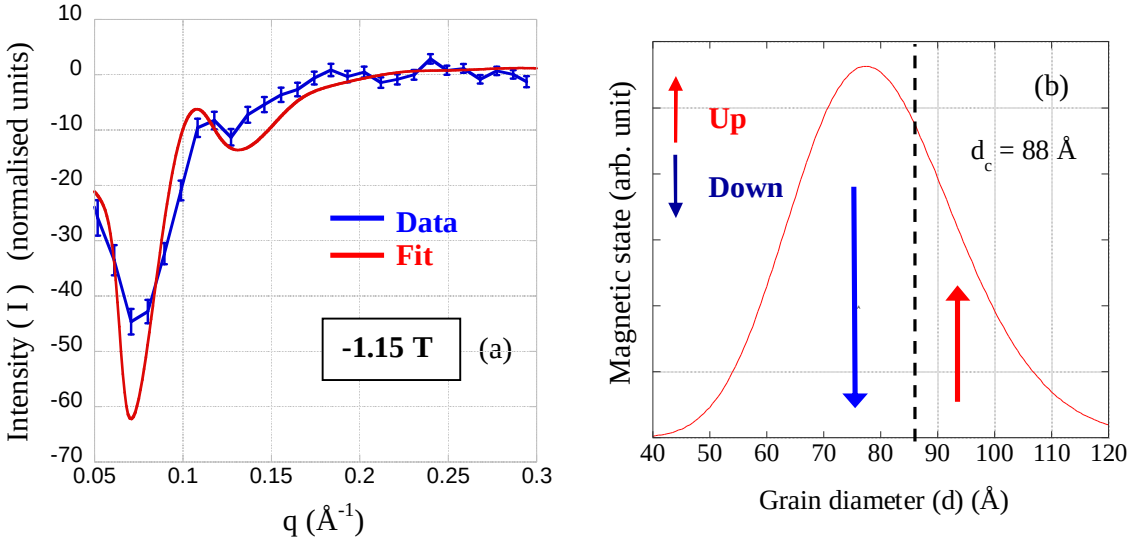


**Figure 5.11** (a) Experimental scattering intensity data $\langle\uparrow|V(\vec{Q})|\uparrow\rangle^2 - \langle\downarrow|V(\vec{Q})|\downarrow\rangle^2$ fitted with the mono approximation analytical model at -1.15 T
(b) Size-dependent magnetic state illustrated by the arrows across the Gamma-Schulz size distribution at an applied field of -1.15 T

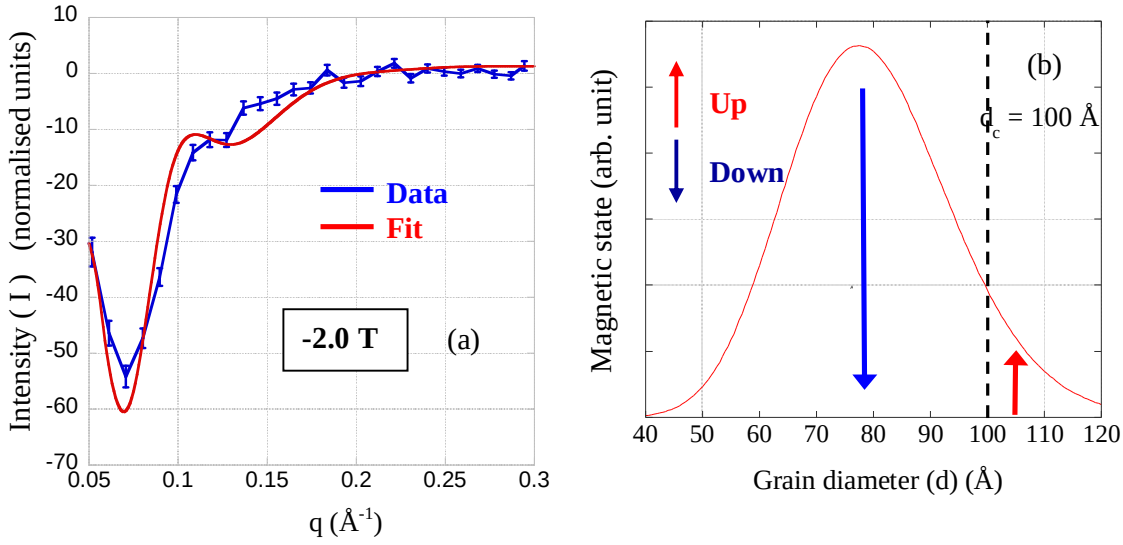


**Figure 5.12** (a) Experimental scattering intensity data $\langle\uparrow|V(\vec{Q})|\uparrow\rangle^2 - \langle\downarrow|V(\vec{Q})|\downarrow\rangle^2$ fitted with the mono approximation analytical model at -2.0 T
(b) Size-dependent magnetic state illustrated by the arrows across the Gamma-Schulz size distribution at an applied field of -2.0 T

**(b) Size-dependent pair structure factor model**

The pair structure factor model that was introduced in Section 3.4 of Chapter 3 is used to determine the threshold (minimal) switching grain diameter ($d_c$) for the different reversed magnetic fields [13,15]. The analytical model is modified to introduce the threshold grain diameter ($d_c$) that determines the threshold size below which the magnetic grains switch magnetic states, as the magnetic field is reversed and driven to saturation in the direction opposite to the initial saturated magnetic state.

Figure 5.13, Figure 5.14, Figure 5.15, Figure 5.16, Figure 5.17, Figure 5.18, Figure 5.19 and Figure 5.20 show the simulated analytical models with increasing values of $d_c$ as the magnetic field is gradually reversed from its initial saturated state. The size-dependent pair structure factor model simulations were found to fit the experimental data better than the size-dependent mono approximation model. This is because the size-dependent pair structure factor model is a better representation of the system as it takes into account the polydispersed nature of the CoCrPt grains in the analytical simulations [15]. Both models still use the form factor of the cylinder as it best represents the shape of the CoCrPt grains [13].

Both analytical models however predict different average grain diameters leading to different threshold switching grain diameters ($d_c$) at different magnetic fields. The different threshold switching grain diameters ($d_c$) determined by using both the pair structure factor model and the mono approximation model are compared with the threshold switching diameters ($d_c$) determined using the size dependent TEM switching model and the results compared are reported [16,17].

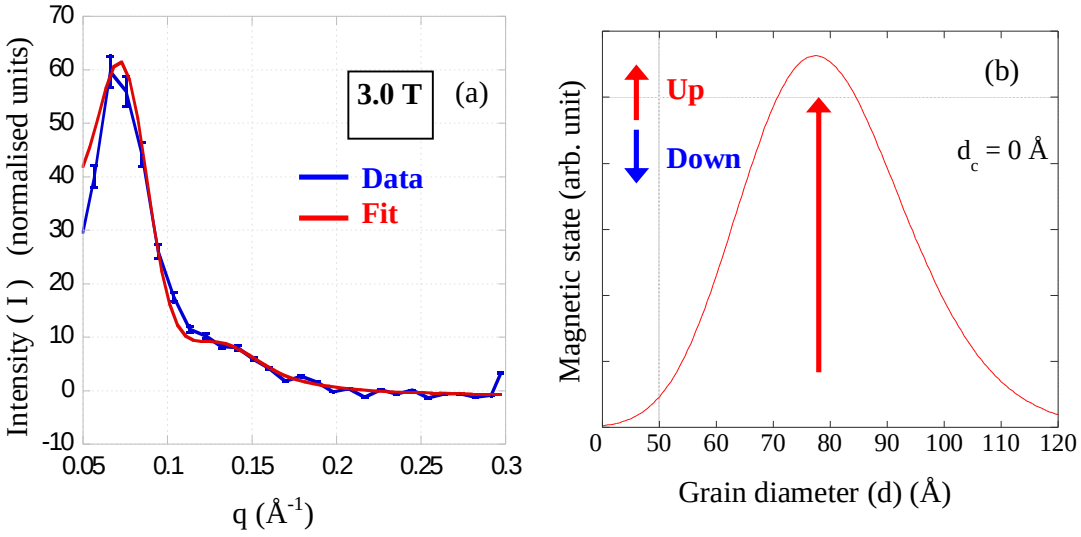


**Figure 5.13** (a) Experimental scattering intensity data $\langle\uparrow|V(\vec{Q})|\uparrow\rangle^2 - \langle\downarrow|V(\vec{Q})|\downarrow\rangle^2$ fitted with the pair structure factor analytical model at 3 T
(b) Size-dependent magnetic state illustrated by the arrows across the Gamma-Schulz size distribution at an applied magnetic field of 3 T

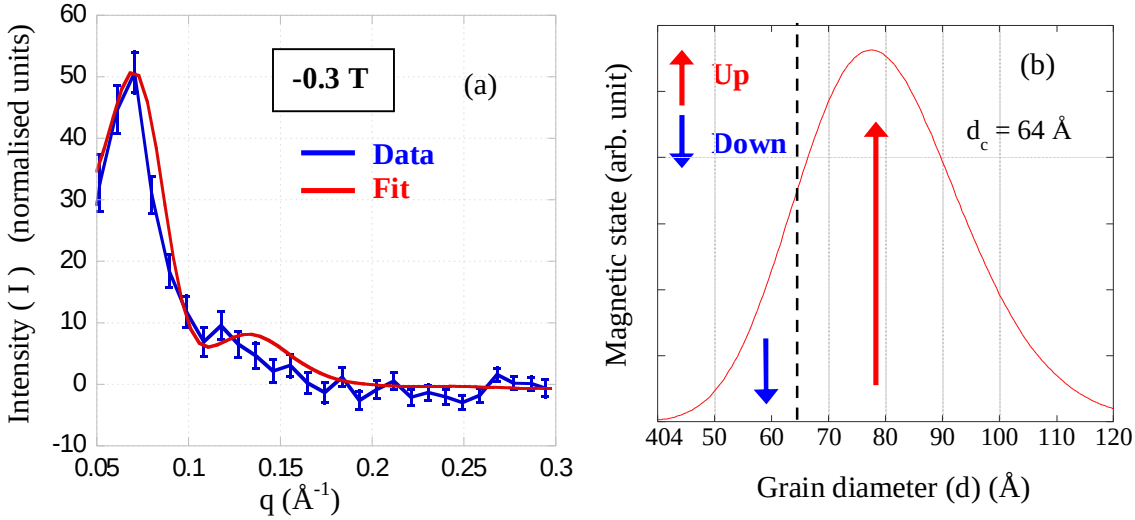


**Figure 5.14** (a) Experimental scattering intensity data $\langle\uparrow|V(\vec{Q})|\uparrow\rangle^2 - \langle\downarrow|V(\vec{Q})|\downarrow\rangle^2$ fitted with the pair structure factor analytical model at -0.3 T
(b) Size-dependent magnetic state illustrated by the arrows across the Gamma-Schulz size distribution at an applied magnetic field of -0.3 T

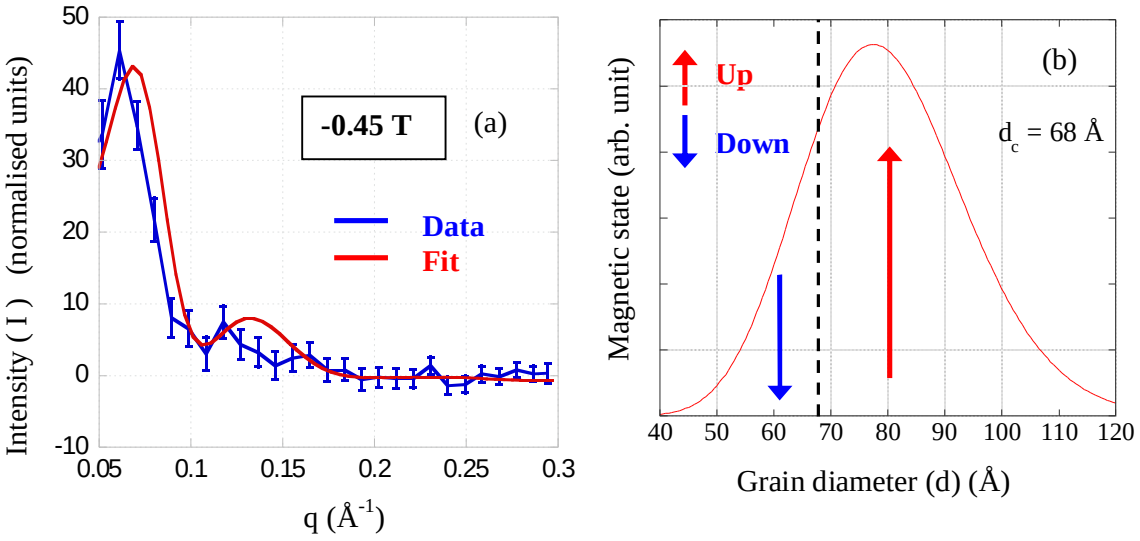


**Figure 5.15** (a) Experimental scattering intensity data $\langle\uparrow|V(\vec{Q})|\uparrow\rangle^2 - \langle\downarrow|V(\vec{Q})|\downarrow\rangle^2$ fitted with the pair structure factor analytical model at -0.45 T
(b) Size-dependent magnetic state illustrated by the arrows across the Gamma-Schulz size distribution at an applied magnetic field of -0.45 T

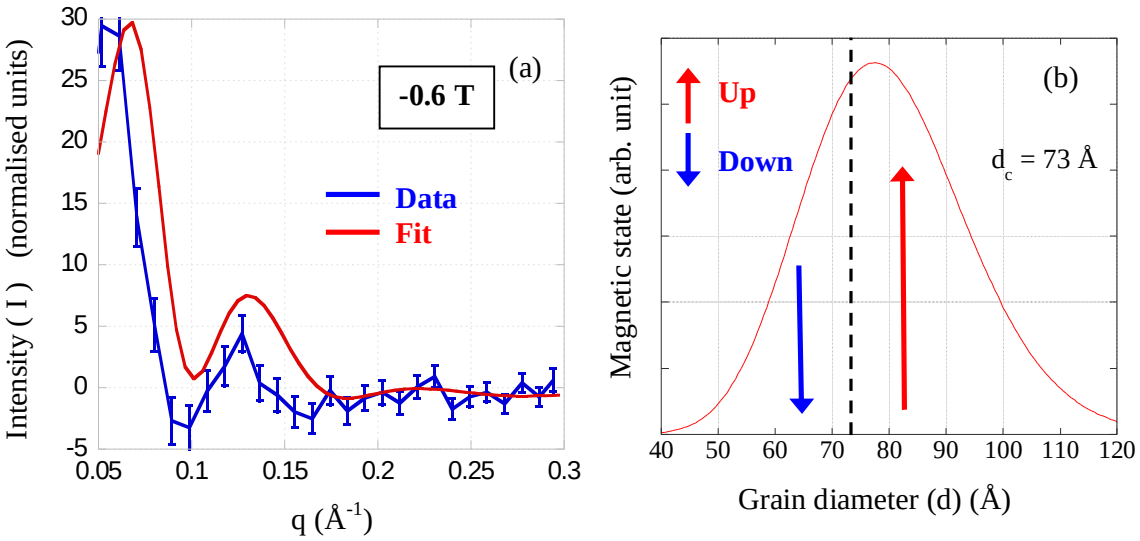


**Figure 5.16** (a) Experimental scattering intensity data $\langle\uparrow|V(\vec{Q})|\uparrow\rangle^2 - \langle\downarrow|V(\vec{Q})|\downarrow\rangle^2$ fitted with the pair structure factor analytical model at -0.6 T
(b) Size-dependent magnetic state illustrated by the arrows across the Gamma-Schulz size distribution at an applied magnetic field of -0.6 T

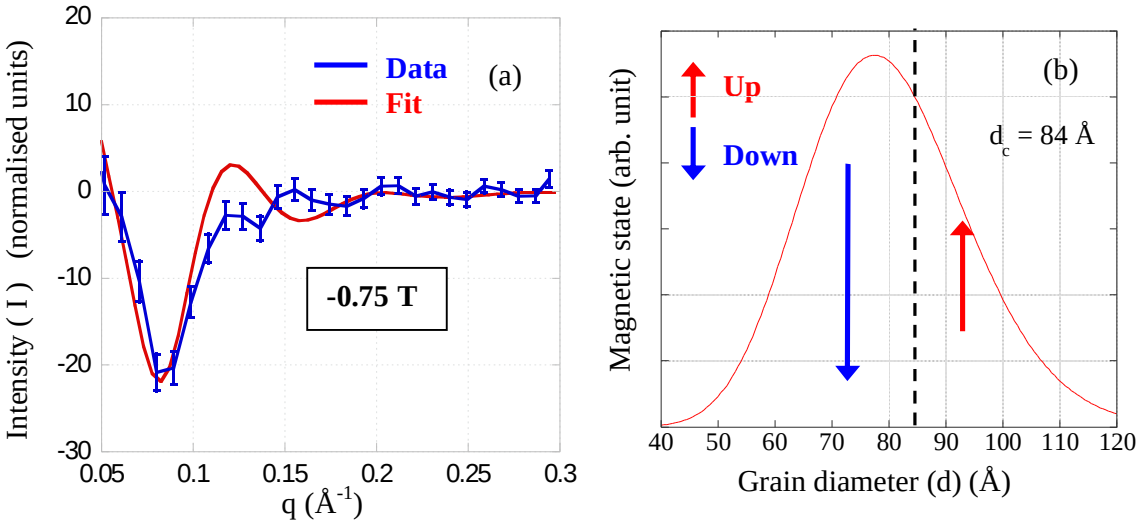


**Figure 5.17** (a) Experimental scattering intensity data $\langle\uparrow|V(\vec{Q})|\uparrow\rangle^2 - \langle\downarrow|V(\vec{Q})|\downarrow\rangle^2$ fitted with the pair structure factor analytical model at -0.75 T
(b) Size-dependent magnetic state illustrated by the arrows across the Gamma-Schulz size distribution at an applied magnetic field of -0.75 T

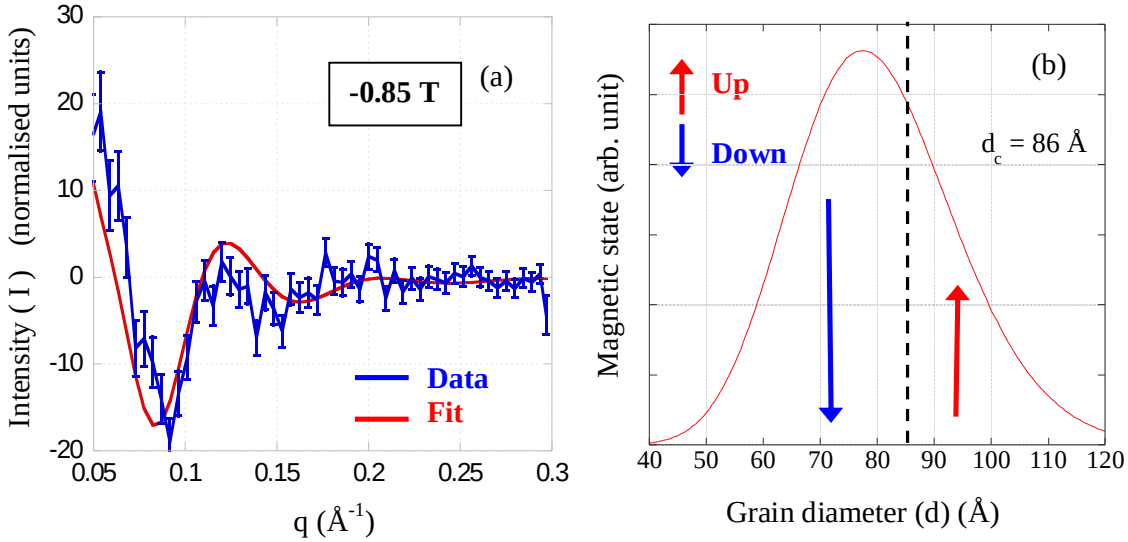


**Figure 5.18** (a) Experimental scattering intensity data $\langle\uparrow|V(\vec{Q})|\uparrow\rangle^2 - \langle\downarrow|V(\vec{Q})|\downarrow\rangle^2$ fitted with the pair structure factor analytical model at -0.85 T
(b) Size-dependent magnetic state illustrated by the arrows across the Gamma-Schulz size distribution at an applied magnetic field of -0.85 T

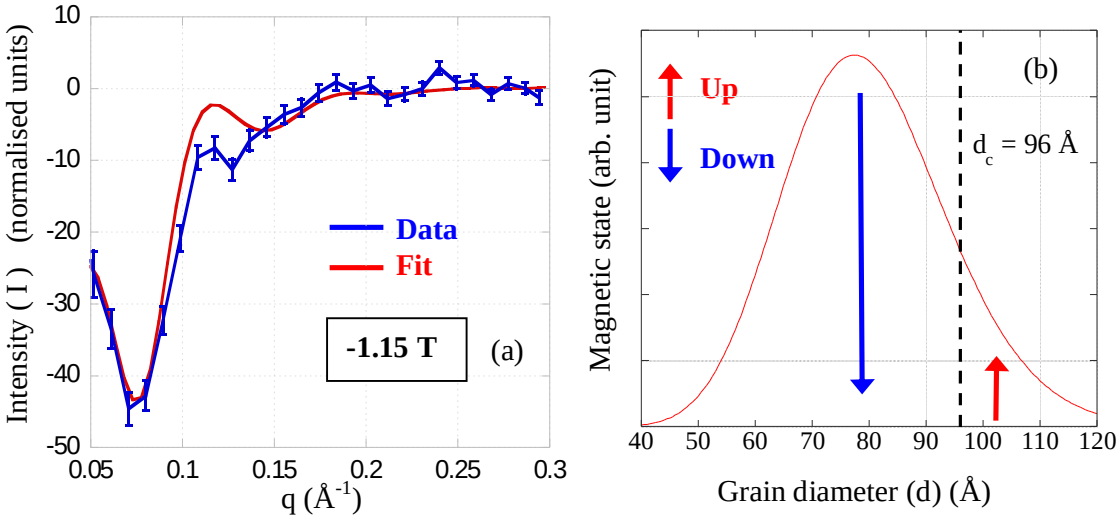


**Figure 5.19** (a) Experimental scattering intensity data $\langle\uparrow|V(\vec{Q})|\uparrow\rangle^2 - \langle\downarrow|V(\vec{Q})|\downarrow\rangle^2$ fitted with the pair structure factor analytical model at -1.15 T
(b) Size-dependent magnetic state illustrated by the arrows across the Gamma-Schulz size distribution at an applied magnetic field of -1.15 T

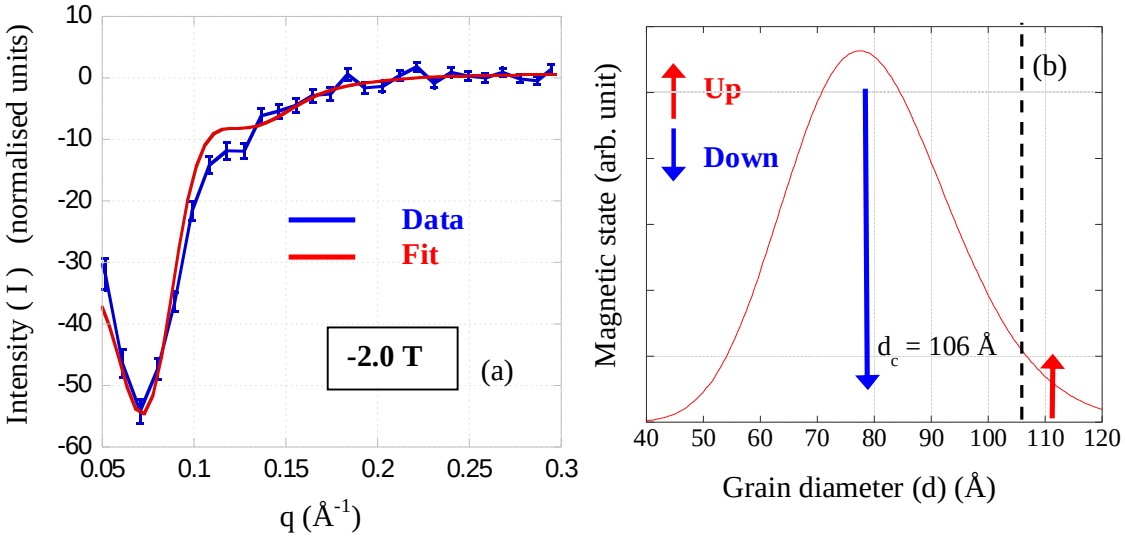


**Figure 5.20** (a) Experimental scattering intensity data $\langle\uparrow|V(\vec{Q})|\uparrow\rangle^2 - \langle\downarrow|V(\vec{Q})|\downarrow\rangle^2$ fitted with the pair structure factor analytical model at -2.0 T
(b) Size-dependent magnetic state illustrated by the arrows across the Gamma-Schulz size distribution at an applied magnetic field of -2.0 T

### 5.4.2. Size-dependent grain switching analysed using numerical TEM model

The TEM based numerical model introduced in Section 3.4.2 of Chapter 3 is used to analyse the size-dependent magnetic switching process in the recording layer [16,17]. The TEM images are processed to clearly define the granular structure in the recording layer of the perpendicular magnetic medium [16,17,27]. The processed images are then imported in a numerical format as an array of numbers using MATLAB. Another version of the image with grains reduced to 80% of initial size is also numerically processed using MATLAB. The processed image with 100% grain sizes represent the physical CoCrPt grains in the model, while the image with 80% reduced grain sizes represent the magnetic grains in the TEM model. The diameters of the all the magnetic grains in the 80% reduced grain size image is determined. By determining the diameters of the magnetic grains in the TEM image, it makes it possible to control the threshold switching diameter ($d_c$) when using the TEM images in the size-dependent TEM switching model [16,17,27].

As described in Section 3.4.2 of Chapter 3, the physical CoCrPt grains are processed numerically using MATLAB as '1's' and their grain boundaries as '0's'. Similarly the 80% reduced magnetic grains in the TEM model are also numerically processed as '1's' and their grain boundaries as '0's'. At the initial saturated magnetic state (3 T) in Figure 5.21, all the magnetic grains are magnetised along the direction of the field. Therefore by determining the radial average of the product of the fast fourier transforms of the numerically processed TEM images of physical and the magnetic grains, a simulated scattering intensity that fits the experimental scattering data in Figure 5.20 is obtained [16,17,24,27].

By gradually reversing the magnetic field from its initial saturated magnetic state, the size-dependent model is used to predict the switching of the magnetic grains in the perpendicular magnetic medium. The threshold diameter ($d_c$) determines the threshold size below which magnetic grains switch magnetic states. The switched magnetic state of the magnetic grain is numerically processed by assigning switched magnetic grains (80% reduced grain size) with a '-1' in the numerical model.

Figure 5.22, Figure 5.23, Figure 5.24, Figure 5.25, Figure 5.26, Figure 5.27 and Figure 5.28 simulate the scattering intensity at the different reversed magnetic fields. The 'red' coloured magnetic grains in the images represent the initial magnetic state of the grains and as the magnetic field is gradually reversed the size-dependent switched magnetic state of the grain is represented by the colour 'blue' [27]. The colour also denotes the numerical value assigned to the magnetic grains in the model. Magnetic grains coloured 'red' are numerically processed as '1' and magnetic grains coloured 'blue' are processed as '-1' in the model. However the nuclear grains are always processed as '1's' and their boundaries are '0's' in the model. It is evident from the simulations that the size-dependent TEM switching models fit the experimental data as the magnetic field is reversed from its initial saturated state [27].

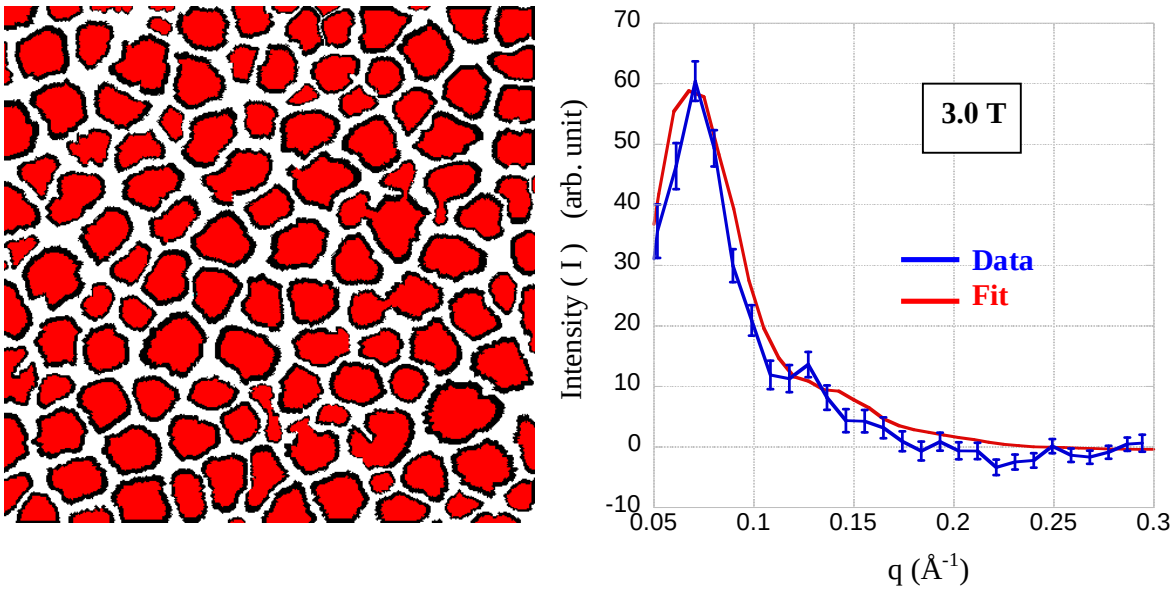


**Figure 5.21** Experimental scattering intensity data $\langle\uparrow|V(\vec{Q})|\uparrow\rangle^2 - \langle\downarrow|V(\vec{Q})|\downarrow\rangle^2$ fitted with the TEM numerical model at 3 T. The initial magnetic state of the grains is denoted by the red grains in the TEM image and the switched magnetic state of the grain is denoted by blue grains.

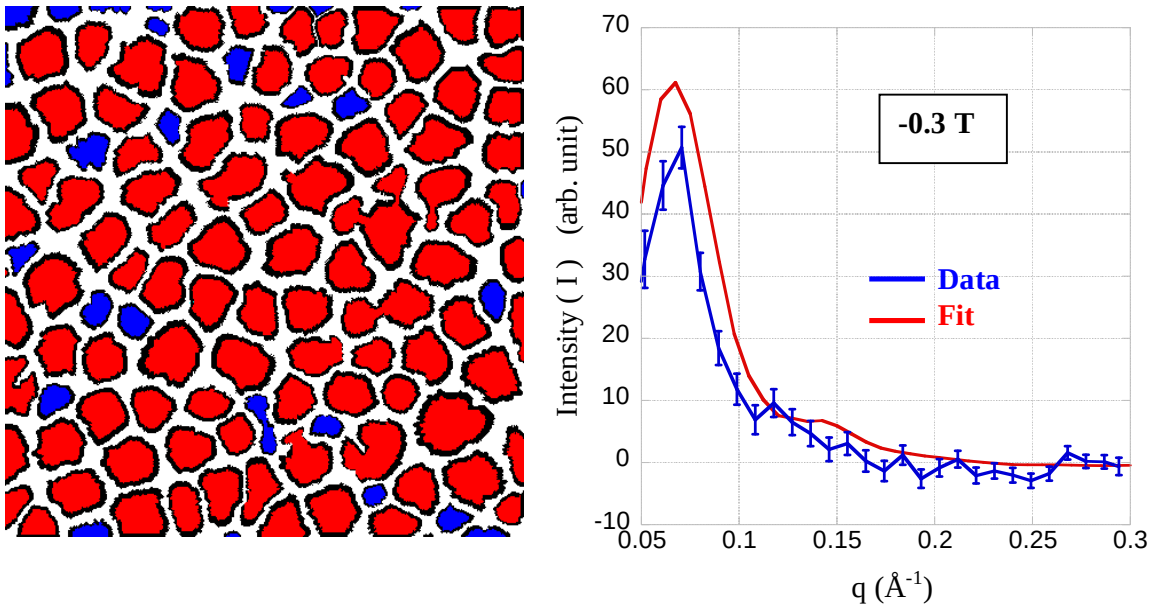


**Figure 5.22** Experimental scattering intensity data $\langle\uparrow|V(\vec{Q})|\uparrow\rangle^2 - \langle\downarrow|V(\vec{Q})|\downarrow\rangle^2$ fitted with the TEM numerical model at -0.3 T. The initial magnetic state of the grains is denoted by the red grains in the TEM image and the switched magnetic state of the grain is denoted by blue grains.

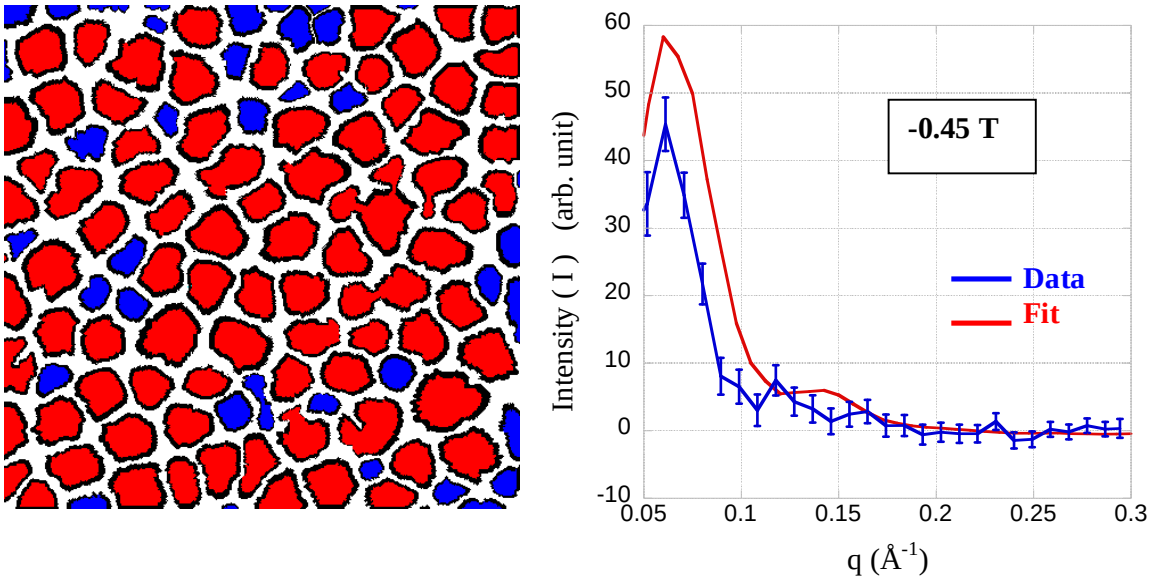


**Figure 5.23** Experimental scattering intensity data $\langle\uparrow|V(\vec{Q})|\uparrow\rangle^2 - \langle\downarrow|V(\vec{Q})|\downarrow\rangle^2$ fitted with the TEM numerical model at -0.45 T. The initial magnetic state of the grains is denoted by the red grains in the TEM image and the switched magnetic state of the grain is denoted by blue grains.

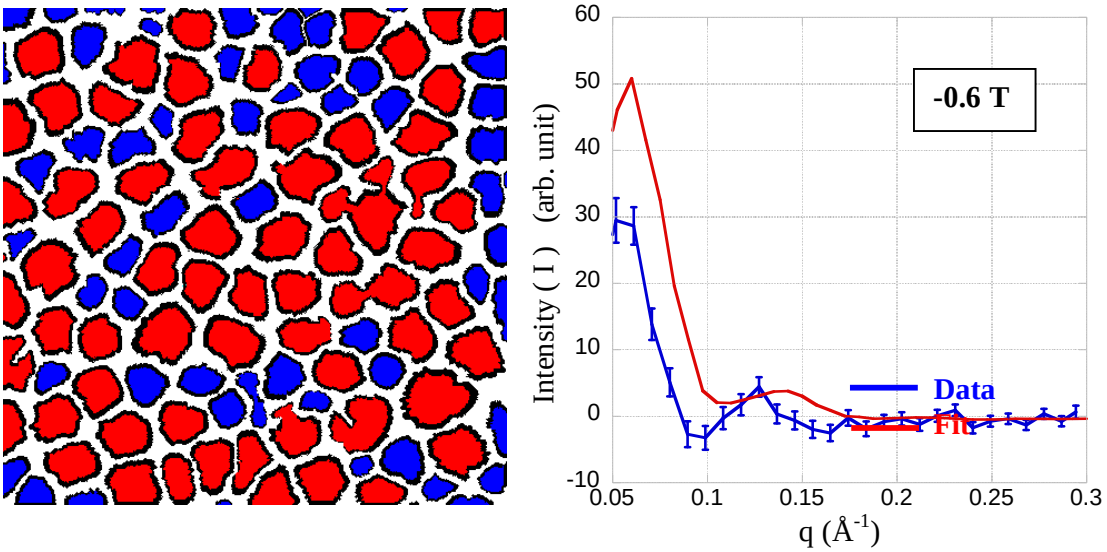


**Figure 5.24** Experimental scattering intensity data $\langle\uparrow|V(\vec{Q})|\uparrow\rangle^2 - \langle\downarrow|V(\vec{Q})|\downarrow\rangle^2$ fitted with the TEM numerical model at -0.6 T. The initial magnetic state of the grains is denoted by the red grains in the TEM image and the switched magnetic state of the grain is denoted by blue grains.

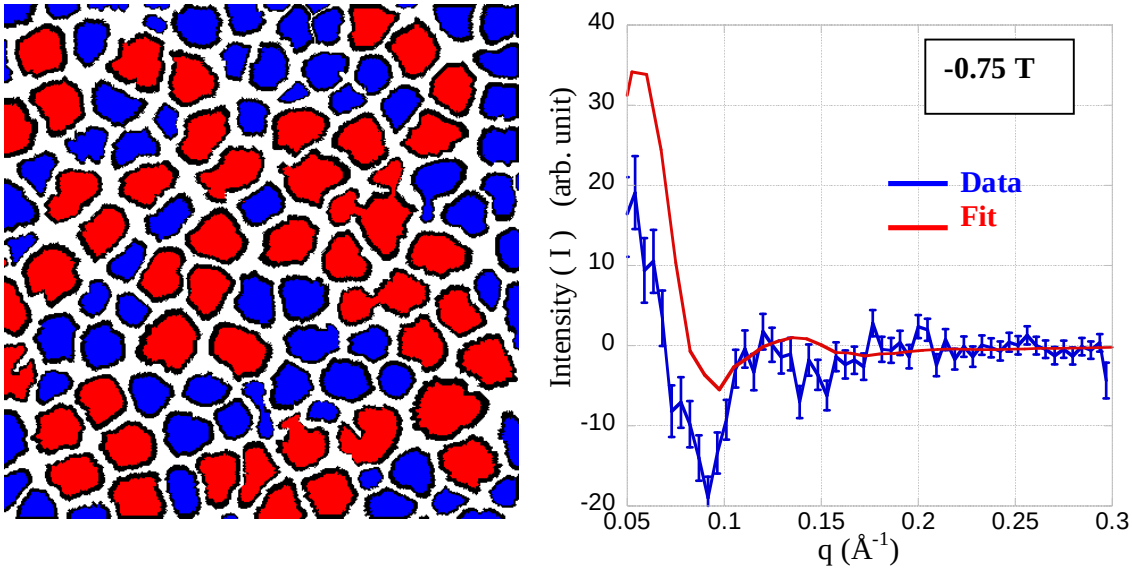


**Figure 5.25** Experimental scattering intensity data $\langle\uparrow|V(\vec{Q})|\uparrow\rangle^2 - \langle\downarrow|V(\vec{Q})|\downarrow\rangle^2$ fitted with the TEM numerical model at -0.75 T. The initial magnetic state of the grains is denoted by the red grains in the TEM image and the switched magnetic state of the grain is denoted by blue grains.

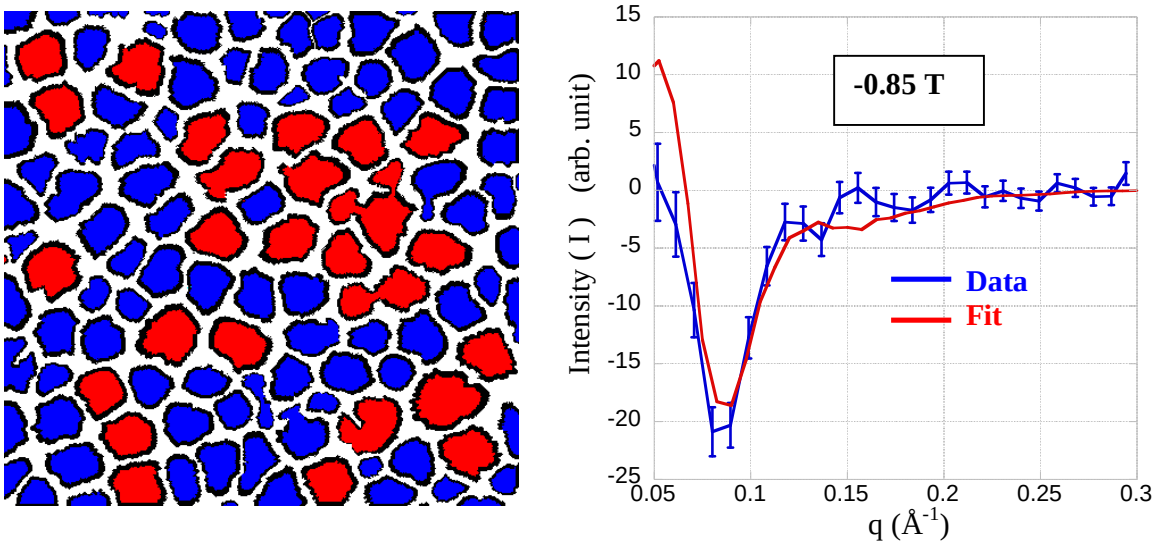


**Figure 5.26** Experimental scattering intensity data $\langle\uparrow|V(\vec{Q})|\uparrow\rangle^2 - \langle\downarrow|V(\vec{Q})|\downarrow\rangle^2$ fitted with the TEM numerical model at -0.85 T. The initial magnetic state of the grains is denoted by the red grains in the TEM image and the switched magnetic state of the grain is denoted by blue grains.

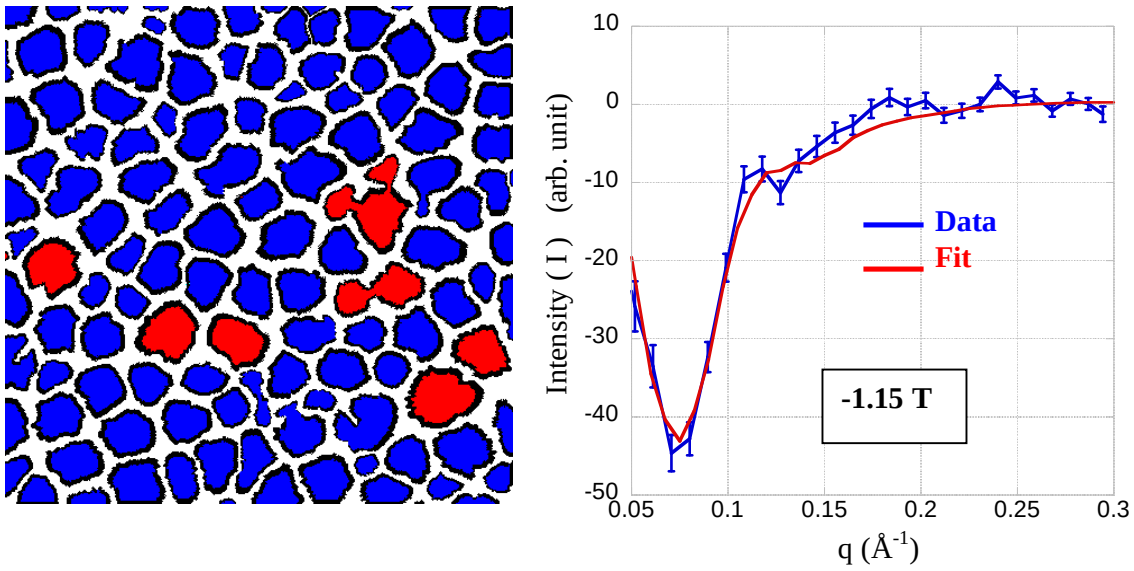


**Figure 5.27** Experimental scattering intensity data $\langle\uparrow|V(\vec{Q})|\uparrow\rangle^2 - \langle\downarrow|V(\vec{Q})|\downarrow\rangle^2$ fitted with the TEM numerical model at -1.15 T. The initial magnetic state of the grains is denoted by the red grains in the TEM image and the switched magnetic state of the grain is denoted by blue grains.

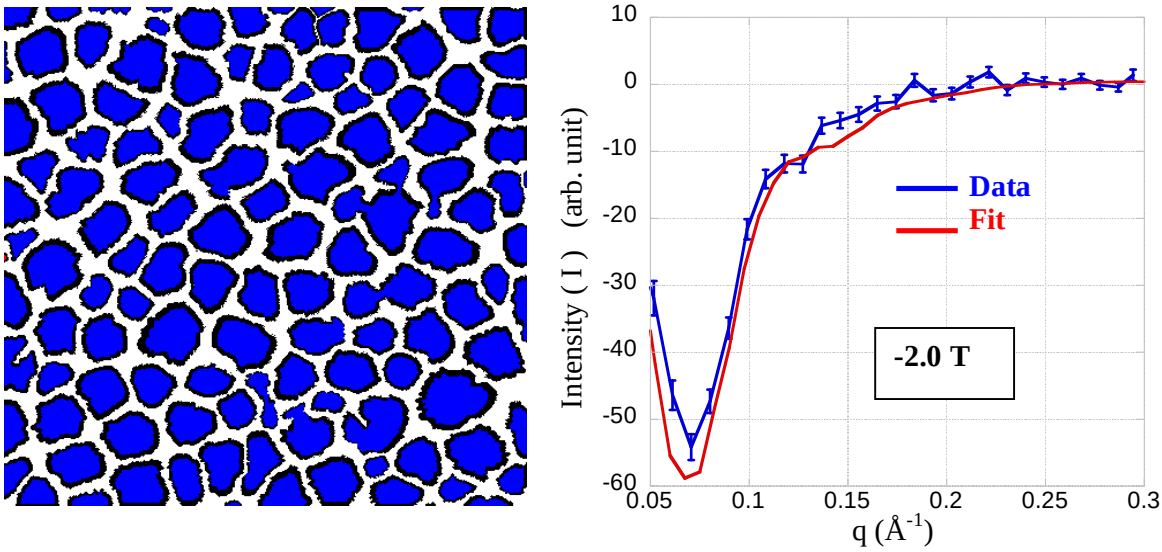


**Figure 5.28** Experimental scattering intensity data $\langle\uparrow|V(\vec{Q})|\uparrow\rangle^2 - \langle\downarrow|V(\vec{Q})|\downarrow\rangle^2$ fitted with the TEM numerical model at -2.0 T. The initial magnetic state of the grains is denoted by the red grains in the TEM image and the switched magnetic state of the grain is denoted by blue grains.

Summarising the analysis, both the analytical models and the TEM numerical model confirm a size-dependent magnetic switching behaviour in the non-interacting exchange decoupled CoCrPt grains present in the recording layer [25]. This is because the CoCrPt grains have well defined oxide grain boundaries that discourage exchange coupling between the grains [3,4,5,25]. However as previously stated, we find that all our models arrive at slightly different average grain sizes resulting in slightly different threshold switching diameters ($d_c$). These results are compared in the next section to better understand them.

### 5.4.3. Comparison of TEM and analytical switching models with Sharrock switching models

Given that the predicted average magnetic grain size determined by the three different models are slightly different, a difference in the predicted threshold switching diameters ($d_c$) at different reversed magnetic fields is observed. On comparing the threshold switching diameters ($d_c$) as a function of magnetic field for the three different models in Table 5.1, a similar trend in the change of the threshold diameter with increasing reversed magnetic field is observed. Figure 5.29 compares the three models and we see that all three models yield a close to linear rise till saturation at 1.5 T.

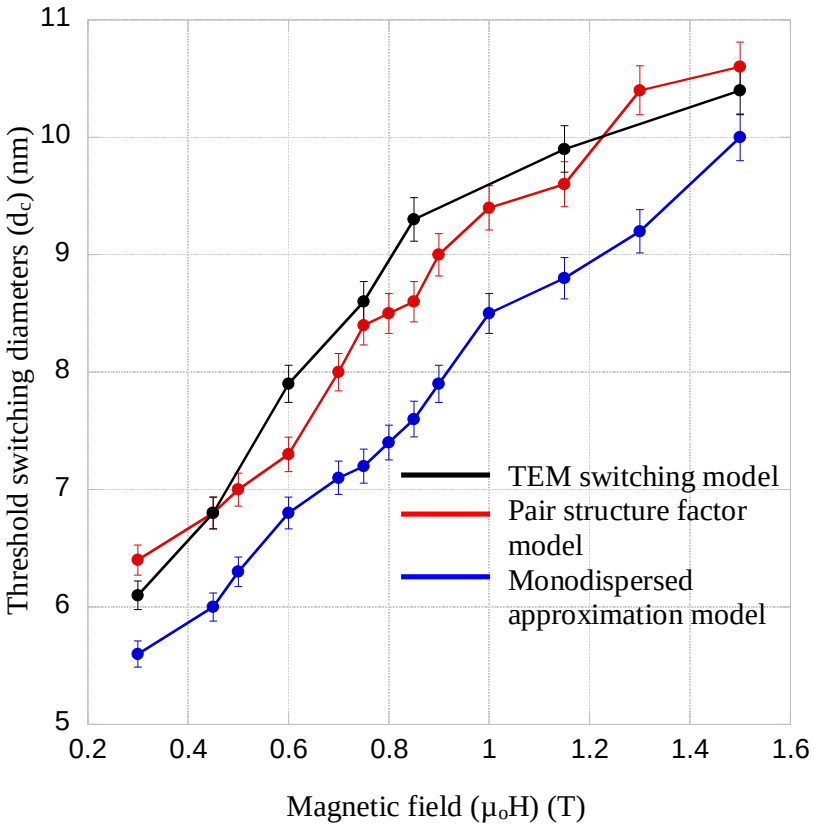


**Figure 5.29** Comparing the threshold switching diameter ($d_c$) at different magnetic fields for TEM and the analytical switching models

**Table 5.1** Table comparing the the threshold switching diameter ($d_c$) at different magnetic fields for the TEM and the analytical switching models

| *Magnetic Field (T)* | *Threshold switching diameter $d_c$ (nm)* | | |
|---|---|---|---|
| | *Pair structure Factor* | *Simple structure factor* | *TEM model* |
| -0.30 | 6.4 | 5.6 | 6.1 |
| -0.45 | 6.8 | 6.0 | 6.8 |
| -0.50 | 7.0 | 6.3 | - |
| -0.60 | 7.3 | 6.8 | 7.9 |
| -0.70 | 8.0 | 7.1 | - |
| -0.75 | 8.4 | 7.2 | 8.6 |
| -0.80 | 8.5 | 7.4 | - |
| -0.85 | 8.6 | 7.6 | 9.3 |
| -0.90 | 9.0 | 7.9 | - |
| -1.0 | 9.4 | 8.5 | - |
| -1.15 | 9.6 | 8.8 | 9.9 |
| -1.3 | 10.4 | 9.2 | - |
| -1.5 | 10.6 | 10.0 | 10.4 |

The next step is the comparison of the linear trends observed from the size-dependent switching models with some magnetic switching theory. The experimental results are compared with theoretical work carried out by Sharrock and Flanders to determine the rate of thermal activation for a non-interacting nanoscale magnetic system based on the Stoner-Wohlfarth switching model [18,19,20].

*Sharrock models*

From theoretical Section 1.3.2 in Chapter 1, the energy barrier ($\Delta E$) for magnetic grain switching is given by Equation 1.16.

$$\Delta E = KV_i\,[1-(H/H_k)]^2 \qquad (1.16)$$

Here $K$ is the perpendicular anisotropy constant, $H_k = 2K/\mu_o M_s$ (Equation 1.10) is the effective perpendicular anisotropy field, $M_s$ the saturation magnetization, and $V_i = \pi r_i^2 t_i$ is the volume of the magnetic grain (for a magnetic grain of radius $r_i$ and thickness $t_i$ ) and H is the applied magnetic field[20].

Now the effective perpendicular anisotropy field $H_k$ could depend on the anisotropy term associated with the threshold magnetic grain switching diameter $d_i$. The reported work presents two analytical models called the simple and modified Sharrock model, with and without a size-dependent anisotropy field term ($H_k$) [20].

**(a) Simple Sharrock model**

The first model called the Simple Sharrock model considers a constant anisotropy term $K$. The anisotropy term $K$ is not size-dependent and it remains constant when considering a system with different grain diameters, like the polydispersed CoCrPt grains in the recording layer [20]. This results in the anisotropy field $H_k = 2K/\mu_o M_s$ remaining constant for different grain diameters ($d_i$).

**(b) Modified Sharrock model**

The Modified Sharrock model, allows the anisotropy field $H_k$ that was initially taken to be a constant to vary with the grain diameter ($d_i$). By using a first order Taylor expansion of $H_k^{(i)}$ around $H_k^{(av)} = H_k(d_{av})$ where $d_{av}$ is the average grain size, we find an approximate linear relation between the grain diameter ($d_i$) and the anisotropy field $H_k$ [20].

The saturation magnetisation ($M_s$) for both models has been determined from the remanence curve data presented in Figure 5.4, obtained using a vector VSM at the University of Manchester, UK. The saturation magnetisation ($M_s$) obtained using vector VSM is 535 emu $cm^{-3}$ [26].

However this magnetisation value needs to be further refined as the recording layer is in principle a non-continuous layer that constitutes a magnetic granular structure, in a non-magnetic medium. The non-magnetic sections in the layer are the oxide boundaries that segregate the magnetic CoCrPt grains in the recording layer [1,17].

The calculated saturation magnetisation ($M_s$) value thereby has in principle contributions from these non-magnetic components and the saturation magnetisation obtained is probably as a result of only 80% of the actual average magnetic grain saturation magnetisation [1,17].

Hence the saturation magnetisation ($M_s$) value when accounting only for the CoCrPt granular structure significantly rises and as a result of this we arrive at an increased average value of about 670 emu $cm^{-3}$, that we consider as the average $M_s$ across the grain[24,25,26]. However $M_s$ determined from neutron experiments show that an $M_s$ as high as 1052 emu $cm^{-3}$ is possible at the core of the grain with the outer region of the grain having an $M_s$ =0 [24].These results are based on our core-shell CoCrPt models, that propose physical CoCrPt grains with magnetic cores [28].

From the theoretical section in Chapter 1, Equation 1.14 determines the rate of switching for an energy barrier ($\Delta E$) with respect to an applied magnetic field (H). By substituting energy barrier ($\Delta E$) for magnetic grain switching (Equation 1.1) in Equation 1.14 the rate of reversal for the Simple and the Modified Sharrock models are determined [20].

$$\lambda(H) = f_0 exp\left(\frac{\Delta E}{k_B T}\right) \tag{1.14}$$

Here $f_o$ is a characteristic frequency that can be written in terms of the characteristic time '$t$' in Equation (1.15) as[20],

$$t = ln\,(2)/\lambda(H)\ (s) \tag{1.15}$$

where the $\lambda(H)$ term here again is determined separately by the size-dependent and the size-independent anisotropic field ($H_k$) models, from their energy barrier for reversals ($\Delta E$). These theoretical models developed based on the vector VSM data are then compared with the size-dependent analytical and numerical magnetic switching models that plot the threshold magnetic switching diameter ($d_c$) as a function increasing magnetic field (H) [13,14,15,16,17,26].

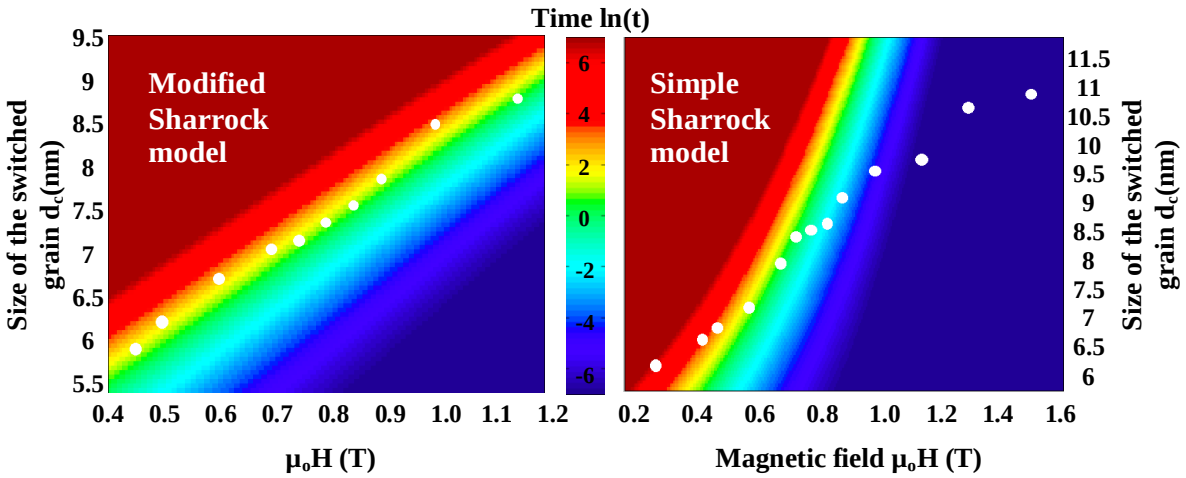


**Figure 5.30** Comparsion of the modified and simple Sharrock models with $d_c(H)$ plots obtained from simulations using the pair structure factor model

Figure 5.30 compares the simple and the modified Sharrock models with the data analysed using the pair structure factor model [15,26]. The modified Sharrock model that is dominated by the linear dependence of the grain diameter ($d_i$) with the anisotropy field $H_k$ is in agreement with the $d_c(H)$ plot determined using the pair structure factor model. The $d_c(H)$ also follows the contours of the experimental time window (~2 hrs) seen as a yellow line on the plot in Figure 5.30 [25,26].

On the other hand, the simple Sharrock model that considers a size-independent anisotropy field ($H_k$) is clearly not in agreement with the $d_c(H)$ determined using the pair structure factor model in Figure 5.30. $d_c(H)$ also determined by using mono approximation model and is compared with the simple and modified Sharrock models to yield a similar analysis in Figure 5.31[14,26]. $d_c(H)$ determined using the mono approximation model matched the linear trend in the modified Sharrock model, but failed to match the results of the simple Sharrock model [25,26].

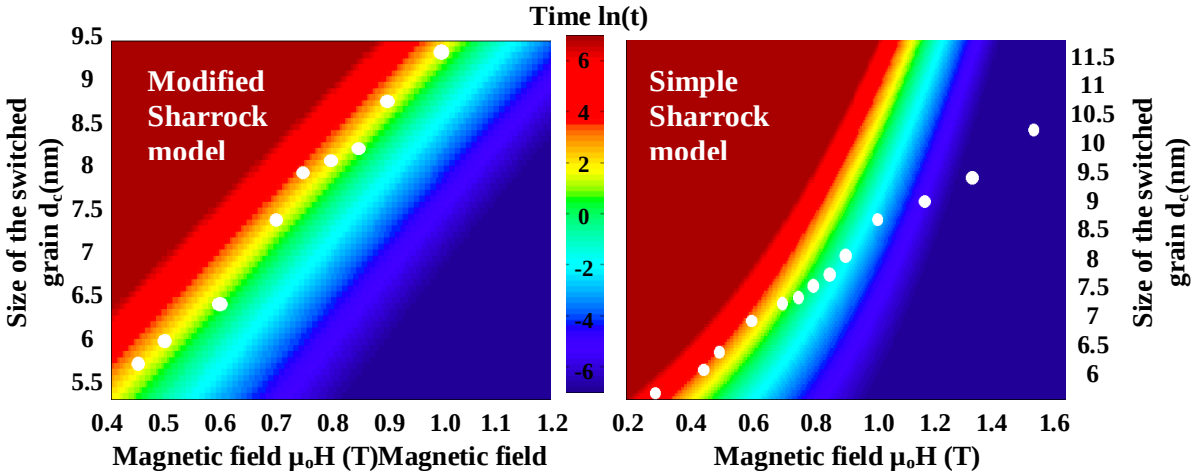


**Figure 5.31** Comparsion of the modified and simple Sharrock models with $d_c(H)$ plots obtained from simulations using the monodispersed approximation model

Figure 5.31 plots the monotonic dependence of the anisotropy field ($H_k$) with the grain diameter (d) that is introduced in the modified Sharrock model using the first order Taylor expansion. This is plotted by determining the values of $H_k$, from mapping of the reversal time in the modified Sharrock models for the mono approximation model and pair structure factor model in Figure 5.30 and Figure 5.31. Figure 5.31 plots $H_k(d)$ for both the mono approximation and pair structure factor model [25].

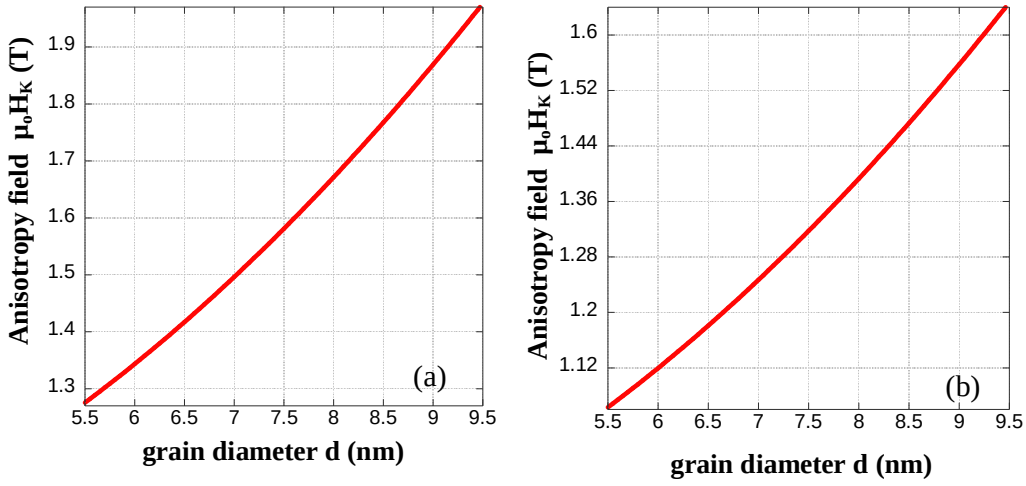


**Figure 5.32 (a)** $H_k(d)$ plot for the mono approximation model. **(b)** $H_k(d)$ plot for the pair structure factor model

The $d_c(H)$ plot determined using the TEM model is also compared with the modified and simple Sharrock models [16,20]. Again the modified Sharrock model that considers a size-dependent anisotropy term was found to best match the linear trend observed in the $d_c(H)$ plot. The simple Sharrock model failed to match this linear trend, suggesting that grain size-dependent anisotropy is dominant in the magnetic switching of the grains [25]. The improved mapping of the reversal field in the modified Sharrock model in Figure 5.33 yields the anisotropy field term ($H_k$) with its derivatives that is then used in the first order Taylor expansion to plot the monotonic dependence of the anisotropy field with the grain diameter in Figure 5.34.

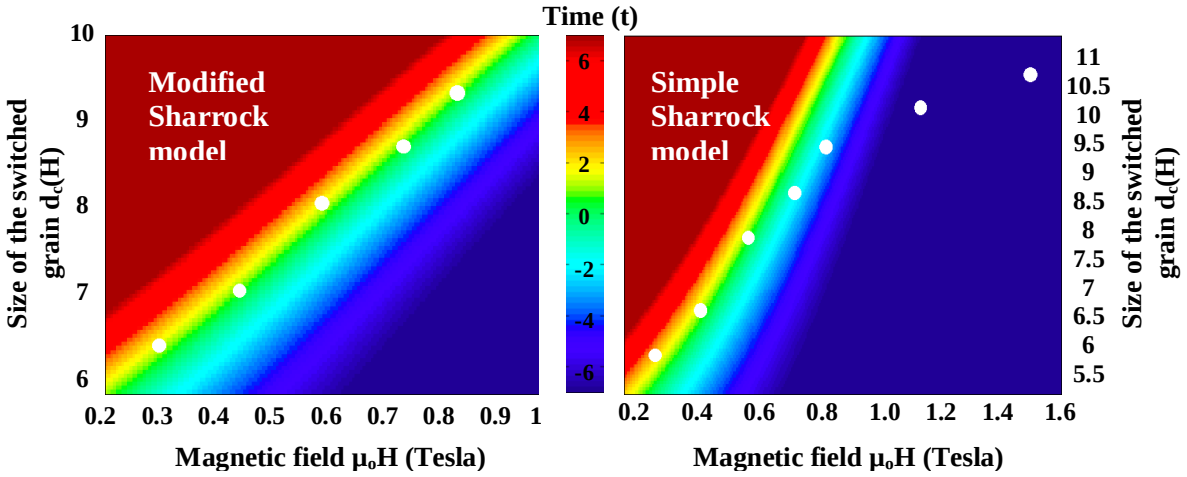


**Figure 5.33** Comparsion of the modified and simple Sharrock models with $d_c(H)$ plots obtained from simulations using the TEM model

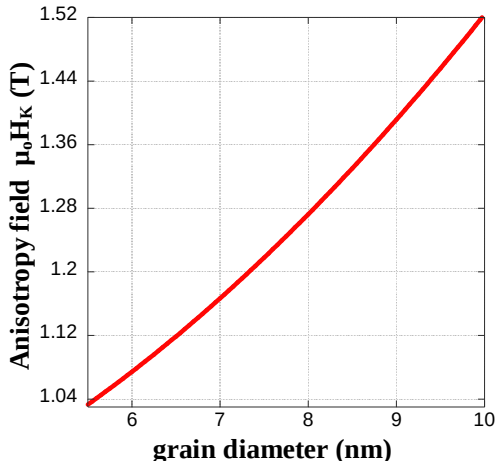


**Figure 5.34** Monotonic dependence of $H_k(d)$ plot for the TEM model

From the analysis it is clear that for the $d_c(H)$ plots determined using the mono approximation, pair structure factor and the TEM models, the modified Sharrock model that considers a size-dependent anisotropy best matches the experimental results [25]. This strongly supports the hypothesis that the anisotropy field ($H_k$) scales with grain size, and larger grains with higher anisotropy fields ($H_k$) require stronger magnetic fields to switch magnetic states [25].

## 5.5 Conclusion

To summarise the reported works first shows a change in scattering intensity as the magnetic field is gradually reversed in the direction opposite to the initial magnetic saturation direction [25]. This is as a result of switching of the magnetic grains in the recording layer of the perpendicular magnetic medium [25].

To determine if this switching is size-dependent the two analytical models and the numerical TEM model are used to analyse the magnetic switching process in the CoCrPt grains of the recording layer [13,14,15,16]. All three models predict a linear dependence of $d_c(H)$ and produce closely matched simulated fits to the experimental data at increasing magnetic fields (H) [25]. All three models also consider, a non- interacting exchange decoupled system of CoCrPt grains, well segregated in an oxide matrix [3].

The linear $d_c(H)$ plots obtained using the two analytical models and the TEM numerical model are then compared to theoretical work on the time dependent magnetic switching work by Sharrock and Flanders [20]. The modified Sharrock model that accounts for a size-dependent anisotropic magnetic field ($H_k$) term, best matches the $d_c(H)$ plots obtained using the two analytical models and the TEM numerical model [25]. The monotonic dependence of anisotropy field ($H_k$) with magnetic grain diameter is also plotted, showing that the anisotropy field ($H_k$) scales with magnetic grain sizes.

In conclusion, this chapter shows that all the analysis carried out on the magnetic switching of the CoCrPt grains in the recording layer suggest a size-dependent magnetic grain switching, with smaller magnetic grains switching at lower fields with a monotonic dependence of the grain diameter on the anisotropic magnetic field ($H_k$) shown using the modified Sharrock model [25].

## 5.6 References


[1] S. N. Piramanayagam “Perpendicular recording media for hard disk drives” J. Appl. Phys. 102, 011301 (2007) (DOI: 10.1063/1.2750414)

[2] Steffen Porthun, Leon Abelmann, Cock LodderO’Grady “Magnetic force microscopy of thin film media for high density magnetic recording”Journal of Magnetism and Magnetic Materials, 182(1–2), (1998)p.238-273 (DOI: 10.1016/S0304-8853(97)01010-X)

[3] Naoki Honda, Kazuhiro Ouchi“Low noise design of perpendicular magnetic recording media”Journal of Magnetism and Magnetic Materials, 235(1–3), (2001)p.289-296(DOI: 10.1016/10.1016/S0304-8853(01)00360-2)

[4] S.J. Greaves, A.M. Goodman, H. Muraoka, Y. Nakamura “Exchange coupling and grain-size distributions in perpendicular recording media”Journal of Magnetism and Magnetic Materials, 287, (2005)p.66-71 (DOI: 10.1016/j.jmmm.2004.10.009)

[5] Yasuo Tateno, Kazuharu Iwasaki “Interparticle interaction and magnetic anisotropy in vacuum evaporated Co–O perpendicular magnetic thin film”Journal of Magnetism and Magnetic Materials, 235(1–3), 2001 p.153-158(DOI: 10.1016/S0304-8853(01)00328-6)

[6] X.W. Wu, H. Zhou, R.J.M. van de Veerdonk, T.J. Klemmer, D. Weller “Measurement of the magnetic easy axis dispersion in perpendicular media” Journal of Magnetism and Magnetic Materials, 278(1–2), (2004) p. 285-288 (DOI: 10.1016/j.jmmm.2003.12.1388)

[7] A. Lyberatos “The switching time of the magnetization in perpendicular recording media” Journal of Magnetism and Magnetic Materials, 246(1–2), (2002) p.303-309 (DOI: 10.1016/S0304-8853(02)00098-7)

[8] J.D. Dutson, D. Litvinov, M.R.J. Gibbs, Y. Inaba, H. Muraoka, K. O’Grady “Magnetisation reversal in media with perpendicular anisotropy”Journal of Magnetism and Magnetic Materials, 304(1), (2006)p.51-54(DOI: 10.1016/j.jmmm.2006.02.003)

[9] D. Suess, T. Schrefl, W. Scholz, J. Fidler“Fast switching of small magnetic particles”Journal of Magnetism and Magnetic Materials, 242–245(1), (2002), p.426-

429(DOI: 10.1016/S0304-8853(01)01140-4)

[10] J. Kohlbrecher, W. Wagner “The new SANS instrument at the Swiss spallation source SINQ”, J. Appl. Cryst. 33, (2000) p.804-806 (DOI:10.1107/S0021889800099775)

[11] TakehitoShimatsu, Hiroyuki Uwazumi, Hiroaki Muraoka, Yoshihisa Nakamura “Thermal stability in perpendicular recording media”Journal of Magnetism and Magnetic Materials, 235(1–3), (2001)p.273-280(DOI: /10.1016/S0304-8853(01)00358-4)

[12] L. He, W.D. Doyle, L. Varga, H. Fujiwara, P.J. Flanders “High-speed switching in magnetic recording media”Journal of Magnetism and Magnetic Materials, 155(1–3), (1996) p.6-12(DOI: /10.1016/0304-8853(96)00652-X,)

[13] A. Guinier, G. Fournet “Small-Angle Scattering of X-Rays” John Wiley and Sons, New York (1955) (DOI: 10.1002/pol.1956.120199326)

[14] N.W. Ashcroft, J. Lekner “Structure and Resistivity of Liquid Metals” Phys. Rev. (145), (1966) p. 83–90 (DOI:10.1103/PhysRev.145.83)

[15] W.L. Griffith, R. Triolo, A.L. Compere “Analytical scattering function of a polydispersePercus-Yevick fluid with Schulz- ( Gamma -) distributed diameter” Phys Rev A, 35(5), (1987) p. 2200–2206 (DOI: 10.1103/PhysRevA.33.2197)

[16] R. Araki, Y. Takahashi,I.Takekuma,S. Narishige “High-Resolution TEM Analysis of Perpendicular CoCrPt-$SiO_2$ Media”IEEE Transactions on magnetics, 44(11), (2008) p.3496 – 3498 (DOI: 10.1109/TMAG.2008.2002415)

[17] M.Futamoto, N.Inaba, Y. Hirayama, K. Ito, Y. Honda “Microstructure and micromagnetics of future thin-film media” Journal of Magnetism and Magnetic Materials, 193(1–3),(1999)p. 36-43 (DOI: 10.1016/S0304-8853(98)00492-2)

[18] E.C. Stoner, E.P. Wohlfarth“A mechanism of magnetic hysteresis in heterogeneous alloys” Philosophical Transactions of the Royal Society A: Physical, Mathematical and Engineering Sciences, 240 (826), (1948)p.599–642 (DOI:

10.1109/TMAG.1991.1183750)

[19] C.Tannous, J.Gieraltowski“The Stoner–Wohlfarth model of ferromagnetism” Eur. J. Phys. 29 475, (2008)(DOI:10.1088/0143-0807/29/3/008)

[20] P. J. Flanders, M. P. Sharrock“An analysis of time-dependent magnetization and coercivity and of their relationship to print-through in recording tapes” J. Appl. Phys. 62, 2918 (1987)(DOI:10.1063/1.339373)

[21] Dmitri Litvinov, Mark H Kryder, SakhratKhizroev“Recording physics of perpendicular media: soft underlayers” Journal of Magnetism and Magnetic Materials, 232(1–2), (2001) p.84-90(DOI:10.1016/S0304-8853(01)00216-5)

[22] Dmitri Litvinov, Mark H Kryder, SakhratKhizroev“Recording physics of perpendicular media: hard layers” Journal of Magnetism and Magnetic Materials, 241(2–3), (2002) p.453-465(DOI:10.1016/S0304-8853(02)00023-9)

[23] Chun-Tao Xiao, Yuki Inaba, TakehitoShimatsu, Hiroaki Muraoka“Microstructure, magnetic properties and their seed layer thickness dependences of granular CoPtCr–SiO2 perpendicular recording media” Solid State Communications, 144 (1–2), (2007), p.58-60(DOI:10.1016/j.ssc.2007.07.014)

[24] S. J. Lister, M. P. Wismayer, V. Venkataramana, M. A. de Vries, S. J. Ray, S. L. Lee, T. Thomson, J. Kohlbrecher, H. Do, Y. Ikeda, K. Takano, and C. Dewhurst“Small-angle polarized neutron studies of perpendicular magnetic recording media” Journal of Applied Physics, 106(6),(2009) p. 063908 - 063908-4 (DOI: 10.1063/1.3213381)

[25] S. J. Lister, T. Thomson, J. Kohlbrecher, K. Takano, V. Venkataramana, S. J. Ray, M. P. Wismayer, M. A. de Vries, H. Do, Y. Ikeda, and S. L. Lee “Size-dependent reversal of grains in perpendicular magnetic recording media measured by small-angle polarized neutron scattering” Applied Physics Letters, 97 (11), (2010) (DOI: 10.1063/1.3486680)

[26] T. Thomson, B. Lengsfield, H. Do, B. Terris “Magnetic anisotropy and reversal mechanisms in dual layer exchanged coupled perpendicular media” Journal of Applied

Physics, 103(7), (2008) (DOI:10.1063/1.2839310)

[27] S.J. Lister, J. Kohlbrecher, V. Venkataramana, T. Thomson, K. Takano, and S.L. Lee, "Analysing SANS data to determine magnetisation reversal processes in composite perpendicular magnetic recording media using TEM images" International Journal of Materials Research 102(9) (2011) p.1142-1146. (DOI: 10.3139/146.110562)

[28]G. Choe, S.J. Chung, R.M. Walser"Correlation between grain morphologies and magnetic properties of CoCrPtCr thin films" Thin Solid Films, 259(2), (1995) p.231-236 (DOI: 10.1016/0040-6090(94)06438-5)

# Chapter 6

# Investigating the effect of the exchange coupled composite (ECC) layer on the perpendicular recording medium using PolSANS

---

**Contents**



---


**Abstract** This chapter investigates the properties and the role of the recently introduced exchange coupled composite (ECC) magnetic layer in perpendicular recording media. This chapter investigates the difference in properties between the ECC layer and recording layer, by comparing the interference term of the nuclear and magnetic scattering obtained in a PolSANS experiment, 'with' and 'without' the use of an ECC layer on perpendicular magnetic media. Once this is established the influence of the ECC layer on the magnetic switching process is investigated using the size-dependent analytical switching models introduced in Chapter 5. The threshold switching diameters ($d_c$) at different reversed fields are compared 'with' and 'without' an ECC layer and the results obtained are interpreted using theoretical magnetic switching models proposed by Sharrock *et al*.

## 6.1 Background and Introduction

The exchange coupled composite (ECC) layer is designed to be a magnetically softer than the recording layer and is sputtered above the recording layer in perpendicular recording media [1,2]. The ECC layer is designed to exchange couple with the recording layer magnetising high anisotropy CoCrPt grains in the recording layer at smaller magnetic write fields [2,3].

The magnetically softer ECC layer is composed of a CoCrPt alloy and it is not known if the ECC layer has a nanoscale grain formation like that observed in the recording layer of perpendicular magnetic media [1,4]. In the recording layer, the oxide present in the CoCrPt-Oxide alloy plays an important role in the CoCrPt grain segregation [4,5]. This chapter investigates the possible existence of a similar grain formation in the ECC layer of the perpendicular recording media. The grain related magnetic properties in the ECC layer are investigated using the PolSANS experimental geometry [6]. The PolSANS experiments would give the interference between the nuclear and magnetic scattering from any grain formation in the ECC layer in the perpendicular magnetic medium [6]. PolSANS results from samples 'with' and 'without' an ECC layer in perpendicular magnetic media are compared to investigate the contribution of the ECC layer to the nuclear and magnetic scattering interference term. These experiments are expected to determine the presence of nanoscale granular structures in the ECC layer.

The next scientific question investigated in this chapter is the influence of the ECC layer on the size-dependent magnetic grain switching in the recording layer [7,8,9]. By applying a magnetic field, the magnetic grain switching in the recording layer 'with' and 'without' an ECC layer are compared using size-dependent analytical switching models and the change in the threshold switching diameter ($d_c$) 'with' and 'without' the presence of an ECC layer is investigated [10,11,12]. This comparison helps draw conclusions on the role of the ECC layer in the magnetic grain switching process in the recording layer. These results are compared with theoretical simulations that investigate the effect of size-dependent anisotropies on magnetic grain switching with a simple thermal activation model [13,14,15].

## 6.2 Samples and Preparation

The samples for this experiment were sputtered at Hitachi Global Storage Technologies (GST) San Jose research centre, California (USA). The sample is identified by Hitachi GST as C9 – 'FS' sample and constitutes an ECC layer sputtered above the recording layer. The thin film structure comprises the silicon substrate, soft under layers (SUL), seed layers, the recording layer (RL) and an ECC layer above the recording layer [1,4]. The SUL has a thickness of around 100 nm that comprises two layers (each ~50 nm) of FeCo, anti-ferromagnetically coupled using a thin (~1 nm) ruthenium layer. The SUL is followed by a seed layers comprising ruthenium with other intermediate layers to thicknesses of around 20 nm. The seed layers are then followed by a CoCrPt+Oxide RL with a thickness of 11 nm. Finally a 6 nm thick ECC layer of a CoCrPt-alloy is sputtered as shown in Figure 6.1.

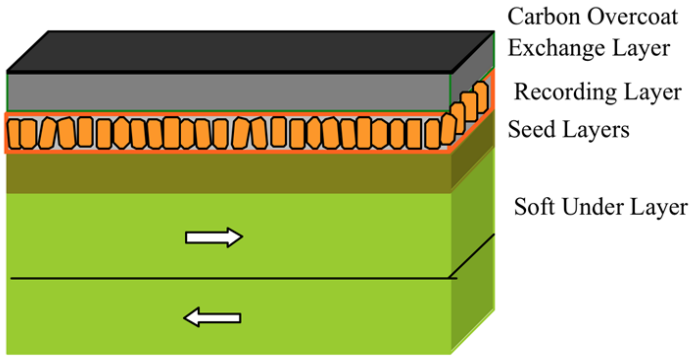


**Figure 6.1** A graphic illustration of the C9 – 'FS' sample structure

A stack of 10 samples are placed in a sample holder as described in Section 3.2 of Chapter 3. The sample holder is then mounted on the sample stick before being placed in the cryostat.

## 6.3 Experiment

The cryostat temperature is set at 250 K and magnetic field is set to 0 T. The detector and the collimator are set to fix the experimental q range [16]. The geometry of the sample is such that the plane of the thin film is perpendicular to the neutron beam and the magnetic field applied is along the direction of the neutron beam, perpendicular to the plane of the film. The magnetic field is then set at 3 T and a PolSANS experiment is performed as described in Section 3.3 of Chapter 3[16,6]. At a magnetic field of 3 T, the CoCrPt grains in the recording layer saturate along the direction of the magnetic field [6]. Similarly the ECC layer also (with or without the presence of a granular structure) saturates along the direction of the magnetic field [7,8]. The incoming 'spin up' and 'spin down' polarised neutrons are scattered by the sample as shown in Figure 6.2. The difference in their scattering intensities shown in Figure 6.3, gives the product of nuclear and magnetic scattering expressed in terms of form and structure factors [6].

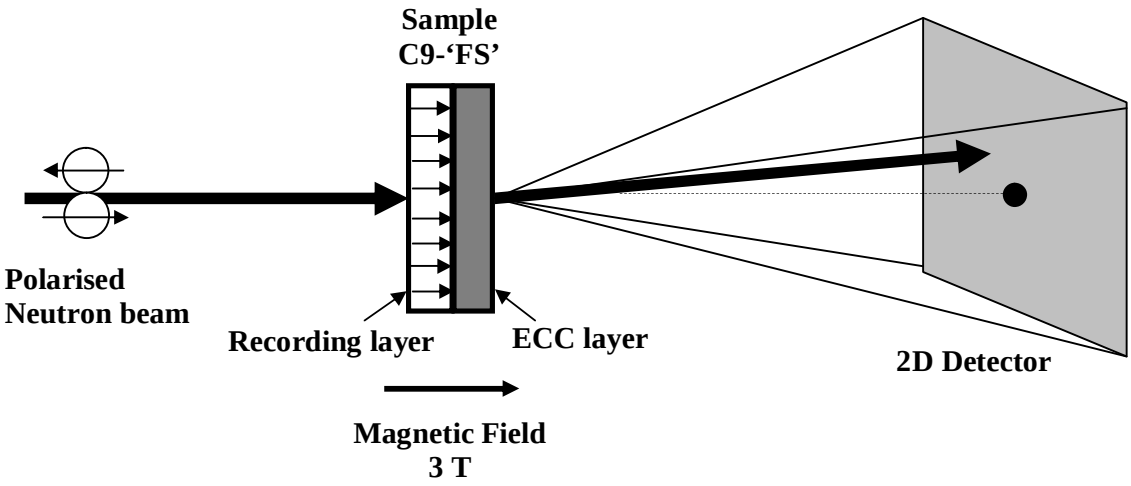


**Figure 6.2** Scattering diagram illustrating the geometry in a PolSANS experiment for the C9-'FS' sample[6]

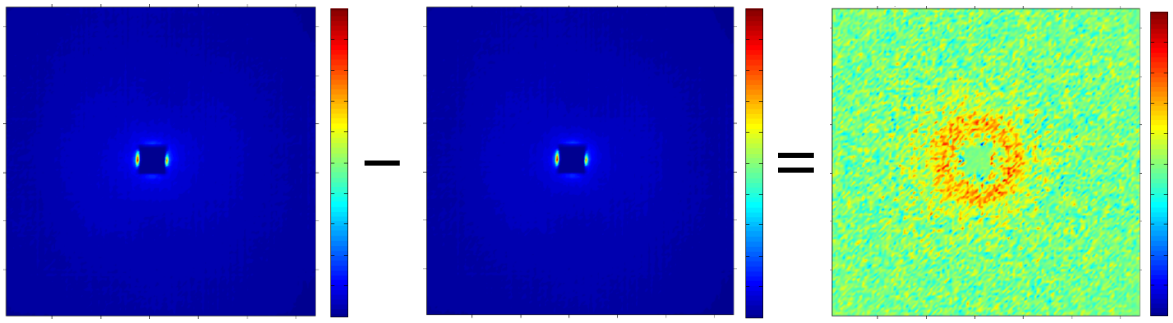


**Figure 6.3** The difference between the ‘spin up’ and ‘spin down’ scattering extracted using the GRASP software. The images depict the scattering intensity across the detector when the difference between the spin up and spin down scattering was obtained for the C9-‘FS’ sample in the PolSANS experiment [17]

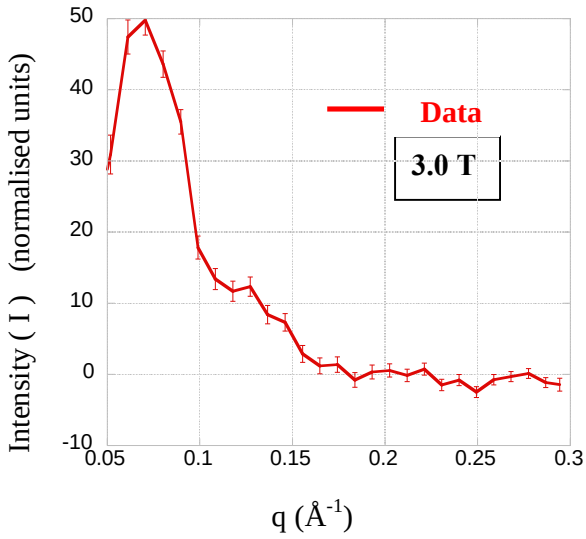


**Figure 6.4** Experimental scattering intensity data $\langle\uparrow|V(\vec{Q})|\uparrow\rangle^2 - \langle\downarrow|V(\vec{Q})|\downarrow\rangle^2$ as a function of ‘q’ for the C9-FS sample at an applied field of 3 T [6]

Figure 6.4 shows the experimental scattering intensity as a function of ‘q’, extracted by obtaining the difference between the ‘spin up’ and ‘spin down’ polarised neutrons scattered off the C9-‘FS’ sample stack at the 3 T magnetic field [6]. The difference in intensities for the ‘spin up’ and ‘spin down’ scattering can be interpreted as an interference term of the nuclear and magnetic scattering and can be further understood in terms of form and structure factors [6]. Analysing this data would not just give an interference term of nuclear and magnetic scattering from the granular structure present in the recording layer, but would but also shed light on any structure and their resulting magnetic properties in the ECC layer of the perpendicular magnetic medium (should any exist in this ‘q’ – range) [6].

On determining the physical and magnetic properties of the ECC layer at 3.00 T, the experiments investigate the role of the ECC layer in the magnetic switching of the CoCrPt grains in the perpendicular magnetic medium[2,8]. Similar to the experiments carried out in Section 5.3 of Chapter 5, the magnetic field is gradually reversed and PolSANS experiments are carried out at the different reversed fields to investigate the magnetic properties of the CoCrPt grain in the thin film medium [18].

PolSANS experiments were carried out at magnetic fields of 0.025 T, -0.100 T, -0.300 T, -0.450 T, - 0.550 T, -0.650 T, -0.750 T, -0.850 T and -1.000 T to observe how the CoCrPt grains switch in the magnetic medium from their initial saturated magnetic state at 3.000 T [18]. The results obtained are analysed and explained in Section 6.4.

## 6.4 Results and Analysis

The experimental data in this chapter is analysed using the mono approximation model and the pair structure factor model described in Section 3.4.1 of Chapter 3 [10,11,12]. A size-dependent switching model used in Section 5.4.1 of Chapter 5 to analyse the magnetic switching of the CoCrPt grains in the recording layer, has been used to analyse the magnetic switching data of the C9-'FS' sample at different magnetic fields [18].

### 6.4.1. Investigating structure in the ECC layer

The first experiment is to investigate the contribution to the magnetic and nuclear scattering interference term from the ECC layer in the C9-'FS' samples. The experimental scattering intensity data at 3.00 T is obtained by radially averaging the difference in scattering intensity between the 'spin up' and 'spin down' scattering at 3.00 T [6]. The intensity is plotted as a function of 'q' giving us the experimental data seen in Figure 6.4. On closely observing the shape and scattering intensity for the C9-'FS' sample in Figure 6.4, a striking resemblence to the scattering intensity peak observed in C9-'Oxide only' sample is evident, with both having similar scattering intensities.

From Figure 6.5, it is evident that at a magnetic field of 3.00 T, very little difference in scattering is observed between C9-'Oxide only' and C9-'FS' samples. We know that the C9-'Oxide only' sample is very similar in structure to C9-'FS' sample with the only difference being the absence of the ECC layer in the C9-'Oxide only' sample. Therefore the similarities in the data, obtained with and without the presence of an ECC layer suggests that there exists no contribution to the interference of the nuclear and magnetic scattering term from the ECC layer in this experimental q range [1,2,3].

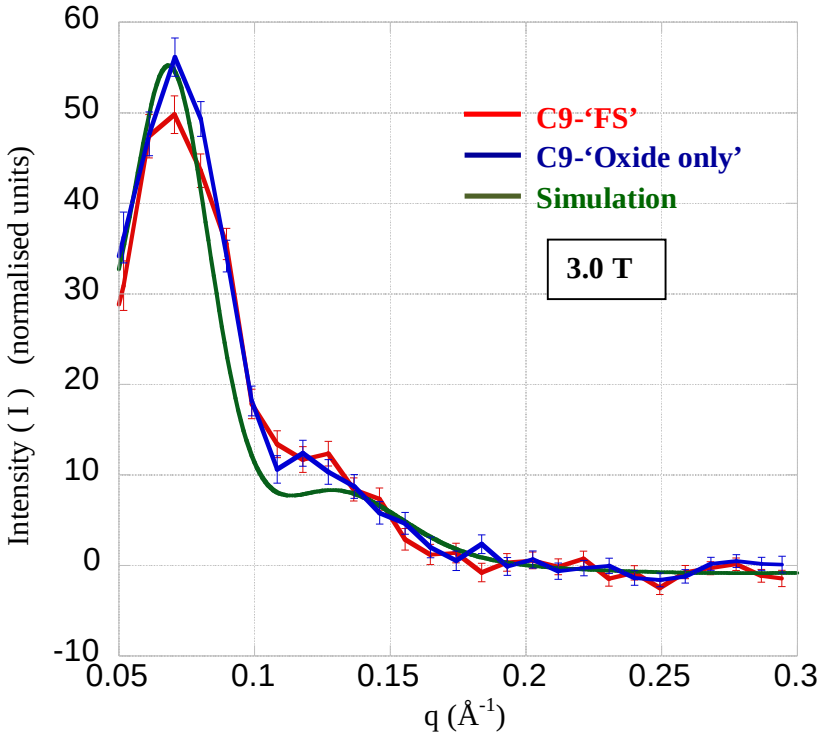


**Figure 6.5** Experimental scattering intensity data $\langle\uparrow|V(\vec{Q})|\uparrow\rangle^2 - \langle\downarrow|V(\vec{Q})|\downarrow\rangle^2$ as a function of 'q' for the C9-'FS' and C9-'Oxide only' samples fitted with a simulation from the mono approximation model [11]

The scattering intensity observed is from the CoCrPt grains in the recording layer, with no significant scattering contribution from the ECC layer of the perpendicular magnetic medium. The scattering intensity for the C9-'FS' sample, is analytically simulated using the mono approximation model, used for the C9-'Oxide only' sample. The mono approximation model predicts an average physical grain diameter of 8.0±0.1 nm, average magnetic grain diameter of 6.4±0.1 nm, magnetic grain diameter to physical grain diameter ratio of 0.8 and the an average inter-granular distance of 8.8±0.5 nm [11]. These results are extracted from the interference of the nuclear and magnetic scattering from the CoCrPt grains in the recording layer, using the mono approximation model [11].

Although this experiment rules out any contribution from the ECC layer to the interference of the nuclear and magnetic scattering term in this q-range, it is incorrect to state that there exists no granular structure in the ECC layer. The PolSANS experimental geometry is only sensitive to the interference term of the nuclear and magnetic scattering, and to investigate the presence of any granular structure in the ECC layer, a conventional SANS experiment should performed [6,19].

### 6.4.2. Grain switching analysed using analytical models

The literature suggests that the magnetically softer ECC layer influences CoCrPt magnetic grain switching in the recording layer [1,2,3,7,8]. To investigate the effect of the ECC layer on the magnetic switching in the recording layer, PolSANS experiments at different magnetic fields along the hysteresis loops are carried out [18]. This is achieved by saturating the magnetic grains with a magnetic field of 3 T and then gradually reversing the direction of the field in small steps. PolSANS experiments are carried out at 0.025 T, -0.100 T, -0.300 T, -0.450 T, -0.550 T, - 0.650 T, -0.750 T, -0.850 T and -1.000 T [18]. The scattering intensity obtained by taking the difference between the 'spin up' and 'spin down' scattering is plotted in Figure 6.6 (a), for the different experimental magnetic fields. The scattering intensities of C9-'Oxide only' and C9-'FS' sample are compared at different magnetic fields in Figure 6.6 (b), Figure 6.7 (a), Figure 6.7 (b), Figure 6.8 (a) and Figure 6.8 (b) [18].

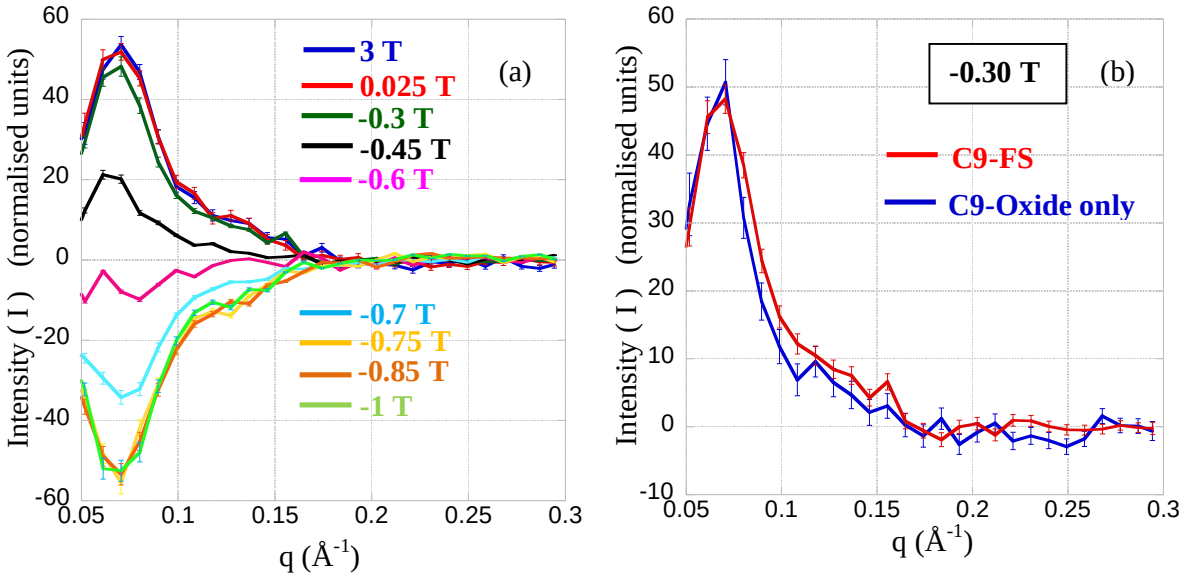


**Figure 6.6 (a)** Experimental scattering intensity data $\langle\uparrow|V(\vec{Q})|\uparrow\rangle^2 - \langle\downarrow|V(\vec{Q})|\downarrow\rangle^2$ as a function of 'q' for the C9-'FS' compared at 3 T, 0.025 T, -0.1 T, -0.3 T, -0.45 T, -0.55 T, -0.65 T, -0.75 T, -0.85 T and -1.0 T **(b)** Experimental scattering intensity data $\langle\uparrow|V(\vec{Q})|\uparrow\rangle^2 - \langle\downarrow|V(\vec{Q})|\downarrow\rangle^2$ as a function of 'q' at -0.3 T compared between the C9-'Oxide only' and C9-'FS' samples

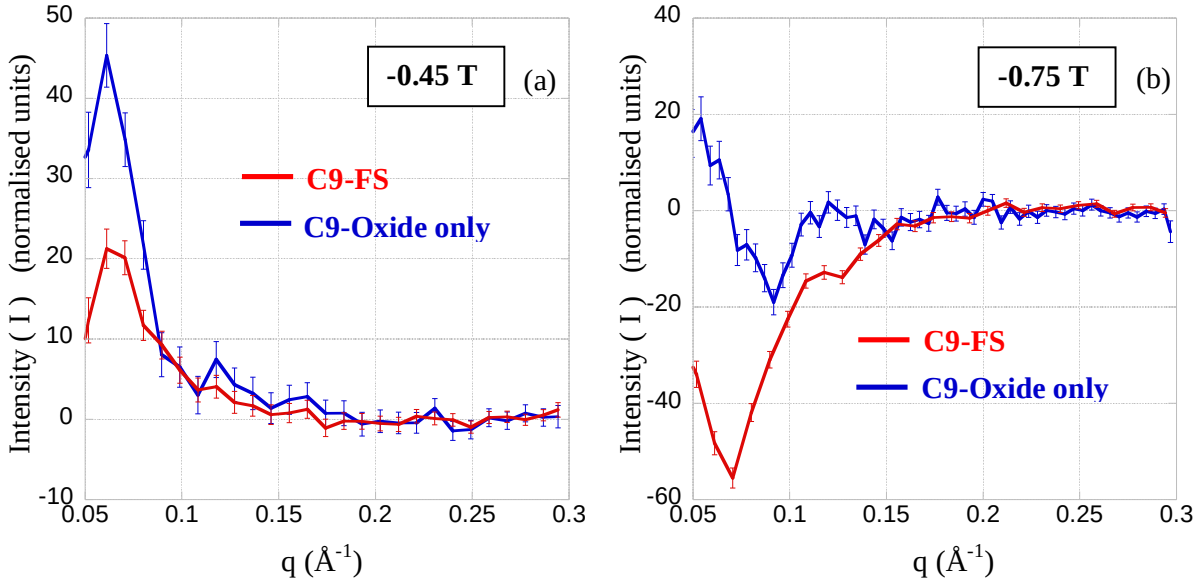


**Figure 6.7 (a)** Experimental scattering intensity data $\langle\uparrow|V(\vec{Q})|\uparrow\rangle^2 - \langle\downarrow|V(\vec{Q})|\downarrow\rangle^2$ as a function of 'q' at -0.45 T compared between the C9-'Oxide only' and C9-'FS' samples **(b)** Experimental scattering intensity data $\langle\uparrow|V(\vec{Q})|\uparrow\rangle^2 - \langle\downarrow|V(\vec{Q})|\downarrow\rangle^2$ as a function of 'q' at -0.75 T compared between the C9-'Oxide only' and C9-'FS' samples

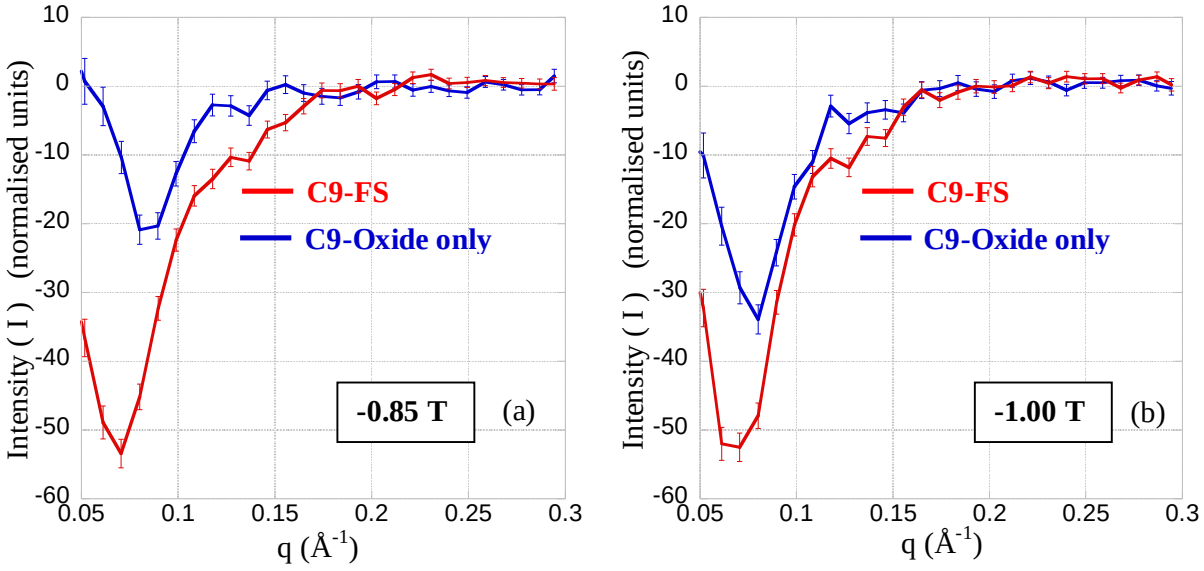


**Figure 6.8 (a)** Experimental scattering intensity data $\langle\uparrow|V(\vec{Q})|\uparrow\rangle^2 - \langle\downarrow|V(\vec{Q})|\downarrow\rangle^2$ as a function of 'q' at -0.85 T compared between the C9-'Oxide only' and C9-'FS' samples **(b)** Experimental scattering intensity data $\langle\uparrow|V(\vec{Q})|\uparrow\rangle^2 - \langle\downarrow|V(\vec{Q})|\downarrow\rangle^2$ as a function of 'q' at -1.0 T compared between the C9-'Oxide only' and C9-'FS' samples

On observing the scattering intensity at - 0.30 T in Figure 6.6 (b), it is evident that the scattering intensities of C9-'Oxide only' and C9-'FS' are almost similar. This suggests a similar threshold magnetic switching diameter ($d_c$), when considering a size-dependent magnetic switching model used in Section 5.4.1 in Chapter 5. On further increasing the reversed magnetic field to -0.45 T, -0.75 T and -0.85 T in Figure 6.7 (a), Figure 6.7 (b) and Figure 6.8 (a) it is evident that the red line representing the scattering intensities for the C9 - 'FS' sample switches faster in comparison to the scattering intensities of the C9-'Oxide only' sample. On comparing the scattering intensity for sample C9-'FS' at -0.85 T and -1.00 T in Figure 6.8 (a) and Figure 6.8 (b), very little change in intensity is observed in sample C9-'FS' which means that at this magnetic field all the CoCrPt grains in the recording have switched magnetic state and have saturated in the reverse magnetisation direction. This shows that the ECC layer has a significant influence on the magnetic switching, influencing the CoCrPt granular magnetic switching in the recording layer[7,8,9].

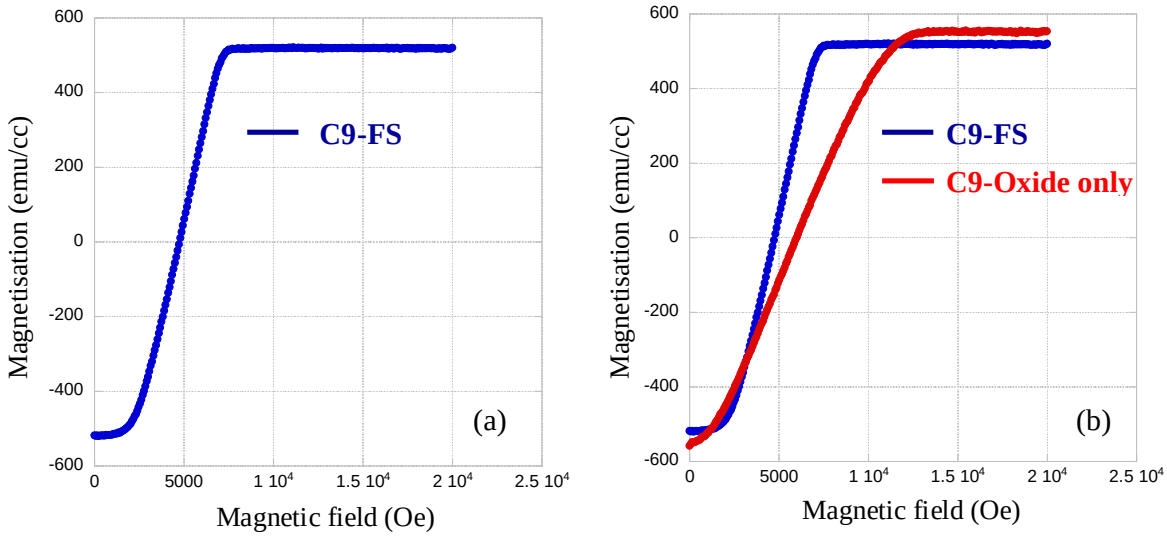


**Figure 6.9 (a)** The remanence curve for the C9-'FS' sample obtained using the remanence curve technique on a vector VSM **(b)** A comparison of the remanence curves obtained for the C9-'FS' and C9-'Oxide only' samples[20]

The vector VSM remanence curve technique, used to obtain the remanence curve of the C9-'Oxide only' sample in Figure 5.4 of Chapter 5, is again used to obtain the remanence curve of the C9-'FS' sample in Figure 6.9 (a). The comparison between the remanence curve data for the C9-'FS' sample and the C9-'Oxide only sample is presented in Figure 6.9 (b). From Figure 6.9 (b) it is evident that in the C9-'FS' sample the CoCrPt grains in the recording layer saturate along the direction of magnetisation at smaller applied magnetic fields, when compared to the C9-'Oxide only' sample [20].

Figure 6.9 (b) shows the significance of the ECC layer on the perpendicular magnetic media structure, facilitating CoCrPt magnetic grain switching grains at smaller magnetic fields. This result also agrees with the PolSANS experimental data in Figure 6.6, Figure 6.7 and Figure 6.8, highlighting the influence of the ECC layer on the recording layer CoCrPt grain switching [7,8,9].

The PolSANS results are now analysed using the size-dependent magnetic switching models to determine the threshold magnetic switching diameter ($d_c$) at different magnetic fields. By using the size-dependent pair structure factor analytical switching model used in Section 5.4.1 of Chapter 5 [10,12], the effect of the ECC layer on the threshold magnetic switching diameter ($d_c$) in the C9-'FS' sample is determined. The criterion for magnetic switching of a CoCrPt grain is determined by the size of the magnetic grain, defined by a critical threshold diameter ($d_c$). The threshold diameter ($d_c$) determines the magnetic state of the grain, as described in Section 5.4.1 of Chapter 5.

Figure 6.10 compares the experimental data for C9-'Oxide only' and C9-'FS' samples with simulated fits determining threshold switching diameters ($d_c$) at different magnetic fields. In Figure 6.10, it is clear that for sample C9-'FS', $d_c$ is significantly larger at all magnetic fields. This suggests that smaller fields switch larger magnetic grains in sample C9-'FS', when compared to C9-'Oxide only' sample. This confirms that for C9-'FS' sample the magnetic field required to switch the magnetic state of a grain is a lot smaller than the C9-'Oxide only' sample [1,2,7,8,9]. Figure 6.10 also shows that by a field of -1.0 T, the magnetic grain in the C9-'FS' sample saturates in its switched state which is not the case for the magnetic grains in C9-'Oxide only' sample.

It must be noted that the size-dependent switching model considers exchange decoupled magnetic grains in the recording layer [21]. This assumption is made considering well segregated CoCrPt grains that discourage exchange coupling effects between them. The analytical simulations carried out based on these assumptions produce good fits to the experimental data, however a more sophisticated model that considers these exchange coupling effects between CoCrPt grains could also be used to simulate the experimental data.

| Magnetic field (T) | C9-'Oxide Only' $d_c$ (nm) | C9-'FS' $d_c$ (nm) |
|---|---|---|
| -0.3 | 6.4 | 6.4 |
| -0.45 | 6.8 | 7.5 |
| -0.75 | 8.4 | 10.9 |
| -0.85 | 8.6 | 10.9 |
| -1.0 | 9.4 | 10.9 |

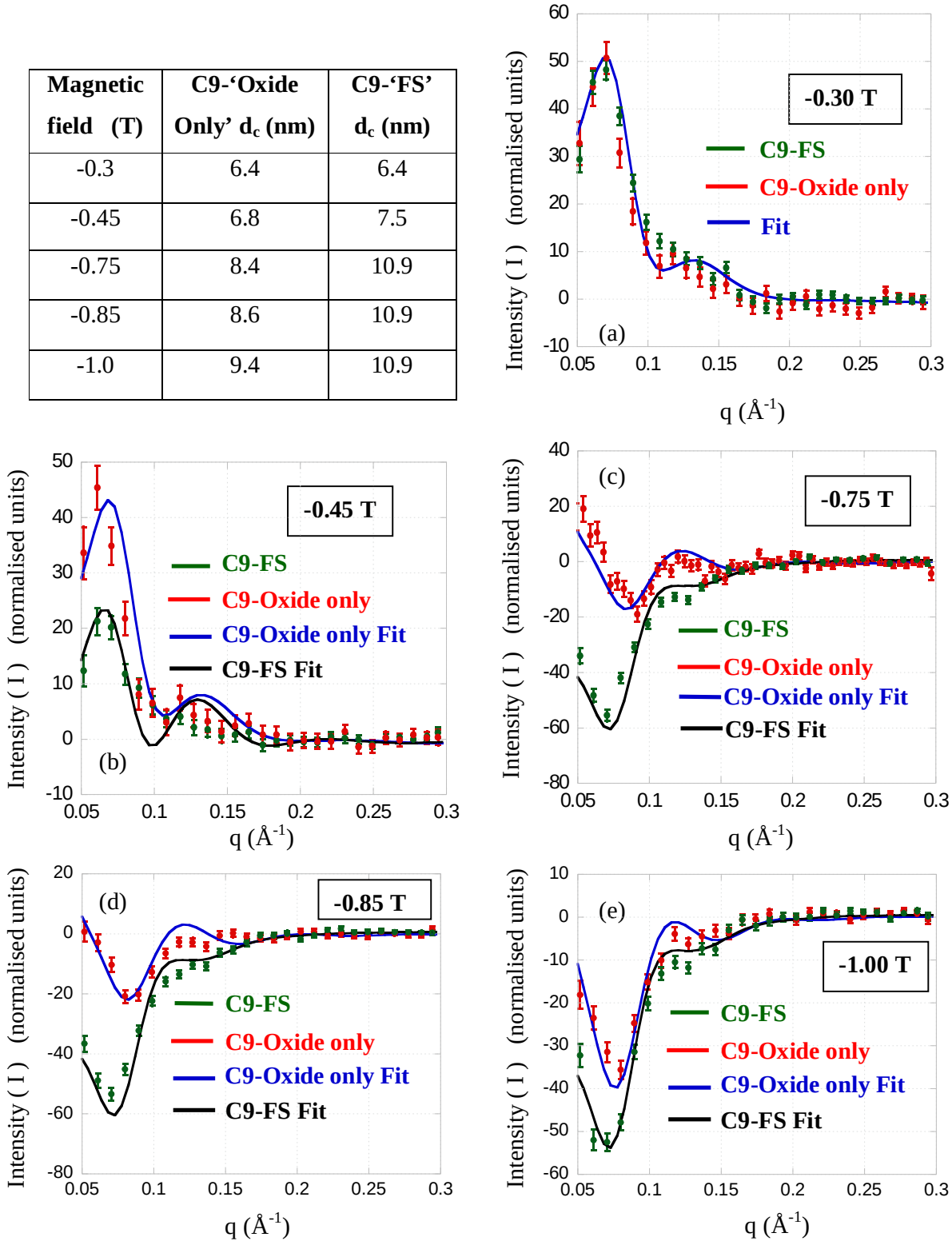


**Figure 6.10 (a) (b) (c) (d) (e)** Threshold switching diameters ($d_c$) determined for the C9-'Oxide only' and C9-'FS' samples from the simulated size-dependent analytical model fitted for the experimental scattering intensity data $\left\langle\uparrow\left|V(\vec{Q})\right|\uparrow\right\rangle^2 - \left\langle\downarrow\left|V(\vec{Q})\right|\downarrow\right\rangle^2$ at -0.30 T, -0.45 T, -0.75 T, -0.85 T and -1.00 T

### 6.4.3. Comparing analytical switching models for samples C9 and C9-FS with theoretical Sharrock switching models

The first half of this section compares the field dependent threshold switching diameters ($d_c$) obtained for the C9-'FS' and the C9-'Oxide only' sample. This comparison is carried out to investigate the effect of the ECC layer on the field dependent threshold switching grain diameter ($d_c$) and how this influences the magnetic switching in the CoCrPt grains. Both the analytical models, namely the mono approximation model and pair structure factor model, have been used to arrive at different sets of field dependent threshold switching diameters ($d_c(H)$) [10,11,12].

On understanding the influence of the ECC layer on the size-dependent magnetic grain switching, the role of the ECC layer in the C9-'FS' sample is further investigated by comparing the analytical model $d_c(H)$ plots with the simple and modified Sharrock models introduced in Section 5.4.3 of Chapter 5 [13,14,15].

#### (a) Mono approximation model

The size-dependent mono approximation model used in Section 5.4.1 of Chapter 5 is reintroduced to determine the magnetic threshold switching diameters ($d_c$) at the different magnetic fields [10,11]. The threshold magnetic switching diameters ($d_c$) obtained for the C9-'FS' and C9-'Oxide only' samples at different reversed magnetic fields are tabulated in Table 6.1 and plotted in Figure 6.11. From Figure 6.11, the influence of the ECC layer in the C9-'FS' sample is evident. By a reversed magnetic field of -0.75 T, the magnetic moments are driven to saturation along the field direction in the C9-'FS' sample. However the same is not the case with the C9-'Oxide only', as even at a reversed magnetic field of around 1 T, all the magnetic grains in the recording layer have not switched magnetic states yet. This clearly shows the influence of the ECC layer on the magnetic switching process of the CoCrPt grains in the recording layer [7,8].

**Table 6.1** Threshold switching diameters ($d_c$) determined using the mono approximation model compared for the C9-'Oxide only' and C9-'FS' samples at different reversed magnetic fields

| *Magnetic Field (T)* | *$d_c$ for C9 (nm)* | *$d_c$ for C9-FS (nm)* |
|---|---|---|
| 0.30 | 5.6 | 5.6 |
| 0.45 | 6.0 | 6.8 |
| 0.50 | 6.3 | - |
| 0.55 | - | 7.5 |
| 0.60 | 6.3 | - |
| 0.65 | - | 8.2 |
| 0.70 | 6.8 | - |
| 0.75 | 7.1 | 8.8 |
| 0.80 | 7.4 | - |
| 0.85 | 7.6 | 8.8 |
| 0.90 | 7.9 | - |
| 1.0 | 8.5 | 8.8 |

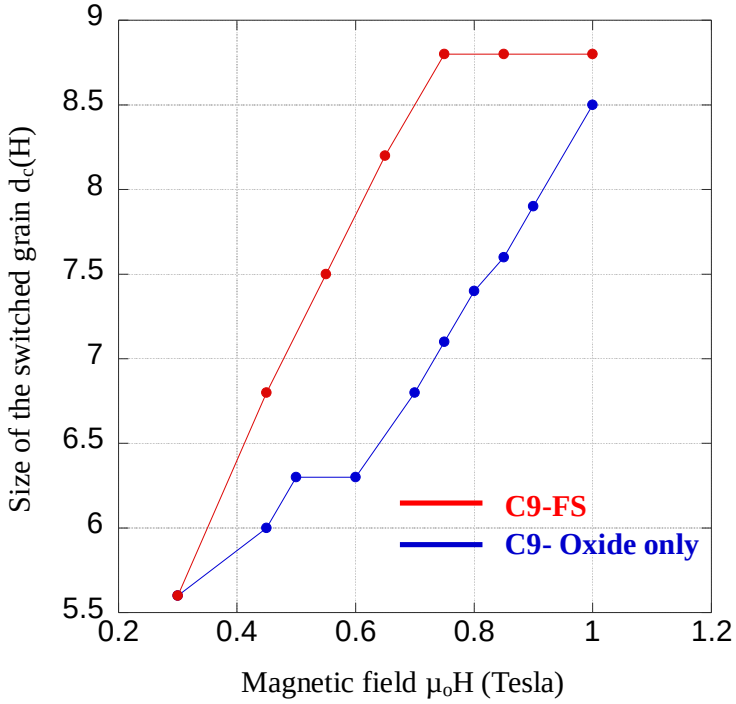


**Figure 6.11** Comparison of the threshold switching diameters ($d_c$) determined using the mono approximation model at different reversed magnetic fields (H) between the C9-'Oxide only' and C9-'FS' samples

Now the field driven threshold grain switching data ($d_c(H)$) determined using the mono approximation model, is compared with the simple and the modified Sharrock models introduced in Section 5.4.3 of Chapter 5 [11,13,15]. The $d_c(H)$ for the C9-'FS' sample determined using the mono approximation model was found to closely match the size independent simple Sharrock model better. The simple Sharrock model states that the anisotropic field ($H_k$) is size-independent and is a constant value [15]. This result is very different from what we observe with the C9-'Oxide only' samples that show that anisotropic field ($H_k$) has a dependance on the size of the magnetic grains [15,18]. Hence by introducing an ECC layer, the simple Sharrock model that considers a size-independent constant anisotropy field ($H_k$) agrees with the $d_c(H)$ plot determined using the size-depedent mono approximation model in Figure 6.12.

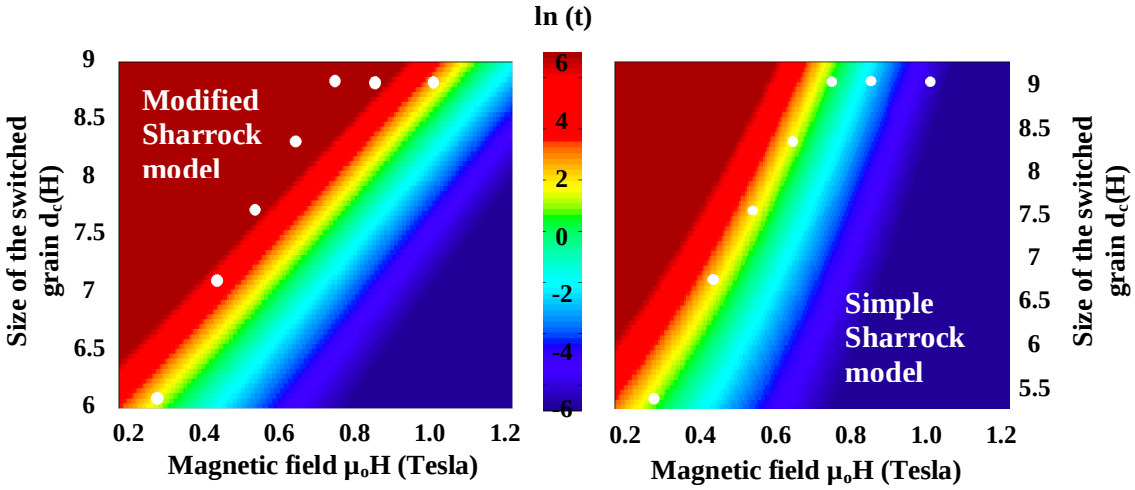


**Figure 6.12** Comparsion of switching colour plots for a modified and simple Sharrock models with $d_c(H)$ plots obtained from simulations using the mono approximation model

### (a) Pair Structure factor model

The pair structure factor analytical model described in Section 5.4.1 of Chapter 5 is used to determine the threshold switching diameter $d_c$ for the CoCrPt grains at different reversed magnetic fields in the C9-'FS' sample [10,12]. As previously predicted by the mono approximation model, when the $d_c(H)$ plot was compared between the C9-'FS'and C9-'Oxide only' samples, larger magnetic grains were found to switch at lower fields in the C9-'FS' sample which suggested that the ECC layer enhances the switching process in the CoCrPt grains of the recording layer [7,8]. The pair stucture factor also shows a similar outcome from Table 6.2 and Figure 6.13. In Table 6.2, it is evident that all the magnetic grains had switched magnetic states in the C9-FS sample by a reversed field of about -0.75 T. However the C9-'Oxide only' threshold switching diameters ($d_c$) in Table 6.2, show that at - 0.75 T the magnetic grains still have not switched their magnetic states. It is observed that even at reversed fields of -1 T, the larger magnetic grains with increased diameters in the C9-'Oxide only' sample have not switched magnetic states.

**Table 6.2** Threshold switching diameters ($d_c$) determined using the pair structure model compared for the C9 and C9-'FS' samples at different reversed magnetic fields

| *Magnetic Field (T)* | *$d_c$ for C9 (nm)* | *$d_c$ for C9-FS (nm)* |
|---|---|---|
| 0.30 | 6.4 | 6.4 |
| 0.45 | 6.8 | 7.5 |
| 0.50 | 7.0 | - |
| 0.55 | - | 8.6 |
| 0.60 | 7.3 | - |
| 0.65 | - | 9.6 |
| 0.70 | 8.0 | - |
| 0.75 | 8.4 | 10.9 |
| 0.80 | 8.5 | - |
| 0.85 | 8.6 | 10.9 |
| 0.90 | 9.0 | - |
| 1.0 | 9.4 | 10.9 |

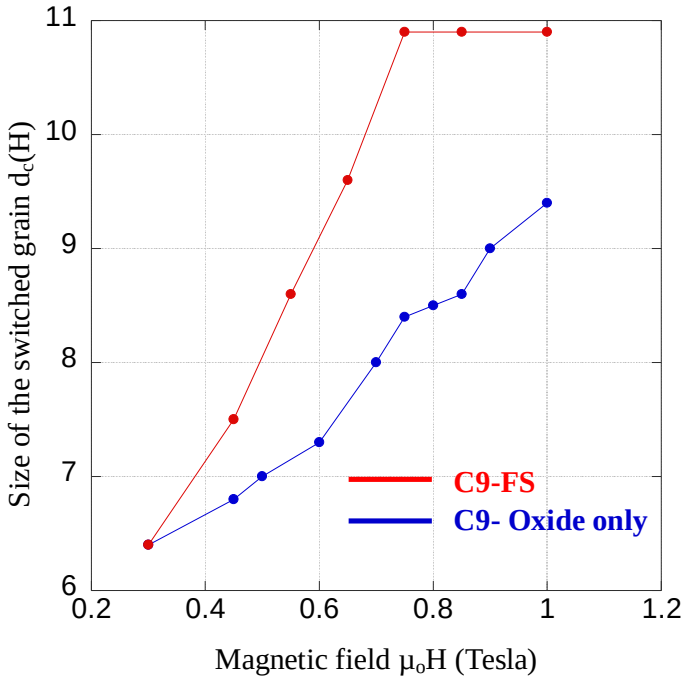


**Figure 6.13** Comparison of the threshold switching diameters ($d_c$) determined using the pair structure factor model at different reversed magnetic fields (H) between the C9-'Oxide only' and C9-'FS' samples

In this section, the pair structure factor analytical model is found to fit the magnetic switching data for the C9-'FS' sample at different magnetic fields. Following this, the influence of the ECC layer on the magnetic switching process is investigated [10,12]. Magnetic switching studies on the C9 -'Oxide only' sample, show that the magnetic switching can be described by a modified Sharrock model introduced in Section 5.4.3 of Chapter 5 [18]. However modelling the C9-'FS' using the mono approximation model has shown that the simple Sharrock model that does not consider the size-dependent anisotropy field ($H_k$) term was found to simulate the switching behaviour of the CoCrPt grains. A similar outcome with the $d_c$(H) results obtained using the pair structure factor model for the C9-FS samples is observed. The $d_c$(H) switching plot in Figure 6.14 is found to agree more with the size-independent anistropy field ($H_k$) adopted by the simple Sharrock model [15]. Hence by introducing a magnetically softer layer the anisotropy field term ($H_k$) that showed a size depedance in the C9 -'Oxide only' sample is replaced by a constant term as the ECC layer doesn't account for a size-depedent anisotropy field term ($H_k$) in its switching process.

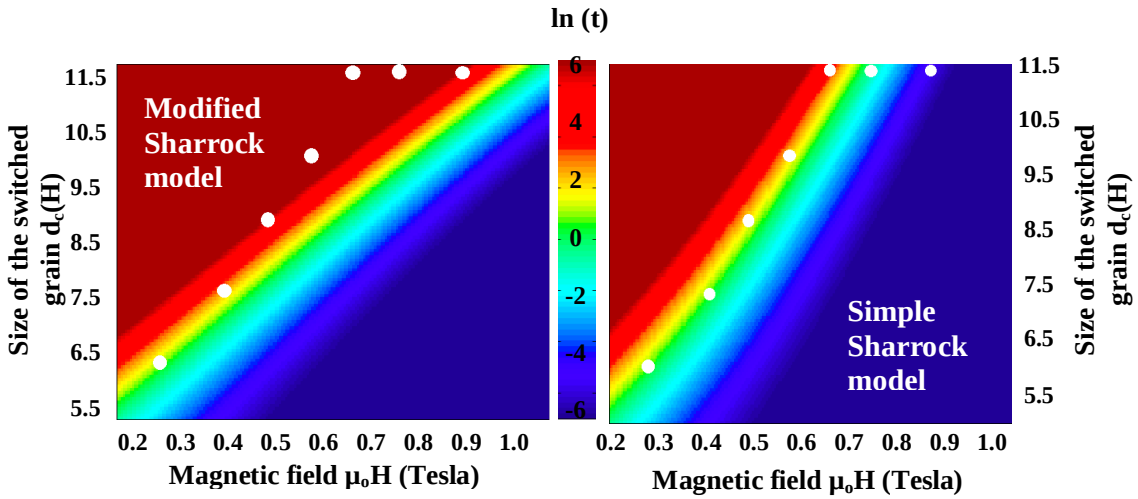


**Figure 6.14** Comparsion of the switching colour plots for a modified and simple Sharrock models with $d_c$(H) plots obtained from simulations using the pair structure factor model

## 6.5 Conclusion

This chapter confirms the absence of nuclear and magnetic interference scattering in the experimental data from the ECC layer in the perpendicular media structure [1,2]. This is determined by comparing the scattering intensities obtained by taking the difference of the 'spin up' and 'spin down' scattering for the C9-'Oxide only' and C9-'FS' sample at 3 T. It is observed that there exists no contribution from the interference of the nuclear and magnetic scattering in this q-range from the ECC layer, confirming the absence of nanoscale magnetic granular structure in the ECC layer.

The reported work investigates the influence of the ECC layer on the magnetic switching of the CoCrPt grains in the recording layer. The influence of the ECC layer on the average switching grain diameter ($d_c$) at different magnetic fields (H) is investigated. It is reported that smaller magnetic fields were required to switch larger magnetic grains in C9-'FS' sample, when compared to the C9-'Oxide only' sample, where larger magnetic fields were required to switch larger grains. This is as a result of exchange coupling between the ECC layer and recording layer in the C9-'FS' sample, which influences the magnetic switching of the CoCrPt grains in the recording layer of the C9-'FS' sample [7,8]. The switching data is modelled using the size-dependent mono approximation switching model and the size-dependent pair structure factor model and the results are presented as $d_c(H)$ plots[10,11,12].

The $d_c(H)$ plots are compared with the simple and the modified Sharrock models introduced in Chapter 5. The $d_c(H)$ plots are found to be more in agreement with the simple Sharrock model, which considers a size-independant anistropy field $H_k$[15]. This result is very different from what is observed in the C9-'Oxide only' sample, where the $d_c(H)$ for both the analytical and TEM models seemed to agree with a modified Sharrock model, which considers a size-dependent anisotropic field term $H_k$[18].

To conclude, the results presented in this chapter of the reported work state that the ECC layer has a significant effect on the CoCrPt magnetic grain switching in the recording layer[7,8]. The ECC layer facilitates magnetic grain switching at lower magnetic fields, when compared to a conventional perpendicular media thin film structure without an ECC layer[7,8]. The ECC layer is also reported to reduce the influence of intrinsic $H_k$ variations in the magnetic switching process [2,9].

## 6.6 References


[1] D. Suess, J. Lee, J. Fidler, T. Schrefl "Exchange-coupled perpendicular media" Journal of Magnetism and Magnetic Materials, 321(6), (2009) p.545-554 (DOI: 10.1016/j.jmmm.2008.06.041)

[2] D. Goll, S. Macke, H. Kronmüller "Exchange coupled composite layers for magnetic recording" Physica B: Condensed Matter, 403(2–3), (2008), p.338-341 (DOI: 10.1016/j.physb.2007.08.044)

[3] T.D. Lee, S.C. Lee, Y.W. Tahk "Micromagnetic studies on exchange-coupled composite media" Journal of Magnetism and Magnetic Materials, 303(2), (2006) p.276-281 (DOI: 10.1016/j.jmmm.2006.01.248)

[4] S. N. Piramanayagam "Perpendicular recording media for hard disk drives" J. Appl. Phys. 102, 011301 (2007) (DOI: 10.1063/1.2750414)

[5] A. Carter, L.E. Fernandez-Outon, Y. Inaba, S.J. Greaves, H. Muraoka, K. O'Grady "Anisotropy dispersion in (CoCrPt)1−x(SiO2)x perpendicular recording media" Journal of Magnetism and Magnetic Materials, 320(18), (2008) p.2269-2272 (DOI: 10.1016/j.jmmm.2008.04.126)

[6] S. J. Lister, M. P. Wismayer, V. Venkataramana, M. A. de Vries, S. J. Ray, S. L. Lee, T. Thomson, J. Kohlbrecher, H. Do, Y. Ikeda, K. Takano, and C. Dewhurst "Small-angle polarized neutron studies of perpendicular magnetic recording media" Journal of Applied Physics, 106(6),(2009) p. 063908 - 063908-4 (DOI: 10.1063/1.3213381)

[7] Dieter Suess "Micromagnetics of exchange spring media: Optimization and limits" Journal of Magnetism and Magnetic Materials, 308(2), (2007), p.183-197 (DOI: 10.1016/j.jmmm.2006.05.021)

[8] Rujun Tang, Sherlyn Chua, Wanli Zhang, Yanrong Li "Effects of soft layer softness on the magnetic properties of perpendicular exchange-coupled nanocomposite films" Journal of Magnetism and Magnetic Materials, 323(21), (2011) p.2569-2574 (DOI: 10.1016/j.jmmm.2011.05.034)

[9] D. Suess, T. Schrefl, R. Dittrich, M. Kirschner, F. Dorfbauer, G. Hrkac, J. Fidler "Exchange spring recording media for areal densities up to 10 Tbit/in$^2$" Journal of Magnetism and Magnetic Materials, 290–291(1), (2005) p.551-554 (DOI: 10.1016/j.jmmm.2004.11.525)

[10] A. Guinier, G. Fournet "Small-Angle Scattering of X-Rays" John Wiley and Sons, New York (1955) (DOI: 10.1002/pol.1956.120199326)

[11] N.W. Ashcroft, J. Lekner "Structure and Resistivity of Liquid Metals" Phys. Rev. (145), (1966) p. 83–90 (DOI: 10.1103/PhysRev.145.83)

[12] W.L. Griffith, R. Triolo, A.L. Compere "Analytical scattering function of a polydisperse Percus-Yevick fluid with Schulz- ( Gamma -) distributed diameter" Phys Rev A, 35(5), (1987) p. 2200–2206 (DOI: 10.1103/PhysRevA.33.2197)

[13] E.C. Stoner, E.P. Wohlfarth "A mechanism of magnetic hysteresis in heterogeneous alloys" Philosophical Transactions of the Royal Society A: Physical, Mathematical and Engineering Sciences, 240 (826), (1948) p.599–642 (DOI: 10.1109/TMAG.1991.1183750)

[14] C. Tannous, J. Gieraltowski "The Stoner–Wohlfarth model of ferromagnetism" Eur. J. Phys. 29 475, (2008) (DOI: 10.1088/0143-0807/29/3/008)

[15] P. J. Flanders, M. P. Sharrock "An analysis of time-dependent magnetization and coercivity and of their relationship to print-through in recording tapes" J. Appl. Phys. 62, 2918 (1987) (DOI: 10.1063/1.339373)

[16] J. Kohlbrecher, W. Wagner "The new SANS instrument at the Swiss spallation source SINQ", J. Appl. Cryst. 33, (2000) p.804-806 (DOI: 10.1107/S0021889800099775)

[17] Charles Dewhurst "GRAS$_{ans}$P: Graphical Reduction and Analysis SANS Manual" Institute Laue Langevin, France. Last modified December 15, 2011. http://www.ill.eu/?id=6300

[18] S. J. Lister, T. Thomson, J. Kohlbrecher, K. Takano, V. Venkataramana, S. J. Ray, M. P. Wismayer, M. A. de Vries, H. Do, Y. Ikeda, and S. L. Lee "Size-dependent reversal of grains in perpendicular magnetic recording media measured by small-angle polarized neutron scattering" Applied Physics Letters, 97 (11), (2010) (DOI: 10.1063/1.3486680)

[19] M. Wismayer, S. Lee, T. Thomson, F. Ogrin, C. Dewhurst, S. Weekes, R. Cubitt "Using small-angle neutron scattering to probe the local magnetic structure of perpendicular magnetic recording media" Journal of Applied Physics, 99(8), (2006) (DOI: 08e707 10.1063/1.2165798)

[20] T. Thomson, B. Lengsfield, H. Do, B. Terris "Magnetic anisotropy and reversal mechanisms in dual layer exchanged coupled perpendicular media" Journal of Applied Physics, 103(7), (2008) (DOI: 10.1063/1.2839310)

[21] K. Srinivasan, S.N. Piramanayagam, R. Sbiaa, R.W. Chantrell "Thermal stability and the magnetization process in CoCrPt–SiO2 perpendicular recording media" Journal of Magnetism and Magnetic Materials, 320(22), (2008) p. 3041-3045 (DOI: 10.1016/j.jmmm.2008.08.014)

# Chapter 7

# Investigating magnetisation in the ECC layer and recording layer of the perpendicular magnetic medium using PNR

---

**Contents**



---

**Abstract**

Polarised neutron reflectivity (PNR) is a neutron characterisation technique that has been used to measure magnetisation as a function of depth, in a direction perpendicular to the surface of the perpendicular magnetic media. PNR has been used to investigate the difference in magnetisation of the recording and ECC layers in the thin film structure, while also determining the nuclear structure and composition of the perpendicular magnetic medium. PNR experiments were carried out at the AMOR instrument at PSI and the reflectivity data were then analysed using a mathematical model. Both the thin film structure and the magnetic profile of the thin film structure in the perpendicular magnetic medium are mapped, providing a detailed depth resolved measurement of the structure and magnetic properties in the thin film perpendicular magnetic medium.

## 7.1 Background and Introduction

The ECC layer plays an important role in influencing the CoCrPt magnetic grain switching in the recording layer of the perpendicular magnetic medium [1,2,3]. The magnetically softer ECC layer is expected to exchange couple with the recording layer in perpendicular magnetic medium, enabling high anisotropy magnetic grain switching at smaller applied magnetic fields [4,5]. PolSANS experiments in Chapter 6 suggest the absence of nanoscale magnetic granular structure in the ECC layer [6,7]. Polarised neutron reflectivity is used in this chapter to investigate the difference in the magnetic properties of the ECC layer and the recording layer and the results are reported [8,9,10].

Polarised neutron reflectivity (PNR) described in Section 2.2 of Chapter 2, is a neutron characterisation technique that is used to measure magnetisation in thin films [11]. The neutrons are reflected and refracted at the various interfaces of the thin film structure, identifying the difference in their atomic packing density and scattering length, relating to the chemical composition of individual layers in the thin film structure [12]. A detailed description of the multiple reflection and refraction processes involved is given in Chapter 2, where the potential step the neutron overcomes during a reflection or refraction process at the interface is explained [11,12,13]. Polarised neutrons also characterise the magnetic state of the thin film, identifying the magnetic properties of individual magnetic thin films. The magnetic state of an individual layer in the thin film structure is identified by the change in intensity the incoming polarised neutrons undergoes when interacting with the magnetised thin film structure [12].

Polarised neutrons are insensitive to any out-of-plane magnetisation during a specular reflectivity process and the in-plane magnetisation is mapped by an increase or a decrease in intensity depending on the polarisation state of the neutron with respect to the magnetisation direction [12,13]. This is because a magnetic contribution is determined by the dot product of the neutron magnetic moment ($\vec{\mu}_n$) and the magnetisation in the material ($\vec{M}(\vec{r})$), and this is maximum only when both the polarised neutrons and the magnetic moments are aligned along the same direction [12,13]. This technique maps the magnetic profile of the thin film structure. The magnetisation in individual layers of the thin film structure is determined under the influence of an applied in-plane magnetic field [12,13].

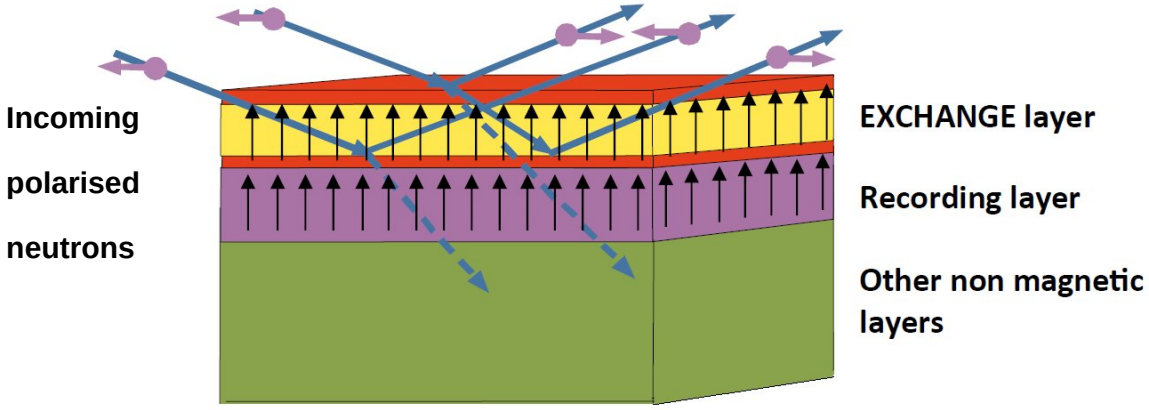


**Figure 7.1** Polarised neutrons interacting with perpendicular magnetic media in the absence of an applied magnetic field

The perpendicular magnetic media structure comprises a magnetic recording layer and an ECC layer with a number of non-magnetic under layers. The samples are also expected to have an exchange control layer (ECL) between the ECC layer and the recording layer [14]. However the PNR experiments carried out in this chapter fail to identify the presence of the ECL in the perpendicular magnetic media structure. The detailed description of the sample composition is given in the next section (Section 7.2) of this chapter.

## 7.2 Sample and Preparation

The samples used for the experiments reported were sputtered at Hitachi Global Storage Technologies (GST), San Jose research centre at California, USA. The samples were designed, such that, the only magnetic layers in the multi-layered structure are the recording layer and the ECC layer [14]. This was done to ensure that any magnetic effect from the usually used FeCo magnetic soft under layers was ruled out. Therefore the conventionally used FeCo soft under layers in the system, have been substituted with layers of nickel tantalum and nickel tungsten [15].

Non-magnetic under layers were chosen to avoid any magnetic contribution from the under layers, when investigating the magnetisation in the recording layer and the ECC layer of the perpendicular magnetic structure [15]. Any magnetisation present in the under layers would contribute to the ‘spin up’ and ‘spin down’ reflectivity, making it difficult to differentiate this

from the magnetic contribution from the recording layer and ECC layer in the sample. The contribution from magnetisation in under layers becomes more significant, when investigating small changes in magnetisation from the recording layer and the ECC layer in the perpendicular magnetic media. Hence for simplification, all the other layers except the recording and ECC layer are non-magnetic. Nickel tantalum and Nickel Tungsten here mimic the normally used FeCo under layers in its physical properties, but are not ferromagnetic like the FeCo soft under layers present in a conventional perpendicular magnetic recording medium [14,15].

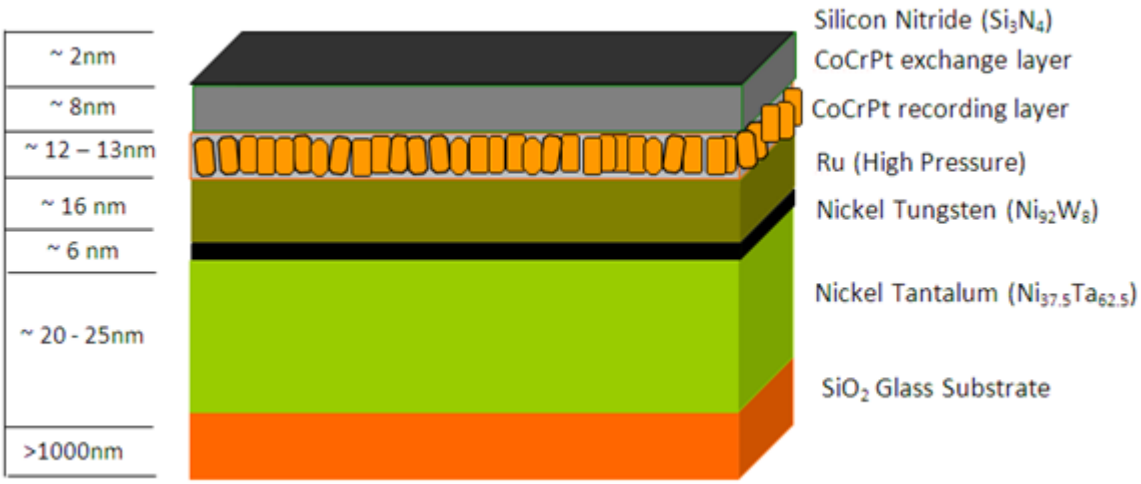


**Figure 7.2** Perpendicular magnetic media sample structure with layer thicknesses and composition

The seed layers comprising ruthenium with other intermediate layers to thicknesses of around 16 nm is grown above the nickel tungsten under layer. The seed layers are followed by the CoCrPt+Oxide recording layer (RL) with 13 nm thickness. An 8 nm thick magnetically softer ECC layer is sputtered above the RL. Finally, a silicon nitride protective over coat is sputtered above the multi-layered thin film structure to protect the thin film perpendicular magnetic media structure. It is important to note that the thin film structure given by Hitachi GST, is largely determined by the parameters set during the growth of the film. Using polarised neutron reflectivity it is possible to give more detailed information on the thin film structure differentiating layer thicknesses and element composition far more precisely than most other techniques, acting as an ideal tool to determine the composition of thin film structures [11,12].

The samples are placed on the sample stage of the AMOR instrument setup at PSI [16]. The samples are held on to the stage using an adhesive, that does very little to affect the alignment of the sample or affect the properties of the sample. The sample stage is then controlled by the instrumental software that is capable of moving the sample stage in all three axes. This allows detecting the sample on the sample holder before performing experiments on the samples [16].

## 7.3 Experiment

Figure 7.3 is the schematic that depicts the geometry of the experiment [12]. The incoming polarized neutrons are incident at an angle $\theta_i$ to the plane of the sample. Considering a specular reflection process, the outgoing neutrons are reflected at an angle $\theta_r$ from the sample [12]. For very small angles of incidence/reflection, the scattering vector is along the y-axis of the sample perpendicular the plane of the thin film sample. The magnetic field is applied along the x-axis direction, which is also the polarisation direction of the incoming neutron beam[12]. In Figure 7.3, the polarization of the incoming neutrons is taken to be parallel and anti-parallel to the plane of the thin film [12,13] . The reported work investigates perpendicular media samples, which are thin film multi-layered structures. Hence the polarised neutrons (as previously stated in the theory (Section 2.2.2 of Chapter 2)) go through a process of multiple refractions and reflections at various interfaces in the multi-layered structure [12,13].

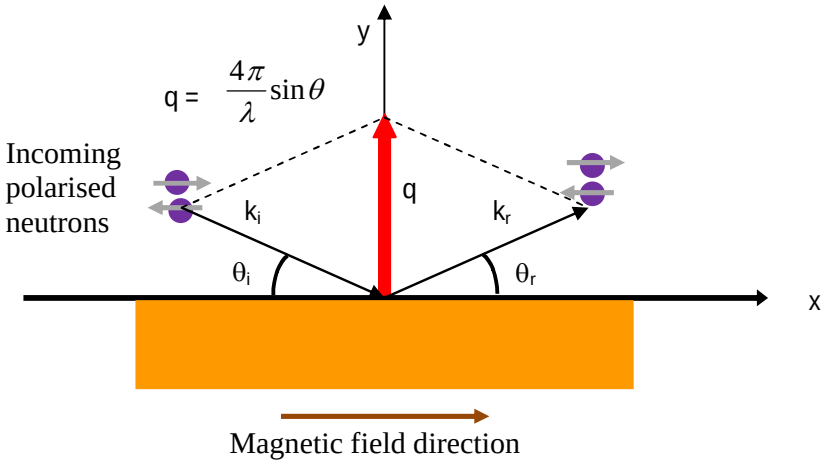


**Figure 7.3** PNR experimental geometry

The experiments were carried out in the time-of-flight mode. A narrow window of wavelengths that correspond to the scale of nanoscale features in the sample is achieved, by introducing a tuneable wavelength velocity selector [16]. The neutrons of a fixed wavelength are passed through a polariser that achieves a single polarised state, which are then given a direction by a guide field followed by a spin flipper that switches 'ON' and 'OFF' enabling 'spin up' and 'spin down' states. This polarized state is along the direction of the plane of the film [13,16].

As described in Section 7.2, the perpendicular media samples have two magnetic layers namely the recording and the ECC layer, along with other non-magnetic layers that in total comprise the entire perpendicular magnetic medium[1,2,14]. The recording layer as earlier explained has a granular structure that is dominated by a strong out-of-plane magneto-crystalline anisotropy [17]. This anisotropy favours magnetisation perpendicular to the plane of the film in the recording layer [17]. The magnetisation of the ECC layer is also designed to be perpendicular. However the ECL layer is designed to be magnetically softer than the recording layer [14].

**(a) Determining the structure and chemical composition of the multi-layered perpendicular magnetic medium**

The first experiments map the structure and chemical composition of the multi-layered thin film perpendicular magnetic medium [14]. Before carrying out an experiment, the samples are magnetised with a strong out-of-plane magnetic field to ensure that all the moments in the recording and ECC layers align out-of-plane.

The angle of incidence is set by tilting the position of the sample holder along its y-axis, thereby determining the experimental q-range. The polarized neutron detector moves on a motorized elevator and its position is determined by the experimental 'q'-range set by the controlled tilt of the sample stage [16]. The magnetic field is then set at a negligible value say 30 Oe so that the magnetic field has no effect on the magnetic state of the ECC and recording layers in the perpendicular magnetic medium. The magnetic field is also set at a small value (30 Oe) to ensure that the incoming polarised neutrons retain their polarisation state before interacting with the sample [12]. A polarized neutron reflectivity experiment for the 'spin up' and 'spin down' neutron reflectivity is performed for different experimental 'q'-ranges and

the data is then stitched to give us the full experimental 'q'- range [12]. No magnetic information is expected to be observed in this setup, as the magnetic moments of the recording layer are perpendicular to the plane of the film and in this geometry the neutrons are insensitive to magnetic information from the sample [9,12].

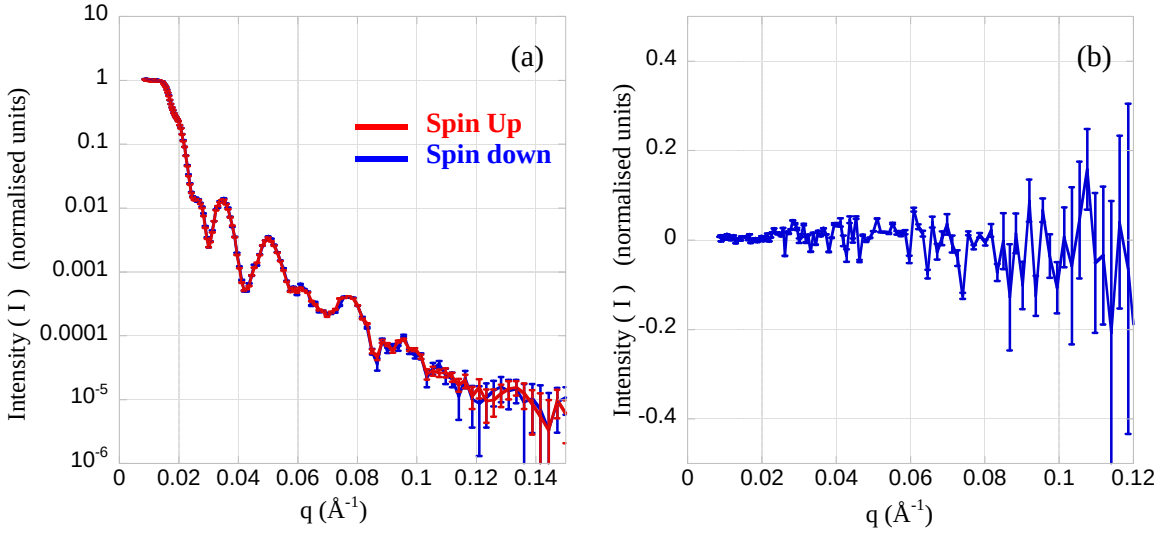


**Figure 7.4** (a) Spin 'up' and Spin 'down' reflectivity plots at an in-plane magnetic field of 30 Oe (b) Spin asymmetry plot at an in-plane magnetic field of 30 Oe

Hence both the spin up and spin down reflectivity plots, at this field are found to be very similar, as the reflectivity plots in this experiment give us only the composition and structural information from the multi-layered structure. This is obtained from the difference in packing densities and scattering lengths which differentiates the layers in the thin film structure.

### (b) Determining the structure and the magnetic profile of the multi-layered perpendicular magnetic medium

After determining the structure and chemical composition of the magnetic multilayer, the negligible magnetic field initially applied is increased gradually in steps. Polarised neutron reflectivity measurements initially carried out using the 'spin up' and 'spin down' polarized neutrons are now carried out at different magnetic fields and 'spin up' and 'spin down' neutrons reflected from the samples are detected [9,12].

On gradually increasing the magnetic field, an increasing difference between the spin up and spin down reflectivity is observed in the experimental data. The spin asymmetry is determined by dividing the difference between the 'spin up' and 'spin down' reflectivity data with the sum of the 'spin up' and 'spin down' data, and this is determined at different magnetic fields [9,12]. Polarised neutron reflectivity measurements are carried out at 1000 Oe, 2000 Oe, 3000 Oe, 4000 Oe, 5000 Oe, 6000 Oe, 8000 Oe and 10000 Oe. In Figure 7.5b, it is observed that as the magnetic field gradually increases the spin asymmetry gradually increases with maximum spin asymmetry occurring at about 10000 Oe. This change in spin asymmetry is associated with effect of magnetic field on the recording and ECC layers. Increasing the in-plane magnetic field gradually orients the magnetic moments along the plane of the thin film until driven to saturation along the direction of the applied field [3,4].

The analytical models used in the reported work determines the magnetisation in the recording and ECC layers with increasing magnetic field establishing a means by which the magnetisation in each layer of the thin film can be mapped subject to a varying in-plane magnetic field [13].

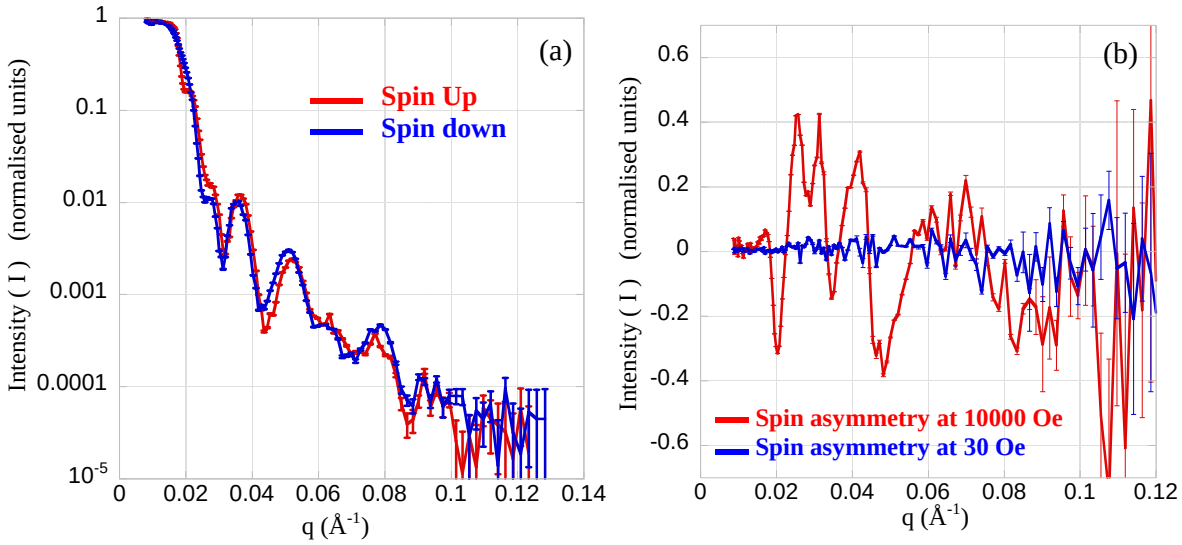


**Figure 7.5** (a) Spin 'up' and Spin 'down' reflectivity plots at an in-plane magnetic field of 10000 Oe (b) Spin asymmetry compared between the 30 Oe in-plane magnetic field data and 10000 Oe in-plane magnetic field data

## 7.4 Analysis, Results and Elucidation

The experimental results obtained are simulated using an analytical model based on the theoretical work carried out by Blundell [13]. A brief discussion of the analytical model is introduced in Chapter 2 and this chapter explains how the analytical model can be used to simulate the experimental results [13]. The parameters of the analytical model are refined using a least squares fitting program that determine the thickness and elemental composition of the thin film structure [18]. Once the structure of the multi-layered perpendicular magnetic medium is determined, the model is extended to account for the magnetisation in the thin film as a result of a gradually increased magnetic field [13].

### 7.4.1. Structural properties of the thin film structure

The structure of the perpendicular magnetic medium is determined by simulating the zero field polarised neutron reflectivity data. Initial parameters of thickness, number density, and scattering length specified by Hitachi GST are introduced into the mathematical model. The simulated reflectivity plot obtained was found to follow the trend of the experimental data and by using the a non-linear least squares fitting program a better simulated fit to the experimental data is obtained [13,18]. Figure 7.6 is a simulated fit obtained using the non-linear least squares fitting program for the 30 Oe data. For the 30 Oe data, no spin asymmetry is expected to be observed when taking the difference between the spin up and spin down reflectivity plots. This is because at 30 Oe, the magnetisation in the recording layer and the ECC layer are expected to be zero. Only parameters like the layer thickness and the scattering length densities are allowed to vary in the analytical model, determining the composition and the thickness of the layers in the thin film structure.

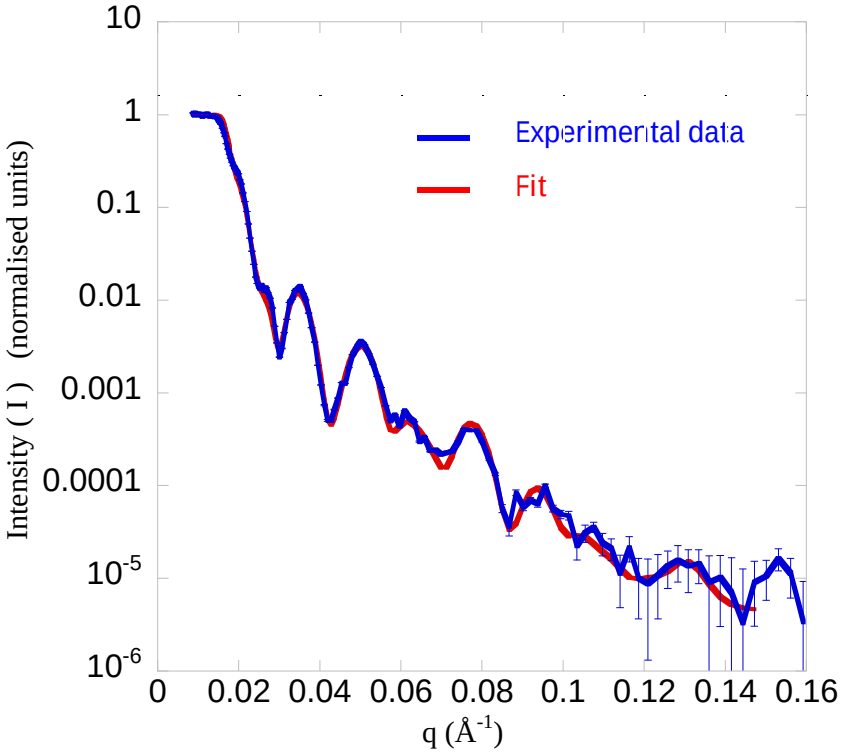


**Figure 7.6** Polarised neutron reflectivity data at an in-plane magnetic field of 30 Oe with fit for nuclear structure of the perpendicular magnetic media

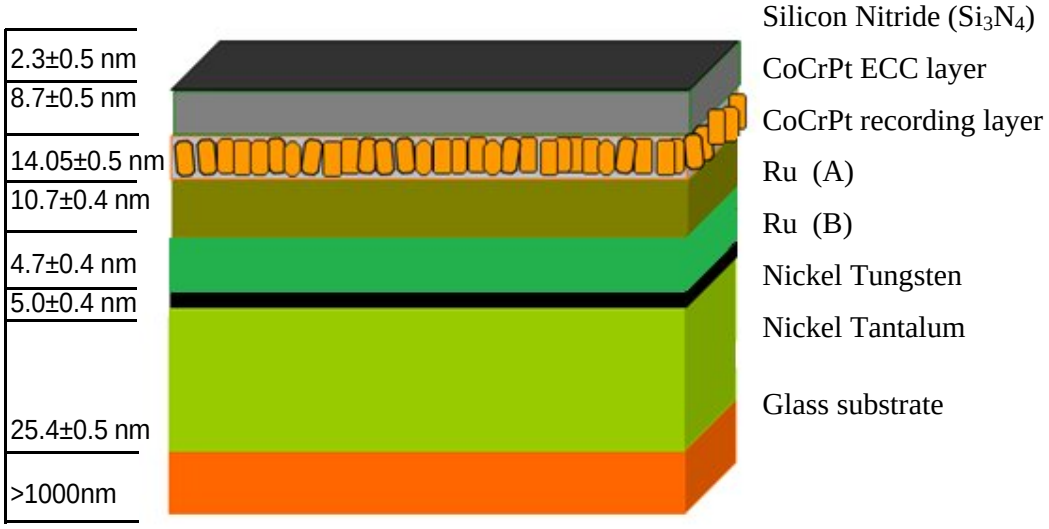


**Figure 7.7** Simulated perpendicular magnetic media structure with layer thicknesses and composition

**Table 7.1** Table comparing the expected values and the simulated fit values for thickness and scattering length densities in the sample

| *Layers* | *Simulated Fit values* | | *Expected values* | |
|---|---|---|---|---|
| | *Thickness (nm)* | *Scattering length density (x $10^{13}$ $m^{-2}$)* | *Thickness (nm)* | *Scattering length density (x $10^{13}$ $m^{-2}$)* |
| Cap layer ($Si_3N_4$) | 2.3±0.5 | 22.8±0.7 | 2.5 | 37.1 |
| ECC layer (CoCrPt) | 8.7±0.5 | 33.3±0.8 | 8.0 | 33.0 |
| Recording Layer (CoCrPt) | 14.5±0.5 | 35.8±0.9 | 13.0 | 33.0 |
| Seed layer (Ru) A | 10.7±0.4 | 45.7±0.4 | 16.0 | 50.6 |
| Seed layer (Ru) B | 4.7±0.4 | 50.8±0.4 | | |
| Nickel Tungsten | 5.0±0.4 | 87.7±0.1 | 6.0 | 86.3 |
| Nickel Tantalum | 25.4±0.5 | 60.6±0.3 | 25.0 | 72.4 |
| Substrate ($SiO_2$ or glass) | > 1000 | 41.9 | >1000 | 41.9 |

The scattering length densities and the thicknesses are tabulated in Table 7.1 with errors. It is evident in Table 7.1 that scattering length densities and thicknesses determined using the fitting program for the experimental data are relatively close to the expected bulk scattering lengths densities for the alloys in the individual layers. It must be noted that the expected scattering length densities in Table 7.1 are determined for bulk materials, and simulated results obtained using the analytical model are for thin films. On comparing the expected and the simulated results it was found that they both agree closely [19].

The simulations also distinguish the two CoCrPt based layers namely the recording layer and the ECC layer, reporting significant differences in their scattering length densities [2]. The recording layer was found to have a slightly higher number density, which could be associated with a possible granular structure in the layer or as a result of the composition variation in the CoCrPt-Oxide alloy [2]. The sputtered thin film structure given by Hitachi GST suggest the presence of an exchange control layer (ECL) of negligible thickness between the recording and the ECC layer. The experimental simulations/fits however fail to pick up the presence of the ECL, but the recording layer and the ECC layer are separately identified. This could be as a result of the ECL being extremely thin, making it very difficult to identify its presence across the limited q range PNR data.

The simulations also report a significant difference in scattering length densities of the Ru seed layers, with the simulations reporting two stacks of ruthenium layers with different scattering length densities. This result on the existence of two stacks of seed layers is expected, as the information provided by Hitachi GST suggest the possibility of a number of 'other layers' along with ruthenium layer [20,21]. The 'other layers' are present to enhance grain formation in the recording layer. The observed difference in properties between the two chunks of Ruthenium could be associated with the presence of the possible 'other layers', whose composition and properties remain confidential [20,21].

Summarising, the composition and the dimensions of the thin film perpendicular magnetic medium are determined using the simulated mathematical model, by producing simulated fits that closely resemble the experimental data [13,14]. Now that the structure and effective composition of the sample has been established, the magnetic properties of the recording layer and the ECC layer are investigated [2,14]. Figure 7.7 is a cartoon of the structure of the perpendicular magnetic medium determined using PNR.

### 7.4.2. Field dependent magnetic profile of the thin film structure

The sample is magnetised gradually in steps and polarised neutron reflectivity experiments are repeated at different magnetic fields. The experimental results obtained report an increasing difference in the spin asymmetry with increasing magnetic field [9]. This confirms that the in-plane magnetisation increases with an increasing applied in-plane magnetic field, and given that only the recording layer and the ECC layer exhibit ferromagnetic properties, this increasing spin asymmetry is associated with the increasing in-plane magnetisation in the recording layer and the ECC layer of the perpendicular magnetic medium. The increasing in-plane magnetisation experienced with increasing magnetic field is accounted for by the mathematical model developed based on Blundell's work [13]. The mathematical model along with the non-linear least squares fitting program are together used to determine the magnetisation across the recording layer and the ECC layer at different magnetic fields [13,18].

Figure 7.8, Figure 7.9, Figure 7.10, Figure 7.11, Figure 7.12, Figure 7.13 and Figure 7.14 plot the spin up and spin down reflectivity plots along with their spin asymmetry determined by increasing in-plane magnetic fields from 2000 Oe to 10000 Oe. The magnetisation in the recording layer and ECC layer is determined at these increasing fields and the spin asymmetry determined is fitted [9,13].

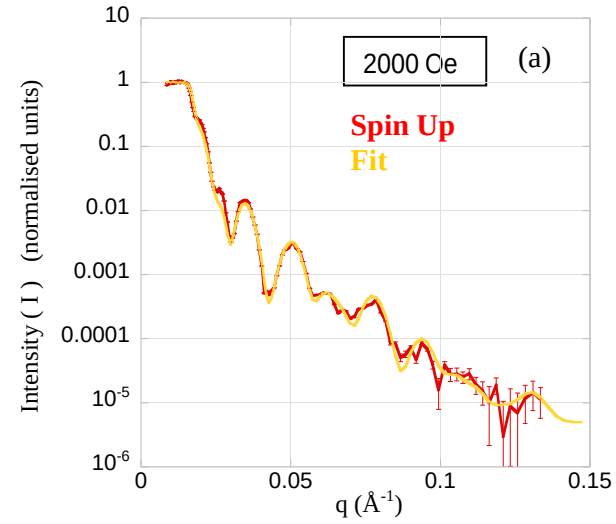


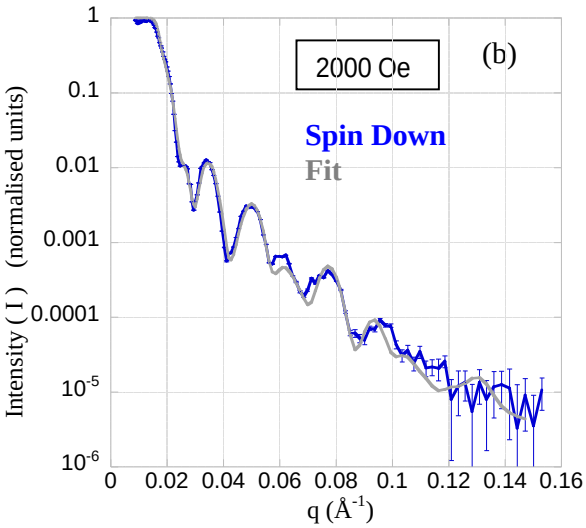


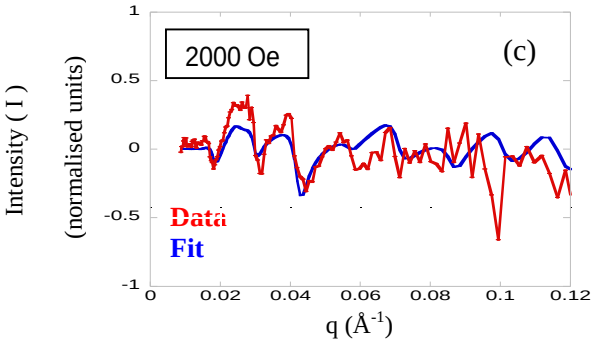


Figure 7.8 (a) and (b) Spin 'up' and Spin 'down' reflectivity plots with simulated fits at an in-plane magnetic field of 2000 Oe (c) Spin asymmetry for the 2000 Oe in-plane magnetic field data with a simulated fit

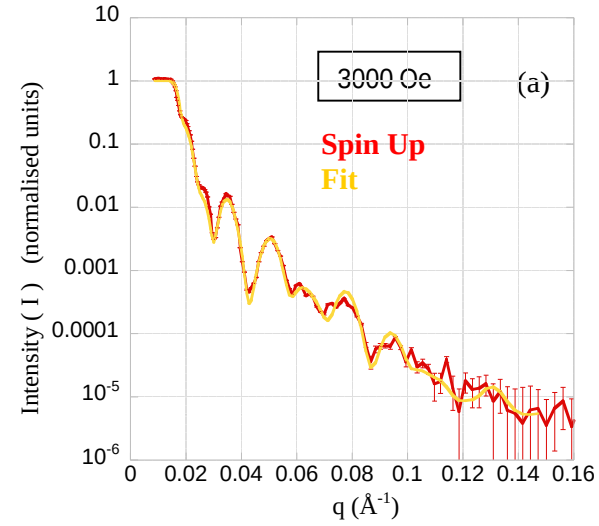


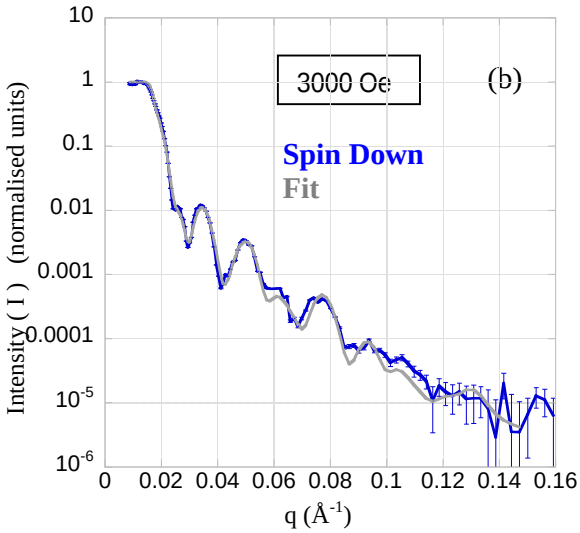


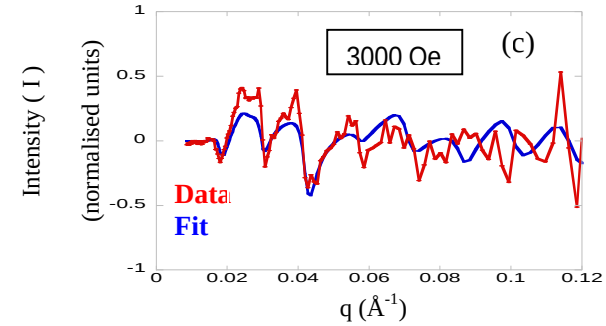


**Figure 7.9** (a) and (b) Spin 'up' and Spin 'down' reflectivity plots with simulated fits at an in-plane magnetic field of 3000 Oe (c) Spin asymmetry for the 3000 Oe in-plane magnetic field data with a simulated fit

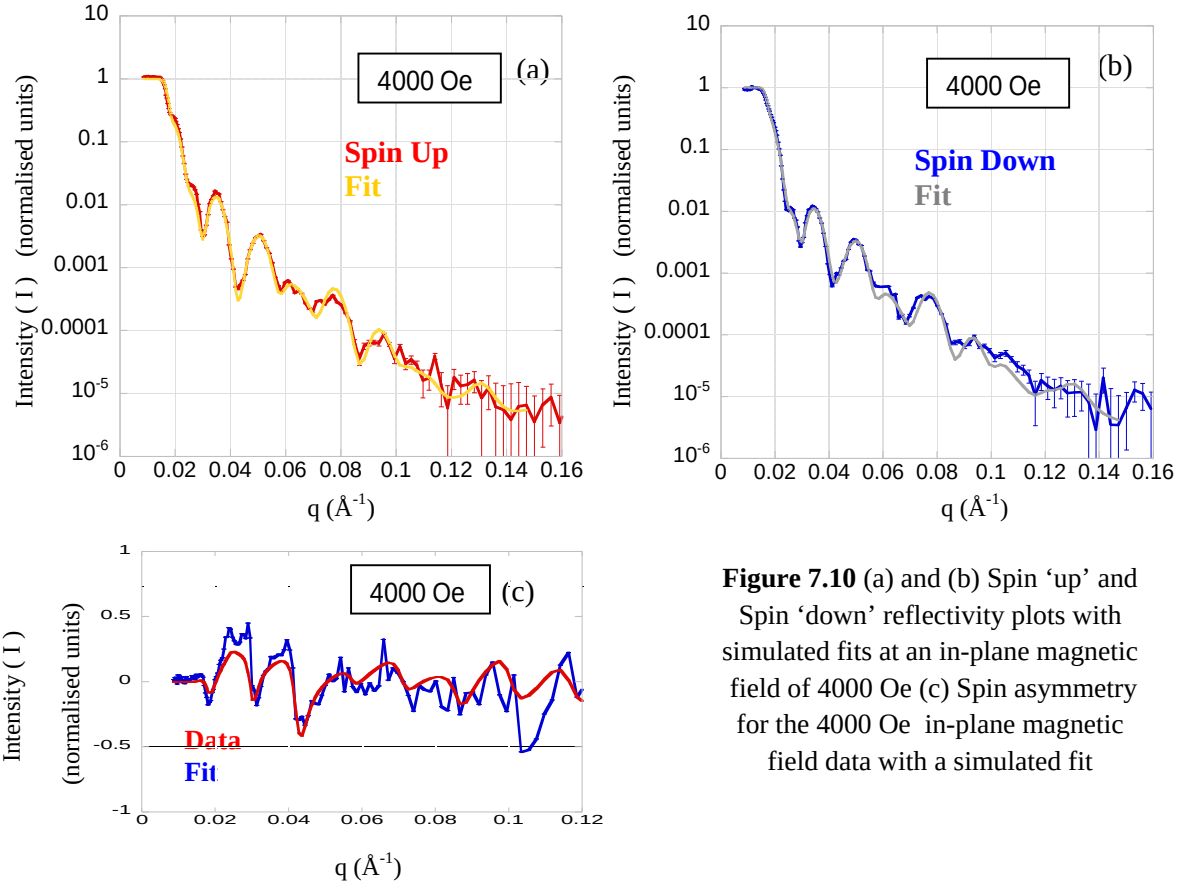


**Figure 7.10** (a) and (b) Spin 'up' and Spin 'down' reflectivity plots with simulated fits at an in-plane magnetic field of 4000 Oe (c) Spin asymmetry for the 4000 Oe in-plane magnetic field data with a simulated fit

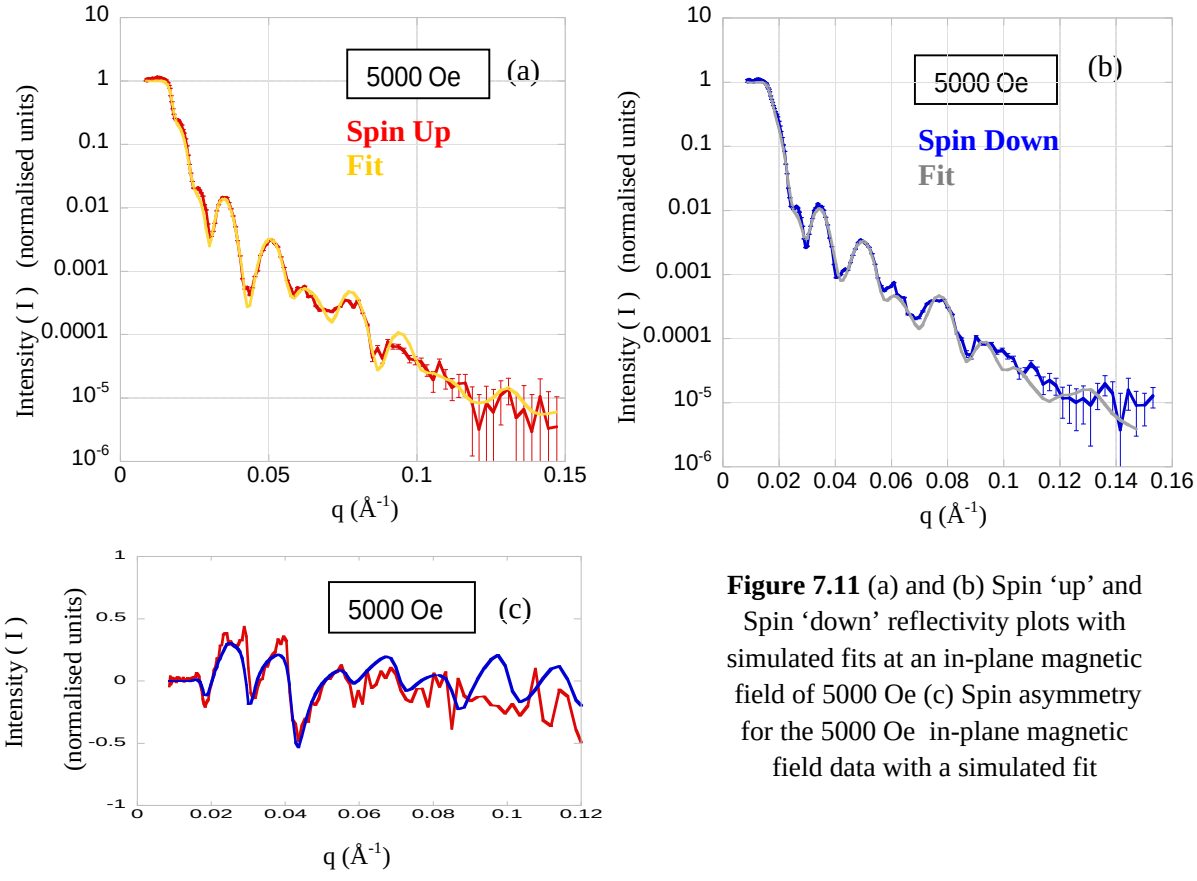


**Figure 7.11** (a) and (b) Spin 'up' and Spin 'down' reflectivity plots with simulated fits at an in-plane magnetic field of 5000 Oe (c) Spin asymmetry for the 5000 Oe in-plane magnetic field data with a simulated fit

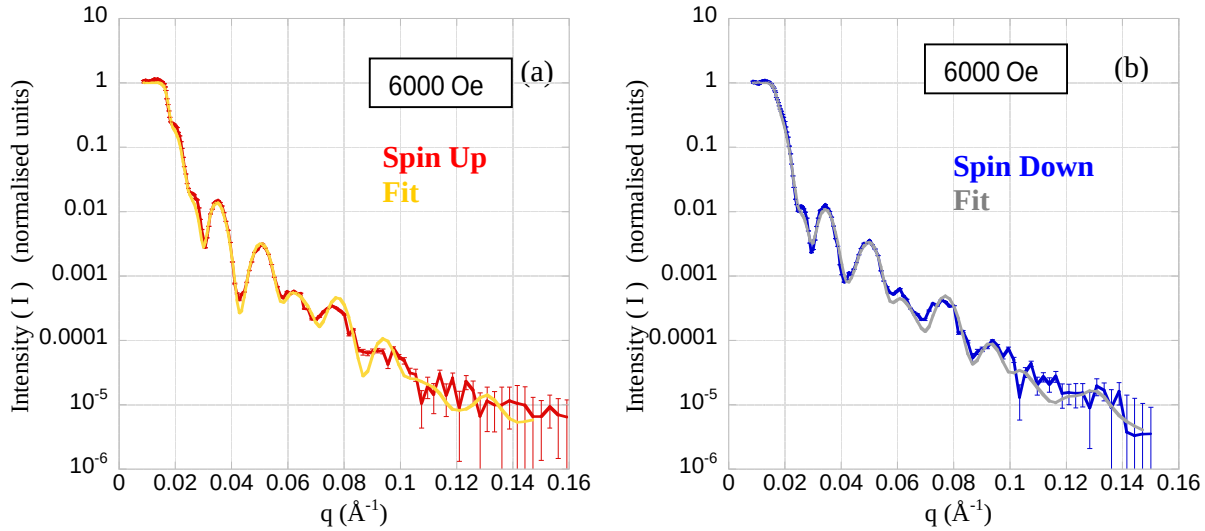


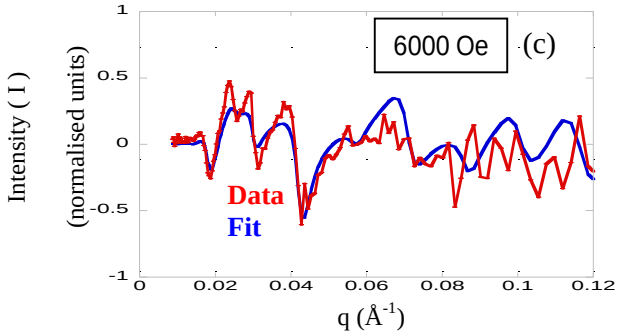


**Figure 7.12** (a) and (b) Spin 'up' and Spin 'down' reflectivity plots with simulated fits at an in-plane magnetic field of 6000 Oe (c) Spin asymmetry for the 6000 Oe in-plane magnetic field data with a simulated fit

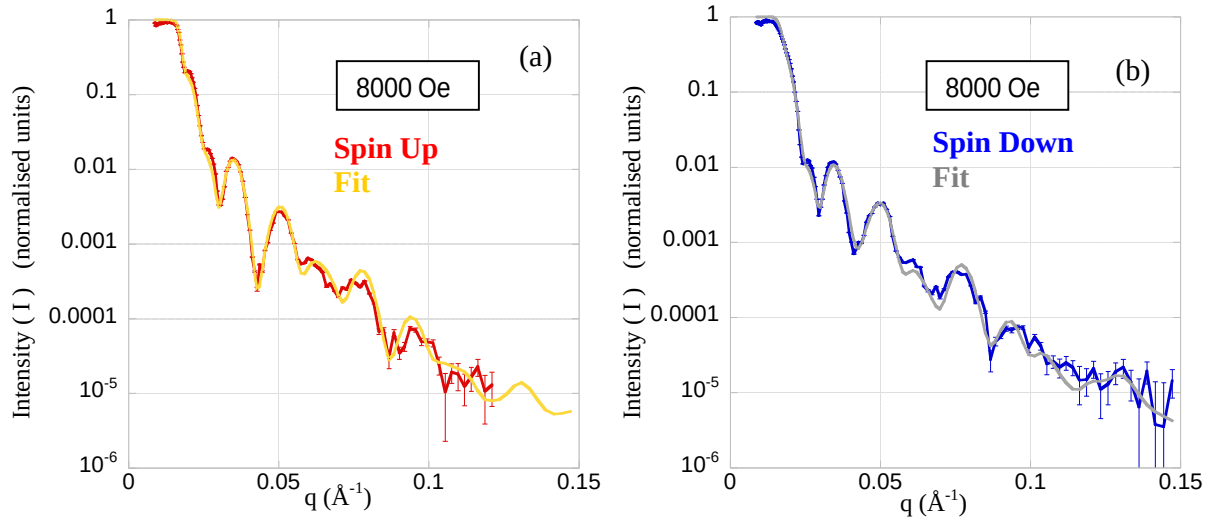


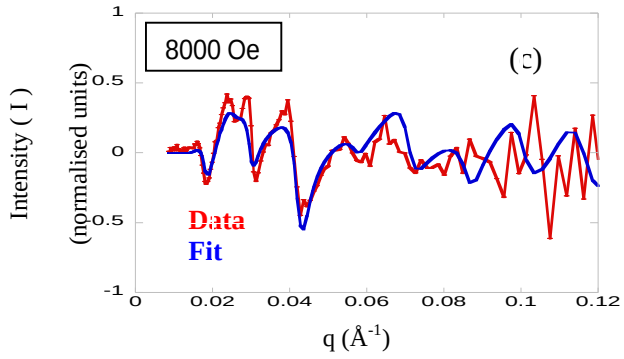


**Figure 7.13** (a) and (b) Spin 'up' and Spin 'down' reflectivity plots with simulated fits at an in-plane magnetic field of 8000 Oe (c) Spin asymmetry for the 8000 Oe in-plane magnetic field data with a simulated fit

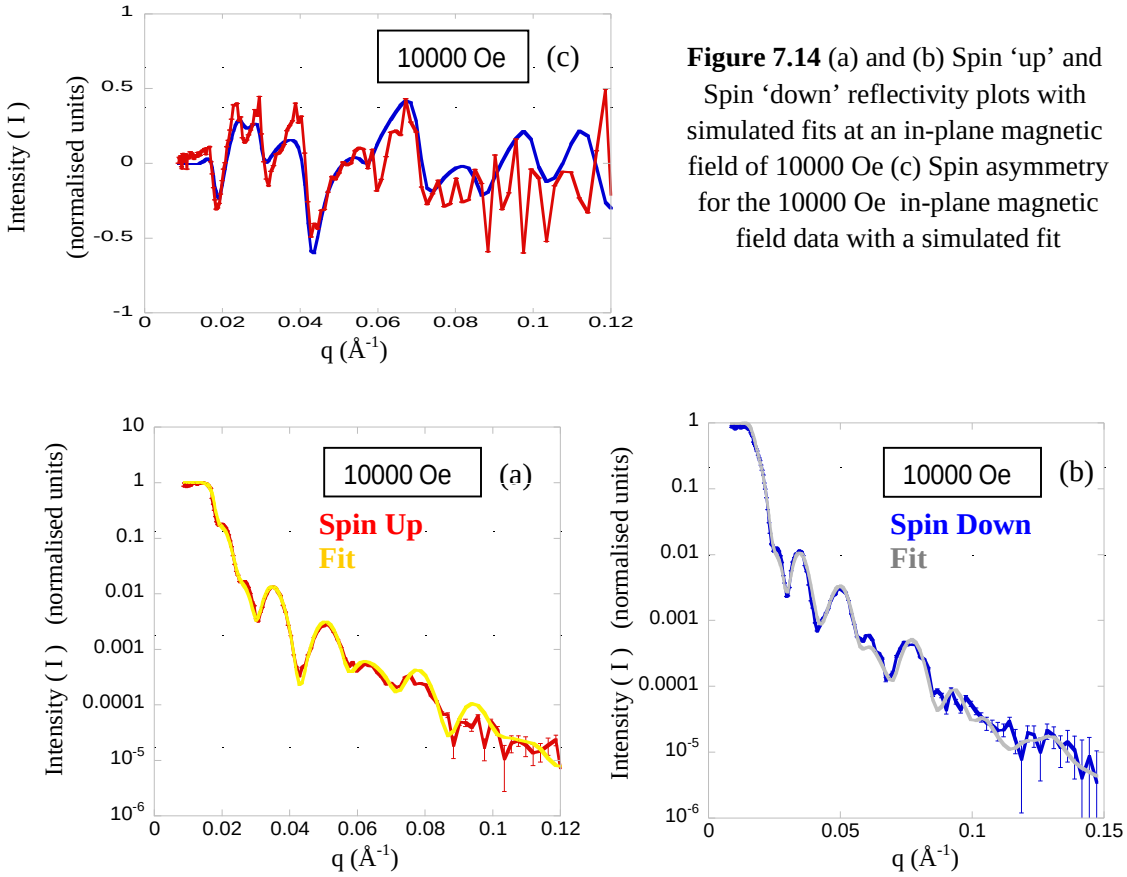


**Figure 7.14** (a) and (b) Spin 'up' and Spin 'down' reflectivity plots with simulated fits at an in-plane magnetic field of 10000 Oe (c) Spin asymmetry for the 10000 Oe in-plane magnetic field data with a simulated fit

From Figure 7.8, Figure 7.9, Figure 7.10, Figure 7.11, Figure 7.12, Figure 7.13 and Figure 7.14 it is evident that the simulated fits for the 'spin up' and 'spin down' data match the reflectivity data plot. The magnetisation values determined using the simulated fit are then compared at different fields in order to understand the difference in magnetic properties of the ECC layer and recording layer, shedding more light on their roles in the perpendicular magnetic system [2].

### 7.4.3 Comparing magnetisation in the recording layer and the ECC layer

The magnetisation in the recording layer and the ECC layer are plotted as function of increasing field. At 2000 Oe, the magnetisation in the ECC layer is larger than that of the recording layer. This increase in magnetisation in the ECC layer with applied in-plane magnetic field is observed up to a magnetic field of 5000 Oe. This states that up to a field of about 5000 Oe the ECC layer magnetises faster than the recording layer. However on further increasing the applied magnetic field, the magnetisation in the ECC layer saturates at around 0.23 A/m, when compared to magnetisation in the recording layer that rises linearly.

Now in order to interpret these results, the magnetic and physical properties of the two layers are investigated [14,17]. From previous results in Chapter 6 and available literature, the recording layer is known to comprise of CoCrPt grains with strong out-of-plane magneto-crystalline anisotropy that dominate the grains [6,17]. The magnetic grains in the recording layer thereby require a strong in-plane magnetic field in order to saturate the magnetic grains in a direction away from its favourable out-of-plane magnetic axis [17,22].

It is found from the analysis that an in-plane magnetic field of 10000 Oe is not sufficient to saturate the magnetic grains along the plane of the films. In order to achieve saturation magnetisation in the recording layer a higher in-plane magnetic field beyond 10000 Oe would be required [22]. This is not possible in this experiment due to limitations in the present experimental setup.

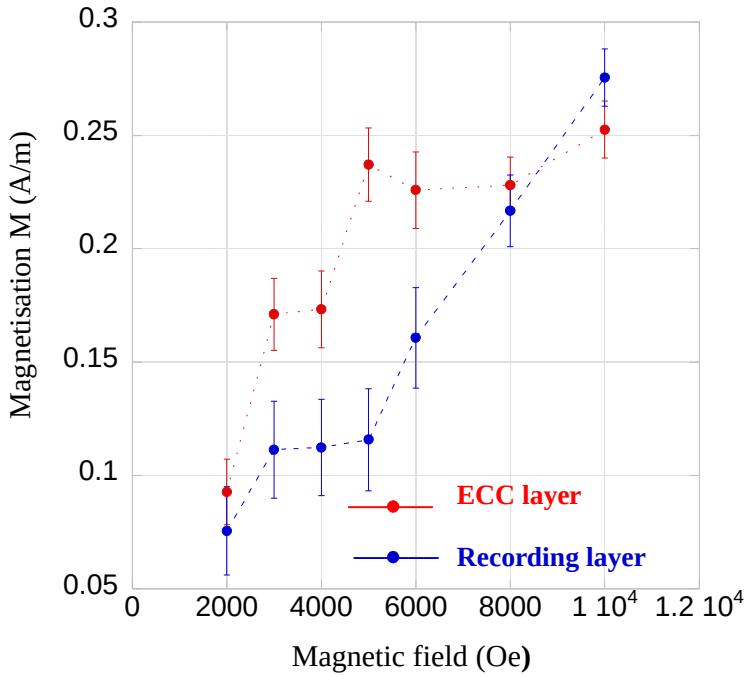


**Figure 7.15** Magnetisation as a function of applied in-plane magnetic field compared between the recording and ECC layers

The ECC layer from its magnetisation behaviour shows higher magnetisation values at lower magnetic field when compared to the recording layer, suggesting a magnetically softer layer that is easily driven to saturation magnetisation at in-plane magnetic field of 5000 Oe [1,2,4]. Hence the ECC layer is very different to the recording layer, with lower in-plane magnetic saturation and no nanoscale magnetic granular structure. The physical and magnetic properties associated with the ECC layer facilitate CoCrPt magnetic grain switching in the recording layer of the perpendicular magnetic medium [14]. The properties of the ECC layer enable high anisotropy magnetic grain switching in the recording layer at low fields by exchange coupling with the recording layer of the perpendicular magnetic medium [1,4].

## 7.5 Conclusion

In this chapter, PNR has been used to successfully characterise the composition and the structure of the perpendicular magnetic medium [9,12]. The multi-layered structure with its varying thicknesses and composition has been characterised in detail with polarised neutrons. The thicknesses and composition to a large extent represent the initial structure given by Hitachi GST, however the exchange control layer (ECL) that was expected to be present between the ECC layer and the recording layer remained undetected in the experimental data. The analytical model also determines scattering length densities in thin films that closely match their expected bulk values.

The chemical composition characterised gives a clear distinction between the recording layer and the ECC layer, which are the only two magnetic layers in thin film [14,17]. A detailed understanding of the magnetisation across the ECC layer and the recording layer is then undertaken by performing polarised neutron reflectivity experiments at increasing magnetic fields mapping out the changing magnetisation in the recording layer and the ECC layer at different magnetic fields [9,12].

The ECC layer was found to be magnetically softer than the granular recording layer [1,12]. The ECC layer was also found to saturate by an in-plane magnetic field of about 5000 Oe, however this was not the case with the recording layer. The recording layer did not saturate even with an in-plane magnetic field of 10000 Oe. This is as a result of a granular structure in the recording layer that exhibits a strong out-of-plane magneto-crystalline anisotropy, hence requiring a large in-plane magnetic field to drive the magnetic grains to saturation along the plane of the thin film [6,17].

## 7.6 References


[1] D. Suess, J. Lee, J. Fidler, T. Schrefl "Exchange-coupled perpendicular media" Journal of Magnetism and Magnetic Materials, 321(6), (2009) p.545-554 (DOI: 10.1016/j.jmmm.2008.06.041)

[2] H.S. Jung, E.M.T. Velu, S.S. Malhotra, G. Bertero, U. Kwon "Comparison of media properties between hard/soft stacked composite and capping layer perpendicular recording media" Journal of Magnetism and Magnetic Materials, 320(22), (2008) p.3151-3156 (DOI: 10.1016/j.jmmm.2008.08.077)

[3] Rujun Tang, Sherlyn Chua, Wanli Zhang, Yanrong Li "Effects of soft layer softness on the magnetic properties of perpendicular exchange-coupled nanocomposite films" Journal of Magnetism and Magnetic Materials, 323(21), (2011) p.2569-2574 (DOI: 10.1016/j.jmmm.2011.05.034)

[4] T.D. Lee, S.C. Lee, Y.W. Tahk "Micromagnetic studies on exchange-coupled composite media" Journal of Magnetism and Magnetic Materials, 303(2), (2006) p.276-281 (DOI: 10.1016/j.jmmm.2006.01.248)

[5] L.H. Lewis, J. Kim, K. Barmak "The CoPt system: a natural exchange spring" Physica B: Condensed Matter, 327(2–4), (2003) p.190-193 (DOI: 10.1016/S0921-4526(02)01725-8)

[6] S. J. Lister, T. Thomson, J. Kohlbrecher, K. Takano, V. Venkataramana, S. J. Ray, M. P. Wismayer, M. A. de Vries, H. Do, Y. Ikeda, and S. L. Lee "Size-dependent reversal of grains in perpendicular magnetic recording media measured by small-angle polarized neutron scattering" Applied Physics Letters, 97 (11), (2010) (DOI: 10.1063/1.3486680)

[7] J. Kohlbrecher, W. Wagner "The new SANS instrument at the Swiss spallation source SINQ", J. Appl. Cryst. 33, (2000) p.804-806 (DOI: 10.1107/S0021889800099775)

[8] J.D. O'Neill, S. Langridge, R.M. Dalgliesh, A.A. Zhukov, J.-M.L. Beaujour, G.J. Bowden, P.A.J. de Groot, B.D. Rainford, R.C.C. Ward, M.R. Wells "Neutron reflectometry studies of exchange springs in DyFe2/YFe2 superlattices" Journal of Magnetism and Magnetic Materials, 272–276 (2), (2004) p.1258-1259 (DOI: 10.1016/j.jmmm.2003.12.093)

[9] Hartmut Zabel, Ralf Siebrecht, Andreas Schreyer "Neutron reflectometry on magnetic thin films" Physica B: Condensed Matter, 276–278, (2000) p. 17-21 (DOI: 10.1016/S0921-4526(99)01469-6)

[10] J.A. Borchers, J.A. Dura, C.F. Majkrzak, S.Y. Hsu, R. Lolee, W.P. Pratt, J. Bass "Polarized neutron reflectivity characterization of weakly coupled Co/Cu multilayers" Physica B: Condensed Matter, 283(1–3), (2000) p. 162-166 (DOI: 10.1016/S0921-4526(99)01920-1)

[11] G.P Felcher "Polarized neutron reflectometry – a historical perspective" Physica B: Condensed Matter, 267–268, (1999) p.154-161 (DOI: 10.1016/S0921-4526(99)00053-8)

[12] Hartmut Zabel "Spin polarized neutron reflectivity of magnetic films and superlattices" Physica B: Condensed Matter, 198(1–3), (1994) p.156-162 (DOI: 10.1016/0921-4526(94)90151-1)

[13] S. J. Blundell and J. A. C. Bland "Polarised neutron reflection as a probe of magnetic films and multilayers" Phys. Rev. B, 46(6), (1992) p.3391-3400 (DOI: 10.1103/PhysRevB.46.3391 )

[14] A. Bill, H.B. Braun "Magnetic properties of exchange springs" Journal of Magnetism and Magnetic Materials, 272–276(2), (2004) p.1266-1267 (DOI: 10.1016/j.jmmm.2003.12.097)

[15] M. Futamoto, Y. Hirayama, N. Inaba, Y. Honda, A. Kikukawa " Effect of Nonmagnetic Underlayer on Structural and Magnetic Properties of CoCr-alloy Thin Film Media" IEIC Technical Report, 100(422), (2000) p.15-20 (ISSN:0913-5685)

[16] D. Clemens, P. Gross, P. Keller, N. Schlumpf, M. Könnecke "AMOR - the versatile reflectometer at SINQ" Physica B: Physics of Condensed Matter, 27, (2000) p. 140-141 (DOI: 10.1016/S0921-4526(99)01386-1)

[17] S. N. Piramanayagam "Perpendicular recording media for hard disk drives" J. Appl. Phys. 102, 011301 (2007) (DOI: 10.1063/1.2750414)

[18] D.W.O. Rogers " Analytic and graphical methods for assigning errors to parameters in non-linear least squares fitting" Nuclear Instruments and Methods, 127(2), (1975) p.253-260 (DOI : 10.1016/0029-554X(75)90496-6)

[19] Albert-Jose Dianoux, Gerry Lander "Neutron Data Booklet" OCP Science, Chicago (2003) (ISBN-13: 978-0970414373)

[20] C.L. Platt, K.W. Wierman, E.B. Svedberg, T.J. Klemmer, J.K. Howard, David J. Smith "Structural and magnetic properties of CoCrPt perpendicular media grown on different buffer layers" Journal of Magnetism and Magnetic Materials, 247(2), (2002) p.153-158 (DOI: 10.1016/S0304-8853(02)00041-0)

[21] Z. Xu, H.N. Hu, S.M. Zhou, S.L. Ren, X.X. Zhang "Combined effects of heat treatment and seed layer materials on magnetic properties of CoCrPt perpendicular media" Thin Solid Films, 516 (8), (2008) p.2071-2077 (DOI: 10.1016/j.tsf.2007.09.045)

[22] T. Thomson, B. Lengsfield, H. Do, B. Terris "Magnetic anisotropy and reversal mechanisms in dual layer exchanged coupled perpendicular media" Journal of Applied Physics, 103(7), (2008) (DOI: 10.1063/1.2839310)

# Chapter 8
# Summary and Future work

The reported work describes how polarised neutrons can be used to investigate both the structure and magnetic properties of perpendicular magnetic media. The achievements of this thesis include,

(a) Identifying the shape, size and distribution of the CoCrPt grains in the recording layer. This is obtained by taking the difference between the 'spin up' and 'spin down' polarised neutron scattering, giving us a product of the nuclear and magnetic scattering from the CoCrPt grains in the recording layer [1].
(b) Identifying the magnetic component of the CoCrPt granular structure, by determining a constant ratio between the physical and magnetic grain sizes [1].
(c) Determining the effect of varying recording layer thickness, on the size, shape and CoCrPt grain distribution using PolSANS.
(d) Understanding magnetic switching of the CoCrPt grains in the recording layer at different magnetic fields using a size dependant switching model [2].
(e) Establishing the absence of nanoscale magnetic granular structure in the ECC layer by observing the absence of nuclear and magnetic interference scattering from the ECC layer in the PolSANS geometry.
(f) Determining the influence of the exchange layer on the size dependant magnetic switching of the CoCrPt grains in the recording layer and finally [3,4].
(g) Determining the magnetic and structural properties of the multi-layered thin film perpendicular magnetic media structure using polarised neutron reflectivity [5].

The reported achievements have been made possible within the defined time frame of the PhD thesis. There however exist numerous areas, where both the characterisation technique used and the materials characterised, could be further researched. Magnetic materials similar to perpendicular magnetic recording media, like other potential magnetic data storage materials could be characterised using polarised neutron characterisation techniques.

Several potential magnetic data storage ideas like patterned magnetic media and magnetic nanoparticles are presently being researched for data storage applications [6,7]. Patterned magnetic media uses lithography techniques, to pattern nanoscale magnetic islands on materials using electron beam or advanced UV photolithography techniques [6]. PolSANS could be potentially used here as a technique to characterise the structure and magnetic properties of the nanoscale magnetic islands in the patterned magnetic recording medium. PolSANS could also be used to investigate field induced magnetic switching of the nanoscale magnetic islands in the patterned magnetic recording medium.

Fe and FePt magnetic nanoparticles are also widely researched for potential magnetic data storage applications [7]. By controlling the size, shape and organisation of nanoscale magnetic particles, nanoscale magnetic particles could be used for future data storage applications [7]. PolSANS can be used here to probe the size, shape and distribution of the magnetic nanoparticles and also understand their physical and magnetic properties. Artificially frustrated magnetic systems are another area of research, for potential data storage applications [8]. Here PolSANS could potentially be used to investigate long range magnetic ordering in the nanoscale magnetic system.

Along with PolSANS, PNR has also been widely used to study magnetic properties of other thin film magnetic structures similar to perpendicular recording media. PNR has been used to study spin valve magnetic structures that are used as magnetic read heads in data storage technology [9]. PNR has also previously been used to characterise organic thin films, investigating their physical and magnetic properties.

Apart from using neutrons to characterise magnetic systems similar to that of perpendicular media, there also exists the possibility to use other large scale characterisation techniques to better understand the physical and magnetic properties of the thin film perpendicular magnetic medium. Although PolSANS identifies the magnetic component of the physical CoCrPt grain, the technique fails to characterise the elemental composition associated magnetisation in individual CoCrPt grains [10].

Resonant soft x-rays with their ability to interact better with the electron clouds provide better compositional information in comparison to neutron scattering techniques [11]. Using Small angle x-ray scattering (SAXS) the composition and the elemental distribution of the CoCrPt grains can be determined. This information along with the PolSANS results could be used to identify the magnetic component of the grain in terms of its elemental composition [11].

Another interesting x-ray experiment would be, carrying out magnetic switching studies on the CoCrPt grains using x-rays. These experiments are expected to give composition based magnetic switching information which would complement the magnetic grain switching results obtained using neutrons. This sort of experiment is possible using the experimental setup based at the POLLUX beam line at PSI, Switzerland where x-ray lenses focus the x-ray beam to nanoscale dimensions to chemically map nanoscale structures. Magnetic switching studies on nanoscale magnetic structures using an applied magnetic field have also been previously carried out at this beam line [11].

## 8.1 References


[1] S. J. Lister, M. P. Wismayer, V. Venkataramana, M. A. de Vries, S. J. Ray, S. L. Lee, T. Thomson, J. Kohlbrecher, H. Do, Y. Ikeda, K. Takano, and C. Dewhurst "Small-angle polarized neutron studies of perpendicular magnetic recording media" Journal of Applied Physics, 106(6),(2009) p. 063908 - 063908-4 (DOI: 10.1063/1.3213381)

[2] S. J. Lister, T. Thomson, J. Kohlbrecher, K. Takano, V. Venkataramana, S. J. Ray, M. P. Wismayer, M. A. de Vries, H. Do, Y. Ikeda, and S. L. Lee "Size-dependent reversal of grains in perpendicular magnetic recording media measured by small-angle polarized neutron scattering" Applied Physics Letters, 97 (11), (2010) (DOI: 10.1063/1.3486680)

[3] D. Suess, J. Lee, J. Fidler, T. Schrefl "Exchange-coupled perpendicular media" Journal of Magnetism and Magnetic Materials, 321(6), (2009) p.545-554 (DOI: 10.1016/j.jmmm.2008.06.041)

[4] A. Bill, H.B. Braun "Magnetic properties of exchange springs" Journal of Magnetism and Magnetic Materials, 272–276(2), (2004) p.1266-1267 (DOI: 10.1016/j.jmmm.2003.12.097)

[5] Hartmut Zabel, Ralf Siebrecht, Andreas Schreyer "Neutron reflectometry on magnetic thin films" Physica B: Condensed Matter, 276–278, (2000) p. 17-21 (DOI: 10.1016/S0921-4526(99)01469-6)

[6] S.N. Piramanayagam, K. Srinivasan "Recording media research for future hard disk drives" Journal of Magnetism and Magnetic Materials, 321(6), (2009) p.485-494 (DOI: 10.1016/j.jmmm.2008.05.007)

[7] S. Mørup, M.F. Hansen, C. Frandsen "Magnetic Nanoparticles" Comprehensive Nanoscience and Technology, 1, (2011) p.437-491 (DOI: 10.1016/B978-0-12-374396-1.00036-2)

[8] Elena Mengotti, Laura J. Heyderman, Arantxa Fraile Rodríguez, Frithjof Nolting, Remo V. Hügli, Hans-Benjamin Braun " Real-space observation of emergent magnetic

monopoles and associated Dirac strings in artificial kagome spin ice ” Nature Physics 7, (2011) p.68–74 (DOI: 10.1038/nphys1794)

[9] A. van der Graaf, A.R. Ball, J.C.S. Kools “Magnetic alignment in spin-valve system studied by polarized neutron reflectometry” Journal of Magnetism and Magnetic Materials, 165(1–3), (1997) p.479-483 (http://dx.doi.org/10.1016/S0304-8853(96)00597-5)

[10] Wim G. Bouwman, Jeroen Plomp, Victor O. de Haan, Wicher H. Kraan, Ad A. van Well, Klaus Habicht, Thomas Keller, M. Theo Rekveldt “Real-space neutron scattering methods” Nuclear Instruments and Methods in Physics Research Section A: Accelerators, Spectrometers, Detectors and Associated Equipment, 586 (1), (2008) p.9-14 (DOI: 10.1016/j.nima.2007.11.045)

[11] Gerrit van der Laan “Studying spintronics materials with soft X-ray resonant scattering” Current Opinion in Solid State and Materials Science, 10(2), (2006) p.120-127 (DOI: 10.1016/j.cossms.2006.11.007)